The build-up of stellar mass in primeval galaxies

Lukas Furtak

To cite this version:

Lukas Furtak. The build-up of stellar mass in primeval galaxies. Astrophysics [astro-ph]. Sorbonne Université, 2021. English. NNT : 2021SORUS408 . tel-03652860

HAL Id: tel-03652860
https://theses.hal.science/tel-03652860v1

Submitted on 27 Apr 2022

Thèse de doctorat en astrophysique

Sorbonne Université

Ecole doctorale n°127 Astronomie et Astrophysique d'Ile de France

Institut d'Astrophysique de Paris

The build-up of stellar mass in primeval galaxies

La formation de masse stellaire dans les galaxies primordiales

Lukas J. Furtak

Directeur de thèse: Dr. Matthew D. Lehnert
Co-encadrant de thèse: Dr. Hakim Atek

Présentée et soutenue publiquement le

23 Novembre, 2021

devant un jury composé de

Dr. Françoise Combes	Observatoire de Paris	Présidente du jury
Dr. Roser Pello	Laboratoire d'Astrophysique de Marseille	Rapporteur
Dr. Sune Toft	Cosmic Dawn Center	Rapporteur
Dr. Charlotte Mason	Cosmic Dawn Center	Examinateur
Dr. Stéphane Arnouts	Laboratoire d'Astrophysique de Marseille	Examinateur
Dr. Matthew D. Lehnert	Centre de Recherche Astrophysique de Lyon	Directeur de thèse
Dr. Hakim Atek	Institut d'Astrophysique de Paris	Invité

“*Ninety per cent of most magic merely consists of knowing one extra fact.*”

— Sir Terry Pratchett, *Night Watch*, 2002

Contents

Abstract

Early star-forming galaxies at redshifts $z \gtrsim 6$ in the epoch of cosmic reionization are at the frontier of observability with the current instrumentation and many of their physical properties remain widely uncertain. Since these galaxies represent the progenitors of present-day galaxies, *the galaxy stellar mass function* (GSMF) out to $z \sim 6-10$ is a robust and crucial tool to study the build-up of stellar mass in the Universe and provides the tightest constraints on cosmological simulations.

These high-redshift galaxies are very faint and thus particularly hard to observe in blank fields. Strong gravitational lensing by massive galaxy clusters however allows to probe $z \sim 6-10$ galaxies down to $10^6\,\mathrm{M}_\odot$, providing valuable constraints on the very low-mass end of the GSMF. Until the *James Webb Space Telescope* (JWST) comes online however, these galaxies can only be observed in a few broad-band *Hubble Space Telescope* (HST) and *Spitzer*/IRAC filters, making the derivation of their stellar mass particularly difficult, i.e. requiring assumptions on parameters such as star-forming history, stellar age, dust content, metallicity, etc. In the first project of this work, we have therefore carefully investigated the impacts of SED-fitting assumptions on $z \sim 6-7$ GSMF measurements in order to assess what is believable in the resulting GSMF when considering these uncertainties. We have found the very low-mass end to be particularly vulnerable to lensing systematics and SED-fitting assumptions.

In the second project of this work, we assemble a photometric catalog of $z \sim 6-10$ galaxy candidates from new HST observations of six massive lensing clusters, the BUFFALO survey. Our analysis of the first cluster, Abell 370, yielded 128 high-redshift candidates. These will present prime targets for the JWST and ground-based facilities for spectroscopic follow-up observations.

The derivation of high-redshift GSMFs further requires accurate knowledge of the effective survey volume. This is usually accomplished for rest-frame UV luminosity functions which are then converted to GSMFs using measured mass-to-light relations. More robust derivations of high-redshift GSMFs however require direct measurements of stellar mass completeness, which includes a comprehensive assessment of the effects of stellar populations properties. The final project of this work therefore consists of our recent efforts to develop completeness simulations that allow us to directly estimate survey completeness in stellar mass through strong lensing clusters. These simulations include the combined effects of gravitational lensing, multiwavelength detections, stellar population assumptions and galaxy physical parameter degeneracies in order to yield the most complete and robust estimates of the GSMF uncertainties as possible. We will test these methods on the high-redshift galaxy samples obtained with BUFFALO.

The results obtained over the course of this work and the methods that we developed will contribute to the overall effort to get the most out of future facilities such as the JWST and pushing the limits of observability ever further towards the cosmic dawn.

Résumé

Les galaxies primordiales à redshift $z \gtrsim 6$ dans l'époque de la réionisation cosmique sont à la frontière de l'observable avec l'instrumentation actuelle et beaucoup de leurs propriétés physiques demeurent largement incertaines. Puisque ces galaxies représentent les stades primordiaux de l'évolution des galaxies, leur *fonction de masse stellaire* (GSMF) est une mesure robuste et cruciale pour étudier l'accumulation de masse stellaire dans l'Univers et fournit les contraintes les plus serrées aux simulations cosmologiques.

Ces galaxies à haut redshift sont très peu lumineuses et donc particulièrement difficiles à observer dans les champs profonds. Le lentillage gravitationnel produit par des amas de galaxies massifs permet en revanche d'observer ces galaxies à $z \sim 6-10$ jusqu'au plus faibles masses ($M_\star \sim 10^6\,\mathrm{M}_\odot$), fournissant ainsi de précieuses contraintes sur leur GSMF à faible masse. Jusqu'au lancement du *James Webb Space Telescope* (JWST), ces galaxies ne peuvent être observées que dans quelques filtres à bande large du *Hubble Space Telescope* (HST) et de *Spitzer*. Cela rend la dérivation de leur GSMF particulièrement délicate et requiert des hypothèses non-vérifiées sur des paramètres physiques tel l'historique de la formation d'étoiles, l'age stellaire, la poussière, la métallicité, etc. Dans le premier projet de cette thèse, nous avons donc soigneusement étudié les impacts de ces hypothèses sur la mesure de la GSMF à $z \sim 6-7$ pour évaluer qu'est-ce qui est crédible dans ce genre d'étude vis-a-vis de ces incertitudes. Nous avons trouvés que la GSMF à faible masses est particulièrement vulnérable aux systématiques des modèles de lentillage gravitationnel et aux hypothèses sur les populations stellaires.

Pour le second projet de cette thèse, nous avons assemblé un catalogue photométrique de candidates galaxies à $z \sim 6-10$ dans de nouvelles observations HST de six amas massifs, le survey BUFFALO. Notre analyse du premier amas, Abell 370, a révélé 128 candidates. Ces galaxies représenteront des cibles parfaites pour des observations de suivi spectroscopiques avec le JWST et d'instruments au sol.

Les dérivations de GSMFs à haut redshift requièrent une connaissance précise du volume observé par le survey. Ceci est normalement déterminé à partir de la fonction de luminosité UV qui est ensuite convertie en GSMF en utilisant des ratios masse-lumière empiriques. Néanmoins, des dérivations plus robustes de la GSMF à haut redshift requièrent une mesure directe de la complétude en masse stellaire en incluant une évaluation complète des effects des propriétés des populations d'étoiles. Le dernier projet de cette thèse consiste donc dans nos efforts pour développer des simulations de complétude qui nous permettront pour le première fois de directement estimer la complétude à travers les lentilles gravitationnelles en masse stellaire. Ces simulations incluent les effects combinés du lentillage gravitationnel, de la photométrie à multiple longueurs d'ondes, les hypothèses sur les populations d'étoiles et les dégénérescences de paramètres physiques des modèles de galaxies, pour fournir les estimations les plus robustes et les plus complètes que possibles des incertitudes de la GSMFs. Nous allons ensuite tester ces méthodes sur les échantillons de galaxies à haut redshift détectés dans BUFFALO.

Les résultats obtenus et les méthodes développées au cours de cette thèse vont contribuer à l'effort général pour exploiter les instrument futures tel le JWST au mieux de leur capacitées et à pousser les limites de l'instrumentation de plus en plus loin vers l'aube cosmique.

Introduction

> "Everything starts somewhere, although many physicists disagree."
>
> Sir Terry Pratchett,
> *Hogfather*, 1996

Less than half a million years after the Big Bang, as the Universe expanded and cooled, protons and electrons could eventually combine to atoms and filled the Universe with neutral gas of hydrogen, helium and trace amounts of lithium. It is out of this neutral gas that the first stars and galaxies formed. Eventually, the massive energy output of of the early generations of stars, galaxies and potentially black holes became intense enough to reionize the neutral hydrogen gas, thus initiating a phase change of almost the whole gas content in the Universe. This was the first and arguably the only occurrence of galaxies facilitating a nearly universal change of state of the whole Universe and it all happened within the first billion years of cosmic history. But how did these stars and galaxies form and evolve in conditions so different from the present-day Universe? For example, 'metals', i.e. elements heavier than hydrogen and helium, are crucial for efficient gas cooling. But by which mechanisms then could the primordial gas cool enough to form the first stars *before* the winds and explosions of these same stars could enrich the hydrogen gas with metals in the first place? Under these different conditions, what was the mass distribution of the dark matter (DM) halos in which the first stars and galaxies formed and what was the mass distribution of the early galaxies that reionized the Universe?

The high-redshift *galaxy stellar mass function* (GSMF), which measures the co-moving volume density of galaxies as a function of stellar mass, provides an invaluable observational measure of the physics of galaxy formation and evolution in the early Universe. Determining the shape of the GSMF, and in particular if and where there are cut-offs on the low- and the high-mass ends, is for example crucial for constraining cosmic reionization since it allows to assess if there were enough galaxies to provide the required ionizing flux. In addition, the low-mass end of the GSMF is in particular interesting for constraining galaxy formation models since the low-mass high-redshift galaxies are not yet evolved very far and thus represent a primordial state of galaxy evolution. It is because of these reasons that it is important to not only accurately measure the high-redshift GSMF but also to robustly probe its uncertainties.

In the last two decades, the advent of deep space-based observations, in particular with the *Hubble Space Telescope* (HST) and the *Spitzer Space Telescope* (*Spitzer*), has extended the reach of extragalactic studies from the local vicinity of the Milky Way all the way into the epoch of cosmic reionization. And yet, the extreme low-mass end of the high-redshift GSMF still remains elusive without a 'boost' in sensitivity provided by strong gravitational lensing (SL) which can increase the depth of deep HST observations by an average of two magnitudes. With the launch of the *James Webb Space Telescope* (JWST; Gardner et al., 2006) and its unprecedented near-infrared (NIR) sensitivity scheduled for December 18, 2021, the field of high-redshift galaxy observations is on the brink of a new era. One of the primary science goals of the JWST will be observing first light and primordial galaxies — the Cosmic Dawn — with supporting ground-based spectroscopy from high-sensitivity facilities such as the *Atacama Large Millimeter/submillimeter Array* (ALMA) and the upcoming *Extremely Large Telescope* (ELT). Nevertheless, even the JWST will require SL magnification to probe the extreme faint low-mass end of the high-redshift GSMF, in particular for ultra-deep imaging campaigns targeted at the lowest-mass galaxies at the highest redshifts. But how do SL uncertainties impact the GSMF measurements? Furthermore, many assumptions on e.g. star-forming history (SFH) or stellar age enter high-redshift GSMF measurements and can have a significant impact on stellar mass and star-forming rate (SFR) measurements. Without understanding these impacts on the measured stellar masses, how could we know if our high-redshift GSMF determination is robust and unbiased?

In an effort towards investigating these questions and preparing for the JWST era, my thesis work focuses on studying the low-mass end of the high-redshift GSMF with HST and *Spitzer* using gravitational lensing provided by six massive galaxy clusters. More precisely, I seek to understand and quantify the impacts that our methods of observation and galaxy modelling have on the resulting low-mass end of the GSMF and its uncertainties. How robustly *can* we constrain the low-mass end of the high-redshift GSMF? What are the limits of gravitational lensing and galaxy modeling techniques, their systematics and assumptions and how do they impact high-redshift GSMF results? And finally, which new methods do we need to develop in order to exploit the full power of the JWST and other future facilities? With these questions and the goal to deliver high-redshift GSMF measurements that *include* all of these impacts in their uncertainties in mind, my thesis work comprises three main projects:

- In chapter 3, which has been published in Furtak et al. (2021), we assess what is believable in high-redshift GSMF observations by robustly probing the uncertainties and systematically investigating the biases and systematics inherent to these kind of measurements.

- Chapter 4 describes our efforts to detect and select photometric high-redshift galaxy candidates in new HST observations of six gravitational lensing clusters, the BUFFALO survey, in order to increase the sample sizes of high-redshift galaxy candidates detected in or around the SL clusters and to provide targets for future instruments such as e.g. the JWST.

- In chapter 5, we develop new methods to for the first time estimate gravitationally lensed high-redshift galaxy sample completeness directly in stellar mass without needing to rely on corrections to rest-frame ultra-violet (UV) luminosity functions.

This manuscript is therefore structured as follows: I first introduce the scientific background and the technical aspects of high-redshift galaxy observations in chapters 1 and 2. The main scientific analyses and results of my thesis work are described in detail in chapters 3, 4 and 5 as mentioned above. I then put the results in the context of future prospects in chapter 6 before summing up my work in the conclusion on page 121. Throughout this work, I adopt a standard flat ΛCDM cosmology with $\Omega_m = 0.3$, $\Omega_\Lambda = 0.7$ and $H_0 = 70\,\frac{\mathrm{km}}{\mathrm{Mpc\,s}}$ and all magnitudes are quoted in the AB magnitude system (Oke & Gunn, 1983).

Publications

I here give a complete list of the scientific publications that resulted from the work accomplished over the course of my thesis.

First author publications:

- **Furtak L. J.**, Atek H., Lehnert M. D. et al. **(2021)**: "*How robustly can we constrain the low-mass end of the $z \sim 6-7$ stellar mass function? The limits of lensing models and stellar population assumptions in the* Hubble Frontier Fields", MNRAS, 501, 1568, doi: 10.1093/mnras/staa3760

Co-authored publications:

- Weaver J. R., Kauffmann O. B., Ilbert O., [. . .], **Furtak L. J.**, et al. **(2021)**: "*COSMOS2020: A panchromatic view of the Universe from $z \sim 10$ from two complementary catalogs*", accepted for publication in ApJS

- Steinhardt C. L., Jauzac M., [. . .], **Furtak L. J.**, et al. **(2020)**: "*The BUFFALO HST Survey*", ApJS, 247, 64, doi: 10.3847/1538-4365/ab75ed

Manuscripts in preparation:

- Atek H., **Furtak L. J.**, Oesch P., et al. **(submitted)**: "*The star formation burstiness and ionizing efficiency of low-mass galaxies*", submitted to MNRAS

- **Furtak L. J.**, Atek H., Lehnert M. D., et al. **(in prep.)**: Working title: "*Stellar mass completeness simulations and $z \sim 6-7$ GSMFs in the BUFFALO cluster Abell 370*"

Chapter 1

The high-redshift Universe

> “In the beginning there was nothing, which exploded.”
>
> ---
>
> Sir Terry Pratchett,
> *Lords and Ladies*, 1996

This thesis focusses on the study of distant galaxies — early star-forming galaxies (cf. section 1.3) — and the measurement of their stellar mass functions (cf. section 1.4). down to the lowest stellar masses. These galaxies formed and evolved when the Universe was less than one billion years old and the physical conditions were much different from the present-day Universe. This chapter therefore serves as an introduction to the early Universe, high-redshift galaxies and the scientific context of the present research.

I first introduce the cosmological background needed in this work in section 1.1 and then give a brief summary of cosmic history in section 1.2, up to the epochs that interest us here: the Cosmic Dawn and the epoch of cosmic reionization. I then describe the characteristics of galaxies in the early Universe in section 1.3 and finally explain the interest in measuring luminosity and stellar mass functions in section 1.4 which is one of the main goals of this work.

1.1 Background cosmology

Since galaxies form and evolve in our Universe, i.e. within a cosmological framework, I will begin by briefly introducing some of the fundamental concepts of cosmology. I will limit this to the concepts needed in this work however and refer the reader to e.g. Ryden (2016) for an exhaustive introduction to cosmology.

Under the most fundamental assumption of cosmology, the Universe is both homogeneous and isotropic, i.e. the Universe looks the same in all directions from any position. This *cosmological principle* is what permits us to describe the Universe with an overall cosmology and is well verified by observations of the CMB (e.g. Planck Collaboration et al., 2020b) and the large-scale ($\gtrsim 100\,\mathrm{Mpc}$) distribution of galaxies (e.g. Maddox et al., 1990; Gregory & Condon, 1991). While the propagation of light emitted by distant galaxies is in general a complicated problem in arbitrary spacetimes, it becomes significantly simpler if we assume the overall geometry of the Universe to be well described by a Friedmann-Lemaître-Robertson-Walker metric (Friedmann, 1922, 1924; Lemaître, 1927, 1933; Robertson, 1935, 1936a,b; Walker, 1937) given in e.g. Hartle (2021) as

$$ds^2 = c^2dt^2 - a(t)^2[dr^2 + S_\kappa(r)^2 d\Omega^2] \tag{1.1}$$

where $a(t)$ is the time-dependent dimensionless *scale factor* that describes the expansion of the Universe and $S_\kappa(r)$ describes the spatial curvature of the Universe (with $S_\kappa(r) = r$ in the flat case relevant for this work). In the expanding Universe, we can define *comoving coordinates* $\vec{r} = \vec{x}(t)/a(t)$ which remain constant with respect to the expansion unlike the physical coordinates $\vec{x}(t)$ which are time-dependent. The relative velocity of two freely falling galaxies in the expanding Universe is then

$$\vec{v}(t) = r\dot{a}(t) = \frac{\dot{a}}{a}\vec{x}(t) \tag{1.2}$$

where we can define the *Hubble parameter*

$$H(t) \equiv \frac{\dot{a}}{a} \tag{1.3}$$

which evaluated at the present time is called the *Hubble constant* $H_0 \equiv H(t_0)$. The most recent measurements of the CMB find the value of the Hubble constant to be $H_0 \simeq 67.4 \pm 0.5\,\frac{\mathrm{km}}{\mathrm{Mpc\,s}}$ (Planck Collaboration et al., 2020a). The Hubble-Lemaître law, equation (1.2) evaluated at t_0, was originally measured from distances and velocities of nearby galaxies (Lemaître, 1927; Hubble, 1929) and the fact that H_0 is always found to be positive is commonly interpreted as a sign that the Universe is expanding. Note that this so-called *Hubble flow* does not mean that galaxies actually move away from each other but rather that the space between them expands with time. Finally, bear in mind that equation (1.2) is only valid at sufficiently large scales where the cosmic expansion dominates the relative velocities of galaxies. On small scales, the relative velocities instead result from local dynamics which can also result in galaxies moving toward each other as is the case for e.g. the Milky Way and Andromeda.

1.1.1 Cosmological redshift

In the special case of a photon, emitted by a galaxy at time t_e with rest-frame wavelength λ_0, the expansion of the Universe results in a dilation of the photon's wavelength because the space the photon is traveling through is expanding. At a time $t_{\mathrm{obs}} > t_e$ the photon will then be observed at wavelength

$$\lambda_{\mathrm{obs}} = \frac{a(t_{\mathrm{obs}})}{a(t_e)}\lambda_0. \tag{1.4}$$

Since $\frac{a(t_{\mathrm{obs}})}{a(t_e)} > 1$, the wavelength is systematically shifted red-wards. We can therefore define the *cosmological redshift* of a galaxy as

$$z \equiv \frac{\lambda_{\text{obs}} - \lambda_0}{\lambda_0} = \frac{1}{a(t)} - 1 \tag{1.5}$$

where $t = t_e$,. As can be seen in equation (1.5), the redshift z and the scale factor a are interchangeable at any given time t so long as a evolves monotonically. In the present, $a(t_0) = 1$ and $z(t_0) = 0$ and galaxies at a higher redshift are more distant. As the redshift can directly be measured by observing a galaxy's spectrum it is often used as a unit of distance and look-back time. Note that for the purposes of this work I refer to $z \gtrsim 6$ as *high* redshift.

1.1.2 Cosmological distances

While we commonly use the cosmological redshift (1.5) as a distance indicator in the Universe, the physical definition and indeed the measurement of a *distance* in an arbitrary space-time is a highly non-trivial matter. Perhaps the most straight-forward definition is that of the *proper distance* $d_p(t)$ defined as the length of the spatial geodesic between two points at a fixed scale factor $a(t)$. The current proper distance to the light-emitting galaxy in section 1.1.1 would then be

$$d_p(t_0) = c \int_{t_e}^{t_0} \frac{\mathrm{d}t}{a(t)}. \tag{1.6}$$

However, in the general case of an arbitrary space-time the proper distance is not a measurable quantity and does not represent the actual path travelled by a photon. Instead the relation between the flux and the luminosity of a galaxy

$$f = \frac{L}{4\pi d_L^2}, \tag{1.7}$$

which can be generalized to

$$f = \frac{L}{4\pi S_\kappa(r)^2(1+z)^2} \tag{1.8}$$

for a curved and expanding space-time (e.g. Ryden, 2016), will define the so-called *luminosity distance* d_L of a galaxy. Combining equations (1.7) and (1.8), the luminosity distance is defined as

$$d_L \equiv S_\kappa(r)(1+z) = \sqrt{\frac{4\pi f}{L}} \tag{1.9}$$

which relates to the current proper distance as

$$d_L = d_p(t_0)(1+z) \tag{1.10}$$

in the case of a flat universe. Knowing the redshift of a galaxy, e.g. from measuring its spectrum, we can therefore use the flux and the redshift to compute that galaxy's emitted luminosity.

In a similar manner we can consider the projection of the physical diameter l of a galaxy to an angular diameter θ on the sky

$$\tan\theta = \frac{l}{d_A} \approx \theta \tag{1.11}$$

to define the *angular diameter distance* d_A assuming $\theta \ll 1$ and a static Euclidean space. Using the metric (1.1) and the definition of the redshift (1.5) the physical diameter of the galaxy reads

$$l = \frac{S_\kappa(r)\theta}{1+z} \tag{1.12}$$

which plugged into equation (1.11) yields the general form of the angular diameter distance

$$d_A \equiv \frac{l}{\theta} = \frac{S_\kappa(r)}{1+z}. \tag{1.13}$$

This relates to the proper distance and the luminosity distance as

$$d_A = \frac{d_p(t_0)}{1+z} = \frac{d_L}{(1+z)^2} \tag{1.14}$$

in a flat universe. Again, knowing the redshift and the angular size of a galaxy on the sky from observations we can use the angular diameter distance to infer its physical diameter. Note that while all three distances d_p, d_L and d_A are the same in a static Euclidean space, they are not the same in the expanding Universe. Over the course of this work both the luminosity distance and the angular diameter distance are used where appropriate (cf. sections 1.4 and 2.2).

1.2 Cosmic History – From Recombination to Reionization

In order to understand the physics of early galaxies at high redshifts, we also need to understand the environment in which they form and evolve, i.e. the high-redshift Universe. In this section, I therefore briefly relate the history of the Universe and the evolution of baryonic matter during the first billion years after the Big Bang which corresponds to the top half of Fig. 1.1. In these times the Universe underwent several phase transitions, going from a completely ionized state to a neutral state and progressively back to the fully ionized state that we can observe today once the first luminous objects formed. More rigorous reviews can be found in Schneider (2006), Glover (2013) and Cimatti et al. (2019).

1.2.1 Cosmic recombination

By the time the baryons were formed and primordial nucleosynthesis had taken place, the Universe was only several thousand years old and consisted of a fully ionized plasma

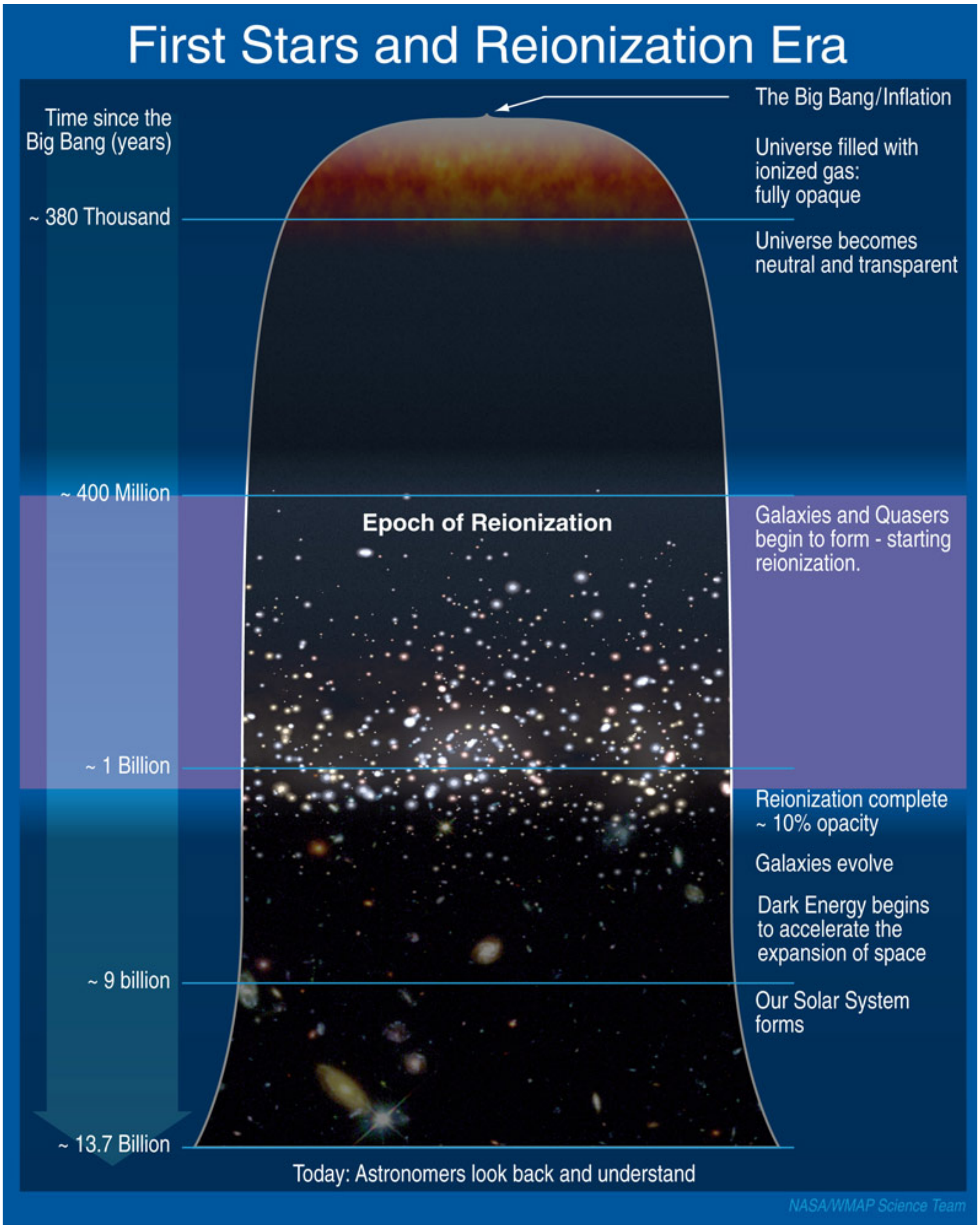

Figure 1.1: Timeline of the evolution of the Universe. The first billion years are marked by the two phase transitions: Recombination at $z \approx 1100$ that saw the free electrons and protons of the primordial plasma recombine to H I and Reionization from $z \approx 20-30$ to $z \approx 5$ during which the Universe got ionized again presumably by the first stars and galaxies. In between lie the so-called dark ages. Figure credit: NASA/WMAP Science Team.

of protons, electrons and atomic nuclei of He and Li. In this state, the plasma remains ionized because of its high temperature $k_B T \gg 13.6\,\mathrm{eV}$, is opaque due to constant scattering of photons by free electrons resulting in very short mean free paths for the photons and radiates as a nearly perfect black body. While the Universe expands however, the density of the plasma gradually decreases which causes the plasma to cool progressively. Eventually, electrons and protons are able to recombine and form neutral hydrogen (H I). This first transition from a fully ionized plasma to a neutral hydrogen gas in the Universe is called *cosmic recombination*.

Upon the onset of recombination, the number of free electrons decreases progressively until eventually Thomson scattering becomes more and more inefficient at scattering photons which are then able to propagate freely through the neutral gas, i.e. the Universe becomes transparent (cf. Fig. 1.1). The so-called last scattering surface of the primordial plasma is still observable at t_0 and forms the *cosmic microwave background* (CMB) already mentioned in section 1.1. Hydrogen recombination was completed by $z \approx 1100$ (0.36 Myr after the Big Bang). The photons of the CMB therefore all originate from that epoch. Note that due to their much larger ionization energies, He and Li recombined much earlier, at $z \approx 2500$ and $z \approx 8600$ respectively. After recombination, the CMB is practically the only source of radiation in the Universe since luminous objects (e.g. stars, emission nebulae, etc.) do not exist yet. This epoch is therefore called the *dark ages*.

1.2.2 The dark ages

Right after recombination, the baryon content of the Universe is nearly homogeneously distributed as is apparent from the near-homogeneity and isotropy of the CMB (e.g. Planck Collaboration et al., 2020b). This primordial gas, often also called *pristine gas*, is to the greatest part composed of H I and is adiabatically cooling due to the expansion of the Universe. While baryons were tightly coupled to the radiation before recombination (cf. section 1.2.1) and therefore could not undergo gravitational collapse, DM which does not couple to electromagnetic radiation, could collapse and created small mass over-densities of order 2-3 σ relative to the average background density. During the dark ages, these over-densities continue to collapse and eventually form so-called DM *minihalos* of virial mass $M_{\mathrm{vir}} \sim 10^6\,\mathrm{M}_\odot$. Now decoupled from the radiation field, the pristine H I gas can also collapse and accrete onto the existing DM minihalos. In order to contract far enough to form molecular clouds which can in turn collapse to stars, the gas needs to overcome its own internal pressure, i.e. cool. As is derived in detail in Cimatti et al. (2019), the baryonic gas in DM halos settles in a hydrostatic equilibrium at the halo virial temperature, given as

$$T_{\mathrm{vir}} \approx 10^4 \left(\frac{M_{\mathrm{vir}}}{10^8\,\mathrm{M}_\odot}\right)^{\frac{2}{3}} \left(\frac{1+z}{10}\right) \mathrm{K}. \tag{1.15}$$

The gas hosted in the minihalos mentioned above therefore has temperatures $T \lesssim 1000\,\mathrm{K}$ at which, in the absence of metals, only very few atomic process are available for radiative cooling since the hydrogen atom is a very inefficient coolant at these temperatures. One of these is e.g. the UV emission line [He II]$\lambda 1640\,\text{Å}$. In addition, the H I gas can possibly cool through rotational and vibrational transitions of a few simple molecules that were able to form in the pristine gas: H_2 and small amounts of HD and LiH. It is however still unclear if these molecules are efficient enough radiative coolants to allow the primordial gas to fully collapse, form the first generation of stars and ignite the Cosmic Dawn.

1.2.3 Cosmic Dawn — The first stars

The very first generation of stars is called *Population III* (Pop. III) stars and represents the first luminous objects in the history of the Universe. They are estimated to have formed around $z \approx 20 - 30$ and due to the relatively high gas temperatures at which they formed, they are estimated to have accreted much more gas than would be possible for present-day stars and thus have much higher masses. Indeed, simulations predict a mass-range of $1\,\mathrm{M}_\odot \lesssim M \lesssim 1000\,\mathrm{M}_\odot$. In addition, these stars are constituted out of pristine gas and therefore have no metallicity[1] $Z \approx 0$. Other properties of Pop. III stars can be estimated using the stellar structure equations (for a review cf. e.g. Bromm, 2013): For example we can expect a $100\,\mathrm{M}_\odot$ Pop. III star to have a radius of $\sim 5\,\mathrm{R}_\odot$, a luminosity of $\sim 10^6\,\mathrm{L}_\odot$ and a surface temperature of $\sim 10^5\,\mathrm{K}$, i.e. much hotter than even an O class star. The expected life-time of Pop. III stars is given in Cimatti et al. (2019) as

$$t_\star \approx 0.007 \frac{Mc^2}{L} \tag{1.16}$$

where 0.007 is the efficiency of the thermonuclear reactions powering the star. This results in very short lifetimes for Pop. III stars, of order 1 Myr, which means that Pop. III stars terminate their life cycle very rapidly and explode as Supernovae (SNe).

During their short lifetimes however, the first stars have a major impact on the medium around them. The intense UV emission heats and ionizes the gas around them and the SN explosions can even blow the gas out of the relatively shallow gravitational wells of the minihalos. In particular, so-called *Lyman-Werner photons* with $11.2 \leq h\nu \leq 13.6\,\mathrm{eV}$ are not absorbed by the neutral hydrogen but can photodissociate the H_2 molecules that are essential for cooling the pristine gas (cf. section 1.2.2). In addition, while the very first generation of stars has $Z \approx 0$, these first stars will enrich the pristine gas with metals, in particular with C, N and O, meaning that any subsequent generations of stars will no longer be Pop. III stars. Because of the short lifetimes of Pop. III stars, the transition to Pop. II stars occurs very rapidly. Simulations indicate that the feedback created by the Pop. III stellar winds and SNe clears most of the gas out of the $\sim 10^6\,\mathrm{M}_\odot$ minihalos which would mean that a second and subsequent generations of stars could not be formed in them. The Pop. III stars might therefore not have made up the first galaxies which instead would have formed subsequently in larger DM halos out of pristine gas and gas that was metal-enriched by the Pop. III stars. The exact circumstances of the formation

---

[1] *Metallicity* Z is defined as the fraction of the total baryonic mass made out of elements other than hydrogen or helium.

of the first galaxies however remain widely unknown and signatures of Pop. III stars in primordial galaxies, e.g. in their stellar and nebular emission, are considered one of the possible ways to observe Pop. III stars. I will talk about the first galaxies, their formation and their properties in detail in section 1.3. Other possible signatures of Pop. III stars include transients and signatures in the gravitational wave background (e.g. Lazar & Bromm (2021) and Martinovic et al. (2021)).

Recent studies suggest the Pop. III *initial stellar mass function* (IMF), which describes the initial distribution of masses for Pop. III stars, to extend all the way down to $1\,\mathrm{M}_\odot$ (e.g. Latif et al., 2021) which means that some Pop. III stars could still be present at t_0 according to equation (1.16). To date, there has been no confirmed observation of Pop. III stars or their signatures yet. There is however at least one Pop. III star complex candidate of $\sim 10^4\,\mathrm{M}_\odot$ at $z = 6.629$, detected in the strong gravitational lensing cluster MACSJ0416.1-2403, that still needs to be confirmed with future observations (Vanzella et al., 2020).

1.2.4 Cosmic reionization

The formation of the first stars and galaxies only accounts for a relatively small fraction of the gas content in the early Universe. The largest fraction remains cold and neutral and located in the spaces between the collapsed structures. It is therefore referred to as the *intergalactic medium* (IGM) and makes up the low-density *baryonic cosmic web*. Since the IGM during the dark ages is almost entirely composed of (neutral) H I, it absorbs the ionizing radiation ($k_B T \geq 13.6\,\mathrm{eV}$ or $\lambda \leq 1215.15\,\mathrm{Å}$) from the first stars and galaxies. As a result, the H I gas is gradually photoionized in expanding bubbles around the DM halos that host the first stars and galaxies until eventually the entire intergalactic hydrogen content of the Universe is ionized. This process is called *cosmic reionization* and represents the last great phase transition of the baryonic Universe. This epoch is often referred to as the *Epoch of Reionization* (EoR, cf. Fig. 1.1).

Measurements of the optical depth for Thomson scattering of CMB photons on free electrons in the (re-)ionized IGM yielded optical depths $\tau \approx 0.05 - 0.06$ which indicates that the cosmic reionization was complete at $z \approx 6$ when the Universe was $\sim 1\,\mathrm{Gyr}$ old (e.g. Fan et al., 2006; Planck Collaboration et al., 2016). More recent measurements using Quasar absorption spectra however place the end of reionization at $z \approx 5$ (e.g. Bosman et al., 2021; Zhu et al., 2021). The main sources of ionizing radiation that powered the reionization are probably the massively star-forming galaxies in the early Universe, in particular the far more numerous low-mass galaxies (Bunker et al., 2010; Oesch et al., 2010; Bouwens et al., 2011, 2015; Robertson et al., 2013, 2015; McLure et al., 2013; Finkelstein et al., 2015; Atek et al., 2015b), but other sources such as *active galactic nuclei* (AGN; e.g. Hassan et al., 2017; Torres-Albà et al., 2020), intermediate mass black holes (e.g. Wang et al., 2010) and even annihilation of DM particles (e.g. Kaurov et al., 2016) have been investigated. I will come back to the sources of cosmic reionization in sections 1.3 and 1.4. The determination of the main sources of ionizing photons at $z \gtrsim 6$ remains difficult because quantities like the IMF of stars, which might not be the same as measured in local Universe, and the escape fraction f_{esc}, which corresponds to the amount of ionizing radiation that is *not* absorbed by a galaxy's own interstellar medium (ISM), are still poorly constrained at high redshifts. This makes it difficult to ascertain the amount of ionizing photons available from stars in the EoR.

1.3 The first generation of galaxies — High-redshift galaxies

The whole subject of this work is the analysis and characterization of galaxies in the EoR (cf. section 1.2.4), the first generation of galaxies or *high-redshift galaxies*. I will therefore dedicate this section to a short summary of what is known about these objects. Since direct observations of high-redshift galaxies is a highly non-trivial matter, as will be explained in detail in chapter 2, most of the following is based on simulations and theoretical predictions. This section is mainly based on reviews by Johnson (2013), Dunlop (2013) and Cimatti et al. (2019).

1.3.1 Formation of the first galaxies

As mentioned in section 1.2.3, the first stars could possibly not have formed the first galaxies on account of their violent feedback effects which drive the gas out of their hosting DM minihalos and destroy the molecules crucial for cooling pristine gas (cf. section 1.2.2), thus suppressing subsequent star-formation. Instead, the first galaxies would have formed some time later in more massive DM halos capable of holding their gas even under stellar feedback.

In order for galaxy formation to take place in general, the halo's binding energy E_{bind} must exceed the energy of stellar feedback provided by stellar winds and SNe E_{wind} (cf. e.g. equation (3.9) in section 3.5.5), i.e.

$$E_{\text{bind}} \sim \frac{GM_{\text{vir}}^2}{r_{\text{vir}}} > E_{\text{wind}} \tag{1.17}$$

where r_{vir} is the virial radius. A detailed example for such an analysis can be found in section 3.5.5. In addition to the condition explained above, in order for star-formation to take place efficiently the virial temperature, given in equation (1.15), should be $T_{\text{vir}} > 10^4\,\text{K}$ in order for pristine gas to cool via atomic line emission. Note that by this time, the pristine gas has been slightly enriched in metals by the Pop. III star SNe, mostly with O and C (e.g. Heger & Woosley, 2002, 2010). These provide potent atomic cooling lines, in particular C II which can be easily maintained in its ionized state by the radiation field present at the time and is very efficient for cooling gas down to very low temperatures (e.g. Bromm & Loeb, 2003).

Numerical simulations indicate the conditions above to be reunited in halos of $M_{\text{vir}} \sim 10^8\,\text{M}_\odot$ at $z \approx 10$. Recent observational studies indicate galaxy formation to have taken place as early as $z = 15$ (e.g. Hashimoto et al., 2018; Laporte et al., 2021). The transition from Pop. III star formation ($z \approx 20-30$, cf. section 1.2.3) to the formation of the first galaxies was therefore very rapid and occurred in $\lesssim 0.1\,\text{Gyr}$. The physics and conditions of the formation of the first galaxies however remain poorly constrained by observations, making the above simulation results fairly uncertain and speculative. In particular the effects of stellar feedback and thus the values of E_{wind} are difficult to model without further observational constraints. This is one of the prime motivations for high-redshift galaxy observations and this work in particular as I will explain in section 1.4 (but cf. also section 3.5.5).

1.3.2 Properties of the first galaxies — Compact star-bursts

The study of high-redshift galaxies is a comparatively recent field that originated less than two decades ago, mainly because high-redshift galaxies are difficult to observe as I will explain in detail in chapter 2. Their properties therefore remain largely unknown and represent one of the most active fields of research in modern astronomy.

Since they represent the first generations of galaxies to have formed in the Universe, high-redshift galaxies are expected to be relatively small and compact structures with low stellar masses and small radii. Indeed, observations find the galaxy populations at high-redshifts to be dominated by relatively low-mass dwarf galaxies (cf. sections 1.4 and 3.4 and Fig. 3.12) with rather steeply evolving mass-to-light relations $L \propto M^{\alpha}$, meaning that more massive galaxies tend to be brighter and lower-mass galaxies to be fainter (e.g. Song et al., 2016a, and section 3.3 of this work). While single massive galaxies with $M_{\star} \sim 10^{11}\,\mathrm{M}_{\odot}$ do exist at high-redshifts (e.g. Mobasher et al., 2005; Ouchi et al., 2009), they are extremely rare (e.g. Dunlop et al., 2007) and the bulk of the galaxy population has lower stellar masses. Morphological analyses furthermore yield steep size-luminosity relations $r_e \propto L^{\beta}$ and particularly small half-light-radii r_e on the very faint end, down to $r_e \sim 0.01\,\mathrm{kpc}$ (Kawamata et al., 2015, 2018; Bouwens et al., 2021).

All high-redshift galaxies are star-forming systems rich in gas because the Universe is not old enough yet for galaxies to undergo major merging, quenching and gas-stripping processes that will eventually rob them of their gas and create a quiescent galaxy population. Instead these galaxies are undergoing massive star-formation with extreme SFRs[2]. Simulations predict their SFRs to be exponentially increasing with time (e.g. Finlator et al., 2011) and come in violent and episodic 'bursts' (e.g. Stark et al., 2009; McLure et al., 2011) making high-redshift galaxies the most extreme star-bursting systems in the Universe. Some artist impressions of what high-redshift star-bursting galaxies might look like in close-up are shown in Fig. 1.2.

As these galaxies formed out of the pristine gas (cf. section 1.2.2), they also have very low metallicities with a range of $Z \sim 0.001 - 0.5\,\mathrm{Z}_{\odot}$ (Harikane et al., 2020; Jeon et al., 2020; Jones et al., 2020). For the same reason, high-redshift galaxies can be expected to have relatively low amounts of interstellar dust since the heavy elements necessary to form dust grains are not very abundant yet and stellar feedback of massive star-formation can also destroy dust grains. While observations do indeed find evidence for very low dust attenuations (e.g. Bouwens et al., 2016; Bhatawdekar & Conselice, 2021), other recent studies have nevertheless detected surprisingly high dust masses and temperatures (e.g. Hashimoto et al., 2018; Laporte et al., 2019; Tamura et al., 2019; Bakx et al., 2020).

---

[2] The star-forming rate ψ is defined as the total mass in stars formed per unit time.

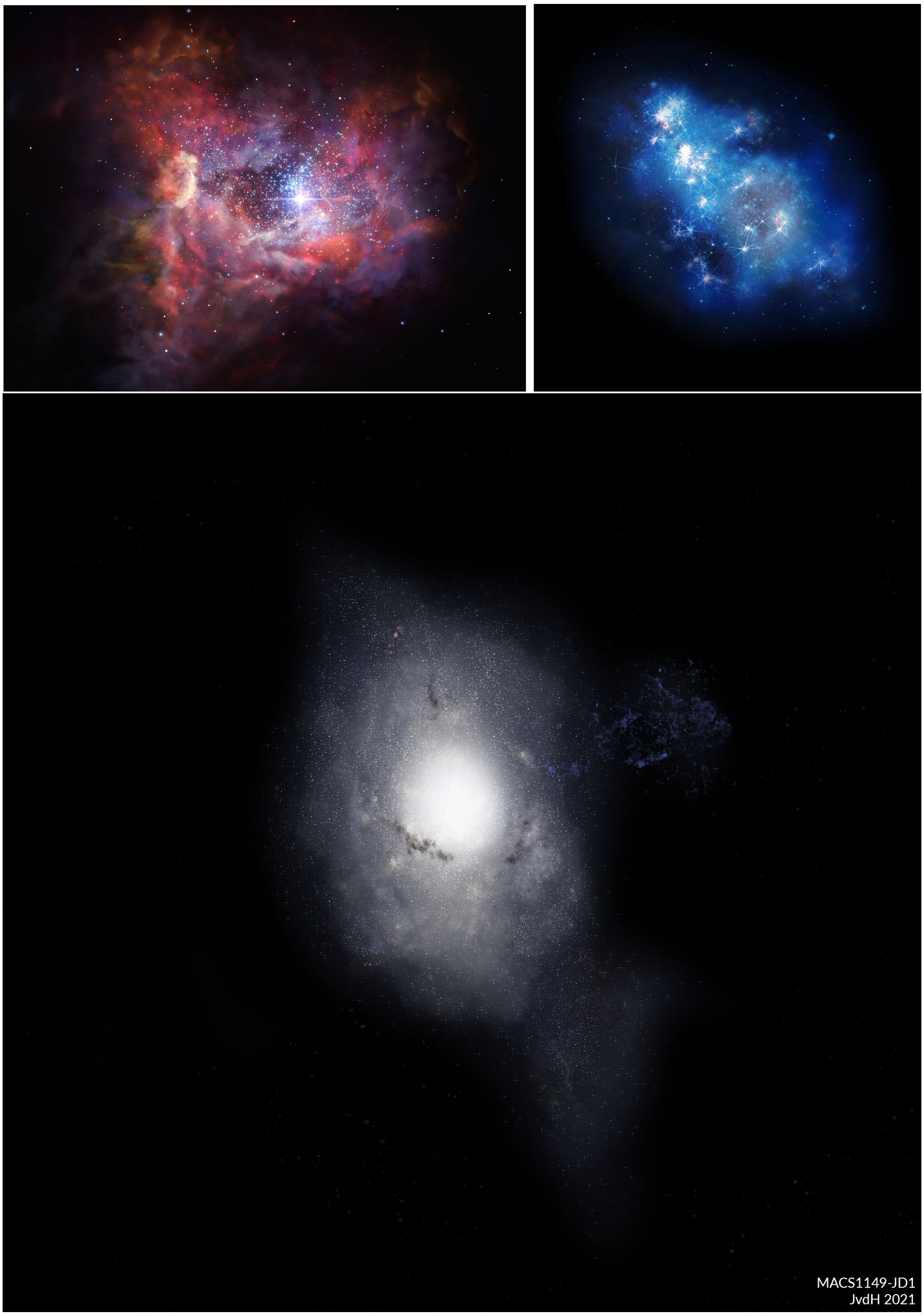

Figure 1.2: Artist impressions of the three most distant galaxies observed to date. High-redshift galaxies are very compact and densely star-forming dwarf galaxies. From left to right and top to bottom: A2744 YD4 at $z = 8.38$ (Zheng et al., 2014; Laporte et al., 2017), GN-z11 at $z = 10.957$ (Oesch et al., 2016; Jiang et al., 2021a,b) and MACS1149-JD1 at $z = 9.11$ (Zheng et al., 2012; Hashimoto et al., 2018). Figure credits: M. Kornmesser, P. C. Budassi and JvdH1.

Finally, note that the properties of high-redshift galaxies described in this section mostly apply to currently *observed* populations of high-redshift galaxies and the results of galaxy simulations. They therefore remain uncertain and prone to biases, degeneracies and statistical uncertainties. A great part of this work is to address these as will be detailed in section 2.4 and in chapters 3 and 5. It is nevertheless also necessary to consider the possibility of other galaxy populations that have not yet been observed in the high-redshift Universe, e.g. massive dust-obscured star-forming galaxies, low surface-brightness galaxies or even quiescent galaxies which do not have high SFRs. I will come back to these possibilities in section 6.1.3.

1.4 Galaxy luminosity and stellar mass functions

Two primary results in the analysis of statistically significant samples of high-redshift galaxies are their luminosity function and their GSMF. They describe the co-moving number density of galaxies as a function of luminosity L and stellar mass $M_\star$ respectively and therefore provide crucial constraints on the cosmic reionization (cf. section 1.2.4) and the formation and evolution of galaxies in the early Universe (cf. section 1.3). These densities are defined as

$$\phi(L)\mathrm{d}L = \frac{N(L)}{V} \tag{1.18}$$

$$\phi(M_\star)\mathrm{d}M_\star = \frac{N(M_\star)}{V} \tag{1.19}$$

where N corresponds to the number of galaxies and V represents the co-moving volume

$$\mathrm{d}V = \frac{c^3}{H(z)}\left(\int_0^z \frac{\mathrm{d}z'}{H(z')}\right)^2 \mathrm{d}z\mathrm{d}\Omega \tag{1.20}$$

with $H(z)$ as the Hubble parameter (1.3) and $\mathrm{d}\Omega$ as the solid angle element. Luminosity and stellar mass functions are commonly parametrized with a Schechter function (Schechter, 1976)

$$\phi(L) = \left(\frac{\phi_0}{L_0}\right)\left(\frac{L}{L_0}\right)^\alpha e^{-\frac{L}{L_0}} \tag{1.21}$$

whose shape is defined by three parameters: The normalization density ϕ_0, a characteristic luminosity L_0 at which the luminosity function drops off exponentially on the bright end and a power-law slope α on the faint end. The effects of the individual parameters on the shape of the Schechter function is illustrated in the right-hand panel of Fig. 1.3. A Schechter parametrization of the GSMF can be found in equation (3.4). There are also alternative parametrizations in use such as e.g. double power-laws (e.g. Dunlop & Peacock, 1990), double Schechter functions (e.g. Weigel et al., 2016) and modified Schechter functions that include a turnover term on the faint end such as defined in equation (3.6) and illustrated in the right-hand panel of Fig. 1.3 (cf. also Jaacks et al., 2013; Bouwens

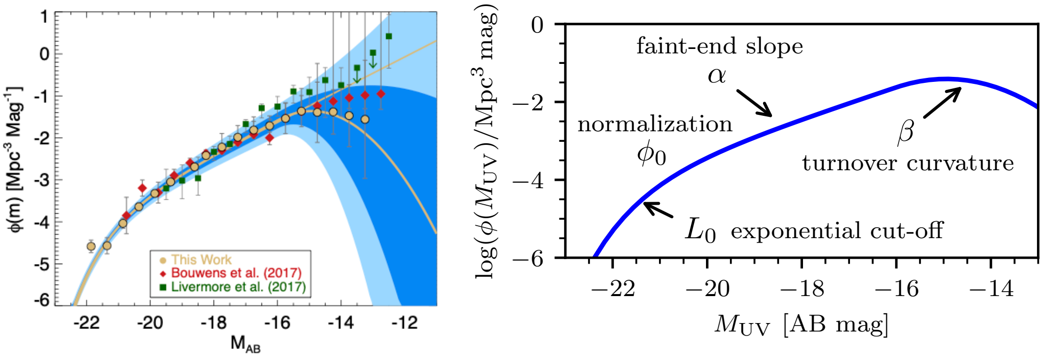

Figure 1.3: *Left*: UV luminosity function at $z \sim 6-7$ by Atek et al. (2018) in comparison to results by Bouwens et al. (2017b) and Livermore et al. (2017). Note the potential downward turnover on the extreme faint end. Figure credit: Atek et al. (2018). *Right*: Schematic illustration of the Schechter parametrization given in equation (1.21). The low-mass end turnover term is defined in equation (3.5) in section 3.4.

et al., 2017b; Atek et al., 2018). Note that only the Schechter and the modified Schechter functions are known to fit high-redshift galaxy observations though.

At high-redshifts, luminosity functions are mostly observed in rest-frame UV wavelengths around $\lambda_{\mathrm{UV}} \sim 1500\,\text{Å}$ for the reasons explained in chapter 2. Note that recent efforts have nevertheless also yielded Lyman alpha (e.g. Hu et al., 2004, 2019; Shimasaku et al., 2006; Ouchi et al., 2008; Taylor et al., 2021; Santos et al., 2021; Wold et al., 2021; Goto et al., 2021) as well as the first rest-frame optical (Stefanon et al., 2017) and even [O III]+Hβ (De Barros et al., 2019), [C II]λ158 µm (Yan et al., 2020; Uzgil et al., 2021) and Hα (Asada & Ohta, 2021) luminosity functions at high redshifts. Once a sample of high-redshift galaxies has been detected (cf. section 2.1), the UV luminosity can be easily computed using the observed (rest-frame) UV magnitude m_{UV} and the redshift as

$$M_{\mathrm{UV}} = m_{\mathrm{UV}} + 5\left(1 - \log\left(\frac{d_L(z)}{\mathrm{pc}}\right)\right) + 2.5\log(1+z) \tag{1.22}$$

where $d_L(z)$ is the luminosity distance computed using equations (1.6) and (1.10). The study of high-redshift UV luminosity functions is of particular interest for constraining cosmic reionization because their integral yields the UV luminosity density in the EoR. This allows to assess the number of ionizing photons provided by galaxies in the EoR and thus yields insight whether or not early star-forming galaxies were responsible for the cosmic reionization (cf. section 1.2.4 and e.g. Finkelstein et al., 2015; Atek et al., 2015b). In addition, high-redshift luminosity functions can also be used to constrain cosmological parameters and DM clustering at high redshifts (Sabti et al., 2021b,a).

While the UV luminosity functions trace the energy budget in the early Universe, the GSMFs trace the build-up of stellar mass in high-redshift galaxies and their evolution in the EoR. They therefore provide crucial constraints on galaxy formation and evolution models and on numerical simulations (e.g. Ocvirk et al., 2020): The measured GSMFs are what the simulations need to reproduce in the end in order to accurately reflect our Universe. Even though stellar mass is much less straight-forward to measure than UV luminosity (cf. section 2.4 and in particular chapters 3 and 5), recent observations agree on a steepening of the low-mass end slope with redshift, from $\alpha \sim -1.6$ at low redshifts to $\alpha \sim -2.0$ at high redshifts (e.g. Duncan et al., 2014; Grazian et al., 2015; Song et al., 2016a) which indicates the galaxy population at high-redshifts to be dominated by faint low-mass dwarf galaxies (cf. section 1.3.2). That being said, while the Schechter parametrization presented in equations (1.21) and 3.4 parametrizes the faint low-mass end with a continuous power-law, in reality there must of course be a lower limit to the GSMF since a galaxy of arbitrarily small mass cannot exist. As explained in section 1.3.1, there is a theoretical lower limit to the mass at which galaxies can form in the early Universe due to quenching by stellar feedback when $E_{\mathrm{bind}} \lesssim E_{\mathrm{wind}}$ and the limits of gas cooling efficiency. In combination with stellar-to-halo mass relations, measuring a drop in number density of low-mass high-redshift galaxies would provide strong constraints on the characteristic DM halo mass scale at which stellar feedback and inefficient gas cooling can suppress the star-formation. This provides valuable insights into the physics of stellar feedback, i.e. stellar winds from young massive stars and SNe, in the first generations of galaxies. In addition, the high-redshift GSMF can be used to constrain the evolution of the IGM in the close vicinity of the galaxies, the so-called *circumgalactic medium* (CGM; e.g. Finlator et al., 2020), and even to test e.g. warm dark matter models (e.g. Rudakovskyi et al., 2021). The latter would in particular leave a significant signature in the GSMFs as warm dark matter 'erases' substructure at small scales and masses. Note that while recent studies have indeed detected a turnover on the extreme faint end of the high-redshift UV luminosity function (cf. Fig. 1.3; Bouwens et al., 2017b; Atek et al., 2018), this has not yet been found in GSMFs (though cf. chapter 3).

For all of these reasons, it is important to precisely measure high-redshift GSMFs down to the lowest stellar masses and paramount to correctly assess their uncertainties. These represent some of the prime motivations for this work as I will develop in the following chapters. Before that it is however necessary to understand the detection processes of high-redshift galaxies and the measurements of their stellar mass which I will explain in chapter 2.

Chapter 2

Observing the high-redshift Universe

> "And it didn't stop being magic
> just because you found out how
> it was done."
>
> Sir Terry Pratchett,
> *The Wee Free Men*, 2003

The identification and observation of galaxies in the EoR at $z \gtrsim 6$ (cf. section 1.2.4) is among the most difficult tasks in modern astronomy. They are extremely faint ($m_{\mathrm{AB}} \gtrsim 25$) and have small angular diameters on the sky ($\theta \lesssim 1''$) which places them beyond the sensitivity and angular resolution of most ground-based telescopes. In addition, at $z \gtrsim 6$ most of the emitted galaxy spectrum is redshifted beyond the wavelength coverage of most instruments. For example, at $z = 6$ the rest-frame UV emission ($\sim 1500\,\text{Å}$) is redshifted into NIR wavelengths ($\sim 10500\,\text{Å}$) according to equation (1.5). To date, only the HST (up to $\sim 17000\,\text{Å}$) and *Spitzer* (from $\sim 30000\,\text{Å}$ to $\sim 50000\,\text{Å}$) are sensitive enough to observe objects as small and faint as these across the whole range of wavelengths into which their emitted light is redshifted. While the HST is most proficient at *detecting* these objects (cf. sections 2.1 and 2.4.1), *Spitzer* observations are invaluable to derive high-redshift galaxy physics (cf. section 2.4.2). Also note that while rest-frame UV spectroscopy of relatively bright high-redshift galaxies with some ground-based instruments (cf. sections 2.4.1 and 4.3), e.g. the *Keck* Observatory, *Subaru* Telescope or ESO's *Very Large Telescope* (VLT), is possible and indeed necessary for redshift confirmation, it is not an efficient process for detecting statistically significant samples. We therefore need to mostly rely on photometric means of identifying high-redshift galaxy candidates.

In this chapter, I will present the three main means of observation and analysis used in my thesis: Section 2.1 details how we use the HST to detect high-redshift galaxies and section 2.2 introduces the physics of the gravitational lensing effect, used in this work to 'boost' our sensitivity towards the faintest high-redshift galaxies. I then present the six galaxy clusters observed for this work in section 2.3 before presenting our main method of analysis, SED-fitting, in section 2.4.

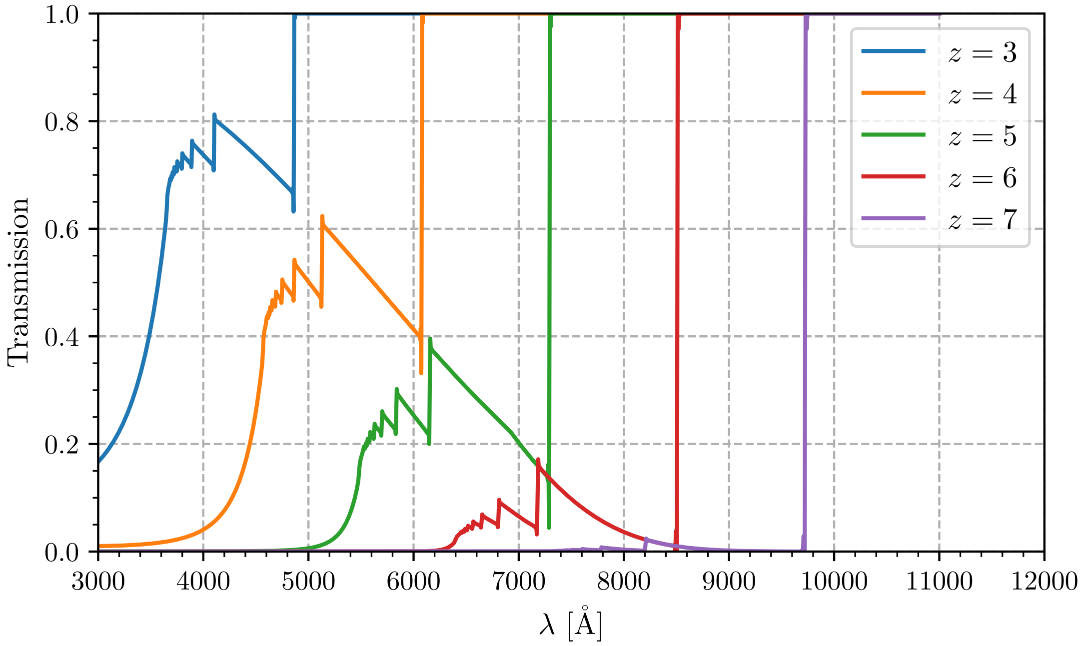

Figure 2.1: IGM transmission curves computed from the latest semi-analytical models by Inoue et al. (2014) for different source redshifts z. At redshifts $z \gtrsim 6$ all emission blue-ward of Lyα is absorbed by neutral hydrogen in the IGM thus creating the Gunn-Peterson trough (Gunn & Peterson, 1965) and the Lyman break observed in high-redshift objects.

2.1 High-redshift dropout detection

Thanks to the unprecedentedly high angular resolution and NIR sensitivity of the HST, it is possible to detect statistically significant samples of high-redshift galaxies. The two main instruments used for this are the *Advanced Camera for Surveys* (ACS), installed on the HST in 2002, and the *Wide Field Camera 3* (WFC3), installed during the last servicing mission on the HST in 2009. Using broad-band filters, these instruments are sensitive enough to image faint high-redshift galaxies by exploiting some of their distinctive key features as detailed in the following sections.

2.1.1 The Lyman break

In the absence of spectroscopy, the main feature we are going to exploit for identifying high-redshift galaxy candidates in broad-band photometry is the so-called *Lyman break*, a sharp break in the continuum of high-redshift galaxies at the (redshifted) wavelength of their Lyman-alpha (Lyα) emission line. The Lyman break arises because the neutral IGM is opaque to hydrogen-ionizing photons $> 13.6\,\text{eV}$, i.e. photons blue-ward of Lyα are absorbed along their way between the source and the observer. While the local IGM is fully ionized and thus translucent to ionizing radiation, the fraction of neutral

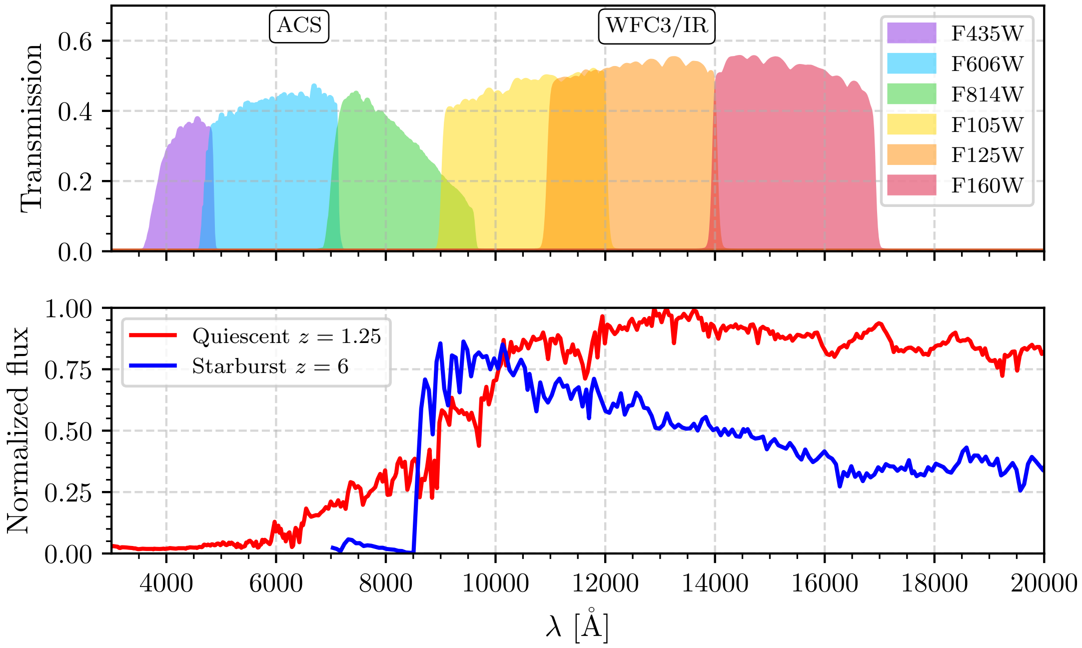

Figure 2.2: *Top*: Transmission curves of some broad-band filters on the HST. *Bottom*: Typical spectra of a star-bursting galaxy at high redshift (blue) and a red quiescent galaxy at low redshift (red) convolved with the corresponding IGM attenuation curves (cf. Fig. 2.1).

hydrogen in the IGM increases with redshift until the IGM is fully opaque to ionizing radiation towards the end of the EoR ($z \gtrsim 6$, cf. section 1.2.4). Typical IGM transmission curves for different redshifts can be seen in Fig. 2.1, computed from IGM attenuation models by Inoue et al. (2014). The absorption of ionizing radiation originating from high-redshift sources, the *Gunn-Peterson* effect, was theoretically predicted by Gunn & Peterson (1965) and observed for the first time by Becker et al. (2001).

At redshifts $z \gtrsim 6$, Lyα and the Lyman break conveniently fall into the bandpass of the HST as is illustrated in Fig. 2.2. In broad-band photometry, a high-redshift galaxy candidate will appear red in the color, i.e. the difference in magnitude, between the filter that contains the Lyman break and the filter red-ward of that. At the same time, the galaxy will be detected in bands red-ward of the break and *not* detected in bands blue-ward of the break. For that reason these objects are also called *dropout* galaxies. Note that dropout objects are often designated by the filter in which the break falls, i.e. F814W-dropouts for $z \sim 6-7$ galaxies, F105W-dropouts for $z \sim 8-9$ galaxies and F125W-dropouts for $z \sim 9-11$ galaxies. A typical example of a F105W-dropout ($z \sim 8$ candidate) identified in the course of this work (cf. section 4.3.1) can be seen in Fig. 2.3.

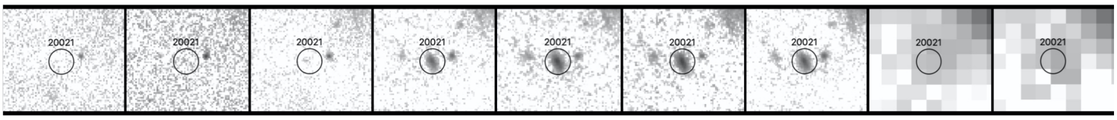

Figure 2.3: Image cutouts of a typical F105W-dropout, the $z \sim 8$ galaxy candidate A370-20021 (cf. section 4.7). From left to right: F435W, F606W, F814W, F105W, F125W, F140W, F160W, *Spitzer*/IRAC1 and IRAC2 (cf. section 3.1). The source is clearly detected in the WFC3/IR bands but shows no detection in the bands blue-ward of the Lyman break.

2.1.2 High-redshift galaxy detection in deep fields

While the Lyman break provides an excellent color-selection criterion for high-redshift galaxies, it is not in itself sufficient to robustly rule out a red lower-redshift object: As illustrated in Fig. 2.2, the Balmer or 4000 Å break (cf. section 2.4.2) of a red (e.g. dusty or elliptical) galaxy at low redshifts can have a color-signature similar to the Lyman break at high redshifts in broad-band photometry. Dropout selection techniques therefore commonly also include a second color criterion to make sure the selected galaxy is slightly blue in the filters red-ward of the break due to the UV-continuum slope (cf. section 2.4.1) of a young high-redshift star-forming galaxy as opposed to the flat or red continuum expected for a dusty or quiescent low-redshift galaxy (cf. lower panel in Fig. 2.2 again), and strict non-detection criteria in bands blue-ward of the break. Selecting high-redshift dropout galaxies from broad-band photometric data requires precision photometry that from HST imaging. Even with the deepest data sets, dropout selection remains prone to significant fractions of red low-redshift galaxies (e.g. Bouwens et al., 2011) and faint cold stars and brown dwarves which present a very similar signature in broad-band photometry (cf. section 4.2.3). Detailed examples of high-redshift dropout selection techniques can be found in sections 3.1.1 and 4.2.3 of this work and in e.g. Bouwens et al. (2015); Atek et al. (2015a); Ishigaki et al. (2018).

While the first deep-field observations with HST, the *Hubble Deep Field* (HDF; Williams et al., 1996) and the *Great Observatories Origins Deep Survey* (GOODS; Giavalisco et al., 2004), obtained multi-band HST photometry to depths of ~ 28 magnitudes, it was not until the installation of WFC3 in 2009 that NIR wavelengths, at which $z \gtrsim 6$ objects can be observed, could be covered by the HST. As a result, the deepest blank field image of the Universe to date, the *Hubble Ultra Deep Field* (HUDF; Beckwith et al., 2006; Ellis et al., 2013; Illingworth et al., 2013; Teplitz et al., 2013, cf. Fig. 2.4), could be obtained in 13 HST bands out to $\sim 29-30$ magnitudes and 4 *Spitzer* bands out to $\sim 27-28$ magnitudes (Stefanon et al., 2021c), depths unattainable with ground-based instruments. Due to its relatively small area on the sky however, the HUDF remains inefficient for robustly constraining high-redshift galaxy populations because of cosmic variance. In an attempt to overcome that, the *Cosmic Assembly Near-infrared Deep Extragalactic Legacy Survey* (CANDELS; Grogin et al., 2011; Koekemoer et al., 2011) observed five separate fields with the HST to depths $\sim 28-29$ magnitudes and an area ~ 100 times that of the HUDF. With numerous ancillary *Spitzer* and ground-based datasets, the HUDF and CANDELS have enabled the detection of > 1000 galaxies at $z \gtrsim 6$ (Bouwens et al.,

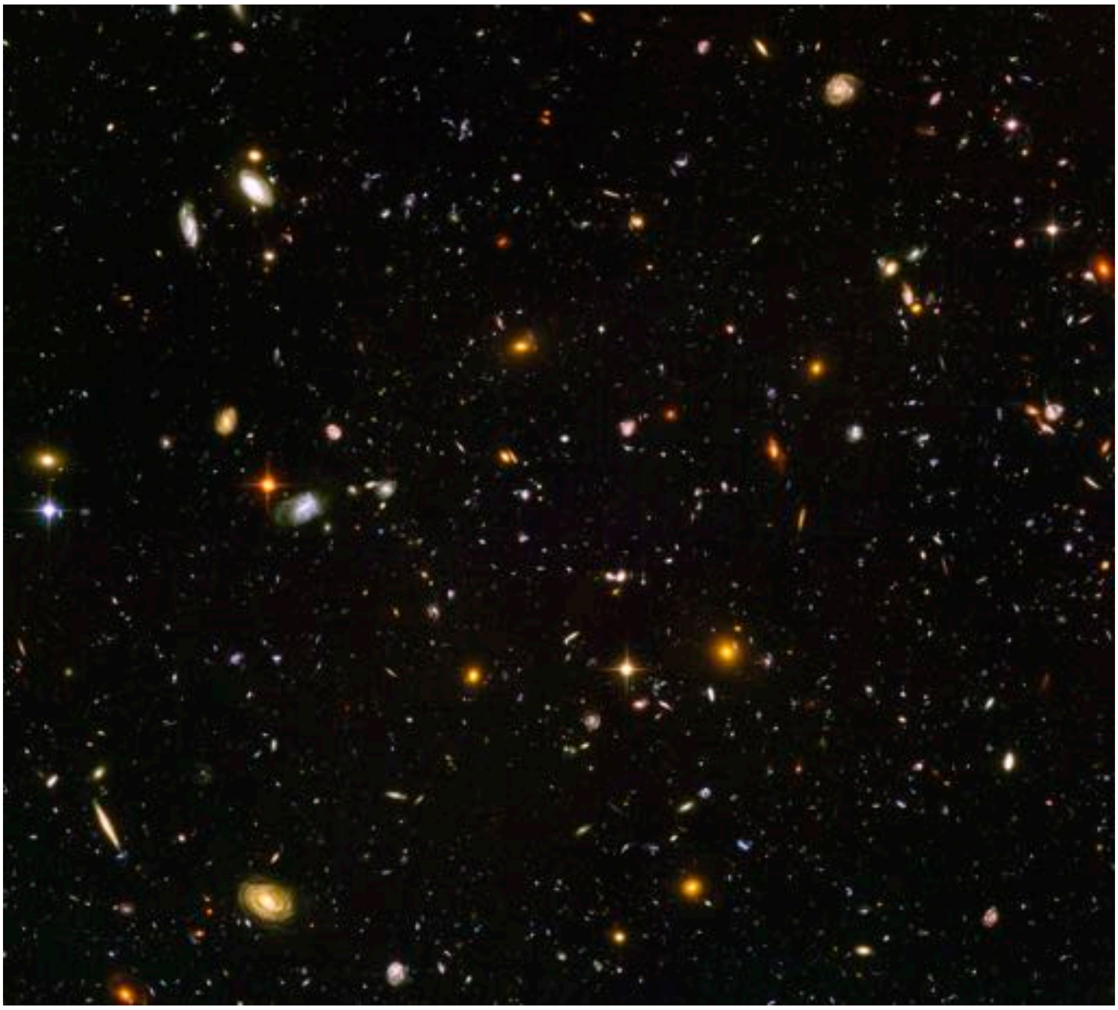

Figure 2.4: Color-composite image of the *Hubble Ultra Deep Field*, the deepest HST image to date, composed of ACS (blue), WFC3 (green) and *Spitzer*/IRAC (red) imaging data. The HUDF maps $2.4' \times 2.4'$ on the sky and contains an estimated ~ 10000 galaxies. Figure credit: NASA, ESA, N. Pirzkal and the HUDF Team (`https://esahubble.org/images/heic0714g/`).

2015; Finkelstein et al., 2015) which led to high-precision $z \gtrsim 6$ GSMF measurements in a stellar mass range $M_\star \sim 10^8 - 10^{11}\,\mathrm{M}_\odot$ (González et al., 2011; Duncan et al., 2014; Grazian et al., 2015; Song et al., 2016a; Stefanon et al., 2021b) and the detection of the most distant known object to date, GN-z11 at $z \simeq 10.957 \pm 0.001$ (Oesch et al., 2016; Jiang et al., 2021a,b). Using a different approach, the *Cosmic Evolution Survey* (COSMOS; Scoville et al., 2007a) combines the widest contiguous area observed with ACS to date ($\sim 2\,\mathrm{deg}^2$; Scoville et al., 2007b; Koekemoer et al., 2007) with deep ground-based and *Spitzer* imaging data. The analysis of the full COSMOS data set is still ongoing and the newest releases of the COSMOS catalogs (Laigle et al., 2016; Weaver et al., 2021) are expected to yield large numbers of bright and massive high-redshift galaxy candidates.

The above mentioned deep fields are the deepest observations obtainable with the HST in so-called *blank fields* and the high-redshift galaxy samples observed in them reach rest-frame UV luminosities down to $\lesssim -17$ magnitudes (e.g. Bouwens et al., 2015; Finkelstein et al., 2015) and stellar masses $\gtrsim 10^8\,\mathrm{M}_\odot$ (Song et al., 2016a; Stefanon et al., 2021b). In order to reach even fainter and lower-mass objects, the regime where the turnover in the GSMF can be expected (cf. section 1.4), we require a 'boost' in depth that can be provided by the magnification of background fluxes by massive galaxy clusters — the gravitational lensing effect.

2.2 Gravitational Lensing

The gravitational deflection and magnification of light emitted by background sources was theoretically expected by Soldner (1804) and Einstein (1916) and observationally confirmed by Dyson et al. (1920). It was however not until 1986 that the first strongly lensed giant arc was discovered in the galaxy cluster Abell 370 (Lynds & Petrosian, 1986; Soucail, 1987). In this section I briefly introduce the physics of gravitational magnification which plays an important role throughout this work. More exhaustive reviews of gravitational lensing and its applications can be found in e.g. Schneider et al. (1992), Narayan & Bartelmann (1996), Meylan et al. (2006) and Dodelson (2017).

To physically describe the propagation of light through gravitational lenses, we basically take the metric defined in equation (1.1) and add local perturbations. These local perturbations are the gravitational distortions of spacetime caused by distributions of matter which act as gravitational lenses. Close to a gravitational lens, the geometry can then be described by a locally flat Minkowski spacetime perturbed by a Newtonian potential Φ, which depends on the mass distribution $\rho(\vec{x})$ of the lens. The effect of the potential Φ on a passing light ray is analogous to that of a refractive index in geometric optics, which is given in Schneider et al. (1992) as

$$n = 1 - \frac{2}{c^2}\Phi = 1 + \frac{2}{c^2}|\Phi|. \tag{2.1}$$

The light is bent by a deflection angle $\vec{\hat{\alpha}}$, which we obtain by integrating the gradient of n perpendicular to the line of sight l along the line of sight

$$\vec{\hat{\alpha}} = -\int \vec{\nabla}_\perp n \mathrm{d}l = \frac{2}{c^2} \int \vec{\nabla}_\perp \Phi \mathrm{d}l. \tag{2.2}$$

In the strong lensing regime, the distances between the observer and the lens and between the lens and the lensed source are very large compared to the radial depth of the mass distribution acting as gravitational lens. We can therefore safely assume the lens to be a thin sheet of mass, which extends transversally to the line of sight l. The light, emitted from a source in the *source plane* at distance D_s from the observer, is then deflected by this two-dimensional mass distribution situated in the *lens plane* at distance D_d from the observer (see Fig. 2.5). The mass density of the lens thus reduces to the projection along l, the surface mass density

$$\Sigma(\vec{\xi}) = \int \rho(\vec{\xi}, l) \mathrm{d}l, \tag{2.3}$$

where $\vec{\xi}$ is a two-dimensional vector in the lens plane. Using this definition and equation (2.2), the deflection angle at any position $\vec{\xi}$ in the lens plane is the sum of the deflections caused by all the mass elements in the lens plane

$$\vec{\hat{\alpha}}(\vec{\xi}) = \frac{4G}{c^2} \int \frac{(\vec{\xi} - \vec{\xi}')\Sigma(\vec{\xi}')}{|\vec{\xi} - \vec{\xi}'|^2} \mathrm{d}^2\xi'. \tag{2.4}$$

As the deflection is only caused by the gravitational potential of the lens, it does not depend on the wavelength of the deflected photons. Gravitational lensing therefore does not present any chromatic aberrations.

2.2.1 The Lens equation

The deflection angle $\vec{\hat{\alpha}}$, defined in equation (2.2), can be used to relate the observed position $\vec{\theta}$ of a lensed image to the true position $\vec{\beta}$ of the source. Note that the angles $\vec{\hat{\alpha}}$, $\vec{\theta}$ and $\vec{\beta}$ are two-dimensional vectors on a sphere. Fig. 2.5 illustrates the situation for a source at distance D_s whose light is deflected by a gravitational lens at D_d and therefore appears as an image to the observer. Separations in the source plane are called η and separations in the lens plane ξ and D_{ds} is the distance between these two planes. Assuming an Euclidean relation between angles and the separation of the lines enclosing them as in equation (1.11), it immediately follows from Fig. 2.5 that

$$\theta D_s = \beta D_s - \hat{\alpha} D_{ds}. \tag{2.5}$$

Dividing by D_s and introducing the reduced deflection angle

$$\vec{\alpha} = \frac{D_{ds}}{D_s} \vec{\hat{\alpha}} \tag{2.6}$$

then yields the *lens equation* of gravitational lensing

$$\boxed{\vec{\beta} = \vec{\theta} - \vec{\alpha}(\vec{\theta})}, \tag{2.7}$$

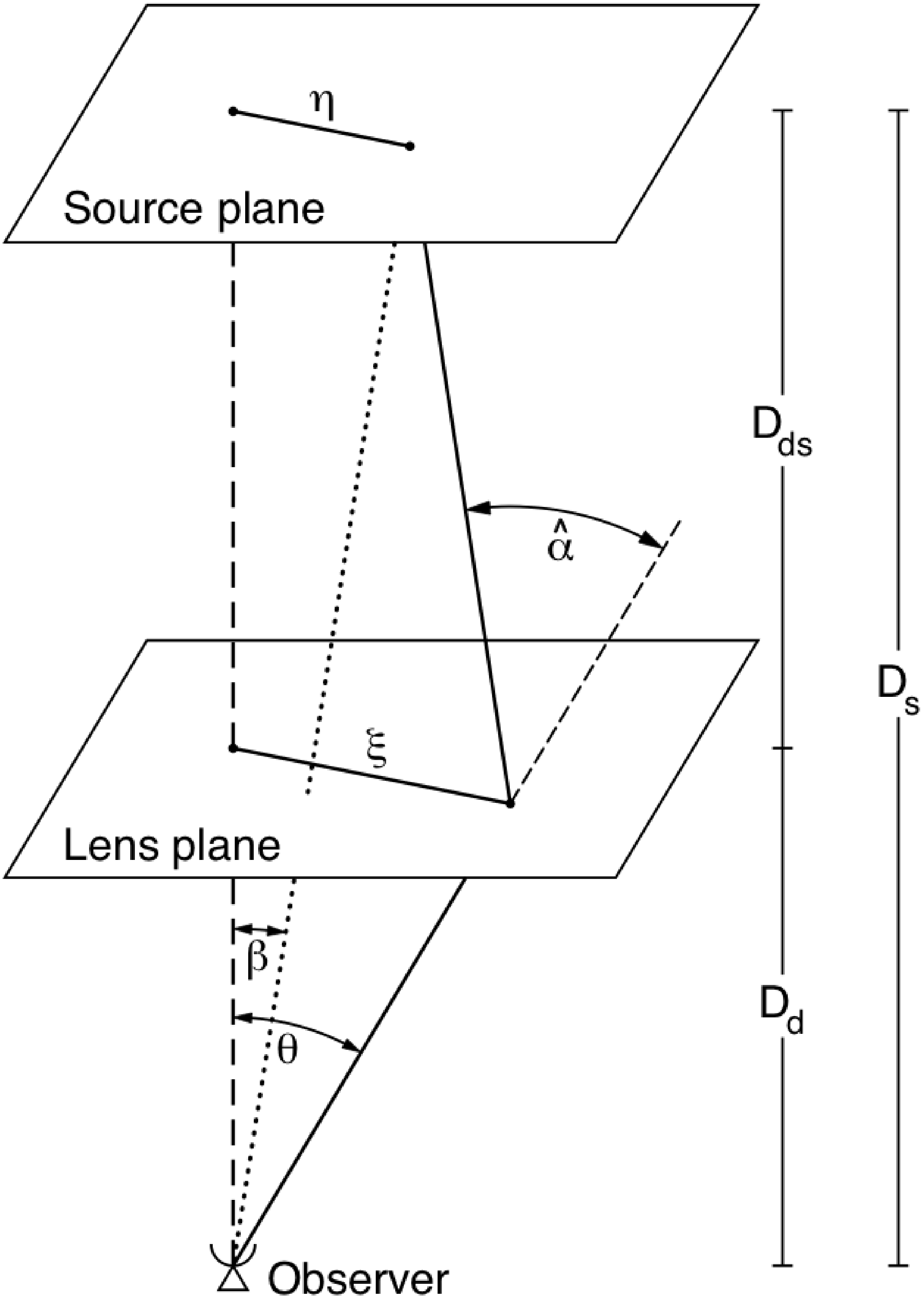

Figure 2.5: Geometrical setup for a thin sheet of mass acting as a gravitational lens at distance D_d from the observer. ξ and η are physical separations in the lens and source plane respectively. The angular position β of the source is related to the observable position θ of the image through the reduced deflection angle α (see equation (2.6)) in the lens equation (2.7). D_s, D_{ds} and D_d are angular diameter distances (see equations (1.13) and (2.8)). Figure credit: Meylan et al. (2006)

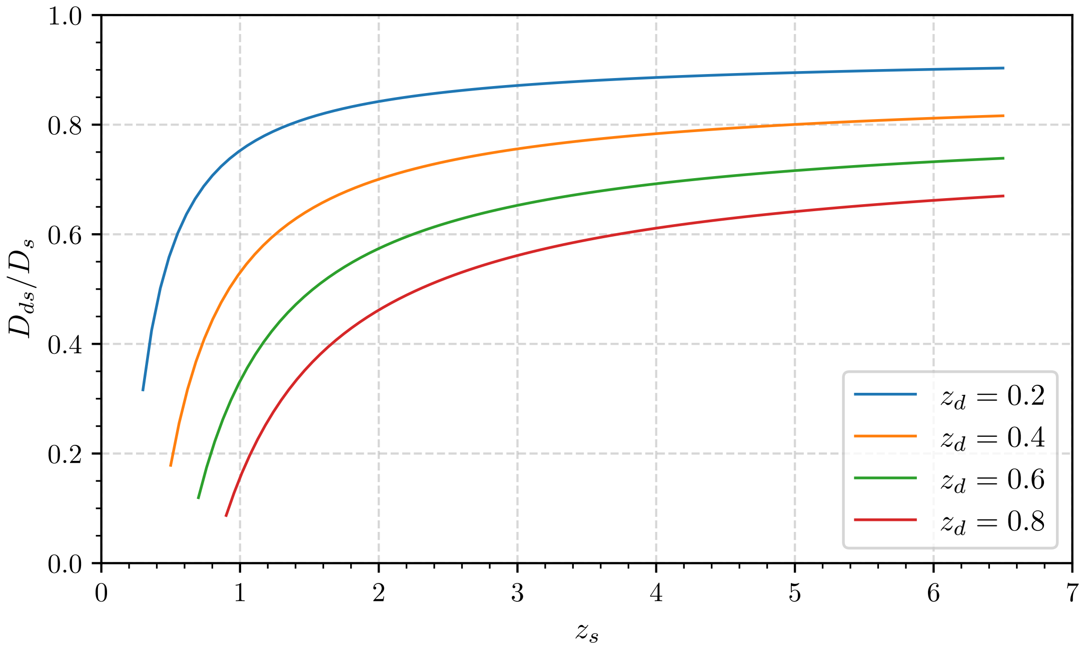

Figure 2.6: Distance ratios $\frac{D_{ds}}{D_s}$ in a flat ΛCDM Universe with $\Omega_m = 0.3$, $\Omega_\Lambda = 0.7$ and $H_0 = 70\,\frac{\mathrm{km}}{\mathrm{Mpc\,s}}$ (the cosmology assumed throughout this work) as function of source redshift z_s computed after equation (2.8) for different lens redshifts z_d. Note that the evolution with source redshift becomes negligible beyond $z \gtrsim 6$.

which in general allows for several lensed image positions $\vec{\theta}$ to correspond to the same source position $\vec{\beta}$, meaning it generally is nonlinear.

The derivation of the lens equation requires the above mentioned Euclidean relation between angles and distances, which is not guaranteed in curved spacetime (see section 1.1.2). This problem can however be avoided by just *defining* the distances used in gravitational lensing as angular diameter distances as in equation (1.13). The angular diameter distance can be computed from the redshifts of two objects, z_1 and z_2 respectively using the cosmological parameters Ω_m and Ω_Λ. For flat spacetimes, the angular diameter distance between two objects is given in Peebles (1993) (chapter 13) as

$$D_A(z_1, z_2) = \frac{c}{H_0}\frac{1}{1+z_2}\int_{z_1}^{z_2}\frac{dz}{\sqrt{\Omega_m(1+z)^3+\Omega_\Lambda}}. \tag{2.8}$$

Fig. 2.6 shows the evolution of the *lensstrength*, the distance ratio $\frac{D_{ds}}{D_s}$ defined in equation (2.6), with source redshift z_s for different redshifts of the lens z_d using the cosmology assumed in this work. For high-redshift galaxy observations we want to select lenses at preferably low redshifts z_d which maximizes the lensstrength and thus the magnification as can be see in Fig. 2.6.

2.2.2 Magnification

Gravitational lensing deforms and distorts the observable shape of a source in the background while preserving its surface brightness. Because of that, when the observed area of a source changes, e.g. is larger, it appears brighter, it is *magnified*. More quantitatively, conservation of surface brightness means that $S_{unlensed}(\vec{\beta}) = S_{lensed}(\vec{\theta})$. The magnification μ is then given by the ratio of fluxes from the source and the image. Since surface brightness is conserved, this just translates to the ratio of the areas

$$\mu \equiv \frac{S_{lensed}(\vec{\theta})d^2\theta}{S_{unlensed}(\vec{\beta})d^2\beta} = \frac{d^2\theta}{d^2\beta} \tag{2.9}$$

which can be expressed in terms of the Jacobian of the transformation from the area of the source $d^2\beta$ to the area of the image $d^2\theta$. Derivating the lens equation (2.7) with respect to $\vec{\theta}$ yields the Jacobian matrix of the lens mapping

$$\frac{\partial \beta_i}{\partial \theta_j} = \begin{pmatrix} 1 - \frac{\partial \alpha_x}{\partial \theta_x} & -\frac{\partial \alpha_x}{\partial \theta_y} \\ -\frac{\partial \alpha_y}{\partial \theta_x} & 1 - \frac{\partial \alpha_y}{\partial \theta_y} \end{pmatrix} \equiv \mathcal{A} \tag{2.10}$$

which is a function of the image position $\vec{\theta}$ and therefore of the deflection angle $\vec{\alpha}$. The magnification μ of a gravitationally lensed object is then nothing else than the inverse of the determinant of the Jacobian matrix $\mathcal{A}$

$$\mu = \frac{1}{\det\mathcal{A}}. \tag{2.11}$$

As can be seen from equation (2.11), μ can be both positive or negative. A negative sign in equation (2.11) just flips the parity of the resulting lensed image. The observed flux of a lensed image on the other hand increases or decreases as $f_{obs} = f_0|\mu|$ relative to the un-lensed source flux f_0. I will come back later to the special case when $\det\mathcal{A} = 0$.

Convergence and Shear

The elements of the Jacobian matrix $\mathcal{A}$ are derivatives of the deflection angle and can therefore be expressed in terms of second derivatives of the lensing potential Φ (see equation (2.2)). With

$$\varphi(\vec{\xi}) = \frac{D_{ds}}{D_d D_s}\frac{2}{c^2}\int \Phi(\vec{\xi}, z)dz \tag{2.12}$$

where $\vec{\xi} = D_d\vec{\theta}$ is a distance in the lens plane, as the scaled and projected potential, we can re-write the Jacobian matrix as

$$\mathcal{A} = \begin{pmatrix} 1 - \kappa - \gamma_1 & -\gamma_2 \\ -\gamma_2 & 1 - \kappa + \gamma_1 \end{pmatrix} \tag{2.13}$$

with

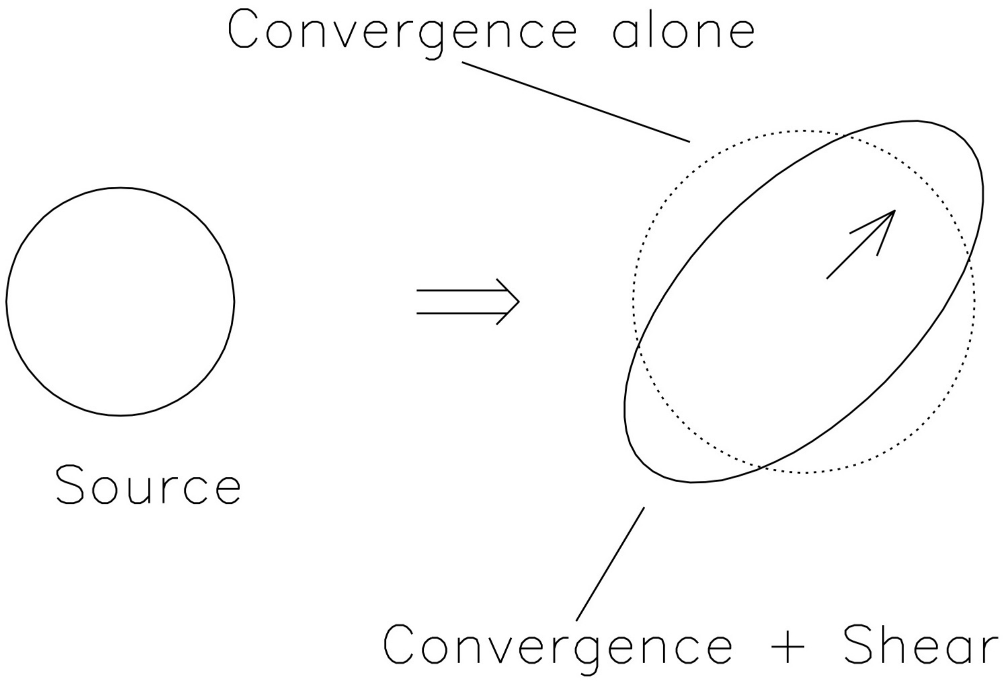

Figure 2.7: Effect of convergence and shear on a circular source. Convergence maps the source isotropically (dotted circle) and shear is responsible for the distortion (solid ellipse). Figure credit: Narayan & Bartelmann (1996)

$$\kappa = \frac{1}{2}\left(\frac{\partial^2\varphi}{\partial\theta_x^2} + \frac{\partial^2\varphi}{\partial\theta_y^2}\right) \tag{2.14}$$

$$\gamma_1 = \frac{1}{2}\left(\frac{\partial^2\varphi}{\partial\theta_x^2} - \frac{\partial^2\varphi}{\partial\theta_y^2}\right) \tag{2.15}$$

$$\gamma_2 = \frac{\partial^2\varphi}{\partial\theta_x\partial\theta_y} = \frac{\partial^2\varphi}{\partial\theta_y\partial\theta_x}. \tag{2.16}$$

These quantities directly depend on the lensing potential φ and fully describe the lens mapping (2.7). The value κ (2.14) is called *convergence* and is equivalent to the surface mass density of the lens. The quantity $\gamma = \sqrt{\gamma_1^2 + \gamma_2^2}$ is called *shear*. The meanings of convergence and shear become clear when considering their effect on the mapping of a circular background source as illustrated in Fig. 2.7. Convergence (dotted circle) magnifies a source isotropically. Shear then adds anisotropy to the mapping, it distorts the circular source in Fig. 2.7 into an ellipse.

Finally, writing the magnification defined in equation (2.11) in terms of convergence and shear yields

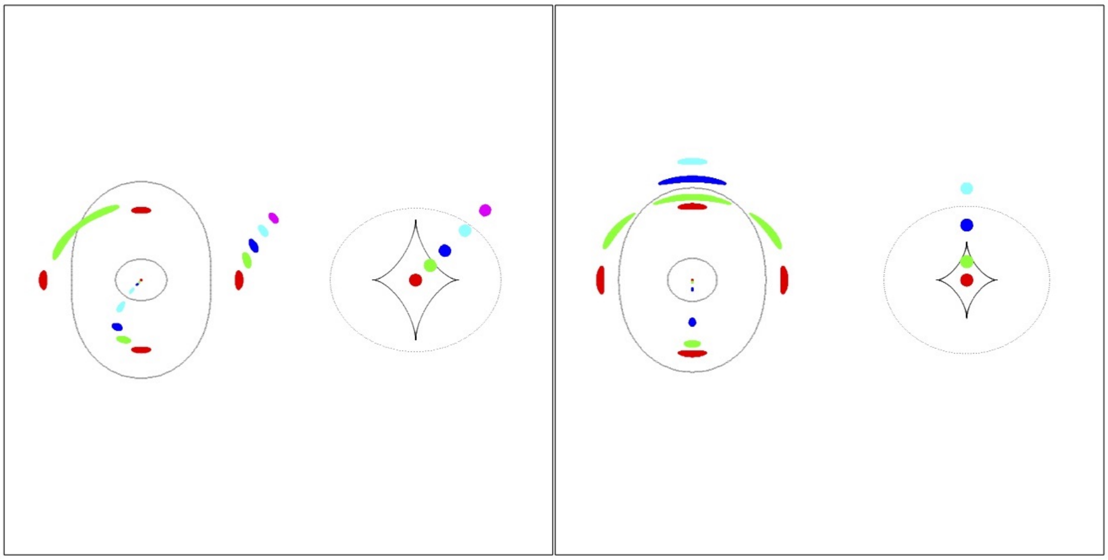

Figure 2.8: Critical curves, caustics and multiple imaging for a source crossing a fold of a caustic (left panel) and a source crossing a cusp of a caustic (right panel) for an elliptical lens. The lens plane is depicted on the left and the source plane on the right of each panel. The green scenario, where the source straddles the tangential caustic, is the one most likely to form a giant arc. Figure credit: Narayan & Bartelmann (1996)

$$\mu = \frac{1}{(1-\kappa)^2 - \gamma^2}. \tag{2.17}$$

Critical curves and caustics

Looking at equation (2.17), it is immediately clear that the magnification becomes singular when $(1-\kappa)^2 = \gamma^2$ (e.g. if $\gamma = 0$ and $\kappa = 1$ or e.g. if $\gamma = \kappa = \frac{1}{2}$). As the magnification is a function of $\vec{\theta}$, this means that images at certain coordinates in the lens plane will be extremely magnified and distorted. These points form the *critical curves* which separate the multiple images of the same background source in the strong lensing regime, which therefore in turn usually appear in the vicinity of the critical curves.

Using the lens mapping (2.7) to map the critical curves into the source plane yields the corresponding lines in the source plane, the so-called *caustics*. The number and positions of multiple images are determined by the position of the source relative to the caustics: A source outside the caustics will only be imaged once and not magnified by a lot (see e.g. the purple source in Fig. 2.8). This is the weak lensing regime. The closer a source gets to the caustic, the closer its image will get to the critical curve and enter the strong lensing regime where it becomes more heavily distorted and magnified.

The exact geometry of the critical curves and caustics depends on the lensing potential (2.12) and hence on the exact mass distribution of the lens. Fig. 2.8 shows the configuration for an elliptical lens which is commonly used as the closest analytical ap-

proximation to a real lens mass distribution. The lens plane is depicted on the right and the source plane on the left side of each panel. Because of the shape of the lens, the caustic corresponding to the outer critical curve is also an ellipse, while the caustic corresponding to the inner critical curve has a diamond shape. As depicted in Fig. 2.8, an extended source close to or inside this diamond-like caustic (the green and red sources) is imaged into long arcs tangential to the outer critical line and a very faint image close to the center of the lens. A source lying inside or close to the outer caustic (which corresponds to the *inner* critical curve) on the other hand (the blue sources) is imaged into radially orientated images, which lie close to the inner critical curve, and tangentially orientated arcs lying outside the outer critical curve. Because of the described properties of the images, the outer critical curve, and thus also the inner caustic, is called *tangential* while the inner critical curve, corresponding to the outer caustic, is called *radial*. This caustic structure allows for numerous complex configurations of multiple images. The left panel of Fig. 2.8 shows what happens to a source crossing a *fold* of the caustic and the right panel shows it for a *cusp* of the caustic. Note that in the case of a circular lens, the tangential critical curve forms a circle whose radius is called the *Einstein radius*.
Of course, real extended gravitational lenses will rarely have an exactly elliptical mass distribution which is only an approximation. The shape of the lensing potential of a galaxy cluster will be affected by the mass of large-scale objects far away, which can be described as an external shear, or by local small-scale substructure in the mass distribution which breaks up the symmetry, not to mention that the lens itself does not necessarily have to be elliptical at all. The caustic structure of gravitational lenses can therefore in general become arbitrarily complex. For an arbitrary surface mass distribution, the surface mass density enclosed by the tangential critical curve is called *critical mass* $\Sigma_{\rm crit}$ which relates to the convergence as

$$\kappa(\vec{\theta}) = \frac{\Sigma(\vec{\theta})}{\Sigma_{\rm crit}}. \tag{2.18}$$

In order to provide a universal scale for the size of a gravitational lens independently of the exact spatial distribution of mass, we use the critical area, i.e. the area where $\Sigma > \Sigma_{\rm crit}$ to define the *effective* Einstein radius θ_E as the radius of a circle corresponding to the critical area.

2.3 Cosmic telescopes – The *Hubble Frontier Fields*

Galaxy clusters are the most massive gravitationally bound structures in the Universe and as such commonly have high super-critical central projected surface mass densities $\Sigma > \Sigma_{\rm crit}$, which result in numerous strong gravitational lensing phenomena. Background galaxies that lie in or close to the caustics of galaxy clusters are lensed into strongly magnified and distorted arcs by the massive and dense cores of the clusters (blue and purple arcs in Fig. 2.9). This is called the *strong lensing* (SL) regime with typical magnifications $\mu \gg 1$. Commonly referred to as 'cosmic telescope', the SL effect can be used to observe magnified faint high-redshift sources that would not be observable in

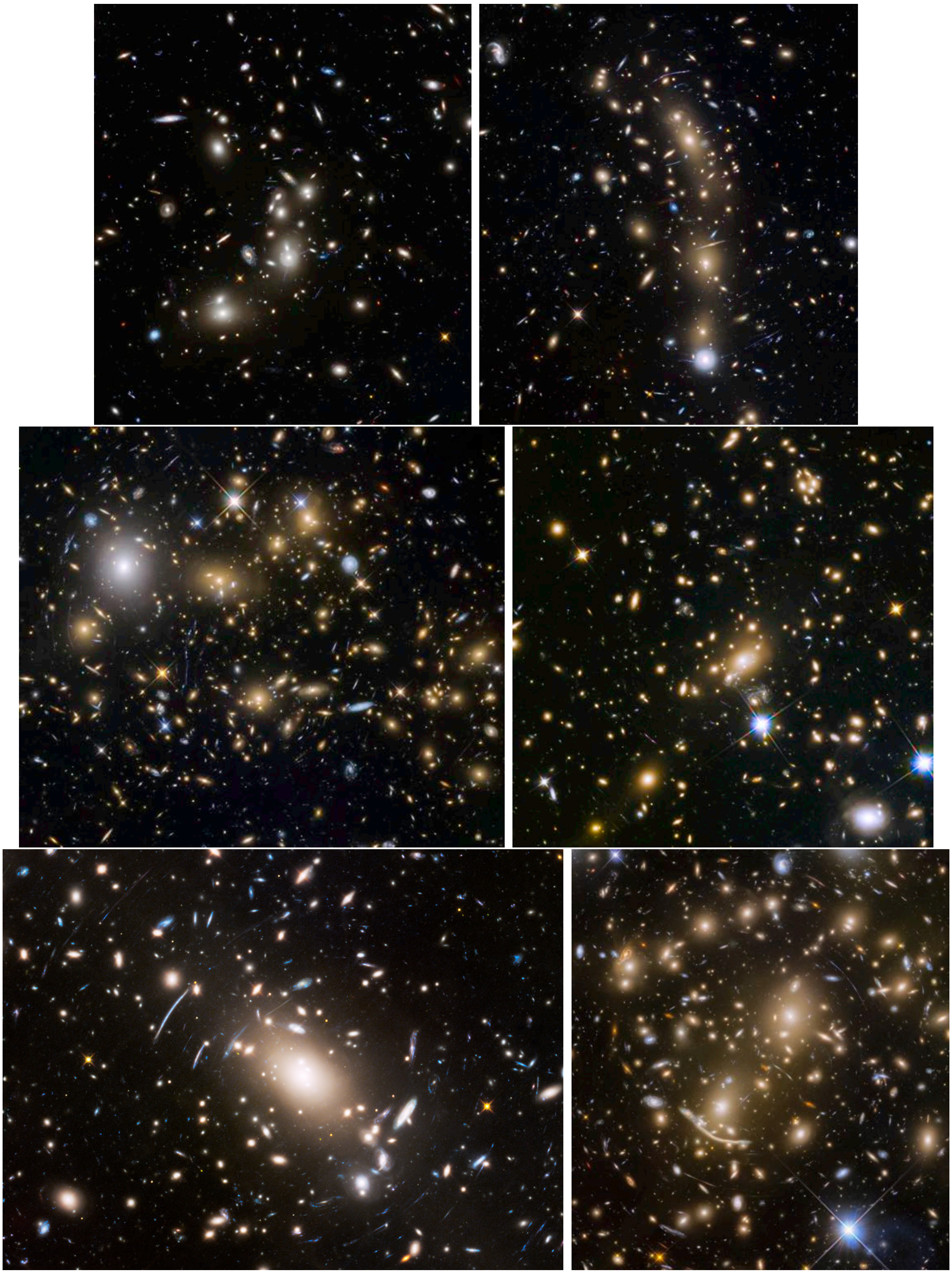

Figure 2.9: Color-composite images of the six *Hubble Frontier Fields* clusters, the best studied strong lensing fields to date. From left to right and top to bottom: A2744, MACS0416, MACS0717, MACS1149, S1063, A370. Cluster galaxies commonly appear red and yellow and strong lensing arcs purple and blue. The giant arc in A370 (bottom right) was the first strong lensing event ever observed in a galaxy cluster (Lynds & Petrosian, 1986; Soucail, 1987) and MACS0717 (middle left) is the cluster with the largest effective Einstein radius observed to date ($\theta_E \simeq 55'' \pm 3''$; Zitrin et al., 2009). Figure credits: NASA, ESA and the HFF Team.

Table 2.1: Properties of the six HFF clusters (cf. Fig. 2.9) taken from Lotz et al. (2017). The HFF were specifically chosen for their probability of magnifying a high-redshift source to $H_{\mathrm{F160W}} \leq 27$ (fourth column) and their low galactic dust extinctions (fifth column).

Cluster	RA	Dec.	z	$M_{\mathrm{vir}}[\mathrm{M}_\odot]$	$P(z=9.6)$	$E_{(B-V)}$
A2744	00:14:21.2	-30:23:50.1	0.308	1.8×10^{15}	0.96 ± 0.07	0.012
MACS0416	04:16:08.9	-24:04:28.7	0.396	1.2×10^{15}	0.63 ± 0.12	0.036
MACS0717	07:17:34.0	+37:44:49.0	0.545	$2-3 \times 10^{15}$	0.84 ± 0.05	0.068
MACS1149	11:49:36.3	+22:23:58.1	0.543	2.5×10^{15}	0.60 ± 0.10	0.020
S1063	22:48:44.4	-44:31:48.5	0.348	1.4×10^{15}	0.69 ± 0.08	0.010
A370	02:39:52.9	-01:34:36.5	0.375	$\sim 1 \times 10^{15}$	0.90 ± 0.08	0.028

blank fields (e.g. Maizy et al., 2010; Kneib & Natarajan, 2011; Sharon et al., 2012; Monna et al., 2014; Richard et al., 2014; Coe et al., 2015, 2019) which is the whole interest of gravitational lensing for this work. Note nevertheless that the *weak lensing* (WL) regime, which typically occurs further away from the cluster centers where $\Sigma \ll \Sigma_{\mathrm{crit}}$, is of great interest for constraining the total mass and thus the lensing potential of clusters in addition to the constraints provided by the SL regime (e.g. Jauzac et al., 2012; Jullo et al., 2014; Niemiec et al., 2020). Galaxy clusters have three main components to their total mass: Galaxies (with all their internal components, i.e. stars, gas, dust and DM halos), *intra-cluster medium* (ICM) gas and DM. While the first two can be observed in visible and X-ray wavelengths respectively, the DM which dominates the cluster mass is not observable and can therefore only be constrained by gravitational lensing mass modeling. Many different lensing modeling techniques, both parametric and non-parametric, have been developed and each have their advantages and disadvantages (for a review of lensing modelling techniques cf. Kneib & Natarajan, 2011; Meneghetti et al., 2017). Since cluster DM mass distributions are in general arbitrarily complex, in particular on the high-critical-area end (e.g. Monna et al., 2015; Zitrin et al., 2017; Lagattuta et al., 2017, 2019; Acebron et al., 2018, 2019; **?**), SL modeling uncertainties and systematics can become very large and strongly depend on the availability of spectroscopic redshifts for the lensed arcs (e.g. Johnson & Sharon, 2016; Acebron et al., 2017). The impact of these uncertainties on high-redshift galaxy stellar mass function measurements is an important part of this work and is discussed in detail in sections 3.2.2 and 3.5.2.

In the context of high-redshift galaxy observations using the gravitational magnification of SL clusters, the *Hubble Frontier Fields* (HFF, Lotz et al., 2017) are without doubt the best-studied SL fields to date. Following the success of programs such as the deep blank fields mentioned in section 2.1.2 and the *Cluster Lensing and Supernova Survey with Hubble* (CLASH, Postman et al., 2012), which succeeded in detecting several highly magnified galaxy candidates up to $z > 9$ (Zheng et al., 2012; Coe et al., 2013; Bouwens et al., 2014), the HFF program was a multi-cycle observing campaign with both HST and *Spitzer*. Reaching ~ 29 AB magnitude depths with HST and ~ 26 AB magnitude depths with *Spitzer*, the HFF program delivered the deepest images of six massive SL clusters to date: Abell 2744 (A2744), MACSJ0416.1-2403 (MACS0416), MACSJ0717.5+3745

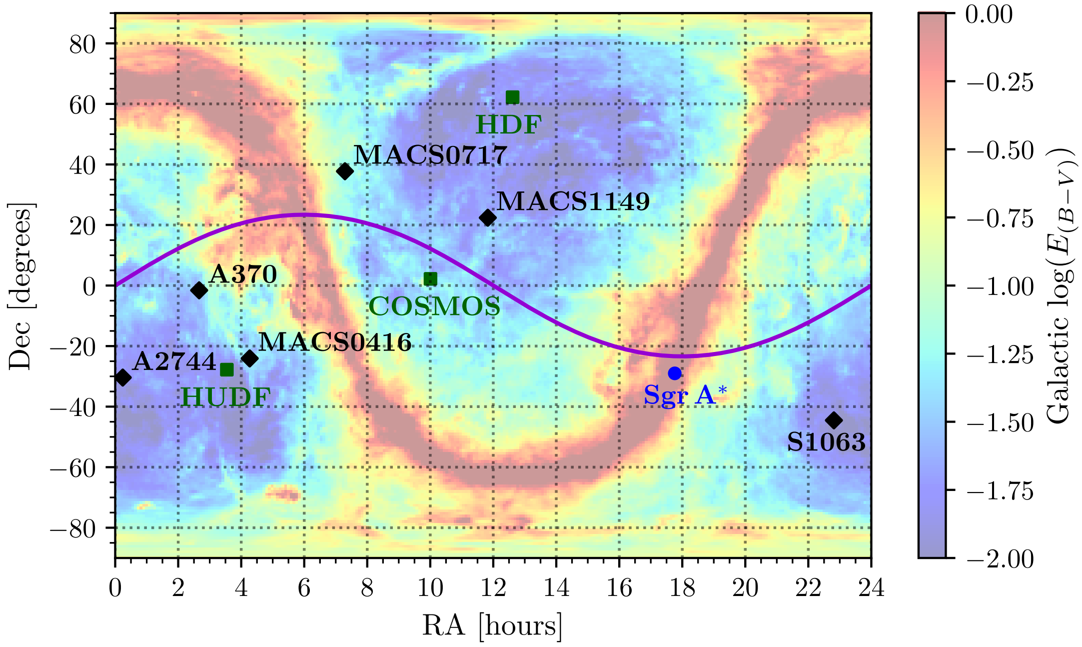

Figure 2.10: The locations of the six HFF clusters (black; cf. Tab. 2.1) plotted over the galactic dust extinction map from Schlegel et al. (1998), similar to Fig. 1 in Lotz et al. (2017). For reference, the locations of the deep blank fields presented in section 2.1.2 are shown in green and the galactic center Sgr A* in blue. The purple line represents the ecliptic. Note that the GOODS-N and GOODS-S fields correspond to the HDF and the HUDF respectively.

(MACS0717), MACSJ1149.5+2223 (MACS1149), Abell S1063 (S1063) and Abell 370 (A370). All six HFF clusters can be seen in Fig. 2.9. These six clusters were specifically chosen by two main criteria: The likelihood of lensing a $z = 9.6$ source to $H_{\mathrm{F160W}} \leq 27$ magnitudes, i.e. their critical area, and low galactic dust extinction, i.e. clusters at high galactic latitudes far from the galactic plane. Some properties of the HFF clusters are summed up in Tab. 2.1 and we show their locations on the sky in Fig. 2.10. The depths in the individual filters can be found in Tab. 3.1. Note that MACS0717 is the cluster with the largest critical area observed to date (Zitrin et al., 2009). All the HFF data and SL models are now publicly available on the `Mikulski Archive for Space Telescopes`[1] (`MAST`). In addition to the HST and *Spitzer* data, the HFF have been observed in numerous additional programs with ground-based facilities such as the VLT, *Keck* and ALMA both with imaging and spectroscopic instruments. Three independent teams have produced complete catalogs and high-level data products of the HFF: ASTRODEEP (Merlin et al., 2016; Castellano et al., 2016; Di Criscienzo et al., 2017; Bradač et al., 2019), HFF-DeepSpace (Shipley et al., 2018) and the Pagul et al. (2021) catalogs. With all this, the HFF have some of the richest data sets in existence and therefore present the perfect

---

[1] `https://archive.stsci.edu/pub/hlsp/frontier`

hunting grounds for lensed high-redshift galaxies.

Indeed, using the SL magnification of the HFF it has been possible to extend the $z \gtrsim 6$ UV luminosity functions down to $M_{\mathrm{UV}} \lesssim -13$ magnitudes (Bouwens et al., 2017b; Livermore et al., 2017; Atek et al., 2018; Ishigaki et al., 2018) and the stellar mass functions down to $M_\star \gtrsim 10^6\,\mathrm{M}_\odot$ (Bhatawdekar et al., 2019; Kikuchihara et al., 2020; Furtak et al., 2021). This translates to a gain of up to ~ 4 magnitudes in UV luminosity and 1-2 orders of magnitude in stellar mass when using SL magnification as opposed to the blank fields in section 2.1.2 and led to the first tentative detections of a faint low-mass end turnover in the high-redshift UV luminosity and stellar mass functions (Bouwens et al., 2017b; Atek et al., 2018, and chapter 3 of this work, published in Furtak et al. (2021)). The HFF also led to the detection of the most distant currently known lensed galaxy, MACS1149-JD1 at $z = 9.11$ (Zheng et al., 2012; Hashimoto et al., 2018).

2.4 Observational constraints on galaxy physics – The galaxy SED

Once statistically significant samples of high-redshifts galaxies are detected with the methods explained in the previous sections, the goal is to measure their physical parameters such as stellar mass, age, star-formation rate, dust extinction, etc. This is in general done by studying the light, or in more general terms the electro-magnetic radiation, that they emit, i.e. their emitted *spectral energy distribution* (SED). Since detailed spectroscopy is usually not available for high-redshift galaxies, because they are too faint and because most of their SED except the rest-frame UV range (cf. section 2.4.1) is redshifted beyond the reach of most spectrographs, we need to infer their physical parameters by fitting synthetic SEDs to the broad-band photometry. Since the luminous matter of a galaxy is made up of three main components, stars, gas and dust, the SEDs typically used for these kinds of fits combine stellar population synthesis models (e.g. Tinsley, 1978; Leitherer & Heckman, 1995; Bruzual & Charlot, 2003; Maraston, 2005; Vazdekis et al., 2010; Conroy & Gunn, 2010; Maraston & Strömbäck, 2011) with nebular emission models (e.g. Charlot & Longhetti, 2001; Ferland et al., 2013; Gutkin et al., 2016) and sometimes also dust emission models (e.g. Dale & Helou, 2002; Peeters et al., 2004; da Cunha et al., 2008; Noll et al., 2009) even though the latter are not of great importance for the wavelength ranges probed at high redshifts. These models however typically depend on many parameters which results in considerable degeneracies, in particular when only several bands of broad-band photometry are available to constrain the SED.

Because of this, the inference of high-redshift galaxy parameters from broad-band photometry is a challenging matter which requires deep understanding of stellar populations (cf. Fig. 2.11), star-formation and nebular physics. Since SED-modeling represents one of the main topics of my thesis, in particular of chapters 3 and 5, I will introduce the galaxy SED at high redshifts and its features and sensitivities in this section. For more exhaustive reviews of galaxy SEDs and physics, I refer the reader to Osterbrock & Ferland (2006), Dunlop (2013) and Cimatti et al. (2019).

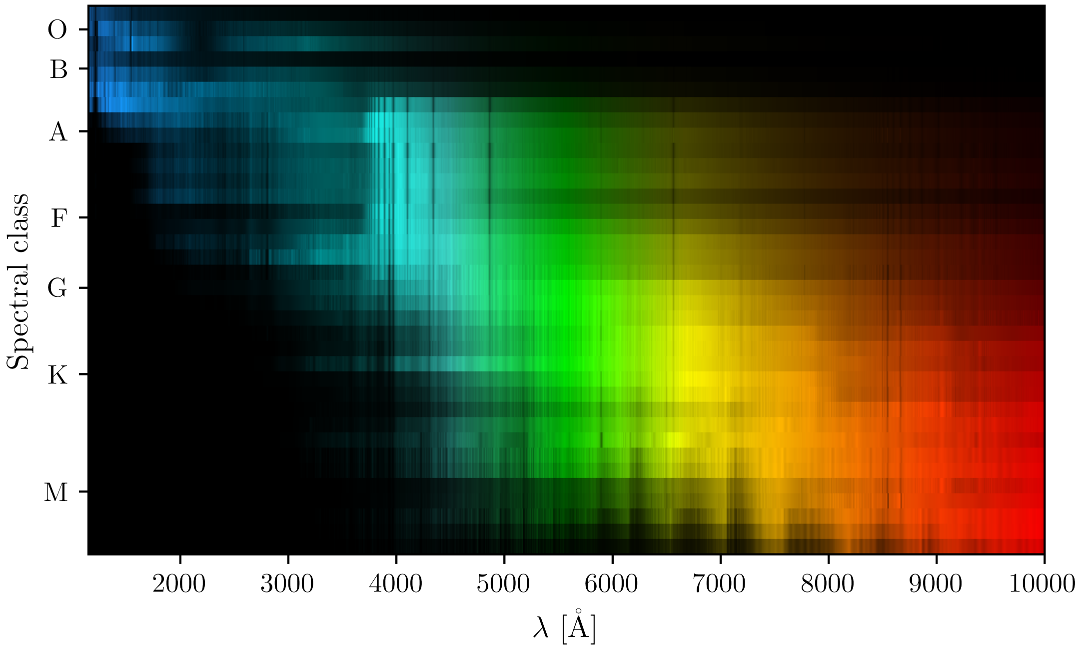

Figure 2.11: False-color plot of main-sequence star spectra (luminosity class V) for different spectral types taken from spectral libraries by Pickles (1998) and Ivanov et al. (2004). Each row corresponds to one spectrum. The spectra clearly show some key features relevant for high-redshift galaxy science such as the prominent Balmer break at $\lambda_0 = 3646\,\text{Å}$ and that O and B class stars essentially emit in the UV range. The spectra are publicly available at `https://www.eso.org/sci/facilities/paranal/decommissioned/isaac/tools/lib.html`.

2.4.1 Rest-frame UV

The rest-frame UV emission at $\lambda_0 \sim 1500\,\text{Å}$ of $z \gtrsim 6$ galaxies can typically be observed with the near-infrared (NIR) filters aboard the HST (cf. Fig. 2.2). At these wavelengths, the most notable feature of the galaxy SED is the Lyman break at $\lambda_0 = 1215.15\,\text{Å}$ which constrains the redshift of the galaxy (cf. section 2.1.1). The UV continuum red-ward of the Lyman break is emitted by hot and massive O and B class stars (cf. Fig 2.11). These stars are very short-lived ($\sim 10^6\,\text{yr}$) and thus only exist in star-forming H II regions. The UV continuum therefore mostly probes the currently ongoing star-formation of the galaxy. The rest-frame UV SED is commonly quantified with the UV continuum slope β, defined as

$$f_\lambda \propto \lambda^\beta \tag{2.19}$$

(e.g. Meurer et al., 1999, where $\beta = -2$ corresponds to a flat spectrum). Since high-redshift galaxies are expected to be very young, metal-poor and highly star-forming systems (cf. section 1.3.2), they are also expected to have substantially bluer UV continuum slopes than observed at $z < 6$. Indeed, recent observations with broad-band photometry

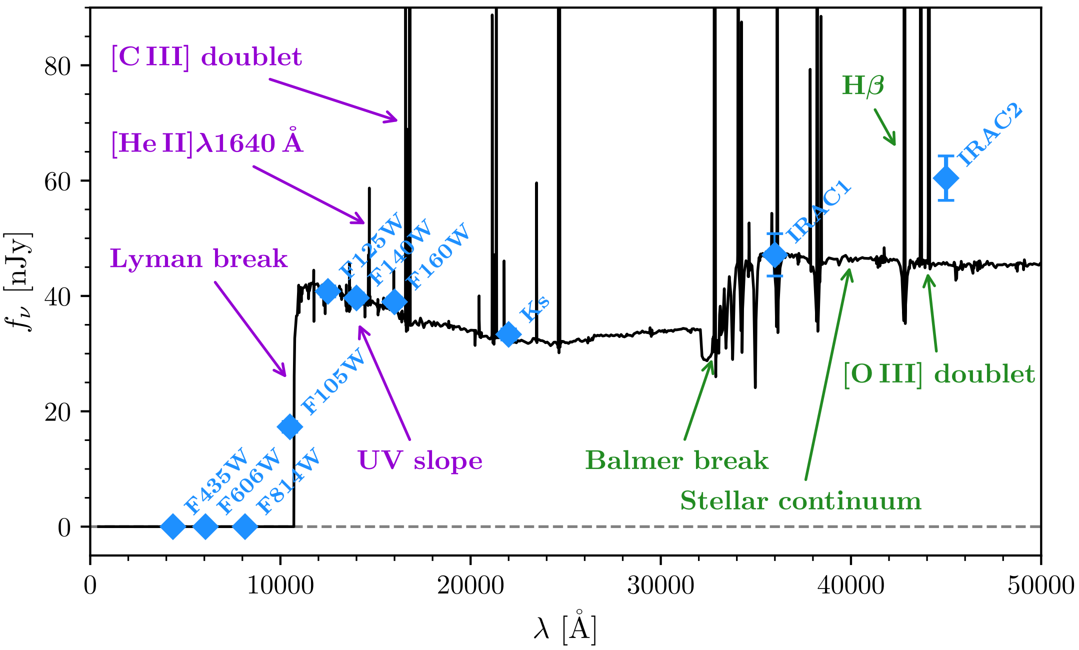

Figure 2.12: Best-fitting SED of the dropout galaxy A370-20021 (cf. section 4.3.1 and Figs. 2.3 and 4.7) at $z \simeq 7.78 \pm 0.05$ (black) and the best-fitting photometry (blue) in each of the HFF bands (i.e. HST, Ks and *Spitzer*; cf. Tab. 3.1). The most prominent rest-frame UV emission features are high-lighted in purple and prominent rest-frame optical features in green. Note that the Lyα line at $\lambda_0 = 1215.15$ Å is not present in this SED because it is often ignored in SED-fitting methods due to the difficulty to model radiative transfer and the decline in number of LAE observed at $z > 6.5$ (Schenker et al., 2014; Pentericci et al., 2018). Hα at $\lambda_0 = 6562.8$ Å is redshifted to 57621 Å in this case and therefore beyond the reach of current instrumentation. The [C III] doublet has rest-frame wavelengths of 1907 Å and 1909 Å, Hβ of 4861.4 Å and the [O III] doublet of 4959 Å and 5007 Å.

result in average UV-slopes $\beta \simeq -2.6 \pm 0.5$ (e.g. Bouwens et al., 2016; Bhatawdekar & Conselice, 2021) which roughly agrees with theoretical expectations (Dayal & Ferrara, 2012) within the error bars. The correct interpretation of UV-slopes however remains unclear since they are sensitive to several parameters such as age, metallicity, nebular contribution and dust attenuation. The latter in particular heavily affects the UV continuum as dust attenuation laws become steeper shorter wavelengths such that visible and UV attenuation typically differ by a factor ×4 (e.g. Calzetti et al., 2000, cf. section 3.5.3). For that reason, blue UV-slopes at high redshifts are commonly interpreted as resulting from a decrease in dust attenuation and maximum stellar age with increasing redshift (Bouwens et al., 2009, 2016; Dunlop, 2013) even though they are also affected by other parameters and have large uncertainties. A typical SED of a high-redshift $z \sim 8$ galaxy is shown in Fig. 2.12 with the UV emission features highlighted in purple.

In addition to the stellar continuum, the rest-frame UV SED typically also shows some nebular line emission which in some particularly bright cases can be observed with ground-based NIR spectrographs. The most notable UV emission line is Lyα and in most cases it also is the only emission line detected in high-redshift spectroscopy. While young high-redshift galaxies are expected to have strong Lyα emission driven by star-formation with equivalent widths of order EW ~ 200 Å (Charlot & Fall, 1993), observations rarely find Lyα EWs exceeding EW $\gtrsim 25$ Å at and measure a decline in the fraction of Lyα emitters (LAEs) in LBG samples at $z > 6.5$ (Schenker et al., 2014; Pentericci et al., 2018). This is due to absorption of Lyα by both the neutral IGM (cf. sections 1.2.2 and 2.1.1) and also the ISM within the galaxies themselves. Another rest-frame UV line emission feature is the [C III]$\lambda\lambda$1907, 1909 Å doublet (cf. Fig 2.12) which is less bright than Lyα in general. Recent observations have nonetheless been able to detect [C III] emission out to $z \sim 9$ and place constraints on galaxy parameters such as metallicity and ionization parameter by combining the [C III] equivalent widths with rest-frame optical photometry (Hutchison et al., 2019; Topping et al., 2021; Laporte et al., 2021). Other UV emission lines include the [C IV]λ1549 Å and [He II]λ1640 Å lines, none of witch has been observed at high redshifts to date. The latter is of particular interest for constraining possible Pop. III stellar populations (cf. sections 1.2.2 and 1.2.3) as it represents one of the only possible cooling lines in primordial gas (e.g. Glover, 2013; Cassata et al., 2013). Finally, recent observations of UV absorption lines at $z \sim 6$ have been able to provide some constraints on stellar metallicity (Harikane et al., 2020). Note however that all the spectroscopic observations described above have been carried out on relatively bright and massive galaxies with $M_{\mathrm{UV}} \lesssim -20$. The inferred properties and relations are therefore not necessarily generalizable to a fainter lower-mass population of galaxies.

2.4.2 Rest-frame optical

While the rest-frame UV emission traces young and massive stars and thus the ongoing star-formation of a galaxy, it is very sensitive to the age and SFH of the galaxy does not represent the bulk of the stellar population (e.g. Salpeter, 1955; Kroupa, 2001; Chabrier, 2003). It does therefore not represent an efficient probe of a galaxy's stellar mass (cf. sections 3.2.3 and 3.5.1 in particular). Most of the stellar mass of a galaxy is instead comprised of redder lower-mass G, K and M class stars (cf. Fig. 2.11) which evolve much more slowly. In order to to measure the stellar mass we therefore need to observe the rest-frame optical $\lambda_0 \sim 5500$ Å continuum emission which is dominated by these lower-mass populations. At $z \gtrsim 6$, these wavelengths are redshifted into *Spitzer* bandpass. As can be seen in in Fig. 2.12, where rest-frame optical emission features are highlighted in green, the optical continuum is degenerate with two other major emission features in broad-band photometry: The so-called *Balmer break* and optical nebular emission lines. The Balmer break at $\lambda_0 = 3646$ Å is, similarly to the Lyman break (cf. section 2.1.1), due to ionization of neutral hydrogen but in the ISM *within* the galaxy and from the *second* energy level of the hydrogen atom through absorption of radiation blue-ward of 3646 Å. It is most prominent in A, F and G class stars (cf. Fig. 2.11) and therefore indicates that a galaxy is building up its lower-mass stellar population, i.e. it traces the stellar age of a galaxy. In addition, the Balmer break is degenerate with the so-called 4000 *Å* *break* which is due to absorption of blue radiation by metals in stellar atmospheres and typically appears in older and quiescent galaxies. These two breaks occur very close to each other in wavelength and are therefore often indistinguishable from each other in observations, in particular when using only broad-band photometry. This creates a degeneracy between stellar mass, age and metallicity when inferring galaxy parameters from photometry.

The other major features of the optical SED are nebular emission lines: Hydrogen lines, mostly Hα at $\lambda_0 = 6562.8$ Å and Hβ at $\lambda_0 = 4861.4$ Å, and the [O III]λ5007 Å and [O III]λ4959 Å lines (cf. Fig 2.12). These lines are emitted by ionized ISM in H II regions and thus also trace the star-formation of the galaxy. Unlike the UV continuum (cf. section 2.4.1) which probes ongoing star-formation over time scales of ~ 100 Myr however, the optical emission lines probe star-formation on shorter time scales ~ 10 Myr. The ratio between UV and emission line inferred SFRs can therefore be used to quantify the 'burstiness' of star-formation (Weisz et al., 2012; Sparre et al., 2017; Emami et al., 2019, Atek et al., in prep.) and thus yield insight in the galaxy's SFH. Optical emission lines are beyond the reach of current spectrographs at $z \gtrsim 6$, i.e. $\lambda_{\rm obs} \gtrsim 3$ µm, and therefore have not yet been directly observed in high-redshift galaxies. They will be one of the most anticipated targets of the upcoming JWST whose unprecedented NIR spectroscopic capacity will enable us to observe rest-frame optical emission lines out to $z \sim 9$ as I will discuss in detail in sections 3.5.3 and 6.2. Recent observations have however revealed relative excesses in the *Spitzer* colors of high-redshift galaxies which have been attributed to optical emission lines with particularly large equivalent widths (EW $\lesssim 3000$ Å; Smit et al., 2014, 2015; De Barros et al., 2019). This is a significant contribution to the flux in the broad-band filters which creates a considerable degeneracy with the stellar continuum used to probe the stellar mass, the impact of which is studied in detail in chapter 3 of this work. Efforts have recently also been made to link *Spitzer* color-excesses to the stellar age of $z \sim 7-8$ galaxies (Stefanon et al., 2021a). Note also that while the rest-frame optical SED is less affected by dust attenuation than the UV range, it still is affected by dust which creates an additional degeneracy with stellar mass (cf. section 3.5.3).

Chapter 3

What is believable in lensed high-redshift GSMF measurements?

> “… nothing is certain, even if you know it is.”
>
> ---
>
> Sir Terry Pratchett, *The Science of Discworld II: The Globe*, 2002

As explained in the previous chapter, recent studies of $z \gtrsim 6$ GSMFs using HFF HST and *Spitzer* data have extended the low-mass end of the high-redshift GSMF down to $M_\star > 10^6\,\mathrm{M}_\odot$, confirming the steep low-mass end slopes found in blank field studies (Bhatawdekar et al., 2019; Kikuchihara et al., 2020). Measuring stellar masses at high redshifts however remains particularly difficult for several reasons: (i) lack of robust rest-frame optical photometry for faint galaxies resulting in poorly constrained stellar masses; (ii) non-trivial systematic effects in the strength and distribution of the strong lensing caustics which significantly impact the derived intrinsic luminosity and hence the stellar mass (Bouwens et al., 2017b; Atek et al., 2018); and (iii) significant degeneracies with other physical galaxy parameters.

In this chapter, we present a derivation of the $z \sim 6-7$ GSMF, using the full data set of the HFF program and for the first time including full treatment of lensing uncertainties and the effects of missing rest-frame optical photometry. We study the impact of various SED-fitting assumptions on the resulting GSMFs in a comparative way by systematically applying different assumptions and parameter ranges in our SED-fitting analysis. Our overall goal is to assess what is believable in high-redshift GSMF studies with the data available from the current instrumentation. This chapter is structured as follows: In section 3.1, we describe the HFF data set that we use and our methods for obtaining photometry with particular emphasis on the infrared *Spitzer* data. In section 3.2, we explain the SED-fitting procedure we use to derive stellar masses. We then present the resulting mass-luminosity relations in section 3.3 and our final GSMFs in section 3.4. Finally, we discuss these results regarding photometry, lensing and SED-fitting uncer-

Table 3.1: Limiting 3σ AB magnitudes of the 10 photometric bands used for this study. The HST limiting magnitudes were computed in Atek et al. (2018), the *Ks* and Spitzer limits in Steinhardt et al. (2020).

Field	F435W	F606W	F814W	F105W	F125W	F140W	F160W	*Ks*	IRAC1	IRAC2
A2744	28.8	29.4	29.4	28.6	28.6	29.1	28.3	26.8	25.9	25.6
MACS0416	30.1	29.1	29.2	29.2	28.8	28.8	29.1	26.8	25.9	26.0
MACS0717	29.5	28.6	29.3	28.9	28.6	28.5	28.8	25.9[a]	25.6	25.7
MACS1149	28.6	28.6	28.6	28.9	29.3	29.2	30.1	26.0[a]	25.8	25.6
S1063	30.1	29.1	29.3	29.0	28.7	28.5	28.8	26.9	25.6	25.6
A370	30.1	29.1	29.3	29.0	28.7	28.5	28.4	26.7	25.7	25.6

[a] The *Ks* band mosaics of MACS0717 and MACS1149 are shallower due to shorter exposure times for the *Keck*/MOSFIRE observations (Brammer et al., 2016).

tainties in section 3.5 and summarize our results in section 3.6. Note that this chapter has been published in Furtak et al. (2021).

3.1 Data

Observations obtained as part of the the HFF program are deep HST optical and NIR data of all six HFF clusters and their parallel fields. The clusters were observed from 2013 to 2016 in HST cycles 21 to 23 in a total of 140 orbits for each field and its parallel field. Optical data were taken with ACS in three broad-band filters F435W, F606W and F814W and NIR data were taken with WFC3 in the F105W, F125W, F140W and F160W bands. The data were reduced and drizzled into mosaics by the HFF data reduction team at the Space Telescope Science Institute[1] (STScI). We refer the reader to Lotz et al. (2017) for a detailed description of the HST data products and the data reduction pipeline. For this analysis we use the ACS mosaics generated using the 'self-calibrating' method and the WFC3/IR mosaics that were corrected for time-variable sky background, available in the `MAST` archive (cf. section 2.3).

In addition to HST observations, ∼1000 hours of Director's Discretionary time on *Spitzer* were dedicated to observing the HFF clusters with the *Infrared Array Camera* (IRAC; Fazio et al., 2004). These observations had total integration times of ∼50 hours each in *Spitzer*/IRAC channel 1 (3.6 µm) and channel 2 (4.5 µm) and resulted in depths of ∼26 mag – deep enough to detect (some) high-redshift galaxies. *Spitzer*/IRAC observations at >3 µm are crucial to the study of galaxies at $z \gtrsim 6$ because IRAC channels 1 and 2 provide photometry at rest-frame optical wavelengths red-ward of the Balmer-/4000 Å break (cf. section 2.4.2). We therefore also use *Spitzer*/IRAC channel 1 (3.6 µm) and channel 2 (4.5 µm) mosaics from the *Spitzer Frontier Fields* program (Lotz et al., 2017) in our analysis (hereafter referring to the two IRAC channels as IRAC1 and IRAC2).

---

[1] `http://www.stsci.edu/`

The HFF clusters were also observed in the *Ks*-band centered around 2.2 µmto sufficient depth to provide an additional photometric band that fills the gap between the reddest HST band and the two IRAC channels used in our study. *Ks*-band data were obtained for the southern clusters with the *High Acuity Wide field K-band Imager* (HAWK-I) on the ESO/VLT and in somewhat shorter integration times with MOSFIRE on the *Keck* telescope of the two northern clusters (cf. Fig. 2.10; Brammer et al., 2016). We use *Ks*-mosaics drizzled to the HST $0.06''$pixel-scale in this study (Shipley et al., 2018).

All 10 broad-band filters used in our analysis and their 3σ limiting magnitudes can be found in Tab. 3.1. We use limiting magnitudes computed in Atek et al. (2018) for the HST bands and in Steinhardt et al. (2020) for the *Ks* and IRAC bands.

3.1.1 HST photometry and Dropout selection

We use the $z \sim 6-7$ sample detected in the six HFF clusters and the HST photometry presented in Atek et al. (2018). This section summarizes the detection and measurement methods and we refer the reader to Atek et al. (2015a, 2018) for a detailed description of the procedure.

All HST frames were convolved to the same *point spread function* (PSF) of the F160W frame using PSF models computed with the `Tinytim` tool (Krist et al., 2011). Sources were extracted using the `SExtractor` software (Bertin & Arnouts, 1996) in dual mode on a weighted and *intra-cluster-light* (ICL) corrected stack of the four WFC3/IR bands as detection image and the original frames in each band as measurement images for the photometry. The ICL-correction was performed on the detection stack with a $2'' \times 2''$ median filter and the `SExtractor` parameters were optimized for detecting the faintest sources. The $z \sim 6-7$ sample is color-color selected using isophotal magnitudes (`MAG_ISO`) estimated by `SExtractor`. The selected $z \sim 6-7$ candidates must satisfy the Lyman break criteria (cf. section 2.1; e.g. Steidel et al., 1996) which are described in detail in Atek et al. (2015a):

$$\begin{aligned}
&(I_{814} - Y_{105}) > 1.0 \\
&(I_{814} - Y_{105}) > 0.6 + 2.0(Y_{105} - J_{125}) \\
&(Y_{105} - J_{125}) < 0.8
\end{aligned} \tag{3.1}$$

All sources must also be detected above the 5σ level in at least two WFC3/IR bands and at 6.5σ in the NIR detection stack and satisfy a *non*-detection criterion in the blue F435W and F606W bands and the stack of the two. A visual inspection of each source eliminates any remaining spurious detections and sources that have sizes that are below that expected for a point source (i.e., smaller than that of the PSF of the image stacks given the signal-to-noise of the source). The final $z \sim 6-7$ galaxy sample that we use contains 303 sources. Photometric redshifts were computed with `Hyperz` (Bolzonella et al., 2011) by Atek et al. (2018).

Table 3.2: Aperture diameters and aperture correction factors used for the *Ks* and the two IRAC bands.

Band	pixel-scale	D_{ap}	D_{in}	D_{out}	c
Ks (HAWK-I)[a]	0.06″/pix	0.5″	1.0″	1.5″	1.98
Ks (MOSFIRE)[b]	0.06″/pix	0.5″	1.0″	1.5″	2.77
IRAC1	0.6″/pix	1.7″	2.0″	3.7″	3.35
IRAC2	0.6″/pix	1.3″	2.0″	3.3″	4.81

[a] For A2744, MACS0416, S1063 and A370
[b] For MACS0717 and MACS1149

3.1.2 *Ks* and *Spitzer*/IRAC photometry

The *Ks* and *Spitzer*/IRAC data have a much lower spatial resolution than the HST images in which our high-redshift objects are detected. Obtaining accurate infrared photometry of high-redshift objects therefore requires great care, especially in crowded fields like the HFF clusters' centers where our very faint sources are likely to be blended with brighter foreground galaxies.

In order to estimate the stellar masses, we need to consider how aperture photometry is related to the total flux. We compute aperture correction factors using measured PSFs from the `HFF-DeepSpace` catalogs (Shipley et al., 2018) for the *Ks* band and from the *Spitzer*/IRAC handbook[2] (warm mission) for the IRAC bands. Our aperture correction factors can be found in Tab. 3.2. We use the `photutils v0.7.2` package (Bradley et al., 2019) to measure photometry in circular apertures whose diameters are optimized to neither overestimate the flux of small sources nor underestimate the flux of large sources. The local background for every source is measured as the mean flux in a circular annulus and then subtracted from the source flux. The diameters of the apertures and their annuli are also shown in Tab. 3.2 for each band.

Since our sample of $z \sim 6-7$ galaxies is very faint and their stellar masses are primarily constrained by their (rest-frame optical) IRAC photometry (cf. section 2.4), we must carefully assess the quality of said photometry. We therefore visually inspected each source in the HST F125W band, the *Ks* band, and the two IRAC 3.6 µm and 4.5 µm bands (referred to as IR bands hereafter) specifically to determine how blended it is with the light profiles of any foreground galaxies. We then assign flags to the IR photometry of each source as follows:

- *Golden* source: Completely isolated source in a blank area of the field without any significant contamination from the light profile of foreground galaxies.
- *Silver* source: Trusted photometry, i.e., there is no other source within this source's aperture or background annulus. There are however other galaxies or ICL in close proximity which might affect its photometry.

---

[2] https://irsa.ipac.caltech.edu/data/SPITZER/docs/irac/calibrationfiles/psfprf/

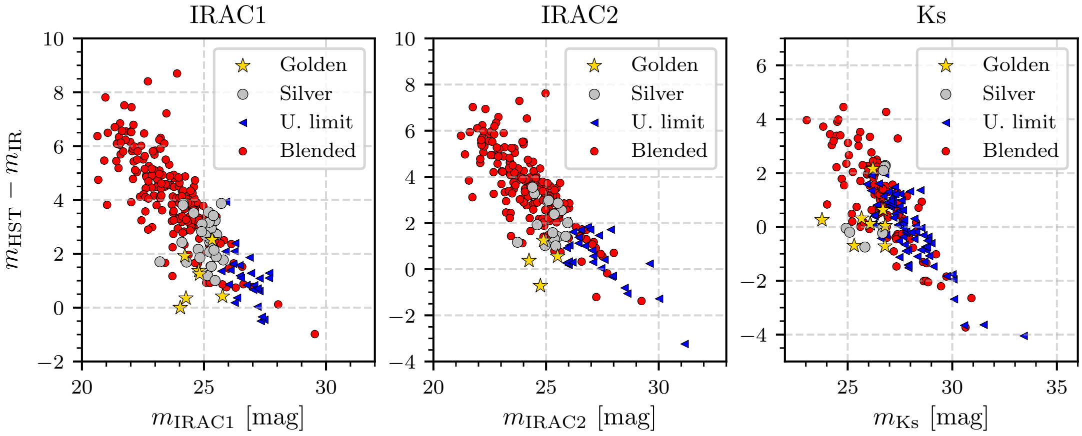

Figure 3.1: Observed magnitude differences with the reddest HST filter (F160W) as a function of IR magnitude in each IR band. Sources $\gtrsim 4$ magnitudes brighter than F160W in IRAC1 and IRAC2 and $\gtrsim 2$ magnitudes brighter in *Ks* are all contaminated by bright foreground objects (red dots). Sources that are not contaminated but lie beyond the 3σ detection limits (listed in Tab. 3.1) are shown as blue triangles. Note that in the *Ks* band (far right panel) the main issue is not blending with foreground sources but rather the fact that most sources are undetected above 3σ.

- *Blended* source: Contaminated photometry, i.e., there is obvious light from another galaxy or star in the source's aperture or background annulus.

We make the distinction between golden and silver sources in order to have a sample of galaxies that can be trusted to have absolutely clean IRAC photometry since determining the impact of having IRAC photometry for some sources and not for others is a major focus of this study. Note however that the majority of these isolated sources are either too faint to be detected in the IRAC bands or subject to very high gravitational magnification factors and therefore large lensing uncertainties, as we will address subsequently in sections 3.2.2 and 3.2.3. We do not use the IR photometry of blended sources in our analysis from here on.
We show the difference between observed IR magnitudes and the reddest HST band (F160W) as a function of IR magnitude for our $z \sim 6-7$ sample in Fig. 3.1. As can be seen, we have a significant number of sources with unrealistically high infrared fluxes, i.e. $m_{F160W} - m_{IRAC} \geq 4$ and $m_{F160W} - m_{Ks} \geq 2$ which are all blended with other objects (Fig. 3.1). Many sources in our sample are fainter than the 3σ-limiting magnitudes in the IR bands (blue triangles in Fig. 3.1). We expected this result since many of our sources are at the very limit of HST detectability. These sources only have an upper limit on their IR fluxes. Out of our sample of 303 high-redshift sources in the six HFF fields only 35 (12 %) have useful, i.e. golden or silver, IRAC1 photometry, 20 (7 %) have useful IRAC2 photometry and only 17 (6 %) have useful *Ks* photometry. In total 39 (13 %) of our sources have useful photometry in either IRAC1 or IRAC2 and we discard

the IR photometry of blended sources entirely. In the following sections, we discuss how SED-fitting using only HST data affects the stellar mass results.

3.2 SED-fitting

To obtain stellar masses and other galaxy parameters, we fitted SED templates (cf. sectionsec:SED) to the photometry of our $z \sim 6-7$ sample using the `BayEsian Analysis of GaLaxy sEds (BEAGLE)` tool (Chevallard & Charlot, 2016). `BEAGLE` is optimized to accurately estimate both redshift and physical galaxy parameters using a Bayesian Monte-Carlo Markov-Chain (MCMC) analysis. By performing the Bayesian MCMC analysis on each SED fit, `BEAGLE` rigorously probes a large parameter space and efficiently quantifies parameter uncertainties. Its modular design allows for maximum flexibility in changing the assumptions and models that underlie the fits such as the stellar population models, nebular emission templates, dust attenuation laws, physical parameters of the models, etc. We take advantage of this feature of `BEAGLE` to probe the impact of various assumptions commonly made in this type of photometric study on the resulting stellar masses as will be explained in section 3.2.1.

SED-fitting of high-redshift galaxies has been found to strongly depend on nebular emission as well as stellar population models. Several studies have shown that SEDs including nebular emission fit such objects significantly better and yield lower stellar masses and ages (e.g Schaerer & de Barros, 2009, 2010; Ono et al., 2010; Atek et al., 2011; McLure et al., 2011; Duncan et al., 2014). We therefore adopt stellar and nebular SED templates computed by Gutkin et al. (2016) which combine the latest version of the Bruzual & Charlot (2003) stellar population models with the photoionization code `CLOUDY` (Ferland et al., 2013). `BEAGLE` then includes the latest analytical IGM absorption models by Inoue et al. (2014) and applies a dust attenuation law to the galaxy templates in order to account for dust attenuation within the fitted galaxy.

We use all ten bands of broad-band photometry in the SED-fitting analysis if available. The total magnitudes were derived using `SExtractor` and are estimated using `MAG_AUTO` for the HST images. The Ks and IRAC total magnitudes were measured as described in section 3.1.2 and are only used for golden and silver sources. We estimate upper limits for all sources that are not detected at the 3σ level in any of the images. We furthermore fix the galaxies' redshift to the values obtained by Atek et al. (2018) with `Hyperz` throughout our analysis (cf. section 3.1.1).

3.2.1 SED-fitting assumptions

The best-fit SED depends on numerous parameters, namely star-formation history (SFH), metallicity, dust attenuation, stellar age and star-formation timescales. Moreover, several parameters, such as e.g., stellar mass and stellar age, are degenerate. In order to obtain accurate stellar masses we need to make a number of assumptions regarding these parameters. However, the physical properties and star formation histories of high-redshift galaxies remain largely unknown (cf. section 1.3.2). We therefore use `BEAGLE`'s modular

Table 3.3: Fit parameters and priors of our SED-fitting analysis with `BEAGLE`. The *Reference model* represents the most basic configuration used here. Parameters that depart significantly from the reference model configuration are also listed.

Parameter	Unit	Prior	Value/range
		Reference model	
$\log M_\star$	$\log \mathrm{M}_\odot$	flat	[5.0, 11.0]
$\log t_\mathrm{age}$	$\log \mathrm{yr}$	flat	[7.37, 8.37]
$\hat{\tau}_V$	-	flat	[0.0, 0.2]
$\log \hat{U}$	-	flat	[-3.0, -1.0]
Z	$\mathrm{Z}_\odot$	fixed	0.1
SFH	-	fixed	$\psi(t) = \psi$
Dust attenuation law	-	fixed	Calzetti
		Metallicity tests	
Z	$\mathrm{Z}_\odot$	fixed	0.01, 0.1, 0.5
		SFH tests	
SFH	-	fixed	$\psi(t) \propto t \exp(-t/\tau)$ $\psi(t) \propto \exp(-t/\tau)$ $\psi(t) \propto \exp(t/\tau)$
$\log \tau$	$\log \mathrm{yr}$	flat	[7.0, 8.5]
		Dust tests	
$\hat{\tau}_V$	-	flat	[0.0, 3.0]
Dust attenuation law	-	fixed	Calzetti, SMC

Note. – $M_\star$: Stellar mass – t_age: Maximum stellar age – $\hat{\tau}_V$: V-band attenuation optical depth – $\hat{U}$: Effective galaxy-wide ionization parameter – Z: Stellar metallicity – τ: Star formation e-folding time

build to test the impact of these assumptions on the main parameter of interest: stellar mass and the resulting stellar mass function at $z \sim 6-7$.

This is done by first defining a *reference model*, a configuration of `BEAGLE` fit-parameters from which other SED-fit runs depart to explore the impact of different parameter assumptions on stellar mass. The reference model is defined as the most basic "minimal" configuration possible to fit stellar mass with four free parameters: Stellar mass $M_\star$, maximum stellar age t_age, effective V-band dust optical depth $\hat{\tau}_V$, and the effective galaxy-wide ionization parameter $\hat{U}$. All other parameters are fixed: We assume a constant SFH, a metallicity of $0.1\,\mathrm{Z}_\odot$, and a Calzetti dust attenuation law (Calzetti et al., 1994, 2000). All parameters and their priors are summarized in Tab. 3.3.

The allowed ranges of t_age and $\hat{\tau}_V$ are carefully chosen to limit degeneracy with stellar mass. The lower and upper bounds on the range of stellar age allowed in the SED modeling represent, respectively, a rough estimate of a galaxies' dynamical timescale given its typical size and stellar mass within the sample of galaxies, t_dyn and $10 \times t_\mathrm{dyn}$. The dynamical time t_dyn is estimated as,

$$t_{\rm dyn} \sim \frac{r}{v} \sim \sqrt{\frac{2r^3}{GM}} \tag{3.2}$$

where r is a characteristic size of the galaxy and v the virial velocity (Verma et al., 2007). We use $r = 0.5\,\mathrm{kpc}$, a typical half-light radius of a galaxy at $z \sim 6-7$ (Kawamata et al., 2015), and $M \sim 10^8\,\mathrm{M}_\odot$ as a typical galaxy mass, resulting in a dynamical time $t_{\rm dyn} \sim 20\,\mathrm{Myr}$. We set the lower boundary of $t_{\rm age}$ to 20 Myr in order to avoid solutions around $t_{\rm age} \sim 10\,\mathrm{Myr}$ with extremely high nebular equivalent widths (EWs) $\sim 7000\,\text{Å}$ for [O III] 5007 Å, which remain unlikely given evidence from observations of low-redshift analogs of high-redshift galaxies (Atek et al., 2011, 2014; Smit et al., 2014; Reddy et al., 2018b) and stellar population models (but see Endsley et al., 2021). We refer the reader to appendix A.1 for further discussion of this issue. Dust attenuation is allowed to vary between $\hat{\tau}_V = 0$, i.e., no dust attenuation, and $\hat{\tau}_V = 0.2$ which corresponds to $A_V \approx 0.2$ and $A_{UV} \approx 0.8$. We chose this upper boundary because high-redshift galaxies are unlikely to have high dust attenuations (e.g. Bouwens et al., 2016).

To gauge the influence of specific assumptions in our reference set of priors and values (when they are fixed), we ran different SED fitting configurations with `BEAGLE` where we change only one or two parameters or priors at a time to study their impact on the resulting stellar mass function. The various configurations we tried are listed in Tab. 3.3. We ran tests to determine the impact of increasing the latitude in the range of the parameters allowed and through changing the functional dependence of parameters of the metallicity, SFH and dust attenuation. We summarize the changes we made in the assumptions in SED fitting as:

- *Metallicity*: To determine the impact of different assumptions for the metallicity, we ran models with the same configuration as the reference configuration except fixing the metallicity, Z, to three different values: $0.01\,\mathrm{Z}_\odot$, $0.1\,\mathrm{Z}_\odot$ and $0.5\,\mathrm{Z}_\odot$, the last of which corresponds to the metallicity measured from absorption spectra of a small sample of bright (i.e. massive) galaxies at $z \sim 6$ (Harikane et al., 2020).

- *SFH*: We determined the impact of the functional changes in the SFH by running models with three additional functional forms of the SFH: a delayed SFH $\psi(t) \propto t \exp(-t/\tau)$ and exponentially rising $\psi(t) \propto \exp(t/\tau)$ or declining $\psi(t) \propto \exp(-t/\tau)$. This approach is similar to that of Grazian et al. (2015) who tested these three SFHs for galaxies at $3.5 \leq z \leq 4.5$. We note though that they did not consider the impact of nebular emission which we do. These SFHs require an additional free parameter, the star-formation e-folding time, τ. The delayed SFH has a peak of star-formation at $t = \tau$.

- *Dust*: We tested the impact of dust attenuation on the results by allowing a wider range of dust attenuation optical depths in the V-band, $\hat{\tau}_V$, compared to that allowed in the reference model (up to $\hat{\tau}_V = 3$ or $A_V = 3.25$). This is similar to the range allowed in Song et al. (2016a); Bhatawdekar et al. (2019); Kikuchihara et al. (2020). Recent results have also indicated that a steeper dust attenuation law than the Calzetti law potentially fits better the SEDs of high-redshift galaxies (Capak et al., 2015; Reddy et al., 2015, 2018a). We therefore also ran a model where we assume an SMC-like extinction law (Pei, 1992) with a wide range of allowed attenuation optical depths, $\hat{\tau}_V \in [0, 3]$, in fitting the SED.

3.2.2 SL magnification

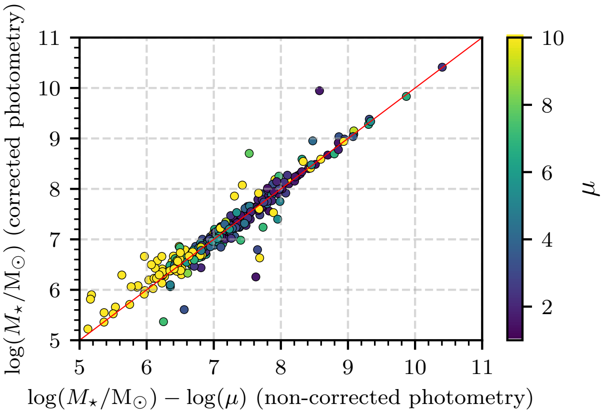

Figure 3.2: A comparison between the stellar masses determined by fitting the SEDs using the observed fluxes with those determined by fitting magnification corrected photometry. The color-coding indicates the median magnification factor, μ, from the six SL models considered in this analysis and its values are shown in the color bar on the right.

In computing rest-frame UV luminosities and stellar masses, we need to determine the gravitational magnification of each galaxy. Several independent teams produced numerous SL models for all six HFF clusters, which are all publicly available in the `MAST` archive.[3] In this study we restrict ourselves to models that are both available for all six clusters and are based on the full and most recent data sets available from the HFF program: CATS (Jauzac et al., 2014, 2015; Limousin et al., 2016; Lagattuta et al., 2017), Diego (Diego et al., 2015), GLAFIC (Kawamata et al., 2016, 2018), Keeton (Ammons et al., 2014; McCully et al., 2014), Sharon & Johnson (Johnson et al., 2014) and Williams (Grillo et al., 2015).

We compute gravitational magnification factors at each galaxy's position and photometric redshift from the convergence κ and shear γ (cf. section 2.2.2) maps provided by the SL modelling teams using equation (2.17). The resulting magnification factors can differ significantly between the models due to different SL modelling techniques and assumptions (e.g. Meneghetti et al., 2017; Acebron et al., 2017, 2018). These differences can significantly affect any deductions made about the luminosity and mass functions of high-redshift galaxies (Bouwens et al., 2017b; Atek et al., 2018). In order to take these differences into account and to assess the systematic lensing uncertainties, we compute the median magnification factor, μ, and the standard deviation between all the models, $\Delta\mu$, and assume the standard deviation is the uncertainty in the lensing strength for each galaxy. We will further discuss the impact of using this estimate as the uncertainties on the lensing strength in section 3.5.2.

The best-fit stellar masses are directly corrected for median magnification as determined

---

[3] see e.g., `https://archive.stsci.edu/pub/hlsp/frontier/abell2744/models/`

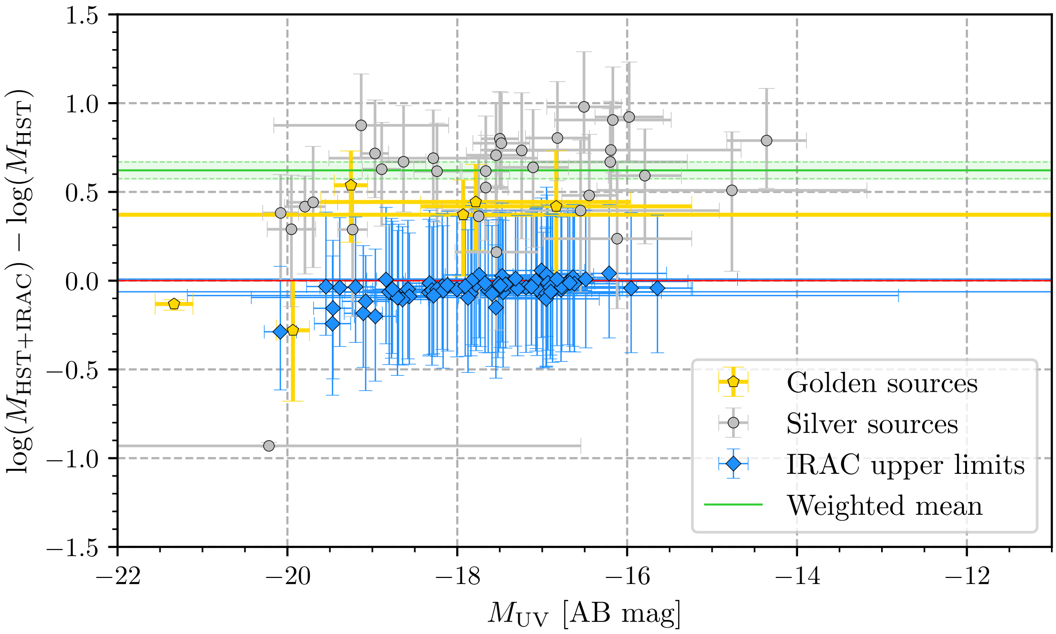

Figure 3.3: Difference in stellar mass derived from fitting HST+IRAC photometry and HST photometry only as a function of UV luminosity, M_{UV} (the absolute magnitude at 1500 Å), using the reference model `BEAGLE`-parameters. Most of the golden and silver sources (cf. text for details) lie above the zero level, indicating that fitting only the HST data significantly underestimates the stellar mass. Sources with upper limits in the flux in both of the IRAC bands (blue squares), lie close to zero, which means that upper limits on IRAC flux are not sensitive enough to provide any additional constrains on the stellar mass. The average correction offset, $\langle\delta\rangle = 0.62\pm0.05$ dex, is shown as the green line and the shaded region indicates its 1σ uncertainties.

from the different lensing models. The validity of this approach is shown in Fig. 3.2: Stellar masses corrected *a posteriori* for the median magnification widely agree with masses fit to magnification-corrected photometry. It also confirms that the galaxies with the lowest masses correspond to those which are most strongly magnified.

3.2.3 Correcting for missing IRAC photometry

As discussed in section 3.1.2, the vast majority of our sources, 87%, do not have reliable *Spitzer*/IRAC photometry in at least one band either because they are severely blended (i.e., there is no information), have unreliable photometry due to possible contamination, or are undetected by the 3σ limits. However, rest-frame optical photometry is crucial for making more robust estimates of stellar masses at $z \sim 6-7$ (cf. section 2.4.2). We only fit the 7 bands of HST for most of our sources and therefore we only have rest-frame UV photometry, which underestimates the stellar mass of these galaxies. We now quantify how much we are underestimating the stellar masses of galaxies when only using rest-frame UV photometry.

In order to estimate the magnitude and difference in using only the HST photometry versus using HST plus IRAC photometry in the final stellar mass, we fitted the SEDs of sources with and without including the IRAC photometry. For this comparison, we used the same set of parameter values when fitting the SEDs and included all golden and silver sources, and robust upper limits in the IRAC photometry. We find that fitting only the HST data underestimates the stellar mass by $\gtrsim 0.5$ dex (Fig. 3.3). Note that sources that are not detected at the 3σ-level in IRAC1 *and* IRAC2, i.e. the blue squares in Fig. 3.3, all lie close to zero in the ordinate. This implies that there is no significant difference in the stellar mass estimate when fitting upper limits in the IRAC bands compared to only fitting the HST photometry. We therefore conclude that the upper limits in the IRAC photometry are not sensitive enough to provide robust constraints on the stellar mass (cf. also Fig. A.5 in appendix A.2).

There are three outliers below zero among the golden and silver sources in Fig. 3.3 with bright rest-frame UV luminosities $M_{\mathrm{UV}} \lesssim -20$. An inspection of their best-fit SEDs reveals a poor fit due to the relatively low upper boundary on dust attenuation used in the reference model (cf. Tab. 3.3). These galaxies require a larger range on $\hat{\tau}_V$ to accurately fit their SED. Since these three galaxies lie at the most luminous end of the M_{UV} range that we probe, we do not consider them representative of our entire sample however.

We compute the mean $\delta = \log(M_{\mathrm{HST+IRAC}}/\mathrm{M}_{\odot}) - \log(M_{\mathrm{HST}}/\mathrm{M}_{\odot})$ from all sources with trusted IRAC photometry (i.e., golden and silver sources), excluding the outliers. We find a correction factor of $\langle\delta\rangle \simeq 0.62 \pm 0.05$ dex (cf. Fig. 3.3). Since this offset appears to be constant over the range of rest-frame UV luminosities that we probe in this work (cf. Fig. A.4 in appendix A.2), we apply this correction to the stellar mass of every galaxy which is either contaminated or only has upper limits in its IRAC photometry. Note that as the galaxies for which we compute the correction $\langle\delta\rangle$ are well detected in at least one of the IRAC bands, they represent a rest-frame optically bright population with relatively high stellar masses given their UV luminosities. We would therefore expect our correction factor to slightly overestimate the stellar mass of the lower-mass galaxies in our sample which would not be IRAC detected (cf. appendix A.2)

3.3 Mass-luminosity scaling relation

In order to determine the scaling relation between the absolute rest-frame UV magnitude M_{UV} and stellar mass $M_{\star}$, we estimate the mass-to-light ratio of our galaxy sample. The rest-frame UV magnitude is defined as the rest-frame luminosity at 1500 Å computed using equation (1.22). At the redshifts studied here, 1500 Å is redshifted into the HST Y_{105} and J_{125} bands. In determining this mass-to-light ratio for each source, we included the median magnification from the SL models and the dispersion between models in the final total uncertainties. In Fig. 3.4, we present the stellar masses obtained for the reference `BEAGLE` configuration (cf. section 3.2.1 and Tab. 3.3) as a function of M_{UV}. As expected, we observe a strong correlation between stellar mass and UV luminosity. At the faint end ($M_{\mathrm{UV}} \gtrsim -17$), the large uncertainties of the gravitational magnification

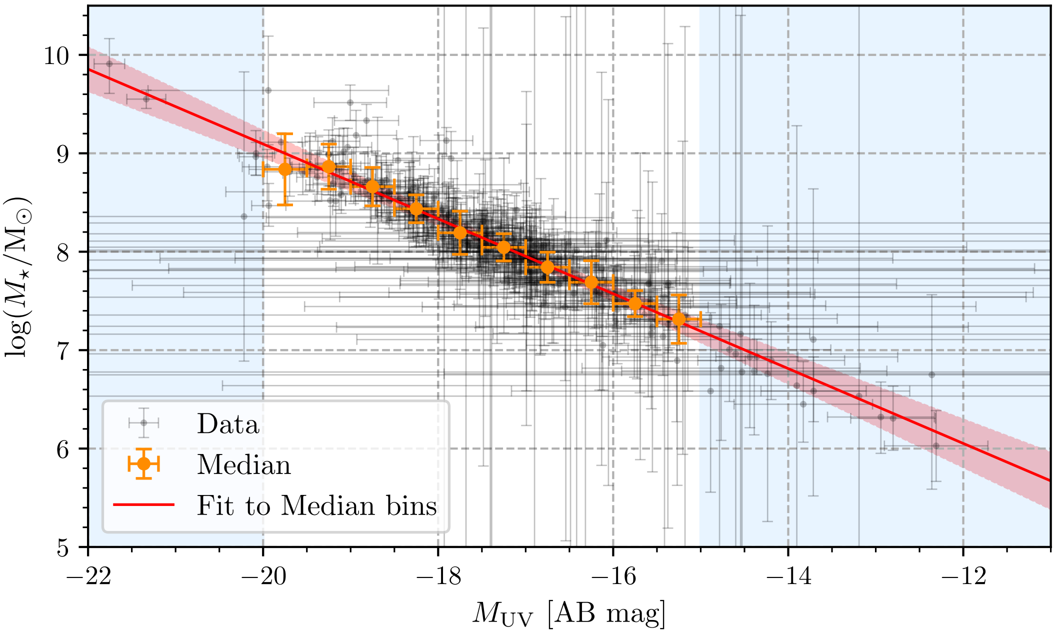

Figure 3.4: Mass-luminosity relation for the reference `BEAGLE` configuration (Tab. 3.3). Black dots represent individual galaxies and their uncertainties in $M_\star$ and M_{UV}. The uncertainties are dominated by the gravitational magnification at $M_{\mathrm{UV}} \gtrsim -17$. Orange dots represent the median-mass bins of 0.5 mag width used for the fit. The best-fit mass-luminosity relation is shown as a red line and its 1σ-range as the red shaded area. The blue shaded areas represent the regions where the luminosity bins contain too few objects to robustly constrain the shape of the $M_\star - M_{\mathrm{UV}}$-relation. We exclude all bins in these two regions from the fit.

estimates (cf. section 3.2.2) begin to dominate the uncertainties in both $M_\star$ and M_{UV}. The data are binned into M_{UV} bins of 0.5 mag width and the median $M_\star$ is taken in each luminosity bin (orange dots in Fig. 3.4). The error bars account for the scatter in stellar mass in each bin. We then fit the relation,

$$\log\left(\frac{M_\star}{\mathrm{M}_\odot}\right) - 8 = a(M_{\mathrm{UV}} + 17) + b \tag{3.3}$$

to the median bins. We exclude luminosity bins fainter than $M_{\mathrm{UV}} > -15$ and brighter than $M_{\mathrm{UV}} < -20$ (blue shaded area in Fig. 3.4) from the fit because these contain too few objects to robustly constrain the relation. We obtain the best linear fit to the median bins via an MCMC analysis with 10^6 steps, using the public software package `emcee` (Foreman-Mackey et al., 2013). The best-fit mass-luminosity relation and its 1σ-range for the reference model are shown as a red line and red shaded area in Fig. 3.4. We proceed in the same manner for all the SED-fitting configurations detailed in section 3.2.1. The best-fit parameters and their 1σ uncertainties are summarized in Tab. 3.4.

We compare the resulting mass-luminosity relations in Fig. 3.5. The upper left panel shows the resulting mass-luminosity relations for the three different metallicities used

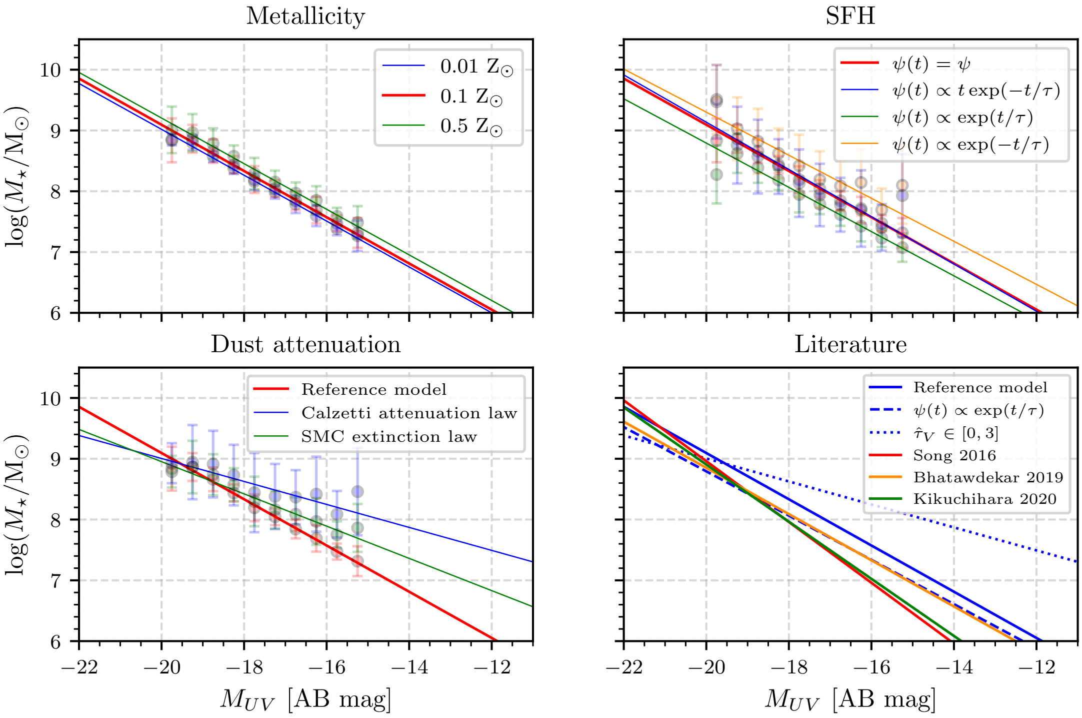

Figure 3.5: Best-fit $M_\star - M_{\mathrm{UV}}$-relations for the different `BEAGLE` configurations as discussed in section 3.2.1. *(Upper left panel)*: Best-fit $M_\star - M_{\mathrm{UV}}$-relations for three different metallicities; *(Upper right panel)*: for the four different SFHs; and *(Lower left panel)*: for three different attenuation laws (all the various assumptions and differences are indicated in the legend in each panel). The data points indicate the median of the mass bins used for the fit and the solid lines represent the median best-fit relations determined from our MCMC analysis. *(Lower right panel)*: We compare our results for our reference model, an exponentially rising SFH, and a wide range of attenuation values (blue solid, dashed and dotted lines respectively). In addition we show the relations determined in other recent studies of high-redshift galaxies: Song et al. (2016a) (red line), Bhatawdekar et al. (2019) (orange line) and Kikuchihara et al. (2020) (green line). Note that while Song et al. (2016a) and Kikuchihara et al. (2020) find steeper relations than ours and that of Bhatawdekar et al. (2019), all relations yield similar stellar masses at the bright end, indicating that the stellar masses for these galaxies are constrained within a factor of ∼0.5 dex.

Table 3.4: Parameters of fits to the mass-luminosity relation given in equation. 3.3. The best-fit parameter values are medians and their 1σ-uncertainties are drawn from our MCMC analysis.

`BEAGLE` Configuration	Slope	Intercept ($\mathrm{M}_\odot$)	$\log M_\star$ ($M_{\mathrm{UV}} = -19.5$) ($\mathrm{M}_\odot$)
Reference Model	-0.38 ± 0.05	-0.05 ± 0.06	8.90 ± 0.06
$Z = 0.01\,\mathrm{Z}_\odot$	-0.38 ± 0.03	-0.11 ± 0.05	8.83 ± 0.02
$Z = 0.5\,\mathrm{Z}_\odot$	-0.37 ± 0.05	-0.08 ± 0.07	9.01 ± 0.07
$\psi(t) \propto t\exp(-t/\tau)$	-0.39 ± 0.12	-0.03 ± 0.17	8.94 ± 0.13
$\psi(t) \propto \exp(t/\tau)$	-0.36 ± 0.05	-0.30 ± 0.07	8.61 ± 0.07
$\psi(t) \propto \exp(-t/\tau)$	-0.35 ± 0.11	0.24 ± 0.15	9.12 ± 0.12
Calzetti attenuation law	-0.19 ± 0.10	0.44 ± 0.17	8.91 ± 0.08
SMC-like extinction law	-0.27 ± 0.07	0.16 ± 0.10	8.82 ± 0.06

in our analysis. The relations for the three metallicities do not differ significantly, all lying within the uncertainties in the medians of the masses. There is a trend towards systematically larger masses and larger scatter when assuming higher metallicity (due to increasing mass-to-light ratios with increasing metallicity, Bruzual & Charlot, 2003). Fig. 3.5 also shows mass-luminosity relations resulting from SED-fits with different assumptions about the SFH. While the three exponential SFHs yield similar slopes as the constant SFH, only the delayed SFH results in similar masses. The exponentially rising SFH instead yields distinctly lower (~ -0.3 dex) and the exponentially declining SFH distinctly higher (~ 0.2 dex) stellar masses but the exact offset depends on M_{UV}. The lower left panel in Fig. 3.5 shows the impact of changing our assumptions for the dust attenuation in the mass-luminosity relation. We find that allowing for large dust attenuation optical depths in our sample leads to a remarkably shallower mass-luminosity relations compared to using the parameters in the reference model. Applying an SMC-like extinction law however yields masses closer to the reference model. Note that the three relations roughly result in the same masses at the bright end, meaning that dust attenuation mostly impacts the mass estimates of the faint, i.e., low-mass, galaxies.

Finally, in Fig. 3.5, we compare our $M_\star - M_{\mathrm{UV}}$-relations to the most recent results in the literature, namely Song et al. (2016a), Bhatawdekar et al. (2019), and Kikuchihara et al. (2020). Our reference `BEAGLE` configuration has a similar relation to Bhatawdekar et al. (2019) with slightly higher masses. Both Song et al. and Kikuchihara et al. find steeper mass-luminosity relations. Our results depart from the literature for different SFH and dust content. We will further discuss these features in section 3.5. Note that our and the $M - M_{\mathrm{UV}}$-relations in the literature yield similar masses at the bright end, e.g., at $M_{\mathrm{UV}} = -19.5$. This indicates that stellar masses at the bright end are relatively insensitive ($\sim$0.5 dex) to the assumed SED modeling parameters and that the most significant differences ($\sim$1 dex) occur for intrinsically, faint low stellar mass galaxies.

3.4 High-redshift Galaxy Stellar Mass Functions

We now use the $M_\star - M_{\mathrm{UV}}$-relations derived in section 3.3 to convert the observed rest-frame UV luminosity function to GSMFs. This approach is commonly used in the study of high-redshift GSMFs because selection and completeness effects are well-studied for UV luminosity functions (e.g. González et al., 2011; Song et al., 2016a; Kikuchihara et al., 2020). To accomplish this transformation, we take the luminosity function from Atek et al. (2018), which was derived from the same HFF $z \sim 6-7$ sample that we use in this study, and transform the luminosity bins into stellar mass bins using the median $M_\star - M_{\mathrm{UV}}$-relations. The GSMF uncertainties in each of the luminosity/stellar mass bins include contributions from the uncertainties in the survey volume and cosmic variance (cf. Atek et al., 2018, for details). In addition, we account for uncertainties in the determination of stellar mass with `BEAGLE` by making 10^4 random realizations drawn from each galaxy's stellar mass posterior distribution and re-binning in stellar mass at each iteration. Doing this means that galaxies, given the uncertainties, can shift between mass bins from iteration to iteration thus providing a robust estimate of the uncertainties in the number of galaxies in each bin and on the final median stellar mass of any particular bin.

We show the resulting GSMF bins for the reference model in Fig. 3.6. All of our final GSMF determinations and their uncertainties can be found in Tabs. A.1 and A.2 in appendix A.3. We observe a possible turnover of the GSMF for masses below $\log(M_\star/\mathrm{M}_\odot) \lesssim 7$ which corresponds to the turnover in the Atek et al. (2018) UV luminosity functions. However, a steepening or no change at all in the slope of the GSMF is less likely but also consistent within the relatively large uncertainties. A low-mass turnover does not appear in any high-redshift GSMFs in the literature. It is however present in the HFF high-redshift UV luminosity functions (Bouwens et al., 2017b; Atek et al., 2018). We combine our results with GSMF bins derived by Song et al. (2016a), who combined results from CANDELS, GOODS and HUDF fields to increase the area analyzed and were able to constrain the high-mass end of the GSMF (cf. also Kikuchihara et al., 2020, for a similar analysis). Following Bouwens et al. (2017b) and Atek et al. (2018), we shift their $z \sim 6$ GSMFs down by 0.15 dex in order to account for the redshift-evolution of the GSMF from their sample to our $z \sim 6-7$ sample.

To fit the observed GSMF bins we adopt a standard Schechter function (Schechter, 1976). The general form of the Schechter function is,

$$\phi(M_\star) = \ln(10)\phi_0 \left(\frac{M_\star}{M_0}\right)^{\alpha+1} e^{-\frac{M_\star}{M_0}} \tag{3.4}$$

where M_0 corresponds to the characteristic stellar mass where the power-law turns into an exponential, α is the low-mass end slope and ϕ_0 the normalization (cf. right-hand panel of Fig. 1.3). Since the observed GSMF bins depart from the classical Schechter form at $\log(M_\star/\mathrm{M}_\odot) < 7.2$ (grey dashed line in Fig. 3.6), we also fit the GSMFs with a modified Schechter function (Bouwens et al., 2017b; Atek et al., 2018) which accounts for a potential turnover at low masses. In the modified Schechter function we multiply

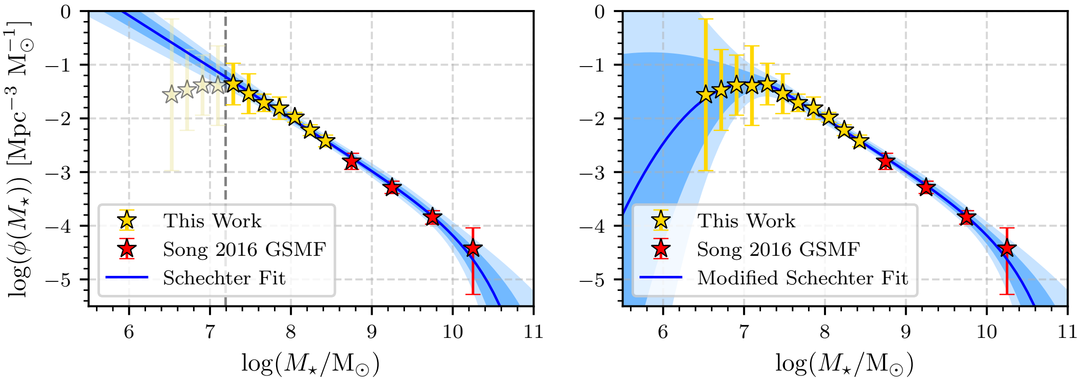

Figure 3.6: Final GSMFs at $z \sim 6-7$ as determined using the parameters from our reference model (Tab. 3.3). Golden colored stars represent the results derived for our $z \sim 6-7$ sample in the HFF and red stars represent the determination of the high-mass end of the GSMF by Song et al. (2016a) using wide-area blank fields. We shifted the Song et al. (2016a) results down by 0.15 dex in order to account for the redshift-evolution between their $z \sim 6$ sample and our $z \sim 6-7$ sample and include them into our fitting procedure. In the *left-hand* panel we fit the GSMF with a Schechter function (equation 3.4). Since the points on the very low-mass end clearly depart from the regular Schechter form, we restrict the fit to mass bins $\log(M_\star/\mathrm{M}_\odot) > 7.2$ (delimited by the grey dotted line) which corresponds to $M_{\mathrm{UV}} = -15$. The mass bins excluded from the Schechter fit are shown as pale golden stars. In the *right-hand* panel, we show the fit to all of the GSMF bins with a modified Schechter function (equation 3.6) which additionally includes a component for a turnover below M_1. The blue shaded areas in both panels indicate the 1σ and 2σ uncertainty ranges as determined from our MCMC analysis.

the expression in equation (3.4) with a turnover term,

$$10^{-\beta \log\left(\frac{M_\star}{M_1}\right)^2} \tag{3.5}$$

for stellar masses lower than M_1. This results in a modified Schechter function as,

$$\phi(M_\star) = \begin{cases} \ln(10)\phi_0 \left(\frac{M_\star}{M_0}\right)^{\alpha+1} e^{-\frac{M_\star}{M_0}} & , M_\star > M_1 \\ \ln(10)\phi_0 \left(\frac{M_\star}{M_0}\right)^{\alpha+1} e^{-\frac{M_\star}{M_0}} 10^{-\beta \log\left(\frac{M_\star}{M_1}\right)^2} & , M_\star \leq M_1 \end{cases} \tag{3.6}$$

where the curvature parameter β allows for a downward turnover of the GSMF if $\beta > 0$ and for an upward turnover if $\beta < 0$ (cf. right-hand panel of Fig. 1.3). We define the turnover mass M_T as the stellar mass corresponding to the maximum in the GSMF in the case of $\beta > 0$, i.e., where $(\mathrm{d}\phi/\mathrm{d}M_\star)_{M_\star = M_T} = 0$. We derive the best-fit Schechter and modified Schechter parameters as the median of the joint posterior distribution of 20 MCMC chains with 5×10^5 steps (after removing the first ~20000 steps as burn-in phase). The likelihood used in this inference can be expressed as,

$$\mathcal{L} = \prod_i \frac{1}{\phi_i} \frac{1}{\sqrt{2\pi}\sigma_i} e^{\frac{(\ln\phi_i - \ln\phi(M_{\star,i}))^2}{2\sigma_i^2}} \tag{3.7}$$

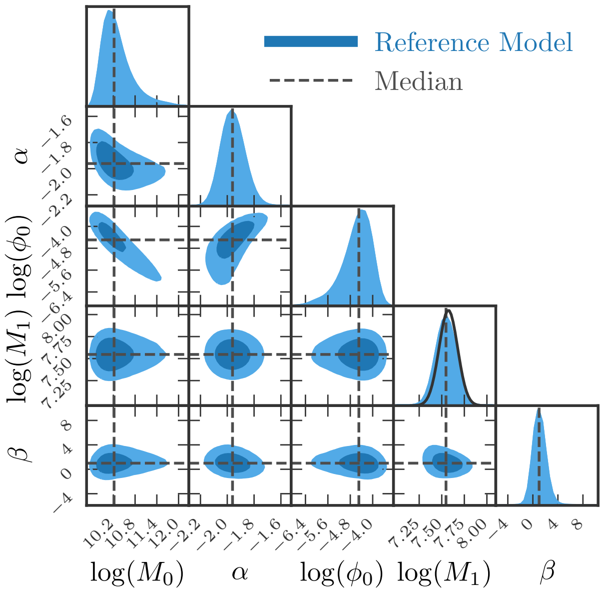

Figure 3.7: Posterior distributions (blue shaded areas) and median values (dashed lines) of the five modified Schechter fit parameters for the reference model (cf. Tab. 3.3). These diagrams illustrate that the fit parameters are in general, not independent, in particular the three 'classical' Schechter parameters M_0, α and ϕ_0. The solid line in the M_1 panel shows the Gaussian prior applied to M_1.

where ϕ_i and σ_i are the observed GSMF bins and their uncertainty respectively and $\phi(M_{\star,i})$ is the GSMF model function evaluated at each stellar mass bin. Note that we only consider $\log(M_\star/\mathrm{M}_\odot) > 7.2$ bins when fitting the Schechter function (3.4) since the mass bins below that (pale golden stars in the left-hand panel of Fig. 3.6) clearly depart from the 'classical' Schechter form and therefore cannot be fit with equation (3.4). For the reference model, fitting all mass bins with equation (3.4) however only marginally impacts the resulting parameters (cf. Fig. A.6 in appendix A.3). The modified Schechter function, equation (3.6), on the other hand is fit to all mass bins. We assume flat priors for the fit parameters, M_0, α, ϕ_0 and β. Atek et al. (2018) found that the best fit to the UV luminosity functions introduces the turnover term for magnitude bins brighter than $M_{\mathrm{UV}} = -16$. To fit the modified Schechter GSMFs, we therefore use a Gaussian prior on M_1 with the stellar mass that corresponds to $M_{\mathrm{UV}} = -16$ and the uncertainties in the $M_\star - M_{\mathrm{UV}}$-relation respectively as the peak and the standard deviation of the distribution. The parameter spaces are limited to $8 < \log(M_0/\mathrm{M}_\odot) < 12$, $-3 < \alpha < -1$, $-10 < \log(\phi_0/\mathrm{Mpc}^{-3}) < 0$, $6 < \log(M_1/\mathrm{M}_\odot) < 9$ and $-20 < \beta < 20$.

The best-fit parameters and their 1σ uncertainties are listed in Tab. 3.5 for all the different SED-fitting runs and we show the posterior distributions of the four modified Schechter parameters for the reference model in Fig. 3.7. Note that the fit-parameters are not independent in general. In particular, there is a degeneracy between the high-mass exponential cutoff M_0 and the low-mass end slope, α. It therefore appears that knowledge of both the high- and the low-mass ends are required to constrain the overall shape of the GSMF. We show best-fit Schechter and modified Schechter functions for the reference model in Fig. 3.6.

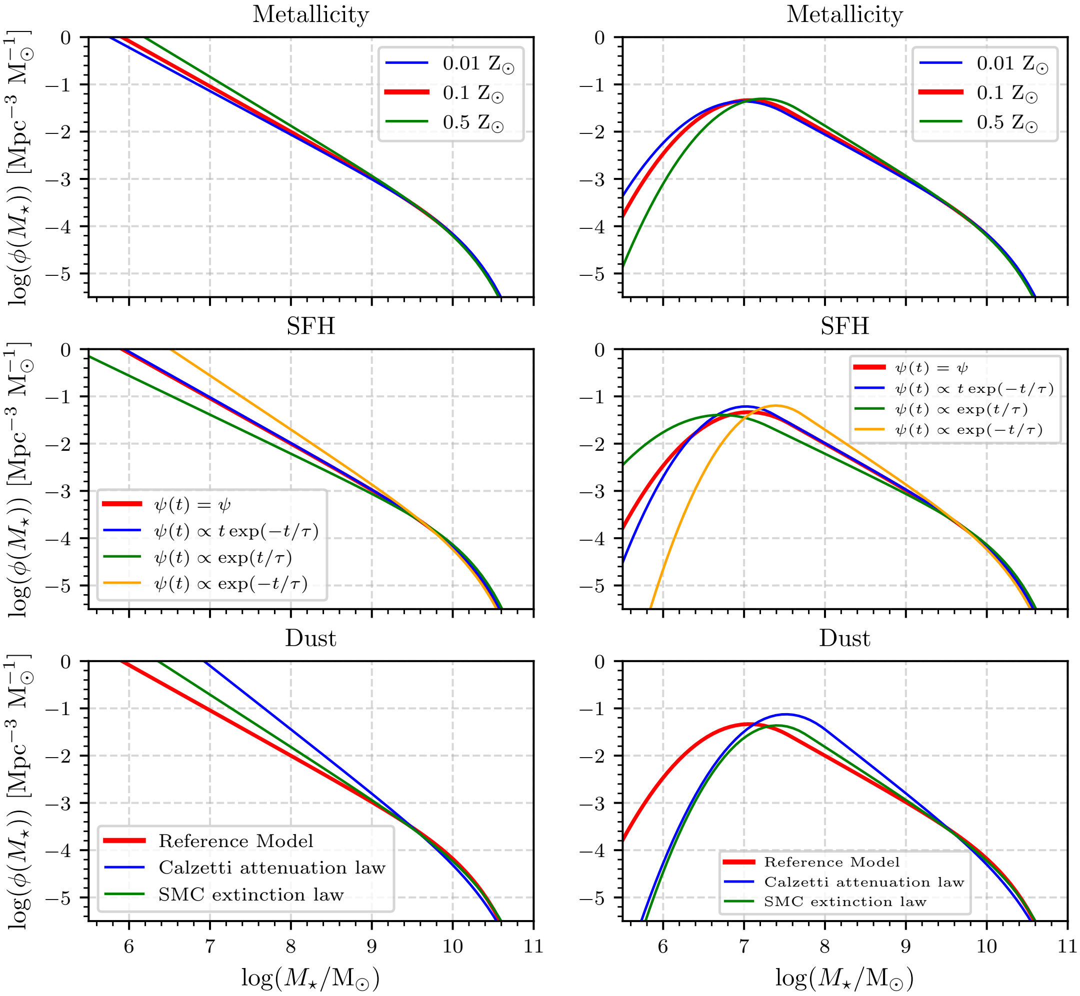

Figure 3.8: Best-fit GSMFs for each `BEAGLE` configuration explored in this work (see section 3.2.1). The data are fitted with a Schechter function (equation 3.4) in the *left-hand* panels and with a modified Schechter function (equation 3.6) in the *right-hand* panels. The GSMF for the reference model is plotted in red in each panel. The label at the top of each panel indicates which parameter is investigated and the legends indicate the parameter values.

Table 3.5: Best-fit Schechter (3.4) and modified Schechter (3.6) function parameters. The best-fit parameter values are medians and their 1σ-uncertainties are estimated from our MCMC analysis.

`BEAGLE` Configuration	$\log M_0$ ($\mathrm{M}_\odot$)	α	$\log \phi_0$ (Mpc^{-3})	$\log M_1$ ($\mathrm{M}_\odot$)	β	$\log M_T$ ($\mathrm{M}_\odot$)
Schechter equation (3.4) fit						
Reference Model	$10.21^{+0.43}_{-0.26}$	$-1.96^{+0.09}_{-0.08}$	$-4.48^{+0.62}_{-0.31}$	-	-	-
$Z = 0.01\,\mathrm{Z}_\odot$	$10.21^{+0.45}_{-0.26}$	$-1.92^{+0.08}_{-0.08}$	$-4.46^{+0.61}_{-0.31}$	-	-	-
$Z = 0.5\,\mathrm{Z}_\odot$	$10.22^{+0.44}_{-0.26}$	$-2.04^{+0.09}_{-0.08}$	$-4.54^{+0.68}_{-0.32}$	-	-	-
$\psi(t) \propto t\exp(-t/\tau)$	$10.21^{+0.44}_{-0.26}$	$-1.96^{+0.09}_{-0.08}$	$-4.48^{+0.63}_{-0.31}$	-	-	-
$\psi(t) \propto \exp(t/\tau)$	$10.19^{+0.47}_{-0.26}$	$-1.82^{+0.08}_{-0.07}$	$-4.38^{+0.54}_{-0.30}$	-	-	-
$\psi(t) \propto \exp(-t/\tau)$	$10.23^{+0.39}_{-0.26}$	$-2.14^{+0.10}_{-0.09}$	$-4.60^{+0.74}_{-0.32}$	-	-	-
Calzetti attenuation law	$10.37^{+0.42}_{-0.29}$	$-2.34^{+0.11}_{-0.10}$	$-5.00^{+1.04}_{-0.34}$	-	-	-
SMC-like extinction law	$10.33^{+0.45}_{-0.29}$	$-2.11^{+0.09}_{-0.08}$	$-4.75^{+0.82}_{-0.33}$	-	-	-
Modified Schechter equation (3.6) fit						
Reference Model	$10.22^{+0.45}_{-0.27}$	$-1.96^{+0.09}_{-0.08}$	$-4.49^{+0.64}_{-0.32}$	$7.55^{+0.10}_{-0.10}$	$1.00^{+0.87}_{-0.73}$	$7.10^{+0.17}_{-0.56}$
$Z = 0.01\,\mathrm{Z}_\odot$	$10.22^{+0.47}_{-0.26}$	$-1.92^{+0.08}_{-0.08}$	$-4.48^{+0.62}_{-0.32}$	$7.50^{+0.07}_{-0.07}$	$0.91^{+0.80}_{-0.74}$	$7.04^{+0.18}_{-0.65}$
$Z = 0.5\,\mathrm{Z}_\odot$	$10.23^{+0.43}_{-0.27}$	$-2.04^{+0.09}_{-0.09}$	$-4.55^{+0.69}_{-0.32}$	$7.67^{+0.12}_{-0.12}$	$1.18^{+0.98}_{-0.78}$	$7.25^{+0.15}_{-0.46}$
$\psi(t) \propto t\exp(-t/\tau)$	$10.19^{+0.42}_{-0.26}$	$-1.96^{+0.09}_{-0.08}$	$-4.45^{+0.62}_{-0.31}$	$7.36^{+0.31}_{-0.30}$	$1.42^{+3.11}_{-1.14}$	$7.01^{+0.19}_{-0.35}$
$\psi(t) \propto \exp(t/\tau)$	$10.19^{+0.47}_{-0.26}$	$-1.82^{+0.08}_{-0.07}$	$-4.38^{+0.54}_{-0.30}$	$7.29^{+0.12}_{-0.12}$	$0.71^{+0.99}_{-0.83}$	$6.85^{+0.18}_{-0.75}$
$\psi(t) \propto \exp(-t/\tau)$	$10.22^{+0.40}_{-0.26}$	$-2.14^{+0.10}_{-0.09}$	$-4.59^{+0.74}_{-0.32}$	$7.71^{+0.27}_{-0.26}$	$1.79^{+3.39}_{-1.36}$	$7.38^{+0.17}_{-0.32}$
Calzetti attenuation law	$10.37^{+0.43}_{-0.29}$	$-2.34^{+0.11}_{-0.10}$	$-4.97^{+1.04}_{-0.35}$	$8.01^{+0.21}_{-0.18}$	$1.37^{+10.16}_{-8.47}$	$7.86^{+0.14}_{-0.31}$
SMC-like extinction law	$10.33^{+0.45}_{-0.29}$	$-2.10^{+0.09}_{-0.08}$	$-4.74^{+0.81}_{-0.33}$	$7.77^{+0.18}_{-0.17}$	$1.56^{+3.85}_{-2.04}$	$7.49^{+0.14}_{-0.44}$

The best-fit Schechter and modified Schechter functions for each `BEAGLE` configuration in Tab. 3.5 are plotted in Fig. 3.8 and we show the corresponding posterior distributions in Fig. A.8 in appendix A.3. The resulting GSMFs do not depend significantly on metallicity within their respective uncertainties. We observe a slight steepening of the low-mass end slope with increasing metallicity, from $\alpha \simeq -1.92^{+0.08}_{-0.08}$ for $0.01\,\mathrm{Z}_\odot$ to $\alpha \simeq -2.04^{+0.09}_{-0.09}$ for $0.5\,\mathrm{Z}_\odot$, resulting in a insignificantly larger turnover mass $\log(M_T/\mathrm{M}_\odot) \simeq 7.25^{+0.15}_{-0.46}$ and curvature $\beta \simeq 1.18^{+0.98}_{-0.78}$ for the highest metallicity case. The effect of changing our assumptions on the form of the SFH on the GSMF is much more severe: While assuming a delayed SFH results in the same GSMF as a constant SFH, the exponentially rising and declining SHFs result in significantly shallower ($\alpha \simeq -1.82^{+0.08}_{-0.07}$) and steeper ($\alpha \simeq -2.14^{+0.10}_{-0.09}$) GSMFs, respectively. Finally, allowing for more dust attenuation in the ensemble of galaxies results in a much steeper GSMF, $\alpha \simeq -2.34^{+0.11}_{-0.10}$, than the reference model. Applying an SMC dust extinction law instead of the Calzetti law however results in a GSMF closer to the reference model in the low-mass end slope, $\alpha \simeq -2.10^{+0.09}_{-0.08}$. Larger dust attenuation insignificantly affects the high-mass end with an exponential cut-off at $\log(M_0/\mathrm{M}_\odot) \simeq 10.37^{+0.43}_{-0.29}$ instead of at $\log(M_0/\mathrm{M}_\odot) \simeq 10.22^{+0.45}_{-0.27}$ in the reference model. We further note a slight correlation between the low-mass end slope, α, and the turnover curvature, β, in general: A steeper slope α results in a larger turnover mass M_T and a slightly higher curvature β. The uncertainties in β become particularly large for the steepest α. This is due to the $M_\star$-bins lying closer together in these cases because the $M_\star - M_{\rm UV}$-relation is shallower. The large uncertainties on the lowest-mass bins therefore allow for a much wider range of acceptable values in the β-parameter space (cf. lower panel of Fig. A.8). While our modified Schechter parametrization of the GSMF also allows for an upward turnover, i.e., $\beta < 0$, this is ruled out by our MCMC analysis at greater than 1σ-level for all models apart from the exponentially rising SFH case (cf. Fig. A.7) and the two models that allow higher values of the dust attenuation although this is a result of the effects already discussed above in these two models.

3.5 Discussion

We presented a determination of the stellar masses of a sample of $z \sim 6-7$ galaxies observed through the gravitational magnification of the six HFF clusters and computed their GSMFs from UV luminosity functions (Atek et al., 2018). We found relatively shallow $M_\star - M_{\rm UV}$-slopes ~ 0.4, consistent with constant mass-to-light ratios. Our GSMFs have relatively steep low-mass end slopes and relatively low exponential cut-offs with $\log(M_0/{\rm M}_\odot) \simeq 10.22^{+0.45}_{-0.27}$, $\alpha \simeq -1.96^{+0.09}_{-0.08}$ and $\log(\phi_0/{\rm Mpc}^{-3}) \simeq -4.49^{+0.64}_{-0.32}$ for the reference SED-fitting model. We also observe a turnover at the very low-mass end of the GSMF at $\log(M_T/{\rm M}_\odot) \simeq 7.10^{+0.17}_{-0.56}$ with a downward curvature parameter $\beta \simeq 1.00^{+0.87}_{-0.73}$. In this section, we discuss these results with regard to the IR (rest-frame optical) photometry, gravitational lensing uncertainties and the impact of SED-fitting prescriptions (sections 3.5.1, 3.5.2 and 3.5.3). Finally, we compare our results with those from the literature and we reflect briefly on the nature of the turnover in the GSMF (sections 3.5.4 and 3.5.5).

3.5.1 Photometry

The rest-frame UV emission in star forming galaxies is dominated by massive O and B stars (cf. Fig. 2.11). Since these stars have very short lifetimes, they critically depend on the recent star-forming activity. One needs to observe wavelengths beyond the 4000 Å break in the rest-frame optical which preferentially probe the photospheric emission from older stellar populations (cf. section 2.4). In this study, we use deep *Spitzer*/IRAC data which sample the emission red-ward of $\lambda \sim 4000$ Å of our galaxies. While these rest-frame *optical* photometric bands are crucial in estimating stellar masses at $z > 6$ (for a complete review see e.g., Dunlop, 2013), they are affected by the assumed SFH as we discuss in section 3.5.3.

Obtaining reliable IRAC photometry is challenging because of two main problems: The limited depth of the *Spitzer* observations, $\lesssim 26$ mag, (Tab. 3.1) and blending with the light profiles of foreground objects. The latter problem is severe due to the IRAC observations having 10× lower resolution than the HST observations used to select high-redshift targets. Since our $z \sim 6-7$ galaxies are mostly unresolved, even in HST detection stacks, with angular sizes $\lesssim 1''$ the pixel scale of the HFF IRAC mosaics of $0.6''$ and the IRAC PSFs with $\sim 2''$ FWHM make them blend into the much higher surface brightness light profiles of foreground galaxies. This effect is moreover amplified by the very nature of our observations: Since we observe the high-redshift galaxies *through* the dense cores of SL clusters we are looking at exceptionally crowded fields, dominated by ICL and cluster galaxies. While we correct for unreliable IRAC photometric measurements by an empirical correction factor (see section 3.2.3), this correction is an average over a relatively small (only 39) subsample of our full sample, 303 (13%). There is a significant scatter in this correction even among sources with reliable IRAC photometry, of about $S_\delta \sim 0.2\,\mathrm{dex}$ (cf. Fig. 3.3). The $z \sim 6-7$ GSMF is sensitive to fluctuations in the overall $M_\star$ distribution of that order of magnitude (cf. e.g. section 3.5.3). Furthermore, we expect a slight bias towards overestimating the lower stellar masses due to selection effects in the sample of galaxies for which we derive the mean correction factor. This bias is difficult to quantify because we can not constrain the actual stellar mass of these objects at the low-mass end without IRAC photometry. We however expect its impact on our results to be relatively small compared to the large uncertainties in the estimated values of the lensing magnification (cf. appendix A.2 for further discussion).

The next generation of high angular resolution facilities such as the JWST will be able to observe the rest-frame optical continuum and nebular emission lines of these $z \sim 6-7$ galaxies with angular resolutions and depths comparable to the current HST observations of distant lensed galaxies. Recent simulations have shown that rest-frame optical photometry with the *Near Infrared Camera* (NIRCam; Rieke et al., 2005) aboard the JWST will be able to constrain the stellar mass of galaxies out to $z \sim 9$ to within $0.2\,\mathrm{dex}$ (Bisigello et al., 2017; Kemp et al., 2019; Kauffmann et al., 2020). This will allow us to robustly constrain the low-mass end of the galaxy mass stellar function.

3.5.2 Gravitational lensing uncertainties

Perhaps the most significant problem inherent in studies of strongly lensed galaxies are the very large differences in the strong lensing models. In our study, we consider these differences as if they were random uncertainties and this is one of our central assumptions. This uncertainty has a significant impact on our conclusions about the robustness of the GSMF, especially at its low-mass (intrinsically faint) end. To illustrate these details, we show in Fig. 3.9 the *relative* magnification uncertainties, i.e., $\frac{\Delta\mu}{\mu}$, as a function of the median magnification μ for each object. As expected, the more strongly magnified galaxies, with $\mu > 10$ that have the faintest UV luminosities $M_{\mathrm{UV}} \gtrsim -16$ (Fig. 3.9), also tend to have the larger uncertainties in their magnifications. This sensitivity in galaxies with high magnifications is due to their generally close proximity to the caustics (cf. section 2.2.2). The positions and shapes of the caustics and their concomitant high magnification are very sensitive to the positions of the cluster galaxies and the assumed total mass and mass profiles of both the cluster DM halo and the cluster galaxies. Large numbers of multiply imaged galaxies with accurate spectroscopic redshifts are therefore required to robustly constrain the shapes and positions of the caustics and the resulting (high) magnifications from the strong lensing models. The quality and quantity of the multiple images used for constraining the cluster SL model can bias magnifications of $\mu > 2$ by up to 60 % within the same SL modelling technique alone (Acebron et al., 2018). The caustics in turn tend to have radically different shapes and positions between

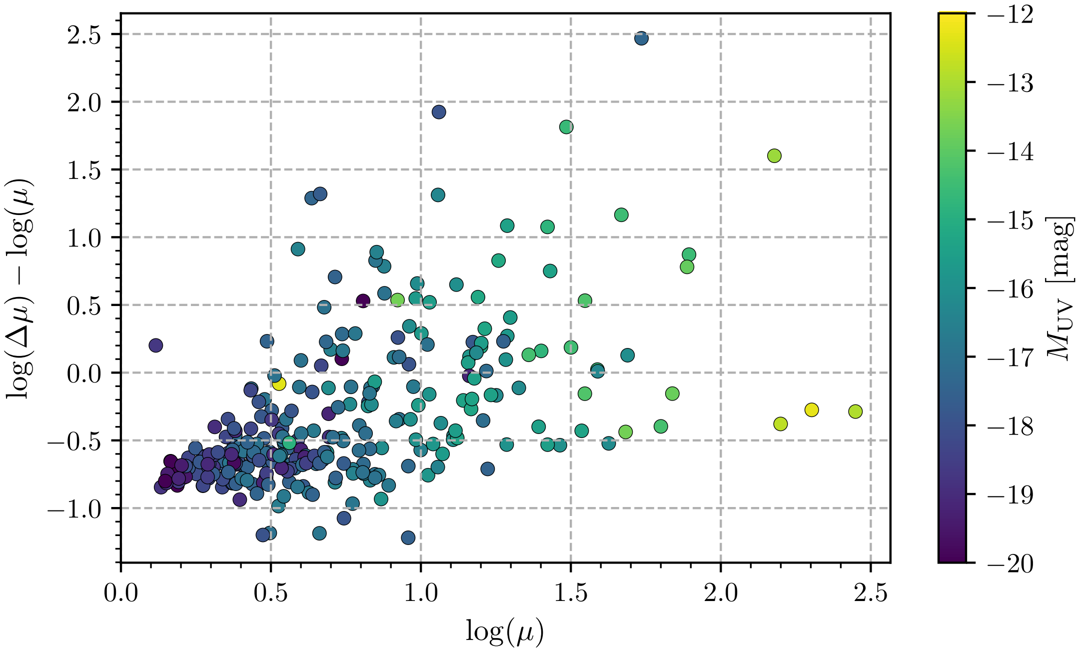

Figure 3.9: Relative magnification uncertainties $\frac{\Delta\mu}{\mu}$ as a function of magnification μ, color-coded with UV luminosity M_{UV} in AB magnitudes. There is a general trend of large relative magnification errors for large μ due mostly to SL modelling systematics between models. A few sources in the very high magnification regime *lower right quadrant* are of particular interest because the major contribution to their magnification comes from the SL cluster BCGs

different SL models, the number of multiple image redshifts available for the SL model, assumptions on cluster DM distributions, etc. This adds large systematic uncertainties to the magnifications which are inherent to the modelling techniques and are, as yet, not very well understood (Meneghetti et al., 2017; Acebron et al., 2017). Since we compute the magnification uncertainty, $\Delta\mu$, as the scatter between the different SL models used in this study (see section 3.2.2), we find that the lensing uncertainties are dominated by the systematic differences in the lensing models. There are a few sources on the very high magnification end which have distributions in magnification that are of the same order as the median magnification (lower right quadrant in Fig. 3.9). Visual inspection revealed that these sources are lensed by massive *brightest cluster galaxies* (BCGs) in the dense centers of the clusters. Significant improvements of their magnifications could therefore come from dynamic modelling of the BCGs and the mass potential within these clusters using *integral field spectroscopy* (IFS; e.g., Chirivì et al., 2020).

While gravitational lensing by massive clusters and their galaxies allows us to *detect* the faintest $z \gtrsim 6$ galaxies, it introduces large systematic uncertainties in de-magnified magnitudes and therefore the luminosities and masses. Improvements in SL modelling techniques (such as proposed by e.g., Niemiec et al., 2020; Chirivì et al., 2020; Yang et al., 2020) and large samples of spectroscopic redshifts of lensed galaxies, especially

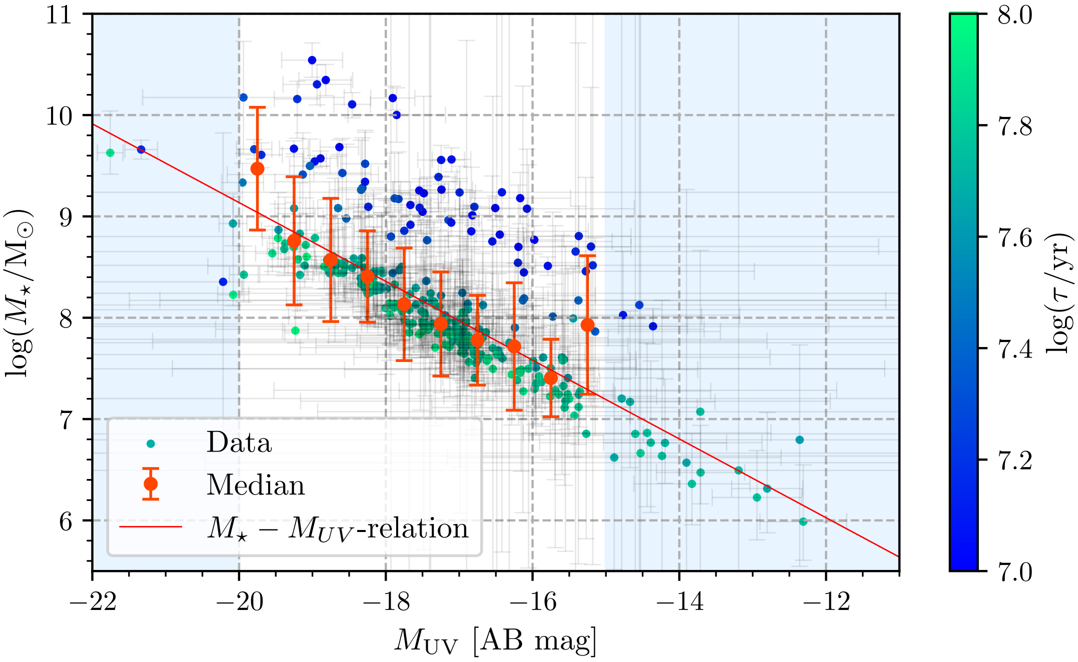

Figure 3.10: $M_\star - M_{\mathrm{UV}}$ distribution for a delayed SFH, $\psi(t) \propto t \exp(-t/\tau)$. The values are color-coded by the SFR e-folding time, τ, as indicated by the color bar on the right. The red line shows the best-fit $M_\star - M_{\mathrm{UV}}$-relation to median-binned data. With this SFH, the galaxy sample separates into two distinct stellar mass populations which illustrates the degeneracy between $M_\star$ and τ: Galaxies with low mass close to their SFR peak at $t_{\mathrm{age}} = \tau$ (green) and galaxies with high mass which are not currently close to the peak in their SFR (blue). This scatter does not appear for a constant SFH (cf. Fig. 3.4). The blue shaded area is the same as in Fig. 3.4.

those with multiple images, are needed to reduce such uncertainties and differences in the models.

3.5.3 Impact of SED-fitting assumptions

We describe the impact of SED-fitting assumptions and constraints on stellar mass and the resulting $M_\star - M_{\mathrm{UV}}$-relation in section 3.3 (Fig. 3.5 and Tab. 3.4) and on the resulting GSMF in section 3.4 (Fig. 3.8 and Tab. 3.5). While we found that the stellar mass (and thus the GSMF) is not strongly dependent on metallicity, we did find significant differences depending on the underlying assumption as to the functional form of the SFH, the range of attenuation optical depths which is allowed in the modeling, and the nature of the attenuation law. We individually address these degeneracies in detail in the following sections.

SFH

Assuming an exponentially rising SFH, $\psi(t) \propto \exp(t/\tau)$, results in stellar masses lower by $\sim 0.3\,\mathrm{dex}$ than a constant SFH (and thus in a shallower GSMF). This is due to the radically different functional form of the exponentially rising SFH compared that used in our reference model. Since the SFR is exponentially *rising* over time, the galaxies are generally fitted with larger current SFRs and thus much larger EWs in optical nebular emission lines such as the O III and H β lines. Large EW nebular emission then contributes a large fraction of the observed flux in the rest-frame optical bands. The rest-frame optical bands play a significant role in constraining both the ages and masses of galaxies (cf. section 2.4.2). Very large SFRs, which result in large EWs of the optical emission lines, then result in lower estimated ages and hence stellar masses for galaxies at these redshifts. Note that the $\sim 0.3\,\mathrm{dex}$ difference in $M_\star$ that we find agrees with the predictions by hydrodynamic simulations of the effect of changing the functional form of the SFH to an exponentially rising form ($\lesssim 0.3\,\mathrm{dex}$; Finlator et al., 2007). Similarly, assuming an exponentially *declining* SFH $\psi(t) \propto \exp(-t/\tau)$ has the opposite effect, the current SFR estimates are generally lower and thus this assumption results in overall larger stellar mass estimates than our reference model. The nebular emission contributes less to the flux in the rest-frame optical photometry and the thus higher estimated optical continuum luminosities yield larger stellar masses.

The delayed SFH, $\psi(t) \propto t\exp(-t/\tau)$, on the other hand yields the same $M_\star - M_{\mathrm{UV}}$-relation as the constant SFH and thus the same GSMF. This is however mainly an effect of the median-binning we use to determine the $M_\star - M_{\mathrm{UV}}$-relation (section 3.3). The individual stellar masses scatter significantly (Fig. 3.10) compared to the constant SFH case (Fig. 3.4). The galaxies separate into two populations: Galaxies with low mass and large SFR e-folding time, τ, and galaxies with large mass and low τ. Since the delayed SFH has a maximum SFR at $t = \tau$, `BEAGLE` can fit the same IRAC photometry either with a galaxy close to its SFR peak, i.e., with a large τ, resulting in smaller stellar mass *or* with a galaxy long after its SFR peak, i.e., with a small τ, which results in larger stellar masses for the same reason discussed above for the exponential SFHs. Applying any of the three exponential SFHs therefore creates a well known degeneracy between $M_\star$ and τ which cannot be resolved with the available data, effectively making τ a 'nuisance' parameter in this type of analysis.

While constant or exponentially decreasing SFHs were previously assumed (e.g. Eyles et al., 2007; Stark et al., 2009; González et al., 2011; Grazian et al., 2015; Kikuchihara et al., 2020), results from hydrodynamical simulations predict exponentially increasing SFRs for high-redshift galaxies (e.g. Finlator et al., 2011). Observations of very high EW optical emission lines of [O III] and Hβ, up to rest-frame EW$\sim 2000\,\mathrm{Å}$, (e.g. Atek et al., 2011, 2014; Reddy et al., 2018b) and of IRAC excesses in high-redshift galaxies (which have been attributed to strong contributions from rest-frame optical emission lines; Smit et al., 2014, 2015; De Barros et al., 2019; Endsley et al., 2021) further support young galaxies with relatively high rates of recent star formation, which could be due to a SFH with an increasing SFR as a function of time. Alternatively, given their compact sizes, the star formation in young high-redshift galaxies might also be episodic with several relatively strong bursts occurring over relatively short duty cycles (e.g. Stark et al., 2009). Such episodic star formation is difficult to parametrize correctly given the relative crudeness of the data available for galaxies at these redshifts. There are however examples of models that combine a continuous SFH with an ongoing recent starburst (e.g. Endsley et al., 2021). Other recent studies infer the SFH from SED-fitting which is however heavily degenerate with stellar mass, age, metallicity and dust attenuation (Duncan et al., 2014; Song et al., 2016a; Bhatawdekar et al., 2019). While Grazian et al. (2015) found no dependence of $M_\star$ on SFH in an experiment similar to ours for $z \sim 3.5-4.5$ galaxies, their SED-fitting analysis did not include nebular emission and would therefore not have been sensitive to some of the degeneracies discussed above.

Progress on determining the SFHs of distant galaxies will also come with the launch of the JWST. Observations with the *Near Infrared Spectrograph* (NIRSpec; Bagnasco et al., 2007; Birkmann et al., 2016) will enable us to resolve and accurately characterize the optical nebular emission lines at $z \sim 6-7$ (Chevallard et al., 2019; Maseda et al., 2019). Observations with the *Mid-Infrared Instrument* (MIRI; Rieke et al., 2015; Wright et al., 2015) will be the first instrument able to detect the rest-frame NIR continuum emission of these galaxies thereby enabling the most robust and most SFH-independent estimate possible of $M_\star$ (e.g. Dunlop, 2013).

Dust attenuation

The other significant impact of SED-fitting parameters on the $z \sim 6-7$ GSMFs comes from allowing the best fits to the SEDs of individual high-redshift galaxies to have a higher dust attenuation optical depth (Fig. 3.5). Allowing a wide range of effective V-band optical depth, up to $\hat{\tau}_V \leq 3$, results in significantly shallower $M_\star - M_{\mathrm{UV}}$-slopes and thus in turn in steeper low-mass end GSMF slopes (Fig. 3.5) than in the case when the range allowed in $\hat{\tau}_V$ is more limited, i.e., $\hat{\tau}_V \leq 0.2$ (section 3.3 and Fig. 3.8). This impact is due to the well-known degeneracy between dust attenuation and stellar mass (cf. Fig. 3.11). This degeneracy is the reason for the considerable scatter in $M_\star$ in all luminosity bins and results in very large uncertainties in the $M_\star - M_{\mathrm{UV}}$-relation. We however also observe that dust attenuation mostly affects the median stellar masses of the faint M_{UV}-bins, i.e., the bins with the highest fractions of galaxies without reliable IRAC photometry. We expected this behavior since these galaxies' stellar mass is constrained only by rest-frame UV photometry which is more strongly affected by amount of dust attenuation compared the rest-frame optical photometry (the typical factor between A_V and A_{UV} is ~ 4 Calzetti et al., 2000).

As can be seen in Fig. 3.11, this degeneracy seems to be reduced by using a steeper SMC-like dust attenuation law (such as observed in e.g., Reddy et al., 2015, 2018a). Fitting the SEDs with $\hat{\tau}_V \in [0,3]$ then results in $M_\star - M_{\mathrm{UV}}$-slopes and a GSMF closer to that obtained by assuming a Calzetti attenuation law and only allowing $\hat{\tau}_V \in [0,0.2]$ (Fig. 3.5 and 3.8). It also results in less scatter in $M_\star$ than the 'dusty' Calzetti law case. The $z \sim 6-7$ GSMF is therefore not only highly sensitive to the range of dust attenuation allowed but also to the shape of the dust attenuation law.

In order to more robustly constrain stellar masses at $z \sim 6-7$ and to limit the impact

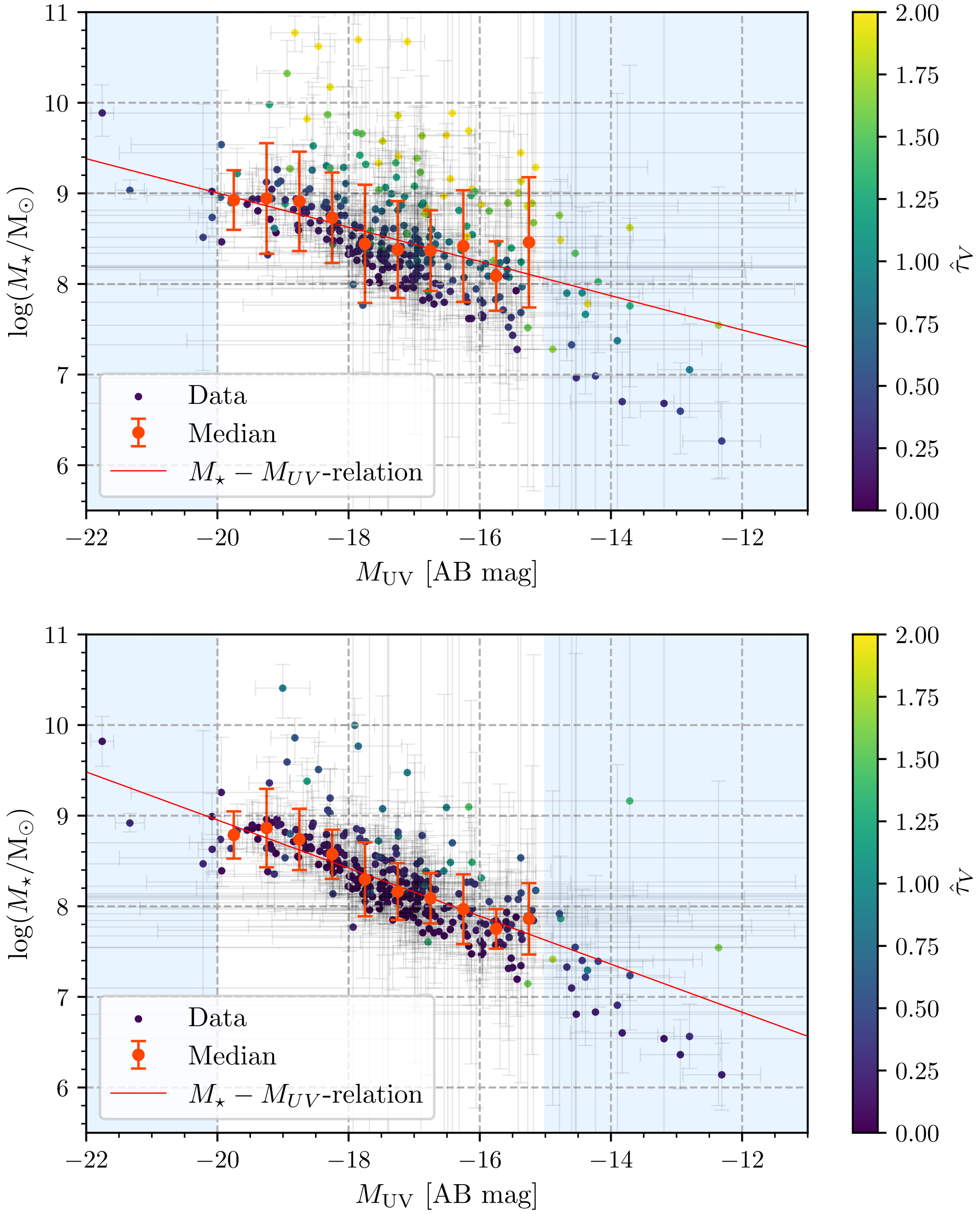

Figure 3.11: $M_\star - M_{\mathrm{UV}}$ distribution for a Calzetti dust attenuation law (*upper panel*) and for an SMC-like law (*lower panel*) when allowing the effective V-band optical depth to vary over a wide range, $\hat{\tau}_V \in [0, 3]$. Each value is color-coded with $\hat{\tau}_V$. The red line shows the best-fit $M_\star - M_{\mathrm{UV}}$-relation to median-binned data. We observe a degeneracy between $\hat{\tau}_V$ and $M_\star$, in particular for the Calzetti law case. For the steeper SMC-like law this degeneracy is less prominent as the galaxies are fit with much less dust attenuation, $\hat{\tau}_V \lesssim 1.5$. The blue shaded area is the same as in Fig. 3.4.

of of the details of the range of the amount and forms of the dust attenuation allowed on the GSMF, one therefore needs to consider the latest observational results. Considering outside information about the dust attenuation observed in the high-redshift galaxy population effectively places another prior on the fitting parameters. High-redshift galaxies are found to have very blue UV-continuum slopes, $\beta_{UV} \lesssim -2$, which indicates very low dust attenuations (Bouwens et al., 2016). This rules out our $\hat{\tau}_V \in [0, 3]$ model and favors the $\hat{\tau}_V \in [0, 0.2]$ model as the more realistic prior in our modeling. Note that recent observations of dust continuum emission (and [O III] and [C II] emission lines) from high-redshift galaxies with the *Atacama Large Millimeter/Sub-millimeter Array* (ALMA) have discovered surprisingly high dust masses in a few high-redshift galaxies (Laporte et al., 2019; Tamura et al., 2019). This does not change our conclusions that the overall dust attenuation must be low for two salient reasons. The first is that high-redshift galaxies have very blue UV slopes which can only be explained by young ages and low dust attenuations (Tamura et al., 2019; Bakx et al., 2020). The other is that the brightest dust continuum emission regions are often not spatially coincident with the UV-bright regions of high-redshift sources. Moreover, many galaxies at these redshifts are completely undetected in the thermal IR continuum (e.g. Capak et al., 2015). Rest-frame far-infrared (FIR) detections with ALMA slightly favor a steep SMC-like extinction law (Capak et al., 2015; Bouwens et al., 2016). While some rest-frame UV observations of low redshift star-forming analogs support a Calzetti-like attenuation law (Scoville et al., 2015) with a steep dependence at long wavelengths (i.e., $\lambda \geq 2500$ Å Reddy et al., 2015), the most recent observations strongly support an even steeper dust attenuation law than the SMC extinction law for high-redshift galaxies (Reddy et al., 2018a). For these reasons, there is no good reason to presuppose that the UV detected galaxies and UV bright regions embedded in what must be larger structures when the dust continuum and UV emission are not co-spatial have high attenuation optical depths such as $\hat{\tau}_V \gtrsim$ a few tenths of a magnitude.

Additional multi-band rest-frame FIR observations with ALMA to deeper flux levels will be required to place stronger constraints on dust content and attenuation in SED-fitting stellar masses at high-redshift. Rest-frame NIR observations with JWST/MIRI will be crucial in breaking the degeneracy with dust attenuation (Kemp et al., 2019) and stellar age since NIR wavelengths are the least affected by dust attenuation as well as having mass-to-light ratios that are less sensitive to stellar age. These additional data will enable us to minimize the impact of various degeneracies in SED modeling and ultimately to make robust estimates of $M_\star$ and thus the GSMF at these redshifts.

3.5.4 Comparison to the literature

Previous studies of the GSMFs at $z \sim 6-7$ include observations of galaxies in both blank fields (González et al., 2011; Duncan et al., 2014; Grazian et al., 2015; Song et al., 2016a) and those lying behind HFF clusters (Bhatawdekar et al., 2019; Kikuchihara et al., 2020). The Song et al. (2016a) $z \sim 6$ GSMFs are based on a large sample of galaxies and UV luminosity functions derived by Finkelstein et al. (2015) in the CANDLES/GOODS, the ERS and the HUDF fields and thus represent the most complete study of high-redshift

Table 3.6: Best-fit GSMF Schechter parameters of our reference model and previously published studies.

Reference	log M_0 ($M_\odot$)	α	log ϕ_0 (Mpc^{-3})
This Work[a]	$10.21^{+0.43}_{-0.26}$	$-1.96^{+0.09}_{-0.08}$	$-4.48^{+0.62}_{-0.31}$
This Work[b]	$10.22^{+0.45}_{-0.27}$	$-1.96^{+0.09}_{-0.08}$	$-4.49^{+0.64}_{-0.32}$
Song et al. (2016a)[c]	$10.72^{+0.29}_{-0.30}$	$-1.91^{+0.09}_{-0.09}$	$-4.86^{+0.53}_{-0.24}$
Bhatawdekar et al. (2019)[c,d]	$10.29^{+0.65}_{-0.67}$	$-1.89^{+0.09}_{-0.10}$	$-4.27^{+0.65}_{-0.26}$
Bhatawdekar et al. (2019)[c,e]	$10.35^{+0.50}_{-0.50}$	$-1.98^{+0.07}_{-0.07}$	$-4.22^{+0.64}_{-0.25}$
Kikuchihara et al. (2020)	$9.58^{+0.23}_{-0.15}$	$-1.85^{+0.07}_{-0.07}$	$-3.74^{+0.30}_{-0.22}$

[a] Using a Schechter function equation (3.4)
[b] Using a modified Schechter function equation (3.6)
[c] $z \sim 6$ sample
[d] Point source results
[e] Disk galaxy results

GSMFs in blank fields thus far. Previous studies (González et al., 2011; Duncan et al., 2014; Grazian et al., 2015) studied sub-samples of the CANDLES/GOODS fields which are all included in the sample studied in Song et al. (2016a). We will therefore rely mostly on the results of Song et al. when comparing blank field results to this work. Song et al. used 12 bands of HST and *Spitzer*/IRAC photometry and include full modelling of the SFH in their SED-fitting as well as allowing a significant range in the dust attenuation, $A_V \in [0, 3.2]$ (about the same range as our 'dusty' model).

The two high-redshift GSMF studies observed through SL clusters (Bhatawdekar et al., 2019; Kikuchihara et al., 2020) are both based on the 7 HST bands, the Ks band and the two deep *Spitzer*/IRAC bands available for the HFF clusters. Bhatawdekar et al. (2019) derive their $z \sim 6$ UV luminosity functions and GSMFs from a sample of galaxies detected in the cluster and parallel field of MACS0416. Their analysis contains two GSMFs for $z \sim 6$ galaxies that were derived in two different ways: One assuming that the galaxies all have Sérsic profiles light profiles and the other in which they assumed all detections are point sources. These assumptions resulted in two different completeness limits and corrections. They also include full modelling of the SFH and dust attenuation ($A_V \in [0, 2]$) in their SED-fitting and their method of treating SL magnification is similar to ours, i.e., they take the median magnification of all SL models available for MACS0416. The GSMFs derived by Kikuchihara et al. (2020) on the other hand are based on a $z \sim 6-7$ galaxy sample detected in all six HFF clusters by Kawamata et al. (2018) and UV luminosity functions derived by Ishigaki et al. (2018). They use the GLAFIC SL models to derive their magnification factors and `BEAGLE` with a constant SFH and $\hat{\tau}_V \in [0, 2]$ for their SED-fitting. Finally, they also use the Song et al. estimates of the co-moving density as a function of stellar mass to constrain the high-mass end of their derived GSMF.

We show our best-fit reference model GSMFs alongside the best-fit results from the

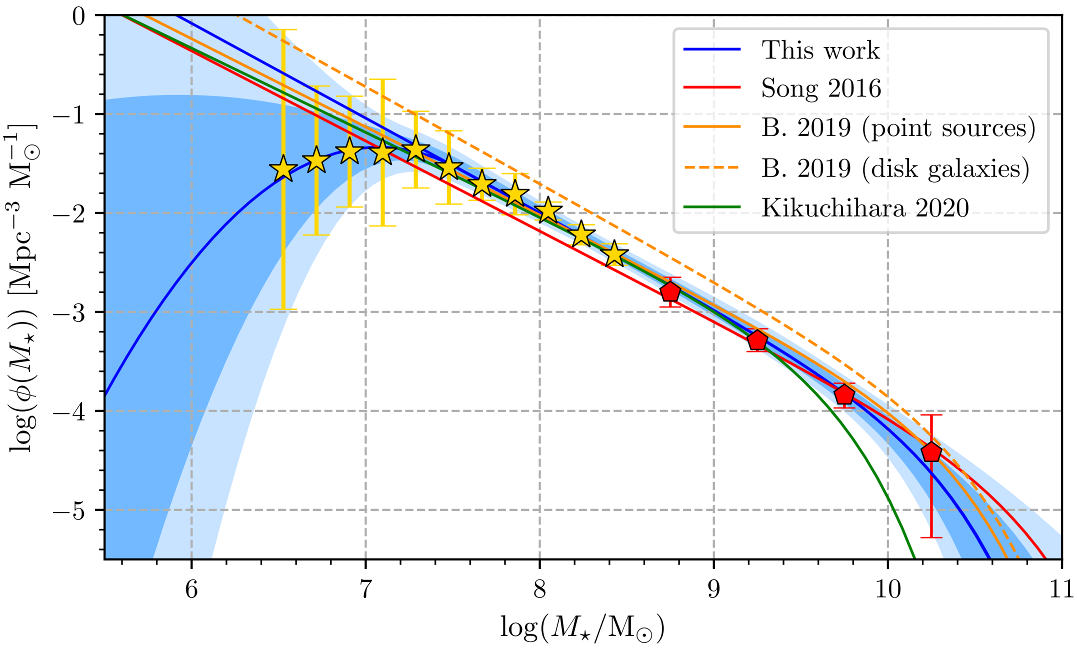

Figure 3.12: The final $z \sim 6-7$ GSMF (for the reference `BEAGLE` configuration, blue curve) compared to GSMFs published in the recent literature. Yellow stars represent our reference model low-mass GSMF points and red pentagons the $z \sim 6$ GSMF points observed in wide-area blank fields by Song et al. (2016a) shifted down by 0.15 dex (see text for details). The blue curves show both our best-fit Schechter and modified Schechter functions while GSMFs by Song et al. (2016a), Bhatawdekar et al. (2019) and Kikuchihara et al. (2020) are shown in red, orange and green respectively (see legend at the top right). The red and purple curves are shifted down by 0.15 dex in order to account for the difference in mean redshift of the two galaxy samples. The orange dotted curve represents the GSMF obtained by Bhatawdekar et al. (2019) for assuming Sérsic light profiles in the completeness analysis rather than point sources. The blue shaded areas are the same as in the right panel of Fig. 3.6, i.e. the 1σ and 2σ areas for the reference model.

literature in Fig. 3.12 and the corresponding best-fit Schechter parameters and their 1σ uncertainties in Tab. 3.6. Overall, our results are in good agreement with results in the literature within the uncertainties. Assuming a disk galaxy light distribution to estimate the completeness, Bhatawdekar et al. (2019) found results that deviate somewhat from the consensus of the results from the literature; their results when they assumed the sources had point-like light distributions in deriving the completeness agree well with ours. This is unsurprising since our $z \sim 6-7$ sample is mostly comprised of unresolved sources. At the low-mass end, we find a slope of $\alpha \simeq -1.96^{+0.09}_{-0.08}$ which is slightly steeper than in the literature but agrees with Song et al. (2016a) and Bhatawdekar et al. (2019) within 1σ. Kikuchihara et al. (2020) on the other hand find a shallower low-mass end slope of $\alpha \simeq -1.85^{+0.07}_{-0.07}$ which differs from our estimated slope at about the 2σ level. We also note a slight discrepancy between Song et al., Kikuchihara et al. and our own results

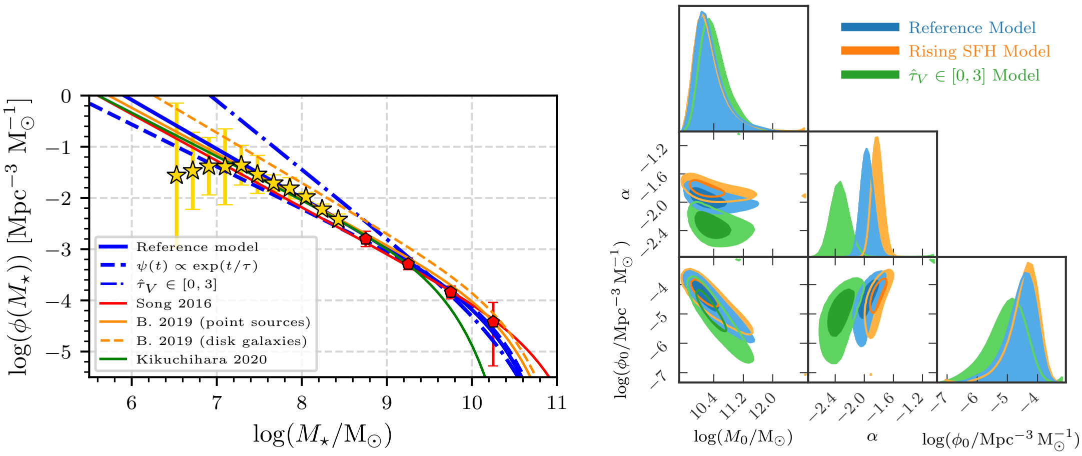

Figure 3.13: *Upper Panel*: The same plot as Fig. 3.12 with in addition the Schechter-fits of the GSMF points derived for an exponentially rising SFH (*dashed blue curve*) and for 'dusty' galaxies (*dash-dotted blue curve*). The two degeneracies, SFH and dust attenuation, have opposite impacts on the best-fit GSMF. These two effect appear to cancel each other out and result in similar GSMFs as our reference model if both the SFH and allowing a wide range of possible dust attenuation optical depths are included in the modelling simultaneously (e.g. Song et al., 2016a; Bhatawdekar et al., 2019). *Lower panel:* Posterior distributions of the three Schechter parameters for the reference model, the exponentially rising SFH model and the 'dusty' $\hat{\tau}_V \in [0, 3]$ model. These plots illustrate the opposing effects of changing the assumed SFH and allowing the dust attenuation to roam over a wide range have on the low-mass end of the GSMF.

at the high-mass end even though these three studies use the same high-mass GSMF results. This is due to the role that the exact properties of the low-mass end GSMF play in constraining the overall shape of the GSMF. The high-mass end exponential cutoff mass, M_0, and the low-mass end slope, α, of the GSMF are not independent parameters as illustrated by the shape of their posterior distributions in Fig. 3.7. This work is the only study of $z \sim 6-7$ GSMFs to date that observes a possible turnover of the GSMF at very low masses at greater than 1σ-level. Note that Kikuchihara et al. (2020) and our work are currently the only studies that probe stellar masses as low as $M_\star \gtrsim 10^6\,\mathrm{M}_\odot$ at $z \sim 6-7$.

Our reference model GSMF results and the literature broadly agree within the uncertainties despite the fact that the different results are based on different sets of assumptions (Fig. 3.12). This does not contradict our conclusions of the importance of parameter choice and assumptions in SED-fitting (section 3.5.3): The degeneracy between $M_\star$ and $\hat{\tau}_V$ results in a steeper low-mass end slope of the GSMF than the reference model and adopting an exponentially rising SFH in a shallower low-mass end slope (see Fig. 3.8). When modelling *both* SFH and dust attenuation in the same SED-fit, as is done in Song et al. (2016a) and Bhatawdekar et al. (2019), these two degeneracies are both present in the fits. However, each of the SFHs and dust attenuations assumed in both studies tend to push the slope in opposite directions and thus effectively and coincidentally cancel each other out, yielding average GSMFs similar to our reference model (Fig. 3.13). While Kikuchihara et al. (2020) also use a constant SFH in their SED-fitting, the degeneracy between dust attenuation and metallicity, which is a free parameter in their study, has a similar effect on their resulting GSMF. While the reference model agrees with the results from the literature, different SFHs and constraints on dust attenuation can lead to significantly different GSMFs. Because of this, it is crucial to explore the impact of different SED-fitting assumptions on the high-redshift GSMF in understanding the robustness of any GSMF.

3.5.5 Theoretical implications

Robust determinations of the form the UV luminosity and stellar mass functions of the first generations of galaxies provide deep insight into and strong constraints on the physical processes which drive galaxy evolution at all redshifts (cf. section 1.4). Given the importance of these determinations, theorists and simulators have expended great effort in predicting UV luminosity and sometimes mass functions of galaxies at $z \gtrsim 6$ (cf. Bromm & Yoshida, 2011, and references therein for a review). There is a general agreement in theory and simulations that both the ionization of the gas within and falling onto galaxy halos by the meta-galactic flux responsible for reionization and feedback from massive stars and perhaps AGN play key roles in shaping the low mass and luminosity ends of the stellar mass and UV luminosity functions (Gnedin, 2016; Liu et al., 2016; Finlator et al., 2018; Ocvirk et al., 2020). Modeling correctly how the UV continuum luminosity and color of any galaxy relate to its stellar (and DM halo) mass is obviously crucial to making the link between the UV luminosity and stellar mass functions at any redshift but particularly at high redshift when galaxies are on average quite young and are only selected by the intensity of their UV continuum or line emission. Several attempts at making a direct comparison between stellar mass and UV luminosity in observations and simulations have been published (Dayal et al., 2014; Duncan et al., 2014; O'Shea et al., 2015; Yue et al., 2016; Liu et al., 2016; Hutter et al., 2020).

The various simulation results that have been published have somewhat different UV luminosity and stellar mass functions. All of them lead to the decrease in the number density of low luminosity and low mass halos (or stellar masses). The virial temperature, T_{vir}, of a DM halo at $z \sim 6-7$ of mass $10^8\,\mathrm{M}_\odot$ is about $10^4\,\mathrm{K}$. Thus if all of the hydrogen is ionized by the meta-galactic flux in halos of this mass, halos below this mass will not be able to retain their baryons. This is the ultimate limit for halos to retain their accreted gas mass and thus, it is likely that halos with masses less than this limit will have strongly suppressed star formation. Including the effects of feedback in the form of heating of the interstellar and circumgalactic gas and driving outflows increases the halo masses at which baryons are ejected. Simulations that include the effects of feedback from massive stars have declines in co-moving number density in their simulated luminosity functions (and in some studies stellar mass functions) at higher halo masses than the limit calculated through the ionization heating limit when $T_{\mathrm{vir}} = 10^4\,\mathrm{K}$. For example, Ocvirk et al. (2020) find that star formation is gradually suppressed below a DM halo mass of $2 \times 10^9\,\mathrm{M}_\odot$ which corresponds to a turnover in the luminosity function at $M_{\rm UV} = -11$ in their models. Other simulations predict a similar turnover or flattening in the luminosity function (e.g. Yue et al., 2016) or at a magnitude or two higher UV luminosities (e.g. Gnedin, 2016; Liu et al., 2016). It is difficult to relate these turnover or flattening magnitudes to the stellar mass but in some of the simulations, the flattening occurs for relatively small DM halo masses (Liu et al., 2016) compared to others, e.g, Ocvirk et al. (2020).

If galaxies in the early universe are forming inefficiently (low ratios of mass accretion rates to SFRs), then we expect young galaxies to have relatively low SFRs and thus relatively high ratios of DM mass to stellar masses ($\sim 0.1\,\%$ or less at $z \sim 6$; see, e.g., Behroozi et al., 2013). We can make a crude estimate of the mass where energy injection rate of massive stars through stellar winds and supernova explosions is sufficient to keep galaxies from forming stars efficiently. A strong criterion for doing this would be the SFR at which the thermalized energy from stellar winds and supernovae becomes about the binding energy of the galaxy halo. Using equation 2 from Bromm & Yoshida (2011), we can estimate the binding energy of a halo as,

$$E_{\rm binding} \sim 10^{57} \left(\frac{M_{\rm vir}}{10^{10}\,{\rm M_\odot}}\right) \left(\frac{\Delta_c}{18\pi^2}\right) \left(\frac{1+z}{10}\right) {\rm erg} \tag{3.8}$$

where $M_{\rm vir}$ is the virial mass, Δ_c is the overdensity of a virialized halo, and z is the redshift. Setting $z = 6$ and $\Delta_c = 18\pi^2$, results in $E_{\rm binding} \sim 7 \times 10^{56} (M_{\rm vir}/10^{10}\,{\rm M_\odot})\,{\rm erg}$. The mechanical energy from young stars through their stellar winds and SNe can be estimated as,

$$E_{\rm wind} \sim 3 \times 10^{56} \left(\frac{\psi}{{\rm M_\odot\,yr^{-1}}}\right) \epsilon_{\rm therm} \left(\frac{t_{SF}}{10^7\,{\rm yr}}\right) {\rm erg} \tag{3.9}$$

where ψ is the star formation rate in ${\rm M_\odot\,yr^{-1}}$, $\epsilon_{\rm therm}$ is the thermalization efficiency defined as the ratio of total outflow energy and the mechanical energy output by young stars averaged over the duration of the (burst of) star formation, $t_{\rm SF}$. To scale the relation between the SFR and the mechanical energy output from young stars, we used $10^{42}\,{\rm erg\,s^{-1}}$ which is the approximate instantaneous mechanical energy output at $\sim$few 10^7 yr and longer for a constant SFR of a solar mass per year (Leitherer et al., 1999). We can recast this equation because of our assumption of a constant SFR in our reference model such that $E_{\rm wind} \sim 3 \times 10^{56} (M_\star/10^7\,{\rm M_\odot})\,\epsilon_{\rm therm}\,(t_{SF}/10^7\,{\rm yr})\,{\rm erg}$. Combining these two equations to estimate the ratio of the wind energy to binding energy of a halo we find,

$$\begin{aligned} \frac{E_{\rm wind}}{E_{\rm binding}} &\sim 0.4 \left(\frac{M_\star}{10^7\,{\rm M_\odot}}\right) \epsilon_{\rm therm} \left(\frac{M_{vir}}{10^{10}\,{\rm M_\odot}}\right)^{-5/3} \left(\frac{t_{SF}}{10^7\,{\rm yr}}\right) \\ &= 0.4 \left(\frac{M_\star}{M_{vir}}\right)_{0.001} \epsilon_{\rm therm} \left(\frac{M_{vir}}{10^{10}\,{\rm M_\odot}}\right)^{-2/3} \left(\frac{t_{SF}}{10^7\,{\rm yr}}\right) \end{aligned} \tag{3.10}$$

where $(M_\star/M_{vir})_{0.001}$ is the ratio of the stellar to virial mass in units of 10^{-3}. Since the stellar mass of a galaxy is approximately linearly proportional to its SFR times its age under the assumption of a constant SFH (and from the empirical relation of stellar mass and SFR), the energy of outflows at constant thermalization efficiency will increase more slowly, only linearly, than the binding energy of the halo as a function of halo mass which increases to the power 5/3. While we do not know the stellar mass to halo mass ratio of galaxies with stellar mass of $10^7\,\mathrm{M}_\odot$ at $z \sim 6$, it is likely to be of order 0.01 (e.g. Behroozi et al., 2013). If the stellar to halo mass ratio declines less rapidly than $M_{\mathrm{vir}}^{2/3}$, then the ratio of the wind energy to the binding energy will also increase more rapidly as the halo mass decreases. In the event of either constant or slowly declining $M_\star/M_{\mathrm{vir}}$ with decreasing halo masses, galaxy formation will become increasingly inefficient with decreasing stellar mass below halo masses of about a few $10^9\,\mathrm{M}_\odot$ (depending of course on the thermalization efficiency, which has been estimated to be ~ 0.5; Strickland & Heckman, 2009). We emphasize that the parameter choices we made for this estimate are somewhat tuned for low halo masses and given the complex physics of outflows, this estimate cannot be simply extrapolated to other galaxy stellar and halo masses. Although crude, the estimate is consistent with the simulations of Ocvirk et al. (2020) in that galaxies residing in halos of masses $\sim$few $10^9\,\mathrm{M}_\odot$ or less will form inefficiently. The results of some simulations and our crude analysis suggest that feedback provided by stellar winds and SNe may provide sufficient energy to keep the formation of galaxies in low mass halos inefficient if the thermalization efficiency is relatively high (Strickland & Heckman, 2009). Observations with JWST will provide a deeper understanding as to whether or not feedback is in fact the culprit in keeping galaxy formation inefficient at high redshift and, in particular, for low-mass galaxies near this mass-turnover.

3.6 Summary and Conclusion

We presented the derivation of high-redshift $z \sim 6-7$ galaxy stellar mass functions under various spectral energy distribution fitting assumptions using a sample of gravitationally lensed galaxies lying behind the six HFF clusters. For the sample of 303 $z \sim 6-7$ galaxies selected via the drop-out technique from deep HST imaging data, we measured the *Ks* and *Spitzer*/IRAC photometry and computed median gravitational magnification factors from the SL models available for the HFF clusters. We derived stellar masses by fitting 10 broad-band photometry filters with the `BEAGLE` SED-fitting tool. In order to test the impact of various SED-fitting assumptions on the resulting GSMF, we first constructed a minimum-parameter model which assumed a constant SFH and a fixed metallicity, $Z = 0.1\,\mathrm{Z}_\odot$, as a reference model. To test how robust the GSMF to changing assumptions in the SFH, metallicity, and range over which the amount of dust attenuation is allowed to roam, we ran SED fitting models with different assumptions for metallicity, the functional forms of the star formation histories, and both the type and range in the amount of dust attenuation allowed. The derived stellar masses were then used to derive $M_\star - M_{\mathrm{UV}}$-scaling relations which allowed us to convert the rest-frame UV luminosity function of our galaxy sample, derived by Atek et al. (2018), to GSMFs. Finally, we determined best-fitting GSMFs and their uncertainty ranges by exploring the parameter space with an MCMC analysis.

The summary and main conclusions of our analysis are:

- We extend the high-redshift GSMF to low masses, $M_\star > 10^6\,\mathrm{M}_\odot$. The best fit parameters for the $z \sim 6-7$ GSMF are a high-mass exponential cutoff at $\log(M_0/\mathrm{M}_\odot) \simeq 10.22^{+0.45}_{-0.27}$, a relatively steep low-mass end slope, $\alpha \simeq -1.96^{+0.09}_{-0.08}$, and a normalization $\log(\phi_0/\mathrm{Mpc}^{-3}) \simeq -4.49^{+0.64}_{-0.32}$ for our reference model (cf. Tab. 3.3). These results are in good agreement with recent results from the literature within the respective error bars.

- The $z \sim 6-7$ GSMF departs from the Schechter form at the very low-mass end with a downward turnover at $\log(M_T/\mathrm{M}_\odot) \simeq 7.10^{+0.17}_{-0.56}$ and a curvature $\beta \simeq 1.00^{+0.87}_{-0.73}$ in the reference model. While the uncertainties on the lowest-mass bins also allow for an upward turnover of the GSMF, most models do not have an upturn and this scenario is ruled out at the greater than 1σ-level by our MCMC analysis for the reference model and most SED-fitting configurations.

- Due to large systematic differences between the various SL models available for the HFF clusters, the gravitational magnification factors are uncertain but are especially high for galaxies with high median magnification factors. While gravitational lensing is very useful for *detecting* faint high-redshift objects, one needs to fully account for lensing uncertainties. Therefore, unless lensing models are better constrained, especially the caustics close to the center of the cluster potential and the BCGs, the utility of using strongly lensed galaxies to probe the low mass end of the GSMF is limited.

- Obtaining accurate rest-frame optical IRAC photometry, vital for constraining stellar masses of individual galaxies in this type of study (cf. section 2.4.2), proves very challenging when observing very crowded fields such as the HFF. Using a subset of galaxies with reliable IRAC photometry, we empirically estimate a correction factor for stellar masses based on using only HST photometry which probes only the rest-frame UV.

- While not strongly affected by metallicity, the determination of high-redshift GSMFs depends significantly on assumptions about the SFH and dust attenuation. For example, a significantly shallower low-mass end slope, $\alpha \simeq -1.82^{+0.08}_{-0.07}$, is the best fit for an exponentially rising SFH, $\psi(t) \propto \exp(t/\tau)$. When allowing for a wider range and higher limit on the amount of dust attenuation, $\hat{\tau}_V \in [0, 3]$, we find a significantly steeper low-mass end slope, $\alpha \simeq -2.34^{+0.11}_{-0.10}$.

- Our results show that variations in the slope of the $M_\star - M_{\mathrm{UV}}$-relation and in $M_\star$ of the order of $\gtrsim 0.1$ dex can significantly impact the resulting GSMFs. Fluctuations of this magnitude arise both from SED-fitting assumptions and the lack of rest-frame optical detections or sensitive upper-limits in the IRAC bands for all galaxies.

- The Schechter parameters of the GSMF are not generally independent. In particular, there is a degeneracy between the high-mass exponential cutoff, M_0, and the low-mass end slope, α. In order to break these degeneracies and to robustly constrain the overall shape and parameters of the GSMF, detections of galaxies at both high and low stellar masses are required.

The derivation and study of high-redshift GSMFs remain susceptible to large uncertainties, parameter degeneracies, and on the specific assumptions made when fitting their SEDs. Our approach of converting rest-frame UV luminosity functions to high-redshift GSMFs does not take into account the non-trivial problem of stellar mass incompleteness, which is not necessarily the same as UV luminosity incompleteness. Future studies will need to address this issue in order to derive robust $z \sim 6-7$ GSMFs, in particular considering how sensitive the GSMF is to fluctuations in the $M_\star - M_{\mathrm{UV}}$-relation used to convert the UV luminosity function to the stellar mass function. Considerable advances in SL modelling techniques, deeper images at more wavelengths which probe the rest-frame optical in distant galaxies, and finding and determining redshifts of multiply lensed galaxies in the cores of the HFF clusters to improve the lensing models are also all required to better constrain the very low-mass end of the GSMF. Deep observations of high-redshift galaxies with ALMA will yield new insights and constraints on the dust properties of these objects and thus help to break one of the major degeneracies in SED fitting. The greatest advancements in the study of very high-redshift galaxies will however come with the launch of the JWST. JWST will provide the first rest-frame optical and NIR spectra of galaxies at $z \gtrsim 6$ and thus the first robust constraints on stellar masses of low mass galaxies. The very faint and low-mass $z \sim 6-7$ galaxies studied in this work are prime targets for follow-up with the JWST.

Chapter 4

High-redshift galaxies in the BUFFALO survey

> "But if it is true that the act of
> observing changes the thing
> which is observed (because of
> Quantum), it's even more true
> that it changes the observer."
>
> Sir Terry Pratchett,
> *Soul Music*, 1994

Building on the success of the HFF program (cf. section 2.3), we have carried out a new HST survey targeting the six HFF clusters — the BUFFALO survey (cf. section 4.1). The goal of this program is to expand the existing data sets of the HFF by covering a wider area around the clusters. As a member of the BUFFALO collaboration, I lead the effort to identify and assemble a catalog of high-redshift galaxy candidates in the BUFFALO field-of-view. This represents the second project of my thesis and is related in this chapter. Note that the catalogs produced over the course of this work will eventually be publicly released on the `MAST` archive alongside the full BUFFALO data sets and data products. The galaxies detected in this work will be used to derive high-redshift GSMFs with new methods to compute sample completeness that will be described in detail in chapter 5. A summary of the detailed description of our pipeline given in this chapter will therefore be published in Furtak et al. (in prep.).

This chapter is structured as follows: I start off by introducing the BUFFALO survey in section 4.1 and then go into the details of our detection and selection process in section 4.2. Finally, I will talk about proposed spectroscopic follow-up observations of high-redshift galaxy candidates and one candidate detected over the course of this project in particular, in section 4.3.

4.1 The BUFFALO survey

The *Beyond Ultra-deep Frontier Fields And Legacy Observations* (BUFFALO; PIs: C. Steinhardt and M. Jauzac; Steinhardt et al., 2020) survey is a Hubble legacy program designed to expand the HST coverage of the HFF clusters (cf. section 2.3) to adjacent areas already covered by the *Spitzer* observations of the HFF program (cf. section 3.1 and Lotz et al., 2017). In the scope of the BUFFALO program, HST observed an area ×4 greater than the HFF coverage. Observing a wider area around the SL clusters mainly serves two purposes: to better model the clusters' underlying DM distributions and hence constrain the properties of DM and to increase the probability to detect rare bright and massive high-redshift galaxies, which can be observed with weaker magnification factors, taking full advantage of the existing deep wide-area *Spitzer* coverage of the HFF (Lotz et al., 2017).

The former is well motivated by recent findings that massive DM substructures far out from the cluster core significantly impact the SL models (e.g. Acebron et al., 2017; Mahler et al., 2018; Lagattuta et al., 2019) and that WL constraints observed in the cluster outskirts also significantly improve the overall lensing models (e.g. Jauzac et al., 2016; Mahler et al., 2018). Following the approach of the HFF program, the BUFFALO collaboration therefore has several teams which independently work on combining SL modeling methods in the cluster cores with WL modeling methods in the cluster outskirts imaged by the new extended HST observations (e.g. Niemiec et al., 2020). A detailed description of the various lensing analysis methods applied to BUFFALO can be found in Steinhardt et al. (2020).

For the second, the detection of $z \gtrsim 6$ galaxies, the extension in area is equally crucial: Not only will the improved lensing models potentially improve the uncertainties of the magnification factors (cf. sections 3.2.2 and 3.5.2), but observing a larger area will also increase the numbers of detected high-redshift galaxies. Indeed, while BUFFALO increases the observed area in the *lens plane* by a factor 4 compared to the HFF, the actual gain in total area observed in the *source plane* is of the order of 15× that of the HFF (cf. Fig. 5.5) due to the distortions induced by gravitational lensing. I will discuss the gains in effective source plane area and their impact in detail in section 5.2.2. While this is mostly limited to moderate magnification factors $\mu \lesssim 4$ (cf. Fig. 5.5 and section 5.2.2), we expect to increase the numbers of newly detected high-redshift galaxies by a factor 2 with the new BUFFALO observations, in particular towards the massive end and the $z \sim 8-10$ range (Steinhardt et al., 2020). In addition to that, the BUFFALO WFC3 coverage of the clusters is designed to match the JWST/NIRSpec (cf. section 6.2) field-of-view which makes the BUFFALO survey ideally suited to provide high-redshift targets for NIRSpec follow-up observations.

Of course there are also other science goals to BUFFALO such as e.g. the study of ICL and detections of SNe and other transients. I refer the reader to Steinhardt et al. (2020) for a detailed description of the various science projects conducted by the BUFFALO collaboration. The observations of the BUFFALO program were completed in the first half of 2020 and all the data are currently internally available to the collaboration. The

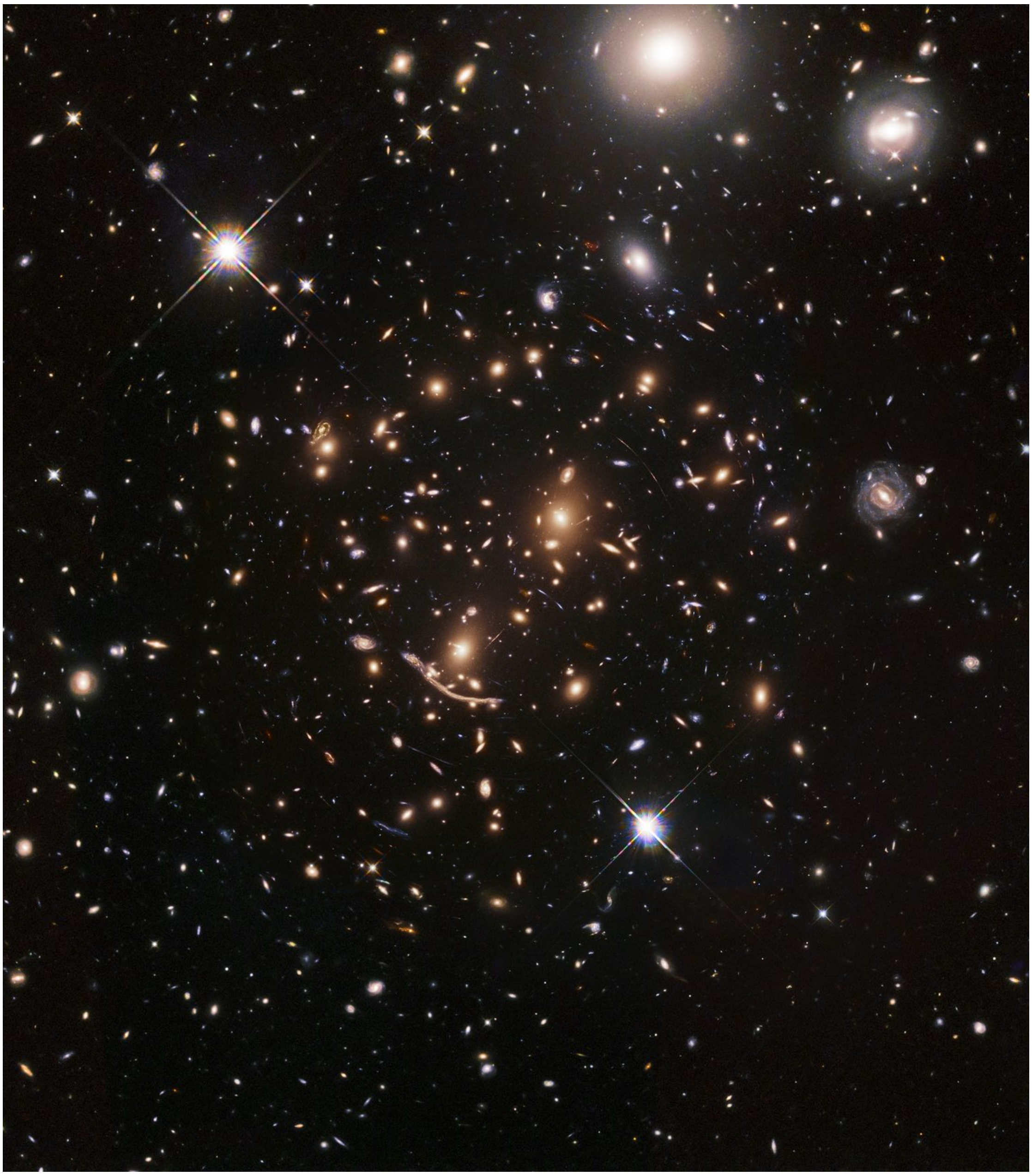

Figure 4.1: Color-composite image of the first BUFFALO cluster, A370. The field-of-view of BUFFALO covers 4× the area of the HFF field-of-view shown in the lower right panel of Fig. 2.9. Figure credit: NASA, ESA, A. Koekemoer, M. Jauzac, C. Steinhardt, and the BUFFALO team.

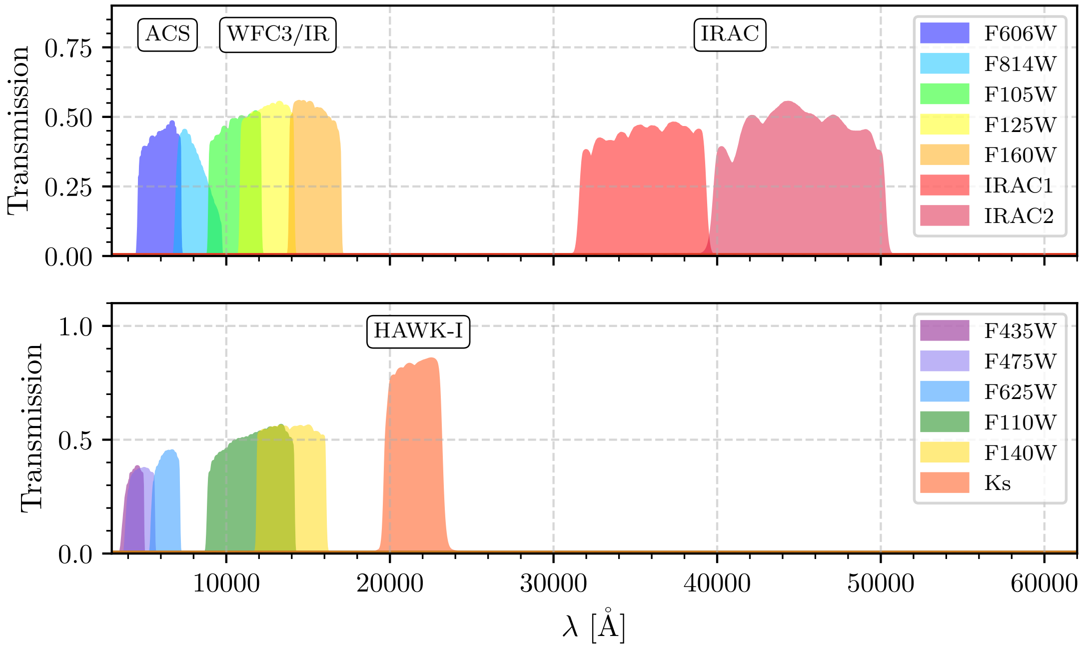

Figure 4.2: Filter transmission profiles for all filters used in this work on A370. The *upper panel* shows the filters that are available for all six BUFFALO clusters and cover the whole BUFFALO area. Ancillary filters available only for some clusters or not covering the whole BUFFALO area such as e.g. the HFF date in the F435W, F140W and Ks bands (cf. section 3.1) are shown in the *lower panel*.

full BUFFALO view of the first cluster, A370, can be seen in Fig. 4.1 (in comparison to the HFF view in the lower right panel of Fig. 2.9). All data and data products such as catalogs and SL models of BUFFALO will be released to the public once all the SL analyses are complete.

4.2 Photometric high-redshift galaxy catalog

General galaxy catalogs and associated data products (PSFs, ICL maps, etc.) in BUFFALO are produced by Pagul et al. (in prep.) based on the methods and pipelines developed for the HFF (Pagul et al., 2021). Complementary to that work, we here build a photometric catalog of $z \sim 6-10$ candidates in BUFFALO using detection and selection methods optimized for high-redshift galaxies. We use and test the pipelines developed for this work on the first BUFFALO cluster, A370 in this section. Once the final $z \sim 6-10$ catalog of A370 is ready for release, we will run the same pipelines on the other five clusters.

4.2.1 Data

For BUFFALO, each of the six HFF clusters was observed for a total of 16 orbits, covering both the main cluster and the parallel field with both ACS and WFC3 (cf. Fig. B.1). The clusters were imaged in five broad-band filters (cf. top panel of Fig. 4.2): F606W and F814W on ACS, and F105W, F125W and F160W on WFC3/IR. For this work, we use the full-depth mosaics of the BUFFALO survey which include all existing HST data of A370 and were produced using updated versions of the pipelines described in Koekemoer et al. (2011). In addition to the new BUFFALO data, existing HST observations of A370 also include the HFF mosaics in the F435W and the F140W bands as well as ancillary data sets in the F475W, F625W and F110W bands. While we use all of these data in our analysis, only the five BUFFALO filters cover the full extended area around the cluster core and the HFF parallel field. Since these final BUFFALO mosaics include all HST data ever taken of A370, they represent the deepest HST images ever made of this cluster. The final BUFFALO mosaics for this cluster were released internally to the BUFFALO team in 2019 and the full set of mosaics of all six BUFFALO clusters was released in 2020. Note that due to the design of the BUFFALO survey, the areas of the mosaics already observed in the HFF, i.e. the cluster cores and the HFF parallel fields, are deeper than the newly observed outskirt regions as can be seen in Fig. B.2 in appendix B. Throughout this work we will therefore refer to the deeper central region of the BUFFALO field-of-view as the *inner* field and to the shallower region corresponding to the new area observed with BUFFALO as the *outer* field (cf. Fig. B.2).

In addition to the HST data, we of course have the *Spitzer* observations of the HFF in the IRAC1 and IRAC2 bands and the ground-based Ks images of the HFF that I already introduced in section 3.1 at our disposal. While the *Spitzer* data easily cover the whole BUFFALO area at uniform depth, the Ks-band images (cf. section 3.1) only cover part of the BUFFALO main and parallel field of each cluster. The transmission curves of each filter used for this catalog are shown Fig. 4.2.

4.2.2 Photometry

We detect objects and measure their photometry in BUFFALO by adapting the methods used in the HFF (cf. section 3.1.1) to the new set-up. The HST mosaics are first PSF-matched to the F160W PSF using empirical PSFs. The PSFs were measured separately for the inner and outer fields in each band by Pagul et al. (in prep.). We therefore take this spatial variance of the PSF into account for the convolutions. The PSF-matched mosaics are then filtered with a $2'' \times 2''$ median filter to remove bright cluster galaxies and ICL. A comparison between an original WFC3 mosaic (the F125W band in this case) and the corresponding PSF-matched and ICL-corrected mosaic can be seen in Fig. 4.3.

For source detection and photometry we use `SExtractor` in dual mode with a stack of foreground-subtracted WFC3 images as the detection and the original mosaics as the photometry image in each filter. In order to account for the redshift evolution of the Lyman break (cf. section 2.1.1) over the $z \sim 6-10$ range, we run the `SExtractor` for each band on three detection stacks, each optimized to detect sources in a specific redshift

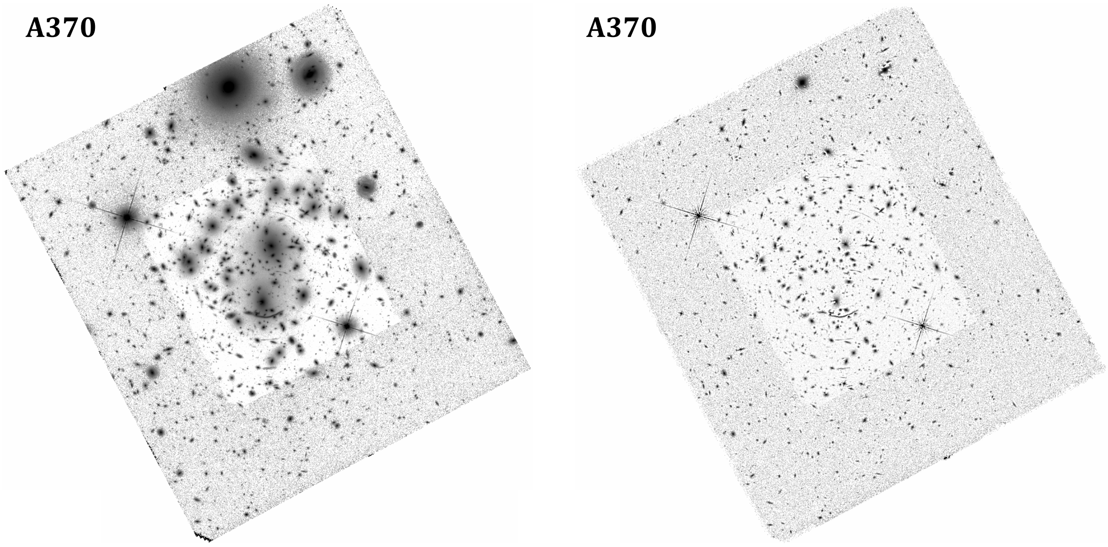

Original mosaic

Foreground-subtracted

Figure 4.3: *Left*: BUFFALO F125W mosaic cutout of the A370 cluster field (cf. Fig. B.2). *Right*: Same image, PSF-matched to the F160W PSFs and foreground-subtracted with a $2'' \times 2''$ median filtered image to remove cluster galaxies and ICL.

window: F105W+F125W+F160W for $z \sim 6-7$ detection, F125W+F160W for $z \sim 8-9$ detection and just the (foreground-corrected) F160W image for $z \sim 10$ detection. In order to take into account the fact that the observations in the outer field are shallower and much less crowded than in the inner field, we perform each of the above runs twice, optimized for detection in the inner and the outer fields respectively. A detailed example of one of our `SExtractor` setups and the different parameters used for the different runs are presented in appendix B.2. The outputs are then merged according to the position of each source in the inner or outer field, yielding a final sample of 14309 sources in A370 and its parallel field with photometry in each HST band. Note that since the BUFFALO mosaics contain both the cluster and the parallel field, we do not need to perform an additional run for the parallel field.

Because of the larger PSF and the lower spacial resolution of the *Ks* and *Spitzer*/IRAC observations (hereafter referred to as IR-bands as previously) and because, as a galaxy cluster, A370 is a naturally crowded field, blending with foreground objects in the IR-bands is a non-negligible effect for high-redshift stellar mass measurements (cf. sections 3.1.2, 3.2.3 and 3.5.1). Following what we did for the HFF in section 3.1.2, we therefore again use the `photutils` package to measure the photometry of each object in a circular aperture of fixed diameter, subtract a local background estimated in a circular non-adjacent annulus, also of fixed diameter, around the source and finally account

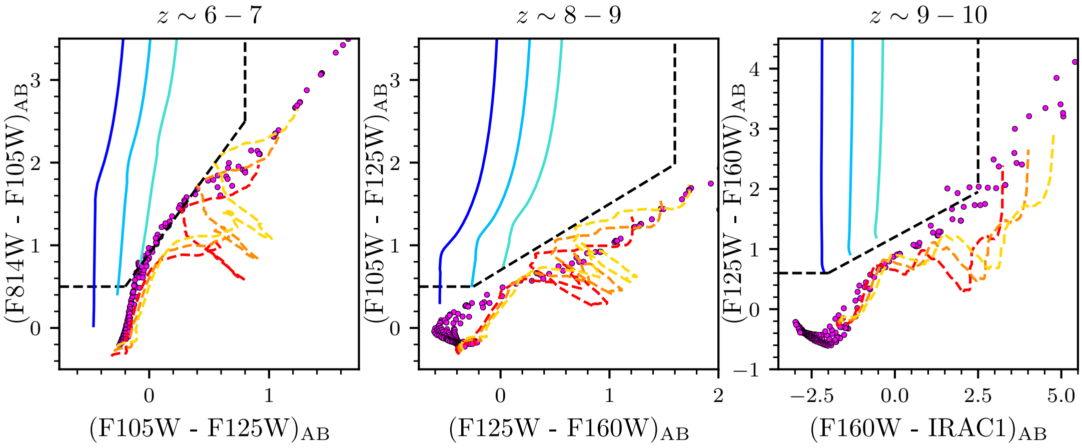

Figure 4.4: Color-color space for the BUFFALO HST bands used to select high-redshift candidates. *Left:* $z \sim 6-7$ selection (4.1), *middle*: $z \sim 8-9$ selection (4.2), *right*: $z \sim 9-10$ selection (4.3). The blue solid lines represent the redshift evolution of a star-forming galaxy template generated with `BEAGLE` (cf. section 3.2) and the red/orange dashed lines a quiescent galaxy template generated with `GRASIL` (Silva et al., 1998). Both templates were processed through IGM attenuation curves by Inoue et al. (2014). The declinations blue to turquoise and red to yellow respectively represent the application of SMC-like dust extinction with $A_V = [0.0, 0.25, 0.5]$. The purple dots represent cold M-class star and brown dwarf templates by Chabrier et al. (2000); Allard et al. (2001).

for the PSF by applying an aperture correction factor. The aperture diameters and correction factors can be found in Tab. 3.2.

4.2.3 High-redshift candidate selection

With the photometry in hand, we color-select samples of $z \sim 6-10$ galaxies using the isophotal magnitudes (`MAG_ISO`) estimated by `SExtractor` and Lyman-break criteria (cf. section 2.1) similar to previous studies in the HFF (cf. e.g. section 3.1.1 and e.g. Atek et al., 2015a, 2018; Ishigaki et al., 2018; Kawamata et al., 2018). These criteria are

$$\begin{aligned}(I_{814} - Y_{105}) &> 0.5\\ (I_{814} - Y_{105}) &> 0.9 + 2.0(Y_{105} - J_{125})\\ (Y_{105} - J_{125}) &< 0.8\end{aligned} \tag{4.1}$$

for $z \sim 6-7$ candidates,

$$\begin{aligned}(Y_{105} - J_{125}) &> 0.5\\ (Y_{105} - J_{125}) &> 0.7 + 0.8(J_{125} - H_{160})\\ (J_{125} - H_{160}) &< 1.6\end{aligned} \tag{4.2}$$

for $z \sim 8-9$ candidates and

$$\begin{aligned}
&(J_{125} - H_{160}) > 0.6 \\
&(J_{125} - H_{160}) > 1.2 + 0.3(H_{160} - \mathrm{IRAC1}) \\
&(H_{160} - \mathrm{IRAC1}) < 0.8
\end{aligned} \tag{4.3}$$

for $z \sim 10$ candidates. We derived these criteria using the redshift evolution of mock low-metallicity star-forming galaxies generated with `BEAGLE` (cf. section 3.2) which can be seen in Fig. 4.4. In case of a 2σ non-detection in the F814W band for (4.1), the F105W band for (4.2) and the F125W and IRAC1 bands for (4.3), we respectively assume a 2σ flux for the color-selection. Our $z \sim 10$ color-selection (4.3) is similar to what has been done in blank-field analyses conducted by e.g. Oesch et al. (2014) and Bouwens et al. (2015) though we allow for a less pronounced Lyman break, down to $(J_{125} - H_{160}) > 0.6$, in order to be sensitive to $z \sim 9$ objects that could have been missed by the $z \sim 8-9$ selection (4.2). Indeed, since we are missing the F140W band over most of the outer field, we are not able to cleanly differentiate between the $z \sim 8$ and $z \sim 9$ dropouts as was done in e.g. Atek et al. (2015a) or Kawamata et al. (2018). Instead we perform a joint $z \sim 8-9$ selection (4.2) that becomes less efficient for $9.1 \leq z < 9.5$ objects whose Lyman break moves towards the (upper) edge of the F125W band. We therefore rely on the $z \sim 9-10$ color-criteria (4.3) to cover the high-redshift end of the $z \sim 9$ sample. Note that since our IRAC photometry was measured in circular apertures (cf. section 4.2.2), we do *not* use isophotal F160W magnitudes to compute the $(H_{160} - \mathrm{IRAC1})$ colors in (4.3) but rather total magnitudes, i.e. `MAG_AUTO`, in F160W and aperture corrected magnitudes in IRAC1 (cf. sections 3.1.2 and 4.2.2 and Tab. 3.2).

In addition to the color-selection criteria (4.1)-(4.3), the dropout objects must satisfy a number of detection and *non*-detection criteria to be selected as high-redshift candidates following previous studies (e.g. Atek et al., 2015a; Kawamata et al., 2018): a 5σ detection criterion in each of the F125W and the F160W bands for the $z \sim 6-7$ candidates, 3σ each in F125W and F160W for $z \sim 8-9$ candidates and $3.\sigma$ each in the F160W and IRAC2 bands for $z \sim 9-10$ candidates. The latter is important because the Balmer/4000 Å break (cf. section 2.4.2) falls between the two IRAC bands at $z \gtrsim 9$. Since at these redshifts the Lyman break falls close to the upper edge of the F125W bandpass or even into the F160W band, there is no further HST filter red-ward of the break to probe the UV continuum slope. We therefore need the constraint on the Balmer break provided by the IRAC1-IRAC2 color in order to be able to fit photometric redshifts. Finally, to help rule out low-redshift interlopers we apply a non-detection criterium to all bands blue-ward of the Lyman break, i.e. 2σ in the F606W band for $z \sim 6-7$ candidates, 1.41σ in a stack of F606W+F814W for $z \sim 8-9$ candidates and 1.15σ in a stack of F606W+F814W+F105W for $z \sim 9-10$. Note that we will test all of these color and detection/non-detection criteria and our overall selection function with the simulations described in section 5.2.

It has nevertheless been found that color-selection and detection/non-detection criteria alone still leave high-redshift samples prone to significant contamination by red low-redshift galaxies (Bouwens et al., 2011). We therefore refine our selection in a last step by fitting photometric redshifts with the SED-fitting code `LePhare` (Arnouts et al., 2002; Ilbert et al., 2006) using the same configuration and galaxy templates as were used for the COSMOS catalogs (Ilbert et al., 2013; Laigle et al., 2016; Weaver et al., 2021). We then select all galaxies with

$$\begin{aligned} z_{\mathrm{phot}} &\geq 5.5 \\ \frac{\chi^2_{\mathrm{min}}}{N_{\mathrm{bands}}-1} &< 10 \end{aligned} \tag{4.4}$$

where z_{phot} corresponds to `LePhare`'s `z_ML` output parameter, i.e. the median redshift of the probability distribution, N_{bands} to the number of bands used in the fit and χ^2_{min} to the best-fitting residual. The second criterium in particular ensures that `LePhare` provides a reasonable fit. Note that we use isophotal fluxes to fit the photometric redshifts and only use the HST fluxes for the photometric redshifts.

Before computing the photometric redshifts however, we visually inspect our selected objects in order to clean the catalog from any spurious detections and to determine if they are blended in the IR-bands. To that end we assign each object a flag ('golden', 'silver' or 'blended') in each IR-band following the procedure employed in Furtak et al. (2021) (discussed in section 3.1.2). Again, we do not use the IR-band photometry of blended objects in any analysis from here on even though it is included in the final catalog (cf. section 4.2.4).

4.2.4 Catalog release versions

The BUFFALO high-redshift galaxy pipeline described in the previous sections went through several stages of development and improvement and is still an ongoing project. We released a first version of the A370 BUFFALO $z \sim 6-10$ galaxy catalog internally to the BUFFALO team in February 2021 which did however not yet contain the results of the final pipeline. The changes made since then are mostly due to the technical constraints and requirements of the completeness simulations developed in chapter 5. I will describe the current version and ongoing improvements in the following.

Current version — v1.0 release

The first version of the A370 BUFFALO $z \sim 6-10$ galaxy catalog differs from the final pipeline presented in sections 4.2.1, 4.2.2 and 4.2.3 in two main points: The foreground subtraction and the computation of photometric redshifts. Instead of the median filter foreground subtraction, we used BCG and ICL models provided by A. Pagul and computed with the same methods as used in Pagul et al. (2021) to subtract the cluster foreground. We however found these to slightly over-subtract the foreground in some areas and thus suppress some of the faintest high-redshift sources in addition to being inefficient to reproduce in each iteration of the completeness simulations (cf. section 5.2.3).

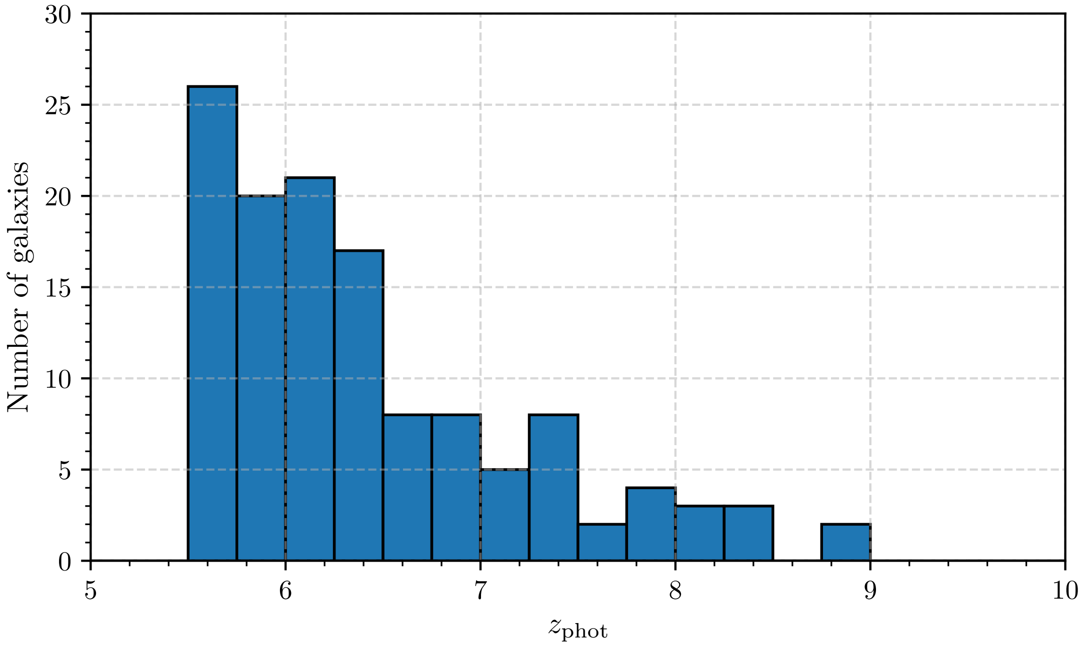

Figure 4.5: Distribution of photometric redshifts ($z_{\rm MAP}$, computed with `BEAGLE`) of the v1.0 release of our BUFFALO $z \sim 6-10$ candidate catalog in A370 and its parallel field.

The photometric redshifts were computed with `BEAGLE` in this version. Since `BEAGLE` provides a full posterior probability density function (PDF), we refined our color-selection with the following criteria

$$\begin{aligned} z_{\rm MAP} &\geq 5.5 \\ \int_{z_{\rm MAP}-1}^{z_{\rm MAP}+1} p(z) dz &\geq 0.6 \end{aligned} \tag{4.5}$$

in which $z_{\rm MAP}$ is the maximum-a-posteriori photometric redshift (i.e. the peak redshift) and $p(z)$ the (normalized) redshift PDF. The first criterion in (4.5) ensures that the peak of the redshift distribution lies in our target $z \gtrsim 6$ range and the second criterion makes sure the primary peak is the dominant solution. Unfortunately, `BEAGLE` has relatively long computation times compared to e.g. `LePhare` which proved impractical for the very large numbers of objects in the completeness simulations (cf. section 5.2.3). We therefore switched to the faster code for the final pipeline.

This release of the catalog contains a total of 127 high-redshift candidates: 113 $z \sim 6-7$ candidates and 14 $z \sim 8-9$ candidates (cf. Fig. 4.5). In addition to the isophotal and total photometry in 13 bands (cf. Fig. 4.2), the catalog contains the photometric redshifts computed with `BEAGLE`, the probabilities used in (4.5), gravitational magnifications μ and

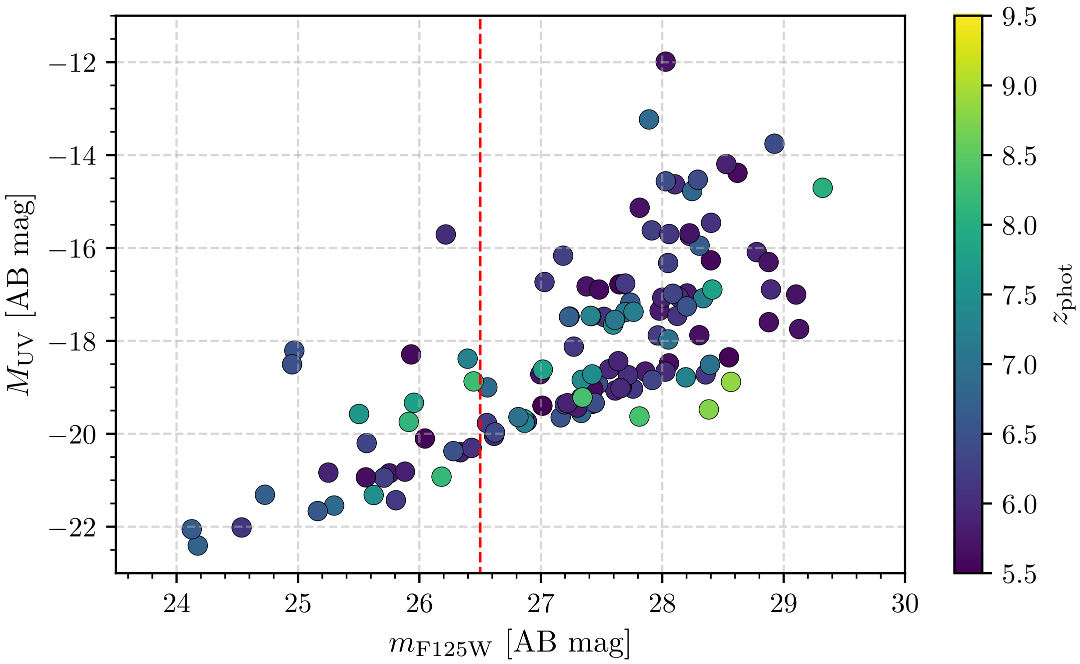

Figure 4.6: Rest-frame UV luminosity distribution of the v1.0 release of our BUFFALO $z \sim 6 - 10$ candidate catalog in A370 and its parallel field as a function of observed F125W-band magnitude. The red dashed line marks $m_{\mathrm{F125W}} = 26.5$ which roughly corresponds to the 'limit of observability' with the most sensitive ground-based NIR spectrographs such as e.g. X-SHOOTER on VLT (cf. section 4.3.1). The limit of 26.5 magnitudes is estimated for a 5σ detection of Lyα using the ESO VLT/X-SHOOTER exposure time calculator in the same manner as for our spectroscopic follow-up proposal (cf. section 4.3.1). The details can be found in the attached proposal in appendix B.3.

their uncertainties $\Delta\mu$ computed with the CATS model of A370[1] (cf. section 5.2.2) and rest-frame UV luminosities (cf. Fig. 4.6) computed with equation (1.22). Note that this version does not contain the blending flags for the IR-photometry yet.

Improved version — planned v2.0 release

The planned second release of our high-redshift candidate catalog will then contain the results of the finalized pipeline, including the IR-photometry flags, more accurate uncertainties on the HST fluxes (cf. appendix B.2 for details) and physical parameters such as $M_\star$ obtained through SED-fitting with `BEAGLE` in configurations similar to the delayed SFH case presented in Tab. 3.3 and section 3.2. We also plan to include more information regarding the gravitational magnification factors in this release: individual magnifications computed from the new BUFFALO SL models of the cluster (cf. section 5.2.2) for each

---

[1] The v4.0 CATS model of A370 by Lagattuta et al. (2017) is available on the `MAST` archive at `https://archive.stsci.edu/pub/hlsp/frontier/abell370/models/cats/v4/`

galaxy, their uncertainties a weighted average magnification μ over all available models and its uncertainty $\Delta\mu$. The latter will consist of the statistical uncertainties (one for each model) *and* the scatter between the models summed in quadrature. We thus assure that μ and $\Delta\mu$ take into account *both* the systematic and statistical SL uncertainties in a concise way and accurately represent *all* the SL information available for each source. Finally, we will also include average magnification factors for objects in the parallel field computed from the Merten SL maps[2] which are large enough to cover the A370 parallel field.

4.3 Spectroscopic follow-up observations

As was mentioned in chapter 2, once *detected* in deep space-based imaging, it is possible to observe high-redshift galaxies with ground-based spectrographs. Part of our work on HFF and BUFFALO high-redshift galaxy catalogs is therefore also to identify promising candidates for spectroscopic follow-up observations and to prepare the corresponding proposals. A particularly promising candidate and our proposed observations are described in section 4.3.1.

We have furthermore submitted a proposal for a VLT large program called *BUFFALO Wide-area INtegral-field Galaxy Survey* (BUFFALO-WINGS; PI: D. Lagattuta) with the goal to cover the whole BUFFALO area of five out of the six clusters (the ones observable from the southern hemisphere) with the *Multi Unit Spectroscopic Explorer* (MUSE; Bacon et al., 2010). MUSE is able to detect Lyα out to $z = 6.7$. This means that it is possible that this program can confirm some of the brighter candidates in our $z \sim 6-7$ sample. We will therefore also crossmatch our high-redshift catalogs (cf. section 4.2) with the MUSE results if and when they are available.

4.3.1 A primeval galaxy under the microscope

Over the course of our work on the HFF and BUFFALO, we have identified a particularly interesting intrinsically faint $z \sim 8$ galaxy candidate in A370 which benefits from a particularly high gravitational magnification. The source presents a Lyman break of $(F105W - F125W)_{\mathrm{AB}} = 0.85$ and a slight excess in the IRAC2 band, typical indicators for a $z \sim 8$ galaxy whose optical [O III]λ5007 Å and Hβ emission features are redshifted to IRAC2 wavelengths (cf. section 2.4.2; Smit et al., 2014, 2015; De Barros et al., 2019; Endsley et al., 2021). This source is observed at an F160W band magnitude of $m_{F160W,AB} = 25.24$ and most recent SL models of A370 (e.g. Strait et al., 2018; Lagattuta et al., 2019) yield gravitational magnification factors of order $\mu \gtrsim 8$ for $z_s = 8$ at the source's coordinates. This means this source is intrinsically faint with a de-lensed relative F160W band magnitude of $m_{F160W,\mathrm{AB}} = 27.50$ and an absolute rest-frame UV magnitude of $M_{\mathrm{UV,AB}} = -19.5$. An SED fit with `BEAGLE` yields very tight constraints on

---

[2] A hybrid very low resolution SL+WL model computed with `SaWLens` (Merten et al., 2009, 2011) available on the `MAST` archive at `https://archive.stsci.edu/pub/hlsp/frontier/abell370/models/merten/v1/`

the photometric redshift, with an estimate of $z \simeq 7.78 \pm 0.05$ and a stellar mass estimate of $\log\left(\frac{M_\star}{\mathrm{M}_\odot}\right) \simeq 8.60^{+0.12}_{-0.24}$ (cf. Fig. 4.7).

To date there are only five galaxies confirmed at $z \sim 8$ (Finkelstein et al., 2013; Oesch et al., 2015; Song et al., 2016b; Laporte et al., 2017; Tamura et al., 2019). All of them were either observed in blank fields or have relatively low gravitational magnification factors $\mu \lesssim 2$. They are therefore intrinsically bright ($M_{\mathrm{UV}} \lesssim -20$) and relatively massive ($M_\star \gtrsim 10^9\,\mathrm{M}_\odot$) and thus constitute an unrepresentative sample of galaxies at high redshift (cf. section 1.3.2). This object on the other hand is intrinsically too faint to be spectroscopically observed in a blank field and therefore constitutes a unique probe of low-mass galaxies at high redshift. Its study across observable wavelengths has the potential to yield invaluable insight into the physics of typical galaxies in the EoR.

We have therefore prepared proposals for the following observations:

Redshift confirmation — Accepted X-SHOOTER program

In this first program, we proposed to use the X-SHOOTER spectrograph on ESO's VLT (Vernet et al., 2011) to detect the Lyα emission line and possibly the [C III]λ1909 Å and [C III]λ1907 Å emission line doublet of our $z \sim 8$ candidate, A370-20021. The main science objectives of this program are the following:

- To accurately determine the redshift of this $z \sim 8$ galaxy candidate and thus to confirm its high-redshift nature. If confirmed, this galaxy will add to the scarce numbers of known $z \sim 8$ galaxies and present a valuable target for future generations of telescopes, especially given its uniquely high magnification factor. Note that a precise measurement of the redshift will greatly improve the chances of success of our ALMA follow-up proposal detailed below.

- To investigate properties such as metallicity, stellar age and ionization parameter. As shown in Hutchison et al. (2019), the combination of [C III] equivalent widths with IRAC1-IRAC2 colors provides constraints on the physical parameters of galaxies at $z \sim 8$. These can be used to provide constraints and priors for SED-fitting methods of statistically significant photometric high-redshift catalogs in order to treat some of the degeneracies inherent to estimating these parameters from broad-band photometry alone (cf. section 3.5.3).

- To measure this galaxy's Lyα velocity offset ($\Delta v_{Ly\alpha}$) from its systemic redshift, inferred with the [C III] lines, which can provide valuable insight into the kinematics and the Lyα escape fraction (e.g. Hutchison et al., 2019). Constraints on the Lyα escape fraction have important implications on the ionizing power of low-mass high-redshift galaxies and their ability to reionize the Universe.

This program has been accepted in ESO Period 108 and the observations were carried out from November 13 to 15, 2021. For more details, we refer the reader to the original proposal document attached in appendix B.3.

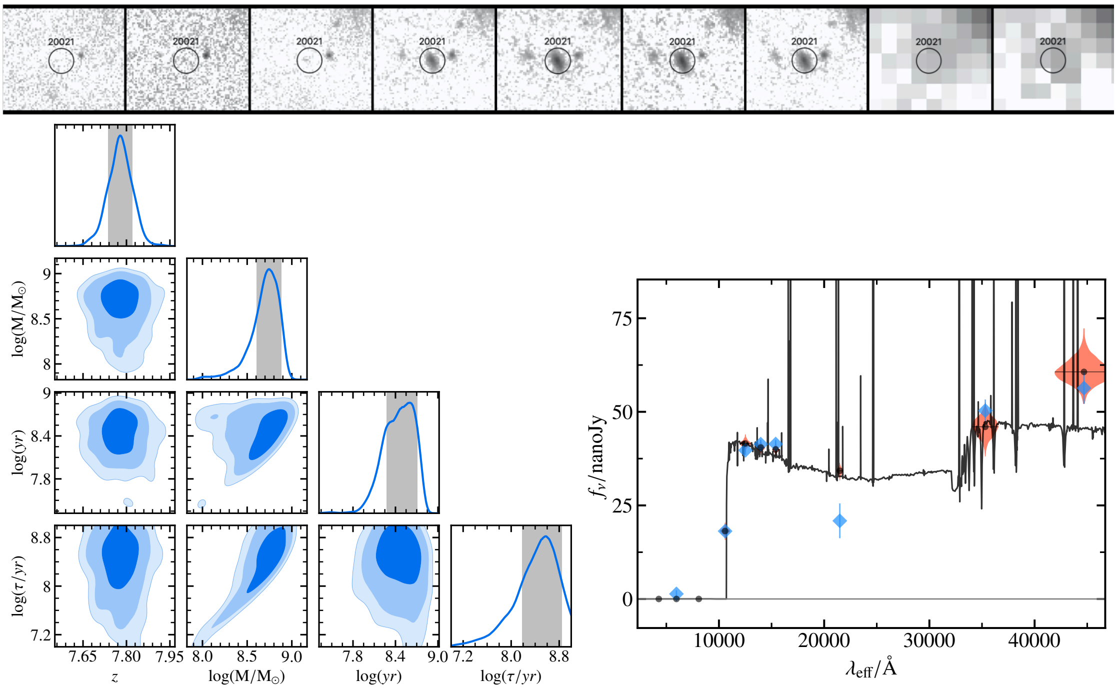

Figure 4.7: *Top panel*: Image cutouts of the $z \sim 8$ dropout candidate A370-20021. From left to right: F435W, F606W, F814W, F105W, F125W, F140W, F160W, IRAC1 and IRAC2. The source is clearly detected in the WFC3/IR bands but shows no detection at the 2σ-level in bands blueward of the break (i.e. the ACS bands). It also shows a slight excess in the IRAC band, a typical feature of galaxies at $z \sim 8$ (e.g. De Barros et al., 2019). The black circle has a diameter of 1”. *Lower left panel*: Posterior distributions of the four fit-parameters (photometric redshift z, stellar mass M, maximum stellar age and star-formation e-folding time τ) in our SED-fit of A370-20021 with `BEAGLE`. *Lower right panel*: Observed spectral energy distribution of the $z \sim 8$ dropout candidate A370-20021 (blue diamonds); maximum-a-posteriori SED predicted by `BEAGLE` (black curve); marginal posterior distribution of fluxes in each band predicted by `BEAGLE` (salmon ‘violins’, with the black circle in each violin representing the posterior median of the predicted flux).

Planned ALMA proposals

Our $z \sim 8$ candidate A370-20021 is bright enough for ALMA follow-up targeted at its rest-frame *far infrared* (FIR) emission. Since high-redshift galaxies are usually only observed in the rest-frame UV range which is heavily affected by dust extinction (cf. section 2.4.1), rest-frame FIR observations with ALMA provide a complementary window to probe galaxy gas and dust physics. For example, the [C II]λ158 µm emission line in particular represents a major coolant-line in high-redshift galaxies and thus encodes valuable physical information about molecular cloud physics in the transition from warm to cold ISM. I will come back to a brief review of high-redshift FIR observations in section 6.3.

We therefore plan to prepare and submit proposals for low-resolution detection experiments of rest-frame FIR emission lines such as e.g. [C II]λ158 µm, [O III]λ88 µm, [O III]λ52 µm and [O I]λ63 µm, but also dust continuum in our $z \sim 8$ candidate with ALMA. These will allow to further constrain star-formation and dust physics at $z \sim 8$ (e.g. Laporte et al., 2017; Tamura et al., 2019; Bakx et al., 2020). In addition, since A370-20021 is almost resolved on HST imaging (cf. Fig. 4.7) due to its high magnification factor, the extended nature of FIR gas emission (Bakx et al., 2020) compared to compact UV emission might enable us to spatially resolve this source with very high-resolution ALMA observations after we have determined its redshift as has recently been achieved for two sources at $z \sim 7$ (Smit et al., 2018). Such a program could potentially deliver the first resolved image of a $z \sim 8$ galaxy and enable the study of its internal structure.

Chapter 5

Stellar mass completeness simulations

> "His job was to make sense of the world, and there were times when he wished that the world would meet him halfway."
>
> Sir Terry Pratchett, *Snuff*, 2011

To date, all high-redshift GSMF measurements heavily rely on a relation between rest-frame ultra-violet (UV) luminosity M_{UV} and stellar mass $M_\star$, either by using the mass-luminosity relation to convert UV luminosity functions to GSMFs (Song et al., 2016a; Kikuchihara et al., 2020; Furtak et al., 2021) or by using UV-magnitude inferred completeness and survey volumes to compute the GSMF (Duncan et al., 2014; Grazian et al., 2015; Bhatawdekar et al., 2019; Stefanon et al., 2021b). This is the common approach because completeness and selection effects are well known and can easily be quantified for UV luminosity (cf. discussion in Song et al. (2016a)) whereas the stellar mass is model-dependent (cf. sections 2.4.2 and chapter 3). As was shown in Furtak et al. (2021), in chapter 3 of this work though, high-redshift $M_{\mathrm{UV}} - M_\star$-relations are prone to significant biases and uncertainties due to modeling assumptions and parameter degeneracies. Completeness in $M_\star$ is therefore not necessarily the same as completeness in M_{UV}. Robust estimates of the high-redshift GSMF and in particular its uncertainties need to take this model dependence of $M_\star$ into account in order to well constrain the $z > 6$ GSMF. These methods will be particularly valuable for future surveys with the upcoming JWST and their unprecedented high-redshift galaxy observing capabilities.

In an attempt to address this last fundamental assumption of high-redshift GSMF measurements, that UV luminosity completeness and stellar mass completeness are equivalent, the final project of my thesis, related in this chapter, consists in developing methods to directly compute the high-redshift GSMF in a robust way without relying on the UV luminosity function and thus without the uncertainties and biases inherent to the $M_{\mathrm{UV}} - M_\star$-conversion. To that end, we developed new completeness simulation methods

that allow us to directly estimate the stellar mass completeness of lensed $z \gtrsim 6$ galaxy samples. These simulations will for the first time combine the effects of SL systematics due to different SL modeling techniques, selection effects and the model dependence of stellar mass in order to produce the most complete and robust estimate of the uncertainties. We plan to test these methods by applying them to the sample of $z \sim 6-7$ galaxies detected in the BUFFALO A370 cluster field described in chapter 4. Note that this is an ongoing project that will be published in Furtak et al. (in prep.).
This chapter is structured as follows: I briefly review the theory of estimating completeness and survey volumina in section 5.1 before describing our galaxy modeling and completeness simulation techniques in section 5.2. Finally, I present the current state of the project and the preliminary results in section 5.3.

5.1 A brief review of survey volumes and completeness

As defined in equation (1.19), the GSMF measures the co-moving volume density of galaxies as a function of $M_\star$. In order to compute the GSMF from the number N of galaxies in a statistical sample, e.g. our A370 $z \sim 6-7$ galaxy catalog (cf. chapter 4), we therefore need the volume of space observed by the survey and a measure of the *completeness*, i.e. the fraction of objects missed by the survey. There are many methods to construct survey volumina and GSMFs (for an overview cf. e.g. Johnston, 2011; Weigel et al., 2016). I will here focus on the approach that is most popular for high-redshift GSMFs and that we use in our analysis, the $1/V_{\mathrm{max}}$ method presented below.

5.1.1 The $1/V_{\mathrm{max}}$ method

With the $1/V_{\mathrm{max}}$ method (Schmidt, 1968), the GSMF is constructed by weighting each galaxy by the maximum volume V_{max} that it can be observed in given its redshift and the depth of the survey. This naturally corrects for the fact that faint low-mass galaxies can only be detected in a small volume whereas more massive and brighter galaxies can be detected in a larger volume, the so-called Malmquist bias (Malmquist, 1920, 1922). In the $M_\star$-bin i that contains N_i galaxies, the GSMF (1.19) is then given as

$$\phi_i \mathrm{d}M_\star = \sum_j^{N_i} \frac{1}{f(M_{\star,j})V_{\mathrm{max},j}} \tag{5.1}$$

where $f(M_{\star,j})$ is the probability to observe the $j$eff galaxy in the bin, i.e. the selection function. The maximum volume is computed by integrating equation (1.20) from z_{min}, the lower boundary of the redshift bin, to $\min(\mathrm{z_{max}}, \mathrm{z_{max}^{M_{\star,j}}})$ where z_{max} is the upper bound of the redshift bin and $z_{\mathrm{max}}^{M_{\star,j}}$ is the maximum redshift at which object j can be observed based on its stellar mass and the mass completeness of the sample. Note that the denominator in equation 5.1 can be seen as the geometrical survey volume (1.20) *distorted* by the survey depth and selection effects. With this so-called *effective* survey volume V_{eff}, the GSMF in equation (5.1) reads

$$\phi_i \mathrm{d}M_\star = \sum_j^{N_i} \frac{1}{V_{\mathrm{eff},j}} \tag{5.2}$$

for the ith stellar mass bin. The difficulty here of course lies in computing the stellar mass completeness and sample selection function for which completeness simulation such as presented in section 5.2 are required. In addition, since we are observing our high-redshift galaxies through SL clusters, we also need to take the effects of gravitational lensing into account in the completeness estimate. In order to achieve that in a robust way, we use a slightly modified version of the $1/V_{\mathrm{max}}$ method as presented in the following section.

5.1.2 The *lensed* effective survey volume

Instead of just integrating the comoving volume element (1.20) as could be done for a blank field survey, we follow the approach used in e.g. Bouwens et al. (2017b) and Atek et al. (2018) to fold the SL effects into the survey volume. The lensed effective survey volume V_{eff} can be pictured as the geometrical co-moving maximal volume V_{max} which is now distorted by both selection effects *and* gravitational lensing. This results in an effective survey volume for each galaxy as

$$V_{\mathrm{eff},j} = \int_0^\infty \int_{\mu_{\mathrm{min},j}}^\infty \left(\frac{\mathrm{d}V}{\mathrm{d}z}\right) f(M_{\star,j}, z, \mu) \mathrm{d}\Omega(\mu, z) \mathrm{d}z \tag{5.3}$$

where V is the co-moving volume defined in equation (1.20), $f(M_\star, z, \mu)$ is the selection function which depends on stellar mass, redshift and SL magnification and $\mathrm{d}\Omega(\mu, z)$ represents the surface element as a function of magnification and redshift. Note that in equation (5.3) the redshift integration limits now go from zero to infinity because we integrate over the sample selection function which means that the effective survey volume naturally accounts for boundaries of the observed redshift bin. The magnification is integrated from $\mu_{\mathrm{min},j}$, the minimum magnification required to push the jth galaxy over the detection threshold given the depth of the survey.

5.2 BUFFALO high-redshift completeness simulations

In order to compute high-redshift GSMFs in BUFFALO, we basically adapt the approach used for UV luminosity functions introduced in Atek et al. (2018) to GSMFs: We inject simulated galaxies directly into the source plane, map them into the lens plane using the SL models and then use the same detection and selection procedures as for the real data (cf. sections 4.2.2 and 4.2.3) to measure the completeness of our sample. This approach already takes into account the effects of SL systematics, source size distribution and depth of the observations (Atek et al., 2018). Our goal in this work is to include the treatment of the model dependence of $M_\star$ into the procedure such as to enable us to directly measure the survey volume as a function of stellar mass rather than UV luminosity. To achieve that, we first carefully construct a toy-model of galaxy parameters in section 5.2.1 which

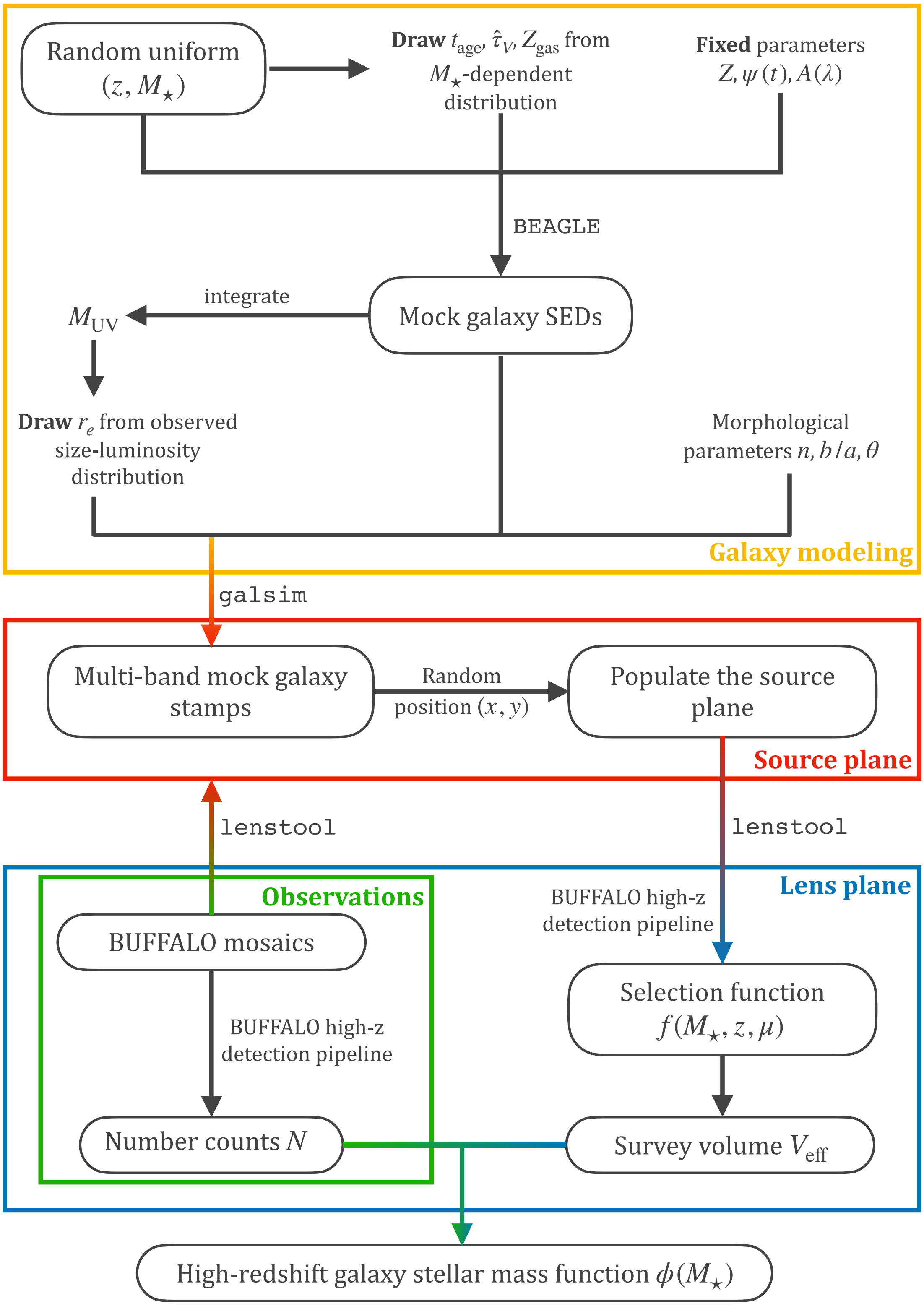

Figure 5.1: Flow-chart illustrating the work-flow of our $M_\star$ completeness simulations and high-redshift GSMF measurements.

is then processed through the simulations in sections 5.2.2 and 5.2.3 which in turn yield our selection function needed for equation (5.3). The complete work-flow of our $M_\star$ completeness simulation code and the GSMF measurements is illustrated in Fig. 5.1.

5.2.1 Simulated galaxy template parameters

For each simulated galaxy, we first draw a random stellar mass in the $M_\star$ interval that we probe $\log(M_\star/\mathrm{M}_\odot) \in [6, 11]$ and then assign a random redshift $z \in [4, 11]$. We include redshifts both lower and higher than in our observed sample in order to account for photometric redshift uncertainties and so that the simulation can be run for different redshift bins. The goal is now for $M_\star$ and z to remain the only *truly* random parameters in the galaxy simulation. To that end, the following physical parameters are linked to $M_\star$ and z:

- *Stellar age*: The most severe impact on stellar mass measurements at $z \sim 6-7$ comes from stellar age due to degeneracies with nebular emission lines in the rest-frame optical bands (Furtak et al., 2021, cf. sections 2.4.2 and A.1). We therefore again use dynamical considerations based on the galaxy's dynamical time scale t_{dyn} (3.2) to link it's stellar age to it's stellar mass: Following considerations in Verma et al. (2007) that high-redshift star-forming galaxies tend towards ages roughly $\sim 5t_{\mathrm{dyn}}$, we draw the galaxy's stellar age from a truncated log-normal distribution with $\mu = \log 5t_{\mathrm{dyn}}$ and upper and lower limits $t_{\mathrm{age}} \in [t_{\mathrm{dyn}}, t_{\mathrm{U}}(z)]$ where $t_{\mathrm{U}}(z)$ is the age of the Universe at the galaxy's redshift. The width of the distribution en-follows from how we compute the dynamical time. The details on how we link the stellar age to $M_\star$ can be found in appendix C.1.

- *Dust extinction*: Observed stellar masses and in particular mass-to-light ratios at $z \sim 6-7$ are also highly sensitive to the dust extinction (Furtak et al., 2021, cf. section 3.5.3). We therefore use stellar mass-reddening relations observed in low-redshift analogs of high-redshift galaxies by Shivaei et al. (2020) to link the effective stellar dust extinction $\hat{\tau}_V$ to the stellar mass since no such relation has been measured at high redshifts yet. We truncate this relation such that $\hat{\tau}_V \in [0, 1]$ to avoid unrealistic values. Note that this relation was measured from a sample of galaxies of relatively high stellar mass $M_\star \sim 10^{10}\,\mathrm{M}_\odot$. Extrapolating this relation down to the lowest stellar masses therefore quickly results in extremely low dust extinctions as can be seen in Fig. 5.2. This is however consistent with the expectation that high-redshift galaxies do not have significant dust extinction (e.g. Bouwens et al., 2016; Bhatawdekar & Conselice, 2021).

- *Gas-phase metallicity*: We link the gas-phase metallicity to the redshift and the stellar mass using observed redshift evolution and mass-metallicity relations from Sanders et al. (2020).

More details on the last two parameter distributions can be found in appendix C.2. In addition, we choose to *fix* the following parameters:

- *SFH*: We assume a delayed exponential SFH $\psi(t) \propto t \exp(-t/\tau)$ which has a maximum SFR at $t = \tau$ and thus allows for some flexibility in the current SFR depending on the galaxy's age. In order to avoid unrealistic combinations where an old and massive galaxy is close to its SFR-peak, which would result in extremely high emission line EWs, we choose to fix $\tau = 10^7\,\mathrm{yr}$. This roughly corresponds to the dynamical time scale of galaxies on the low-mass end (cf. appendix C.1) and therefore ensures that younger galaxies tend to be closer to their SFR-peak.

- *Stellar metallicity*: The stellar metallicity is fixed to $Z = 0.01\,\mathrm{Z}_\odot$, which is consistent with recent observations of $z \sim 6-7$ galaxies (Jeon et al., 2020). Note that metallicity has however been found to not greatly impact stellar mass measurements at $z \sim 6-7$ (Furtak et al., 2021, cf. section 3.4).

- *Dust extinction law*: We apply an SMC-like dust extinction law (Pei, 1992) which has been observed to match high-redshift galaxies best (Capak et al., 2015; Reddy et al., 2015, 2018a), in particular in the very low metallicity regime that we probe (Shivaei et al., 2020).

The physical galaxy model parameters drawn above are then passed through `BEAGLE` in 'mock-mode' (cf. Chevallard & Charlot, 2016) to generate an SED including stellar and nebular continuum and emission lines and apply the appropriate Inoue et al. (2014) IGM attenuation. We assume our simulated galaxies to have Lyα EW $= 0$ since less than 10 % of high-redshift galaxies have been found to have even moderate Lyα emission (cf. section 2.4.1; Schenker et al., 2014; Pentericci et al., 2018). All other nebular emission lines are included though. We integrate the resulting galaxy SED in the BUFFALO band-pass (cf. section 4.2.1 and Fig. 4.2) that contains 1500 Å in order to compute the UV luminosity M_{UV}. We then determine the half-light-radius of the galaxy using observed size-luminosity distributions by Kawamata et al. (2018) for $z \gtrsim 6$ galaxies and by Huang et al. (2013) for $z \sim 4-5$ galaxies to complete our simulated galaxy toy model. Note that we would ideally use an $M_\star - r_e$ distribution here but to date all available measured high-redshift $M_\star - r_e$-relations assume a model-dependent mass-luminosity relation (Bouwens et al., 2017a; Kikuchihara et al., 2020) which would introduce exactly the kind a bias that we aim to avoid in our simulations. Our method of integrating the SED to obtain a UV luminosity and using it to draw a half-light radius instead ensures that $M_\star$ and z remain the only random parameters in this analysis and the galaxy model remains consistent in every step of the simulation.

The histograms of the parameters of 50000 realizations of this galaxy model are shown in Fig. 5.2. While the mass-to-light and stellar age distributions (upper panels) are relatively broad, the main goals of preventing extremely young massive and low-mass dusty galaxies are achieved and the model at the same time allows for a broader range of dust extinction on the high-mass end. The size-luminosity distribution (lower left panel) presents a secondary 'tail' of slightly larger radii on the faint end. This is due to the fact that the Huang et al. (2013) size-luminosity relations at $z \sim 4-5$ are much shallower than the Kawamata et al. (2018) results at $z \gtrsim 6$. Atek et al. (2018) found the source size

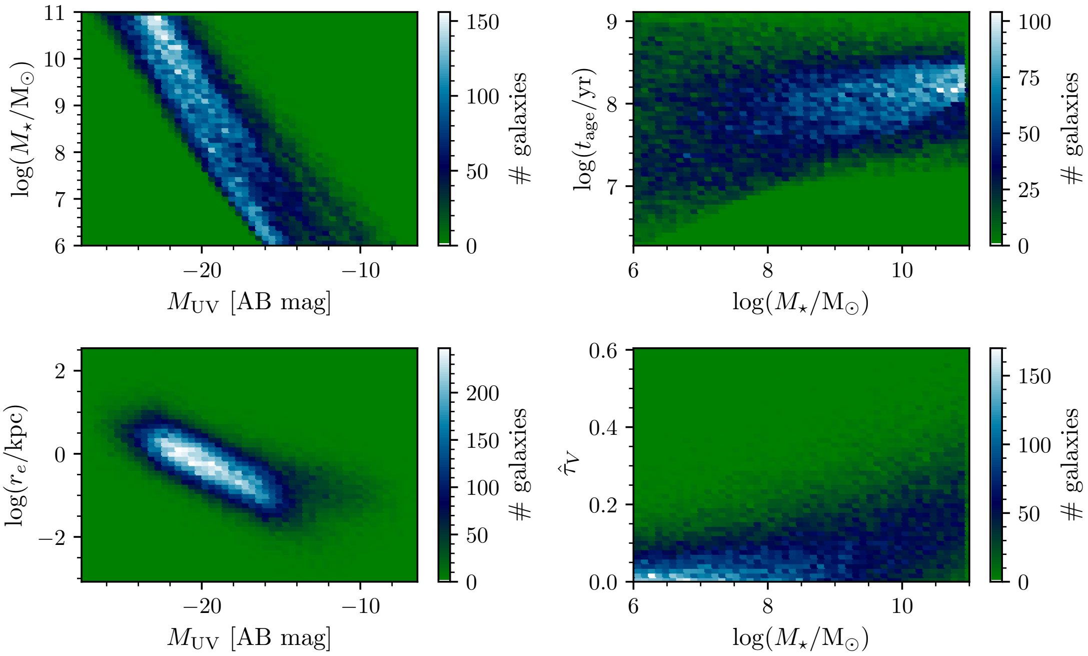

Figure 5.2: 2D galaxy parameter distributions drawn from 50000 realizations of the simulated galaxy model. *Upper left*: $M_\star - M_{\mathrm{UV}}$-relation from integrating the resulting galaxy SEDs in the band-pass containing 1500 Å. *Upper right*: $t_{\mathrm{age}} - M_\star$-relation based on dynamical considerations detailed in appendix C.1. *Lower-left*: $r_e - M_{\mathrm{UV}}$-relations based on observations by Kawamata et al. (2018) and Huang et al. (2013). *Lower right*: $\hat{\tau}_V - M_\star$-relation based on low-redshift analogs of high-redshift galaxies observations by Shivaei et al. (2020).

distribution to greatly impact high-redshift sample completeness estimates, in particular on the extreme faint end of the UV luminosity function. Prompted by findings that faint high-redshift galaxies tend to have sizes far below the sizes predicted by typical size-luminosity relations (Bouwens et al., 2017a) we therefore follow the approach of Atek et al. (2018) and run two simulations: one with just the Kawamata et al. (2018) relation and one with fixed $r_e = 0.003''$ for galaxies with $M_{\mathrm{UV}} \geq -16$. Note that we can forego the fixed $r_e = 0.02''$ and $r_e = 0.05''$ configurations also probed in Atek et al. (2018) because the Kawamata et al. (2018) relation is steep enough to be below those values on the extreme faint end.

5.2.2 The BUFFALO source planes

In the completeness simulations, the simulated galaxies will be injected into the source plane in order to take the effects of SL into account. For that, we first need to construct the source plane of the BUFFALO view of A370. This is done by mapping each point of the observed BUFFALO image of A370 into the source plane with the SL modeling code `lenstool` (Kneib et al., 1996; Jullo et al., 2007; Jullo & Kneib, 2009) using

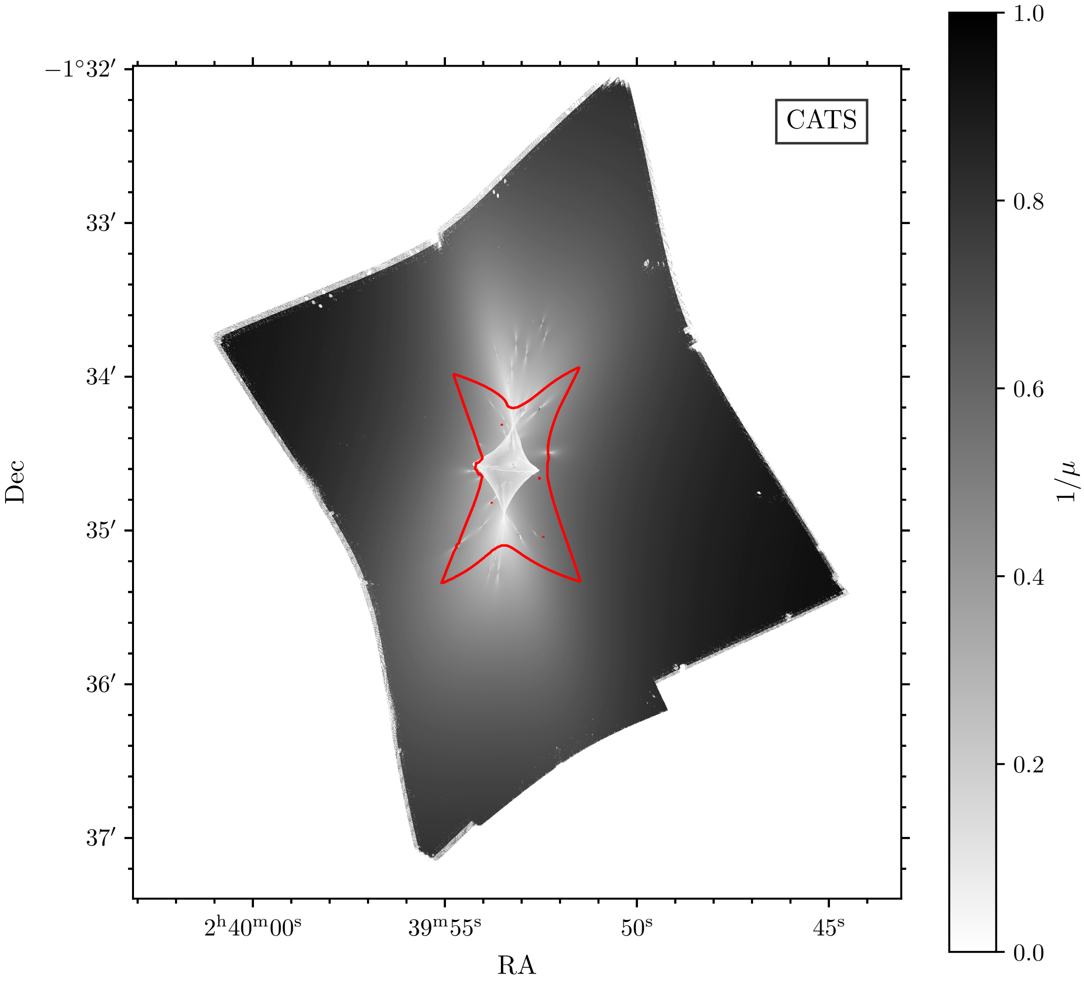

Figure 5.3: Source plane at $z = 6.5$ of the BUFFALO field-of-view of A370 for the CATS model in units $1/\mu$, constructed with `lenstool`. The red contour shows the footprint of the original HFF source plane of the CATS model. This plot therefore nicely illustrates that while the BUFFALO survey covers ~ 4× the area of the HFF in the lens plane, the effectively observed source plane is actually ~ 15× larger (cf. also Fig. 5.5).

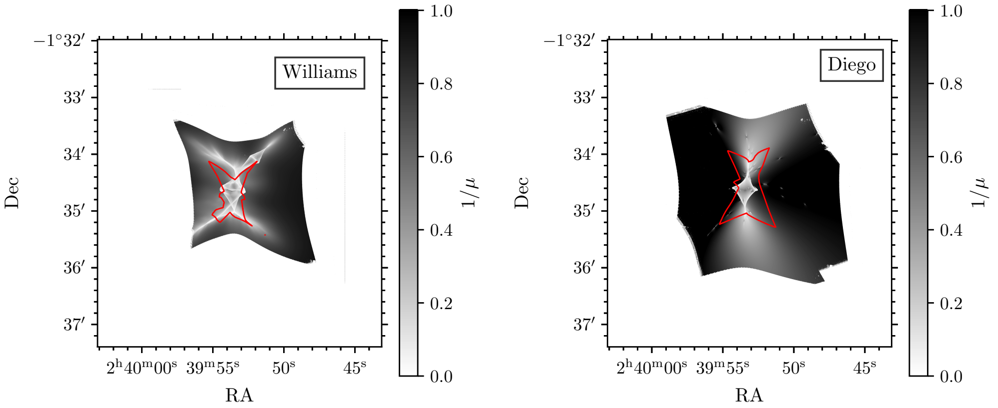

Figure 5.4: Source planes at $z = 6.5$ of the BUFFALO field-of-view of A370 for the Williams and Diego models in units $1/\mu$, constructed with `lenstool`. As in Fig 5.3, the red contours show the footprints of the corresponding HFF model source planes respectively.

equation (2.7). For this work we use three SL models of A370 produced by three modeling teams: The `Clusters As Telescopes` (CATS) model (Lagattuta et al., 2017) is a parametric SL model obtained with `lenstool` and is based on the HFF data set. The Williams model (Ghosh et al., 2021) and the Diego model (cf. e.g. Diego et al., 2018) are both non-parametric free-form models obtained with `GRALE` (Liesenborgs et al., 2006, 2007; Mohammed et al., 2014; Meneghetti et al., 2017) and `WSLAP+` (Diego et al., 2005, 2007; Sendra et al., 2014) respectively and represent the first generation of SL models based on the new BUFFALO observations (cf. section 4.1). Both of the free-form models are based on the latest MUSE spectroscopy of A370 (Lagattuta et al., 2017, 2019).

The $z \sim 6-7$ CATS source plane of A370 corresponding to the BUFFALO field-of-view is shown in Fig. 5.3 and the corresponding source planes for the Diego and the Williams model can be found in Fig. 5.4. The red contours show the corresponding source planes computed with the latest HFF versions of models derived with the same SL modeling techniques[1]. While the CATS model is based on the HFF data, it is so-far the only available SL model that is able to cover the full increased area of BUFFALO. This is due to the fact that the two free-form models, while based on the BUFFALO data, cannot be extrapolated beyond the region where there are SL constraints as opposed to the parametric model whose fully analytical form allows this kind of extrapolation even though these outer regions will be poorly constrained. For that reason the new Williams and Diego models used in this analysis do not cover the full BUFFALO field-of-view. As can be seen from the red contours in in Fig. 5.4, the BUFFALO source planes of these two models are indeed larger than their HFF counter parts but lack the ‘tips’ of the diamond-shaped BUFFALO source plane visible in Fig. 5.3 for the CATS model. More quantitatively, the new BUFFALO observations increase the total area of

---

[1] These models are publicly available on the `MAST` archive at `https://archive.stsci.edu/pub/hlsp/frontier/abell370/models/`

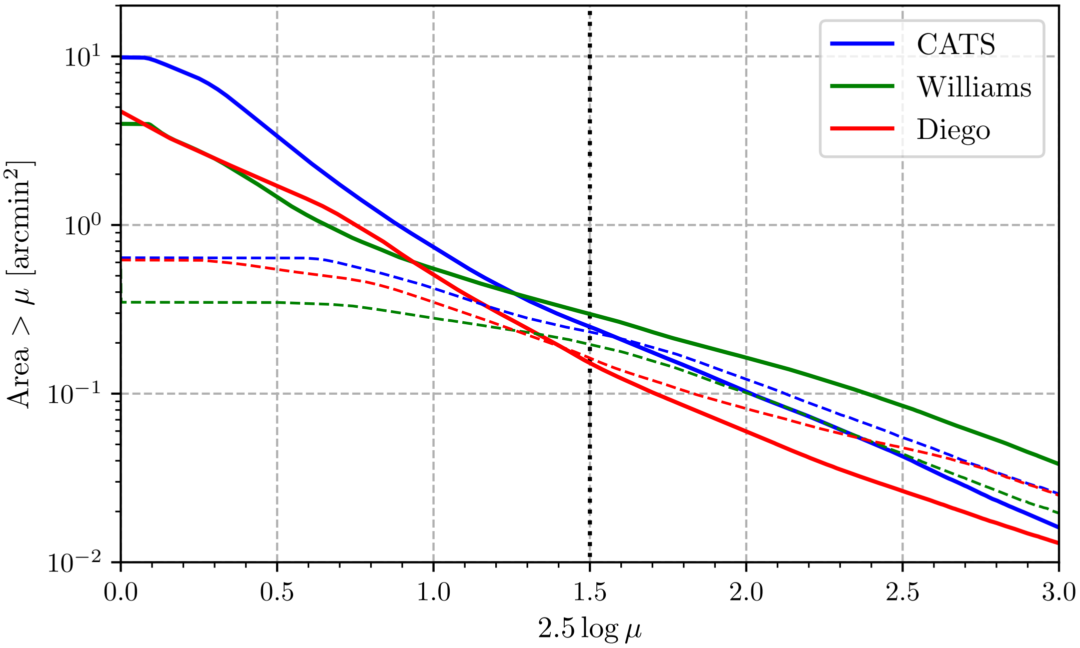

Figure 5.5: Cumulative source plane area at $z = 6.5$ as a function of gravitational magnification μ. We compute the cumulative area for each SL model used in this analysis both for BUFFALO (solid lines) and for the corresponding HFF models (dashed lines).

the observed source plane by a factor 15.4 in the CATS model and by factors of 7.2 and 12.3 in the Williams and Diego models respectively due to the lacking coverage of the complete BUFFALO lens plane. A look at the cumulative source plane area as a function of magnification in Fig. 5.5 reveals that this gain in area mostly concerns regions with $\mu \lesssim 3$ as expected when probing the outer regions of the cluster. Beyond $\mu \sim 3$ there is no significant difference in the cumulative magnification area between the HFF and the BUFFALO models because the high-magnification regimes only occur in the cluster core. An exception to this is the BUFFALO Williams model (solid green line in Fig. 5.5) which presents the largest cumulative magnification area at $\mu \gtrsim 4$ between the models. As can be seen in the upper panel of Fig. 5.4, this is in great part due to the prominent SL substructure at 250 kpc east of the cluster center which was not covered by the HFF model. We refer the reader to Ghosh et al. (2021) for an in-depth discussion of this feature.

5.2.3 Forward modelling

For our completeness simulations we draw 50000 realizations of the galaxy model SED detailed in section 5.2.1. The galaxies are modeled as elliptical Sérsic profiles (Sérsic, 1963). Following e.g. Bhatawdekar et al. (2019), we assign each simulated galaxy a random Sérsic index n drawn from a log-normal distribution roughly corresponding to

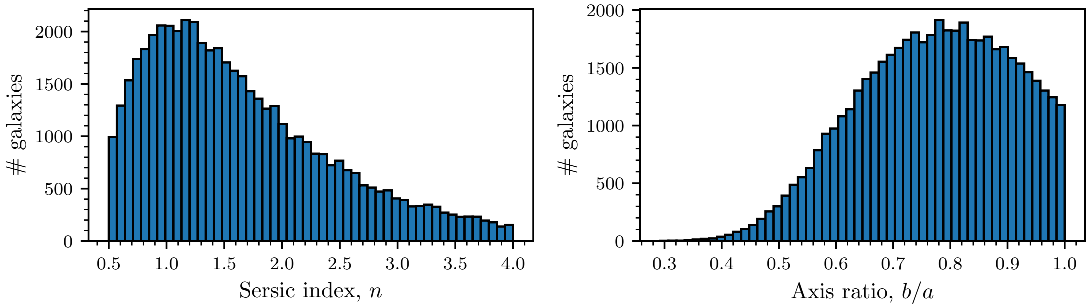

Figure 5.6: Morphological parameter distributions of the 50000 simulated galaxies used in our completeness simulations. *Left-hand panel*: Sérsic index n. *Right-hand panel*: Axis ratio b/a. Both parameters are drawn from log-normal distributions.

observations by Ravindranath et al. (2006). We optimize the Sérsic parameter distribution such that 30 % have $n \leq 0.8$, 40 % have $0.8 < n < 2.5$ and another 30 % have $n \geq 2.5$ to reflect the Ravindranath et al. (2006) findings and place upper and lower limits $n \in [0.5, 4]$ on the distribution. These distributions are shown in Fig. 5.6. In addition, each galaxy is assigned a random axis ratio b/a from a log-normal distribution peaked around 0.8 (cf. e.g. Bhatawdekar et al., 2019; Livet et al., 2021) and a random position angle. We then use the publicly available `galsim` (v2.2.5; Rowe et al., 2015) package to draw images of each simulated galaxy in each of the HST bands used in this analysis (cf. section 4.2.1 and Fig. 4.2).

The simulated `galsim` images are each assigned random coordinates in the BUFFALO source planes (cf. section 5.2.2) and then mapped into the lens plane with `lenstool`. Finally, we convolve the simulated galaxy light profiles to the inner or outer field F160W PSF, depending on their positions (cf. section 4.2.2), and add them to the observed images in each band before running `SExtractor` and `LePhare` and processing the results through the dropout (4.1) and photometric redshift (4.4) selection criteria to simulate our selection process as detailed in section 4.2.3. In order to avoid clustering and source confusion, we run the simulation in iterations of 100 galaxies at a time. We run three simulations in the cluster field (cf. Fig. B.2), one for each SL model, and one in the parallel field. Note that we do not map sources through the SL models for the parallel field but directly inject the un-lensed light profiles into the observed images. The resulting survey volume for the parallel field will be corrected by a constant average magnification factor inferred from the Merten lensing maps of A370 (cf. section 4.2.4).

5.3 Current state of the project and outlook

Just like the BUFFALO high-redshift galaxy catalogs presented in chapter 4, our completeness simulations are an ongoing work in progress and developed in parallel to our BUFFALO high-redshift galaxy pipeline. In its current state, the simulation code is completed from start, i.e. the galaxy model (cf. section 5.2.1), to finish, i.e. the selection function (cf. section 5.3.1) and in the process of being tested on full-length simulations. We are now entering the process of testing and choosing different galaxy parameters and their relations. Note that we especially built the simulation code in a modular way in order to be able to easily change the underlying assumptions, recipes and methods involved in each step of the completeness simulation process. I will present the latest results of our completeness simulations in section 5.3.1 and then proceed to listing the remaining issues of the code and the planned solutions in section 5.3.2

5.3.1 Preliminary results: The selection function

The first tests of the simulation were run on the cluster field using the CATS model and the Kawamata et al. (2018) relation for the source-size distribution. With the preliminary results of these first tests of the simulation we can compute the selection function $f(z, M_\star)$ as a function of redshift z and $M_\star$ by comparing the number of recovered galaxies to the number of injected galaxies in each $(z, M_\star)$ bin.

The resulting preliminary selection function is shown in Fig. 5.7. It shows the expected shape: a high recovery fraction on the high-mass end with a declining tail towards the lowest stellar masses and a symmetrical shape in redshift space. We are currently conducting tests with our simulation code to make sure our completeness estimates are as robust as possible. Note that our preliminary simulations show that using the Kawamata et al. (2018) relation for the source sizes and fixing the extreme faint-end half-light radii to $0.003''$ (cf. section 5.2.1) only marginally affects the selection function (cf. appendix C.3). This means that the Kawamata et al. (2018) size-luminosity relation is steep enough to reproduce the extreme small source sizes observed on the faint end by Bouwens et al. (2017a) for the purposes of these simulations.

We also use the simulation output to assess the efficiency of `LePhare` in recovering the injected galaxies' redshifts. As can be seen in Fig. 5.8, we loose a fraction of $z \sim 6-7$ galaxies which `LePhare` instead believes to be at $z_{\text{phot}} \sim 1-2$. This is accounted for in the selection function. Our photometric redshift selection also includes some contamination by poorly fit $z \gtrsim 8$ galaxies and by lower redshift sources. As can be seen from the selection function in Fig. 5.7 though, we do not select any significant amount of galaxies outside of the targeted $z \sim 6-7$ range. We therefore conclude that our overall high-redshift selection process is efficient at ruling out both lower- and higher-redshift interlopers.

5.3.2 Open issues and future development

As mentioned above, we are currently investigating the remaining issues with the simulation code and choosing galaxy parameter relations and distributions that best represent the samples of $z \sim 6-7$ galaxies that we are observing. The next steps in the development of our completeness simulations are the following:

- *Size-luminosity relations*: We take possible differences from the chosen size-luminosity relations on the low-mass end into account in our simulated galaxy model (cf. section 5.2.1). However, the Kawamata et al. (2018) relation is very steep because it

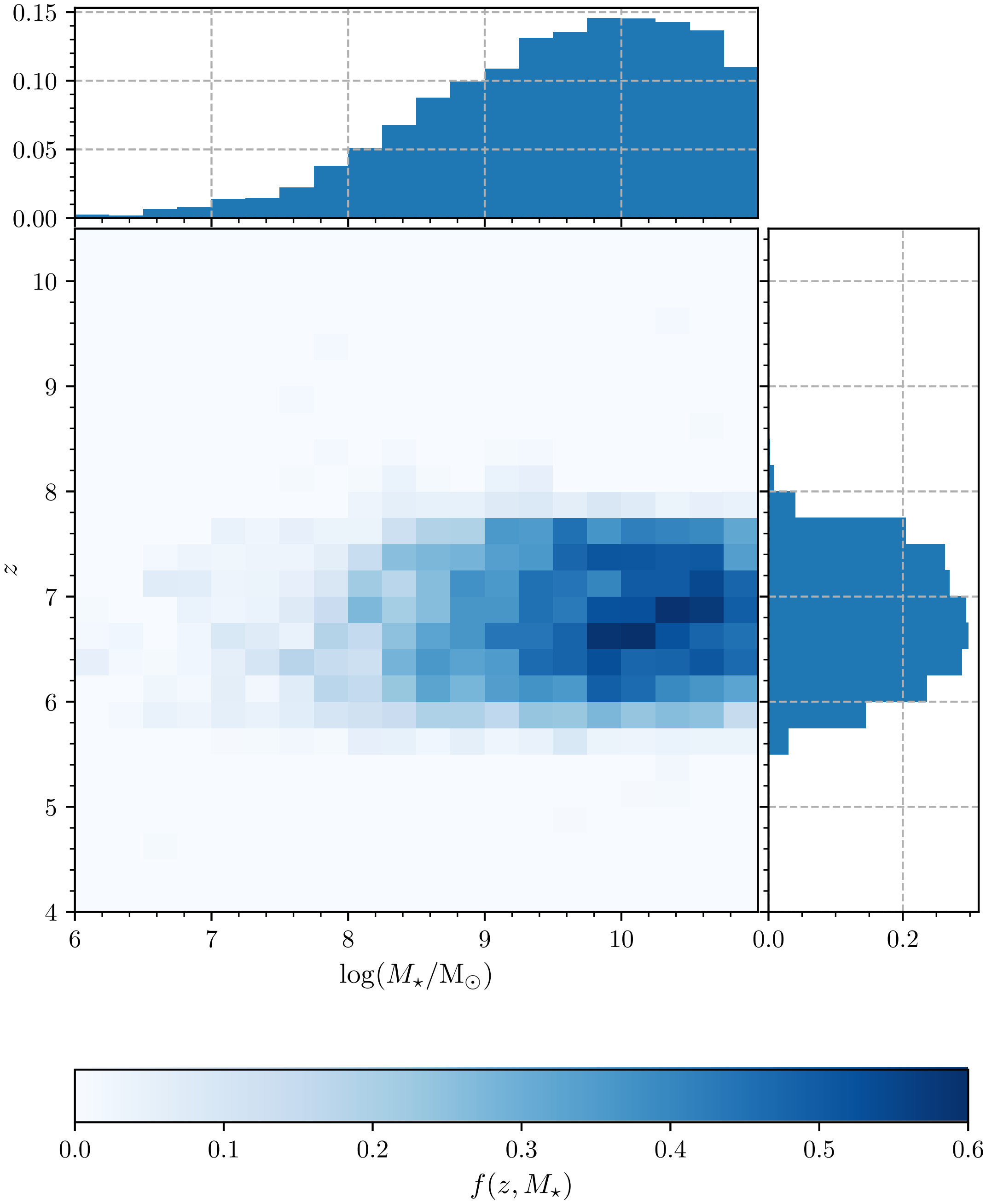

Figure 5.7: Preliminary selection function $f(z, M_\star)$ as a function of redshift z and stellar mass $M_\star$ as computed from the CATS model simulation of A370. The central panel shows the two-dimensional selection function as the ratio of selected and injected sources in each $(z, M_\star)$ bin. The upper and right-hand panels respectively show the ratios of selected and injected sources in each uniformly populated $M_\star$ and z bin.

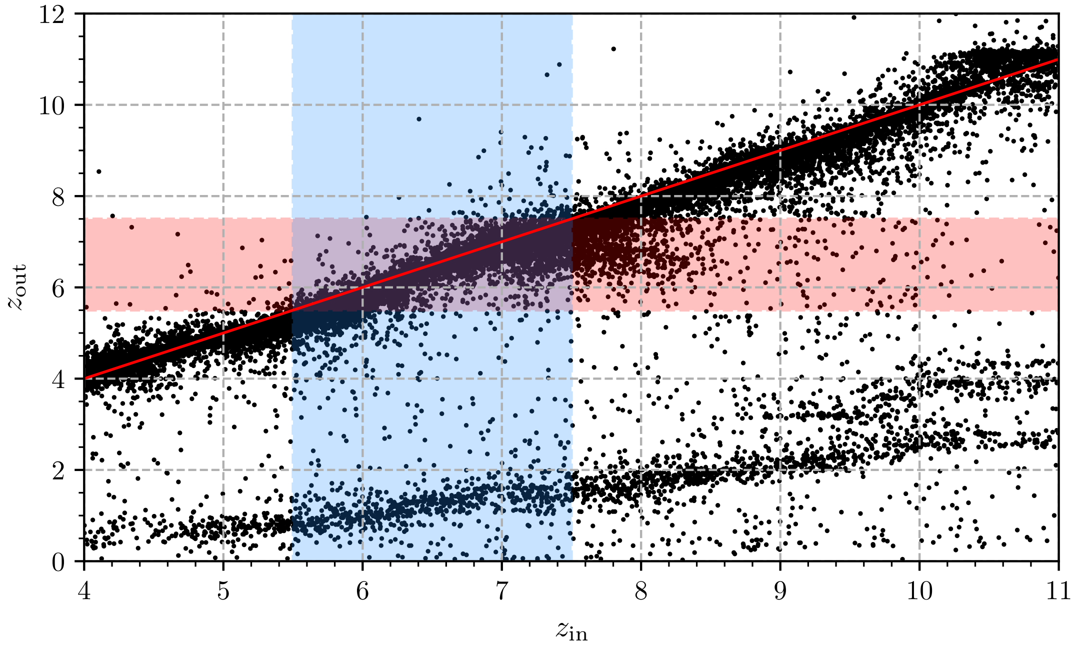

Figure 5.8: Comparison of the input and recovered redshifts in the preliminary completeness simulation. The $z_{\rm phot}$-selection window $5.5 \leq z < 7.5$ is shaded in red and the input $z \sim 6-7$ range in blue.

was observed with a sample of intrinsically faint lensed galaxies in the HFF. While this steep relation is well suited for $10^6\,{\rm M}_\odot \lesssim M_\star \lesssim 10^9\,{\rm M}_\odot$ galaxies, observations in blank fields suggest a significantly shallower size luminosity relation for bright and massive galaxies $M_\star \gtrsim 10^9\,{\rm M}_\odot$ (Huang et al., 2013; Shibuya et al., 2015). In the next step we will therefore implement a transition from the Kawamata et al. (2018) to the Shibuya et al. (2015) relation around $\sim 10^9\,{\rm M}_\odot$. This might also result in a higher recovery rate on the massive end since the high-mass sources will be more compact and thus easier to detect.

- *Mass-age relations*: As explained in detail in appendix C.1, the dynamical time constraints that we put on the stellar age of our simulated galaxies requires an estimate of the galaxy's size as is apparent from equation (3.2). While we currently use the Kawamata et al. (2018) size-luminosity relations for a rough estimate of the dynamical time scale (cf. appendix C.1), this is not necessarily a very accurate estimate since it is based on a rest-frame UV inferred radius. The UV half-light radii do indeed correspond to what we can typically *observe* with the HST, but recent observations of high-redshift galaxies with e.g. ALMA suggest that the galaxies extend up to ~ 3 times their UV-emitting size (e.g. Fujimoto et al., 2020). We therefore intend to explore ways to more accurately estimate the dynamical time scale, possibly by adapting relations for rest-frame optical or IR sizes measured for lower redshift galaxies like we have done for the dust extinction and metallicity such as e.g. Emami et al. (2021).

- *Stellar metallicity*: Recent observations of low-redshift analogs of high-redshift galaxies in the COSMOS fields (cf. section 2.1.2) have yielded new results on the evolution of stellar metallicity with stellar mass (Kashino et al., 2021). While we have previously found that high-redshift GSMFs do not strongly depend on metallicity (cf. section 3.4), observations of high-redshift galaxies do suggest an evolution of metallicity between the low- and the high-mass ends (Harikane et al., 2020; Jeon et al., 2020). We will therefore nonetheless test the impact of using such a mass-dependent relation in a similar manner as we do for the dust extinction and the nebular metallicity (as opposed to fixing the stellar metallicity) on our completeness simulations in order to make sure our galaxy model is as realistic as possible.

- *Photometry*: The simulation code in its current state does not yet include the median filtering foreground-subtraction on the detection stacks and the latest variance extraction procedures detailed in sections 4.2.2 and B.2. These will be added in future versions of the code.

Chapter 6

Overall discussion and prospectives

> “ ‘. . . you know how it is with boundaries,’ Ridcully mumbled. ‘You look at what’s on the other side and you realize why there was a boundary in the first place.’ ”
>
> ---
>
> Sir Terry Pratchett,
> *Unseen Academicals*, 2009

In chapters 3 to 5 I have presented our recent efforts towards robust measurements of the high-redshift ($z \gtrsim 6$) GSMF and in particular a complete treatment of all of its sources of uncertainty. In this final chapter, I will place these results in the context of the current state of high-redshift GSMF studies in section 6.1, in particular with regard to redshifts higher than the $z \sim 6-7$ range mostly probed in this work, and discuss some remaining issues. I will then outline the future of high-redshift galaxy and GSMF observations in sections 6.2, 6.3 and 6.4.

6.1 Discussion — The high-redshift GSMF and its open issues

We have already extensively discussed our high-redshift GSMF results with regard to sources of uncertainty, systematics and the literature in section 3.5. In this section, I will therefore only relate some final remarks and outline some open issues that future high-redshift GSMF studies will need to address. As can be seen in e.g. Fig. 3.12, to date the $z \sim 6-7$ GSMF is in general relatively well constrained in the range $10^{7.5}\,\mathrm{M}_\odot \lesssim M_\star \lesssim 10^{10}\,\mathrm{M}_\odot$. At both higher and lower stellar masses, the uncertainties become larger and different models and studies start to disagree. While the larger sample sizes that we can expect to observe in the remaining five BUFFALO clusters (cf. chapter 4) will eventually enable us to probe the evolution of the GSMF towards higher redshifts

$z \sim 8-10$, these two 'open' ends of the high-redshift GSMF will remain an outstanding issue for future observations. I will reflect upon these in sections 6.1.1 and 6.1.2 before some closing remarks on completely decoupling high-redshift GSMF measurements from the UV luminosity function in section 6.1.3.

6.1.1 The low-mass end turnover and its significance

In Furtak et al. (2021) (cf. chapter 3), we report the first tentative detection of a down-ward turnover on the low-mass end of the $z \sim 6-7$ GSMF at $M_T \sim 10^7\,\mathrm{M}_{\odot}$ at greater than 1σ-level and discuss the implications of this feature in section 3.5.5. The main reason we detect this turnover is because our HFF $z \sim 6-7$ GSMF is computed by converting the Atek et al. (2018) UV luminosity function, which presents a faint end turnover, to stellar mass (cf. section 3.4) even though the assumed galaxy model does have some influence on the significance of the GSMF turnover (cf. sections 3.4 and appendix A.3). To date, the UV luminosity function faint end turnover has only been detected in two measurements by Bouwens et al. (2017b) and Atek et al. (2018). Both have in common that they are the only studies to date that use high-redshift galaxy samples detected in all six HFF clusters *and* that include full treatment of SL systematics in their completeness estimates. Does this mean the detected tentative turnover is an artifact of SL systematics or that it is a true physical feature of the high-redshift GSMF revealed by the full treatment of these systematics and the observations across several fields to overcome cosmic variance? We have good theoretical and observational reasons to expect this turnover: Simulations predict a low-mass end cut-off or turnover (e.g. Yue et al., 2016; Ocvirk et al., 2020) since there are limits to the ability of DM halos to retain their baryons as already discussed in sections 1.3.1 and 3.5.5. Moreover, infrared background observations imply the luminosity function to never diverge, i.e. there must be a turnover on the faint end. Another open question would be: How does the low-mass end turnover, if it is real, evolve with redshift? If star-formation becomes more efficient at higher redshifts (as suggested by e.g. Finkelstein et al., 2021), one would expect the turnover mass M_T to increase with redshift. Future studies will need to address these questions with further observations and complete treatment of uncertainties as we attempt in chapter 5.

In a first step, we should therefore see if the low-mass end turnover is robust under our $M_\star$ completeness simulation methods presented in chapter 5, i.e. without passing through the UV luminosity function, in order to determine if it is a 'true' feature of the GSMF or a particularity of the rest-frame UV luminosity function. Note however that the latter is rather unlikely since it would imply radically different mass-to-light ratios than observed so-far. It will then also be interesting to see if and how robustly the turnover is detected with data from ongoing and future surveys of SL clusters, e.g. BUFFALO (cf. chapter 4) or the *REionization Lensing Cluster Survey* (RELICS; Coe et al., 2019) which observed 41 SL clusters and detected samples of ~ 300 lensed high-redshift galaxy candidates that rival the HFF sample (Salmon et al., 2018, 2020; Strait et al., 2020, 2021). While these surveys do not probe as low a stellar mass regime as the HFF, they might nevertheless be able to determine if M_T really does increase with redshift. Major advancement will however come with the JWST (cf. section 6.2) and ultra-deep NIRCam imaging campaigns of SL clusters to fully and robustly probe $M_\star \lesssim 10^7\,\mathrm{M}_\odot$ regime where we detect the turnover.

6.1.2 What about the high-mass end?

The focus of this work lies on the low-mass ($M_\star \lesssim 10^9\,\mathrm{M}_\odot$) end of the high-redshift GSMF but, as we have shown in section 3.4, the high- and low-mass ends of the GSMF cannot be treated completely independently from each other. The extreme high-mass end of the high-redshift GSMF is also prone to uncertainties since very bright high-mass ($M_\star \gtrsim 10^{10}\,\mathrm{M}_\odot$) galaxies are rare at high redshifts and require very large survey areas to be observed.

A census of the bright end of $z \gtrsim 6$ UV luminosity functions from current blank field samples revealed a possible departure from the Schechter form (1.21) on the extreme bright end and suggests a smooth power-law evolution instead of the exponential cut-off, i.e. an overdensity of the brightest $M_{\mathrm{UV}} \sim -23$ galaxies (Bowler et al., 2020; Finkelstein et al., 2021). This could be explained either by star-formation being more efficient or dust extinction being less efficient than expected at high redshifts (Finkelstein et al., 2021). The most recent blank field high-redshift GSMF measurements however do not find such a behavior on the extreme high-mass end (Song et al., 2016a; Stefanon et al., 2021b) which favors the second option since more efficient star-formation would result in higher stellar masses whereas dust extinction only affects the fraction of UV radiation that escapes the galaxy independently from its stellar mass. In addition, these samples of extremely UV-bright galaxies might also be contaminated by significant fractions of AGN which are impossible to tell apart from galaxies without spectroscopy and would result in extreme UV luminosities for relatively moderate stellar masses.

Samples of these very bright and massive galaxies are however scarce at high redshifts. We will require larger area blank field observations, such es e.g. COSMOS (cf. section 2.1.2; Weaver et al., 2021) to increase these samples and prepare follow-up spectroscopy. The next great deep blank field survey will be carried out with the *Euclid* spacecraft, scheduled to launch in late 2022. The *Euclid Deep Fields* (EDF; Scaramella et al., 2021) will cover up to ~ 40 square degrees in the sky to NIR depths ~ 26 magnitudes, deep enough to observe massive and bright $z \gtrsim 6$ galaxies, and will be ideally complemented with multiwavelength imaging from the *Cosmic Dawn Survey* (Toft et al. in prep.) with *Spitzer* (Moneti et al., 2021) and ground-based facilities (e.g. Zalesky, 2021; Weaver et al., 2021). Major progress on the bright and massive end of the high-redshift GSMF will also come with further generations of extremely wide area surveys such as e.g. the *Legacy Survey of Space and Time* (LSST; Ivezić et al., 2019) in the optical, which might enable us to rigorously constrain AGN populations up to $z \sim 5-6$, and large area NIR surveys conducted with the *Nancy Grace Roman Space Telescope* (cf. section 6.4 for more details).

6.1.3 Beyond the UV — Advanced high-redshift galaxy completeness estimates

While the $M_\star$ completeness simulation methods presented in chapter 5 will enable GSMF measurements that do not rely on measured $M_\star - M_{\mathrm{UV}}$-relations anymore, even these high-redshift GSMF measurements will still have one remaining bias: All high-redshift galaxy samples to date are *detected* by their rest-frame UV emission. While high-redshift galaxies are indeed all expected to be star-forming systems that significantly emit in the UV (cf. section 1.3.2), we still need to consider the possibility of UV-dark galaxy populations at high redshifts in order to derive a realistic GSMF. This is of course not necessary for UV luminosity functions but, as already explained in section 2.4, UV-emission does not necessarily account for all of the stellar mass. Accurate GSMF measurements therefore also need to take UV-dark galaxies into account.

One possibility for such UV-dark galaxies are massive, strongly star-forming, dust-obscured galaxies. Recent observations of 39 galaxies at $z \sim 3-7$ that are not detected in the rest-frame UV with *Spitzer* and ALMA have found SFRs of $\sim 200\,\mathrm{M}_\odot\,\mathrm{yr}^{-1}$ and stellar masses $\sim 10^{10.5}\,\mathrm{M}_\odot$ and suggest that these galaxies could dominate the SFR density on the high-mass end at $z \gtrsim 3$ (Wang et al., 2019). If that is also the case at $z \gtrsim 6$, it would mean that we are missing a certain fraction of galaxies on the very high-mass end of the high-redshift GSMF. The significance of this fraction of course still needs to be determined. Recent ALMA observations have for the first time serendipitously detected and confirmed two dust-obscured star-forming galaxies at $z \simeq 6.7$ and $z \simeq 7.4$ (Fudamoto et al., 2021). It however remains unclear if these are detections of a relatively rare type of galaxy or if they make up a significant fraction of galaxies at $z \gtrsim 6$. The former case would further be supported by the findings of Bowler et al. (2020) and Finkelstein et al. (2021) (cf. section 6.1.2) that suggest a stronger decrease in dust extinction with redshift than expected. Note also that with current samples, the UV-inferred SFR density function at the highest redshifts (i.e. $z \sim 10$) roughly agrees with the evolution of the DM halo mass functions (Oesch et al., 2018) which does not leave a lot of room for hitherto undetected UV-dark populations of galaxies.

Another possible galaxy population that surveys with HST, and for that matter also with the JWST (cf. section 6.2), are not sensitive to is low-surface-brightness galaxies (LSBGs). At low redshifts, cosmological simulations such as e.g. `NewHorizon` (Dubois et al., 2021) find the low-mass dwarf galaxy population to be dominated by such LSBG systems (Jackson et al., 2021). If these objects also exist at high redshifts, then we might also be missing a fraction of galaxies on the low-mass end of the GSMF.

In order to derive a 'true' GSMF at high-redshifts, we nevertheless need to include these possible UV-dark galaxy populations into the sample incompleteness estimates. Since these galaxies cannot be detected in the rest-frame UV, it would of course be impossible to just include them in the parameter distributions of our simulated galaxies in the completeness simulations (cf. section 5.2.1) since they would never be detected in any case. Instead, we will need to estimate and quantify the fractions that these galaxies represent in the overall number density at $z \gtrsim 6$, using observations such as e.g. the study conducted by Wang et al. (2019) and cosmological simulations such as e.g. `NewHorizon`, `CoDa II` (Ocvirk et al., 2020), `THESAN` (Kannan et al., 2021; Garaldi et al., 2021; Smith et al., 2021) or `ASTRID` (Bird et al., 2021). These fractions can then be used to include these sources in the parameter and size distributions of our stellar mass completeness simulations in correct amounts and thus derive the 'true' $M_\star$ completeness of observed samples.

6.2 Outlook — The JWST era

In the near future, the major progress in high-redshift galaxy observations will come with the unprecedented NIR capacities of the JWST which is scheduled to launch on December 18, 2021. With a mirror diameter of 6.5 m, $\sim 3\times$ that of HST, the JWST will reach depths ~ 2 magnitudes deeper than HST, right into the regime where we expect the low-mass end turnover. The JWST will carry four instruments: NIRCam, NIRSpec and MIRI, already introduced in sections 3.5.1 and 3.5.3, and the *Near-Infrared Imager and Slitless Spectrograph* (NIRISS; Doyon et al., 2012). NIRCam, NIRSpec and NIRISS will cover the wavelength range $0.8\,\mu\mathrm{m} \leq \lambda \leq 5\,\mu\mathrm{m}$, i.e. those of WFC3, IRAC *and* the gap between them, with imaging and spectroscopy and MIRI will be able to observe wavelengths $5\,\mu\mathrm{m} \leq \lambda \leq 28\,\mu\mathrm{m}$ which have so-far been unavailable for high-resolution space-based observations.

The JWST is ideally designed to initiate the next era in high-redshift galaxy observations. As already mentioned in section 3.5.3, NIRSpec will, for the first time, enable the observation of rest-frame optical emission lines (cf. section 2.4.2) up to $z \sim 9$ which will allow us to disentangle stellar mass from SFH and stellar age and thus potentially lift one of the major degeneracies that we have encountered in this work (cf. section 3.5.3 and appendix A.1). While simulations predict the rest-frame optical emission lines to theoretically be detectable down to $m_{\mathrm{F160W}} \leq 30$ with NIRSpec (e.g. Chevallard et al., 2019; Maseda et al., 2019), this of course depends on the actually emitted line fluxes which are not yet known (cf. e.g. discussion on EWs in appendix A.1). Currently planned observations are mostly expected to detect these emission lines for relatively bright and massive galaxies, meaning that we will still be mostly relying on photometry to constrain the physics of low-mass end galaxies. This will however be of much better quality than before since NIRCam imaging will, also for the first time, provide rest-frame optical photometry at *Spitzer* wavelengths but with HST resolutions and thus not only overcome the blending and source contamination issues that lame current studies of the low-mass end of the $z \gtrsim 6$ GSMF (cf. sections 3.1.2, 3.2.3 and 3.5.1 and appendix A.2), but also allow morphological studies of high-redshift galaxies in the rest-frame optical. Finally, some simulations also predict large numbers of serendipitous rest-frame optical emission line detections with NIRSpec (Maseda et al., 2019) in addition to targeted spectroscopy of previously identified high-redshift galaxy candidates. However, while the NIRSpec spectroscopy in combination with NIRCam imaging and MIRI observations will constrain $z \sim 6-9$ GSMFs to unprecedented precision (Chevallard et al., 2019; Maseda et al., 2019; Kemp et al., 2019), the low-mass end in particular will remain prone to both the large uncertainties induced by lensing systematics (cf. sections 3.2.2 and 3.5.2) and galaxy modeling assumptions (cf. section 3.5.3). The completeness simulation methods introduced in Atek et al. (2018) and in chapter 5 of this work will therefore still be required for robust high-redshift galaxy studies. There are many planned programs to observe optical emission of high-redshift galaxies with the JWST, too many to list here[1]. An example, of one of the largest ones is the guaranteed time observation program *CAnadian NIRISS Unbiased Cluster Survey* (CANUCS; PI: C. J. Willott) which will target galaxies on the low-mass end of the high-redshift GSMF using five SL clusters, among them three of the HFF/BUFFALO clusters (MACS0416, MACS1149 and A370).

Aside from the rest-frame optical follow-up of the $z \sim 6-9$ galaxy populations currently observed in the UV with HST, the JWST and in particular its imaging instruments NIRCam and MIRI, will open up whole new ranges of hitherto unobserved wavelengths and redshifts for galaxies in a similar manner as WFC3 did when it was first installed. Deep MIRI imaging will for the first time probe the *rest-frame* NIR range and thus allow high-redshift galaxy observations unaffected by dust extinction. This will not only help to better constrain the low-mass end of $z \gtrsim 6$ GSMFs by probing the reddest stellar populations (cf. section 2.4.2 and Fig. 2.11) and overcome the degeneracy of stellar mass and dust extinction (cf. section 3.5.3; Kemp et al., 2019) but also enable the search and detection of heavily dust-obscured galaxies such as mentioned in section 6.1.3. These galaxies would present prime targets for follow-up observations with ALMA (cf. section 6.3) and we would be able to begin to quantify the fraction of the total number of galaxies that these objects represent at high redshifts. Arguably the most significant progress in high-redshift galaxy observations will however come from ultra-deep imaging with NIRCam aimed at rest-frame UV emission which will push the redshift frontier from $z \sim 10$ with HST all the way up to $z \gtrsim 13$. In the absence of rest-frame optical spectroscopy at these redshifts, these studies will however require methods such as e.g. presented in chapter 5 in order to robustly probe galaxy physics since they will in turn also be subject to lensing and galaxy modeling systematics and biases. An example for such a program is the *Ultra-deep NIRCam and NIRSpec Observations Before the Epoch of Reionization* program (UNCOVER; PI: I. Labbé) targeted at A2744 which is expected to reach depths down to ≤ 30 magnitudes (and ~ 2 magnitudes more with the SL magnification) with 70 h of observations dedicated to this cluster. Finally, NIRCam also has the potential to detect prominent signatures of possible Pop. III stellar populations in $z \sim 10-13$ galaxies with the aid of lensing (Woods et al., 2021).

All that being said, the JWST will, just like the HST, be relatively inefficient at detecting possible populations of LSBGs (cf. section 6.1.3) which means that a potentially significant fraction of stellar mass at high-redshifts will remain elusive. Future surveys such as LSST in the optical and *Roman* in the NIR (cf. section 6.4) will be more sensitive to diffuse sources and possibly bring the first constraints on high-redshift LSBG populations.

---

[1] A complete list of observing programs that will be carried out in Cycle 1 of JWST operations is however available at `https://www.stsci.edu/jwst/science-execution/approved-programs`.

6.3 Outlook — The ALMA era

The advent of very high sensitivity sub-millimeter interferometry with ALMA has put a new wavelength range of $z \gtrsim 6$ galaxy emission, the rest-frame FIR, within observational reach. While ALMA is not a survey instrument and therefore cannot efficiently serve for the search and detection of significant high-redshift galaxy samples (with some exceptions as detailed below), it is however well suited for follow-up observations of high-redshift galaxies previously identified with HST. As mentioned in section 4.3.1, the rest-frame FIR range represents a complementary window to the UV and optical wavelengths in which the high-redshift Universe is usually observed since it probes the otherwise elusive physics of dust, cold neutral gas and molecular clouds in $z \gtrsim 6$ galaxies. This is because FIR dust-continuum emission is in fact the *re-emission* of stellar UV continuum previously absorbed by the dust. The dust continuum therefore traces star-formation and is better suited for constraining the SFR of a galaxy than the rest-frame UV emission (e.g. Khusanova et al., 2021). The bright FIR emission line [C II]$\lambda 158\,\mu$m on the other hand originates from gas cooling at the interface between ionized H II regions and the cooler, neutral gas around them. It therefore represents a valuable probe of gas cooling and ionization rate in the cold ISM and CGM of high-redshift galaxies. I refer the reader to e.g. Osterbrock & Ferland (2006) or Cimatti et al. (2019) for more detailed reviews of the rest-frame FIR SED.

ALMA observations targeted at single bright galaxies have detected [O III]$\lambda 88\,\mu$m and [C II]$\lambda 158\,\mu$m emission out to redshifts $z \sim 8-9$ (e.g. Laporte et al., 2017, 2019; Hashimoto et al., 2018; Tamura et al., 2019; Bakx et al., 2020). More recently, ALMA has also delivered the first detections of [N II]$\lambda 122\,\mu$m (Sugahara et al., 2021) and molecular lines (Jarugula et al., 2021) at $z \sim 7$. In slightly lower redshift ranges $z \sim 4-6$ more systematic observing programs targeted at statistically significant samples of galaxies, such as e.g. the *ALMA Large Program to Investigate* C^+ *at Early Times* (ALPINE; Le Fèvre et al., 2020; Béthermin et al., 2020; Faisst et al., 2020) and the *ALMA Lensing Cluster Survey* (ALCS; PI: K. Kohno), have delivered the first constraints on the [C II]$\lambda 158\,\mu$m luminosity function out to $z \sim 6$ (Yan et al., 2020; Uzgil et al., 2021) and the physics of early dust formation at $z \gtrsim 6$ (e.g. Fudamoto et al., 2020; Burgarella et al., 2020; Sommovigo et al., 2020; Khusanova et al., 2021; Bakx et al., 2020, 2021).

These observations also show that systematic rest-frame FIR observations of high-redshift galaxies with ALMA can provide constraints on parameters relevant for high-redshift GSMF measurements such as dust extinction, SFR and even $M_\star$ (e.g. Fudamoto et al., 2020; Khusanova et al., 2021), at least for bright galaxies, which complement the rest-frame UV and optical studies usually conducted at high redshifts for the reasons explained above. For our completeness simulations and galaxy models presented in sections 5.2 and 5.2.1 in particular, the findings of ALPINE (e.g. Fudamoto et al., 2020) provide interesting constraints on dust extinction that we could test in future applications of our code. In addition, ALMA has already proven its usefulness for spectroscopically confirming the redshifts of photometric high-redshift candidates (e.g. Tamura et al., 2019) since [O III]$\lambda 88\,\mu$m and [C II]$\lambda 158\,\mu$m are exceptionally bright emission lines.

Future high-redshift galaxy studies with HST and JWST will therefore routinely need to be accompanied by sub-millimeter follow-up observations in order to constrain star-formation from both UV and FIR probes in a statistically significant manner. The next large high-redshift galaxy ALMA observation program is the ongoing *Reionization Era Bright Emission Line Survey* (REBELS; PI: R. Bouwens), a 70 h ALMA large program, which will observe statistical samples of [O III]λ88 µm and [C II]λ158 µm emission of bright galaxies at $z \sim 7 - 10$. This program has already delivered the two first serendipitous detections of heavily dust obscured and thus UV-invisible galaxies at $z \sim 6 - 7$ (Fudamoto et al., 2021, cf. section 6.1.3). By constraining total dust content independently from the UV, studies of this nature will also be able to answer the question if the suggested over-density of extremely bright UV emitting galaxies at high redshifts mentioned in section 6.1.2 can be caused by less efficient dust extinction at high-redshifts (cf. e.g. Finkelstein et al., 2021).

6.4 Closing remarks — Towards a complete census of star-formation in the Universe

In conclusion, the advancements in high-redshift galaxy physics with JWST and ALMA described in the previous sections will push the limits of observability towards higher redshifts $z \gtrsim 13$ and have the potential to reduce the uncertainties on both the high- and the low-mass ends of the GSMF. And beyond that? In the mid-2020s, the next great space observatory after the JWST will take up operations: The *Nancy Grace Roman Space Telescope* (*Roman*; Spergel et al., 2015) will have a field-of-view 100× larger than that of HST and will map up to 2000 square degrees with deep NIR imaging which is expected to deliver samples of up to ~ 1000 galaxies at $z \sim 10$ (e.g. Drakos et al., 2021). This will in addition be ideally complemented by the LSST (cf. section 6.1.2) in the optical to rule out low-redshift interlopers. The combination of ultra-deep JWST observations of SL clusters to probe the extreme faint and low-mass ends of the $z \gtrsim 10$ luminosity function and GSMF with extreme wide-area *Euclid* and *Roman* observations and their JWST and ALMA spectroscopic follow-up observations will have the potential to deliver a complete census of star-formation history over the whole stellar mass range out to $z \gtrsim 10$ and maybe make the first detections of Pop. III stars.

In the future, we might also possibly be able to compare the spatial distributions of high-redshift galaxies from ultra-deep *Roman* NIR imaging in combination with JWST spectroscopic follow-up observations on significant areas of the sky with ground-based H I power-spectrum mappings out to the highest redshifts (e.g. Koopmans et al., 2015) with the *Square Kilometer Array* (SKA) in order to fully constrain cosmic reionization and the build-up of stellar mass across Universe.

Summary and Conclusion

> “Sometimes, if you pay real close attention to the pebbles you find out about the ocean.”
>
> Sir Terry Pratchett,
> *Lords and Ladies*, 1996

The high-redshift GSMF represents a uniquely crucial observational constraint on cosmic reionization and the build-up of stellar mass in the Universe since these primeval galaxies at $z \gtrsim 6$ represent both the most likely candidates for the sources that have driven cosmic reionization and the earliest stages of galaxy evolution. In this manuscript, I have presented my thesis work on the observation of the low-mass ($10^6\,\mathrm{M}_\odot \lesssim M_\star \lesssim 10^9\,\mathrm{M}_\odot$) end of the $z \gtrsim 6$ GSMF using the SL magnification of the six HFF clusters (A2744, MACS0416, MACS0717, MACS1149, S1063 and A370) and a rigorous treatment of all of its sources of uncertainty. To that end, we measured precision photometry in broad-band imaging data from both HST and *Spitzer*, carefully disentangled the flux of the faint high-redshift sources from foreground contamination and discarded contaminated bands.

Using a sample of 303 galaxies detected in the dense cores of the six HFF clusters, we computed the $z \sim 6-7$ GSMF down to $M_\star \gtrsim 10^6\,\mathrm{M}_\odot$ by convolving the rest-frame UV luminosity function with an empirical $M_\star - M_{\mathrm{UV}}$-relation, both of which were measured with the same galaxy sample. For this analysis, we assessed and quantified the impacts of discarding contaminated *Spitzer*/IRAC photometry, SL systematics and SED-modeling assumptions and parameter degeneracies on the resulting $z \sim 6-7$ GSMFs. We in particular found high-redshift GSMFs and their uncertainties measured in this manner to be heavily affected by model assumptions due to the resulting shapes of the $M_\star - M_{\mathrm{UV}}$-relation.

In order to increase high-redshift galaxy sample sizes, in particular on the high-mass end and higher redshifts, and to rigorously include *all* of these sources of uncertainty into the final GSMF errors, we then adapted our source detection and photometry methods to new HST observations of the HFF clusters, the BUFFALO survey, and developed new completeness simulations for this survey. These for the first time estimate the high-redshift galaxy completeness directly in stellar mass rather than in UV luminosity and therefore include the effects of SED-modeling into the GSMF uncertainties. In this

work, we tested these new methods on a sample of $z \sim 6-7$ galaxies detected in the first BUFFALO cluster, A370, before they will be applied to all six clusters and the entire $z \sim 6-10$ range probed with the BUFFALO survey in an ongoing project.
The main results of my thesis can be summarized as the following:

- Our reference model (cf. Tab. 3.3) $z \sim 6-7$ GSMF measurement in the HFF yields a high-mass exponential cutoff at $\log(M_0/\mathrm{M}_\odot) \simeq 10.22^{+0.45}_{-0.27}$, a relatively steep low-mass end slope, $\alpha \simeq -1.96^{+0.09}_{-0.08}$, and a normalization $\log(\phi_0/\mathrm{Mpc}^{-3}) \simeq -4.49^{+0.64}_{-0.32}$ which is in good agreement with recent results from the literature considering the respective error bars. Different SED-fitting assumptions can however yield significantly different low-mass end slopes, spanning a range from $\alpha \simeq -1.82^{+0.08}_{-0.07}$ to $\alpha \simeq -2.34^{+0.11}_{-0.10}$. We furthermore for the first time measure a tentative down-ward turnover on the extreme low-mass end of the $z \sim 6-7$ GSMF. In the reference model, this turnover is detected at greater than 1σ-level at $\log(M_T/\mathrm{M}_\odot) \simeq 7.10^{+0.17}_{-0.56}$ and has a curvature of $\beta \simeq 1.00^{+0.87}_{-0.73}$.

- We find the extreme low-mass end of the $z \sim 6-7$ GSMF ($M_\star \lesssim 10^7\,\mathrm{M}_\odot$) to be dominated by large uncertainties induced by SL systematics whereas the low-mass power-law slope ($10^7\,\mathrm{M}_\odot \lesssim M_\star \lesssim 10^9\,\mathrm{M}_\odot$) is most heavily affected by missing IRAC photometry and the effects of SED-fitting assumptions and parameter degeneracies, in particular with SFH, dust attenuation and stellar age. Our results show that variations in the slope of the $M_\star - M_{\mathrm{UV}}$-relation or in $M_\star$ of the order of $\gtrsim 0.1$ dex are sufficient to significantly impact the resulting GSMF and that fitting SEDs without rest-frame optical IRAC photometry underestimates $M_\star$ by $\langle\delta\rangle \simeq 0.62 \pm 0.05$ dex.

- Our analysis of the A370 BUFFALO fields yielded a catalog of 128 $z \sim 6-10$ galaxy candidates, $\sim 2\times$ the number detected with the HFF observations of the same cluster, which confirms predictions that BUFFALO would double the numbers of high-redshift galaxies detected in or around the HFF clusters. We furthermore find that the larger area observed with BUFFALO in the lens plane, $4\times$ larger than that of HFF, translates to an effective gain in source plane area by a factor ~ 15.

- Our newly developed completeness simulation code for GSMF measurements in BUFFALO successfully links physical parameters that impact the SED and fluxes in the detection bands, including the source-size, to z, $M_\star$ and SL magnification μ and thus allows to compute the selection function $f(z, M_\star, \mu)$ of our sample directly in stellar mass. This simulation code is now complete from end to end and in the process of being tested and applied to our $z \sim 6-7$ sample detected in BUFFALO.

The methods developed over the course of this work will fully fold the effects of SL systematics, selection effects and the model dependence of stellar mass into the GSMF derivation and thus produce the most complete and robust estimate of the high-redshift GSMF and its uncertainties. This will be particularly valuable for future surveys of

high-redshift galaxies through SL clusters with the upcoming JWST which will initiate a new era in high-redshift galaxy observations.
The next generations of ultra-deep surveys, JWST imaging of SL clusters to probe the extreme faint low-mass end of the $z > 10$ UV luminosity and stellar mass functions and deep wide-area *Roman* surveys with supporting JWST and ALMA follow-up observations will push the limits of observability towards higher redshifts and expand our understanding of galaxy formation and evolution. Ultimately, these will pave the way to one day enable direct observation of the very first stars and galaxies and study the complete build-up of stellar mass in the Universe — all the way back to the Cosmic Dawn.

Bibliography

> “There is no higher life form
> than a librarian.”
>
> Sir Terry Pratchett,
> *The Science of Discworld*, 1999

Acebron A., Jullo E., Limousin M., Tilquin A., Giocoli C., Jauzac M., Mahler G., Richard J., 2017, MNRAS, 470, 1809

Acebron A., et al., 2018, ApJ, 858, 42

Acebron A., et al., 2019, ApJ, 874, 132

Allard F., Hauschildt P. H., Alexander D. R., Tamanai A., Schweitzer A., 2001, ApJ, 556, 357

Ammons S. M., Wong K. C., Zabludoff A. I., Keeton C. R., 2014, ApJ, 781, 2

Arnouts S., et al., 2002, MNRAS, 329, 355

Asada Y., Ohta K., 2021, arXiv e-prints, p. arXiv:2111.01447

Atek H., et al., 2011, ApJ, 743, 121

Atek H., et al., 2014, ApJ, 789, 96

Atek H., et al., 2015a, ApJ, 800, 18

Atek H., et al., 2015b, ApJ, 814, 69

Atek H., Richard J., Kneib J.-P., Schaerer D., 2018, MNRAS, 479, 5184

Bacon R., et al., 2010, in McLean I. S., Ramsay S. K., Takami H., eds, Society of Photo-Optical Instrumentation Engineers (SPIE) Conference Series Vol. 7735, Ground-based and Airborne Instrumentation for Astronomy III. p. 773508, doi:10.1117/12.856027

Bagnasco G., et al., 2007, Overview of the near-infrared spectrograph (NIRSpec) instrument on-board the James Webb Space Telescope (JWST). SPIE, p. 66920M, doi:10.1117/12.735602

Bakx T. J. L. C., et al., 2020, MNRAS, 493, 4294

Bakx T. J. L. C., et al., 2021, MNRAS, 508, L58

Becker R. H., et al., 2001, AJ, 122, 2850

Beckwith S. V. W., et al., 2006, AJ, 132, 1729

Behroozi P. S., Wechsler R. H., Conroy C., 2013, ApJ, 770, 57

Behroozi P., Wechsler R. H., Hearin A. P., Conroy C., 2019, MNRAS, 488, 3143

Bertin E., Arnouts S., 1996, Astronomy and Astrophysics Supplement Series, 117, 393

Béthermin M., et al., 2020, A&A, 643, A2

Bhatawdekar R., Conselice C. J., 2021, ApJ, 909, 144

Bhatawdekar R., Conselice C. J., Margalef-Bentabol B., Duncan K., 2019, MNRAS, 486, 3805

Bird S., Ni Y., Di Matteo T., Croft R., Feng Y., Chen N., 2021, arXiv e-prints, p. arXiv:2111.01160

Birkmann S. M., et al., 2016, The JWST/NIRSpec instrument: update on status and performances. SPIE, p. 99040B, doi:10.1117/12.2231837

Bisigello L., et al., 2017, ApJS, 231, 3

Bolzonella M., Miralles J.-M., Pelló R., 2011, Hyperz: Photometric Redshift Code (ascl:1108.010)

Bosman S. E. I., et al., 2021, arXiv e-prints, p. arXiv:2108.03699

Bouwens R. J., et al., 2009, ApJ, 705, 936

Bouwens R. J., et al., 2011, ApJ, 737, 90

Bouwens R. J., et al., 2014, ApJ, 795, 126

Bouwens R. J., et al., 2015, ApJ, 803, 34

Bouwens R. J., et al., 2016, ApJ, 833, 72

Bouwens R. J., Illingworth G. D., Oesch P. A., Maseda M., Ribeiro B., Stefanon M., Lam D., 2017a, arXiv e-prints, p. arXiv:1711.02090

Bouwens R. J., Oesch P. A., Illingworth G. D., Ellis R. S., Stefanon M., 2017b, ApJ, 843, 129

Bouwens R. J., Illingworth G. D., van Dokkum P. G., Ribeiro B., Oesch P. A., Stefanon M., 2021, arXiv e-prints, p. arXiv:2106.08336

Bowler R. A. A., Jarvis M. J., Dunlop J. S., McLure R. J., McLeod D. J., Adams N. J., Milvang-Jensen B., McCracken H. J., 2020, MNRAS, 493, 2059

Bradač M., et al., 2019, MNRAS, 489, 99

Bradley L., et al., 2019, astropy/photutils: v0.7.2, doi:10.5281/zenodo.3568287, `https://doi.org/10.5281/zenodo.3568287`

Brammer G. B., et al., 2016, ApJS, 226, 6

Bromm V., 2013, Asociacion Argentina de Astronomia La Plata Argentina Book Series, 4, 3

Bromm V., Loeb A., 2003, Nature, 425, 812

Bromm V., Yoshida N., 2011, ARA&A, 49, 373

Bruzual G., Charlot S., 2003, MNRAS, 344, 1000

Bunker A. J., et al., 2010, MNRAS, 409, 855

Burgarella D., Nanni A., Hirashita H., Theulé P., Inoue A. K., Takeuchi T. T., 2020, A&A, 637, A32

Calzetti D., Kinney A. L., Storchi-Bergmann T., 1994, ApJ, 429, 582

Calzetti D., Armus L., Bohlin R. C., Kinney A. L., Koornneef J., Storchi-Bergmann T., 2000, ApJ, 533, 682

Capak P. L., et al., 2015, Nature, 522, 455

Cassata P., et al., 2013, A&A, 556, A68

Castellano M., et al., 2016, A&A, 590, A31

Chabrier G., 2003, PASP, 115, 763

Chabrier G., Baraffe I., Allard F., Hauschildt P., 2000, ApJ, 542, 464

Charlot S., Fall S. M., 1993, ApJ, 415, 580

Charlot S., Longhetti M., 2001, MNRAS, 323, 887

Chevallard J., Charlot S., 2016, MNRAS, 462, 1415

Chevallard J., et al., 2019, MNRAS, 483, 2621

Chirivì G., Yıldırım A., Suyu S. H., Halkola A., 2020, A&A, 643, A135

Cimatti A., Fraternali F., Nipoti C., 2019, Introduction to Galaxy Formation and Evolution: From Primordial Gas to Present-Day Galaxies. Cambridge University Press, `https://books.google.fr/books?id=rJCuDwAAQBAJ`

Coe D., et al., 2013, ApJ, 762, 32

Coe D., Bradley L., Zitrin A., 2015, ApJ, 800, 84

Coe D., et al., 2019, ApJ, 884, 85

Conroy C., Gunn J. E., 2010, ApJ, 712, 833

Dale D. A., Helou G., 2002, ApJ, 576, 159

Dayal P., Ferrara A., 2012, MNRAS, 421, 2568

Dayal P., Ferrara A., Dunlop J. S., Pacucci F., 2014, MNRAS, 445, 2545

De Barros S., Oesch P. A., Labbé I., Stefanon M., González V., Smit R., Bouwens R. J., Illingworth G. D., 2019, MNRAS, p. 907

Di Criscienzo M., et al., 2017, A&A, 607, A30

Diego J. M., Protopapas P., Sandvik H. B., Tegmark M., 2005, MNRAS, 360, 477

Diego J. M., Tegmark M., Protopapas P., Sandvik H. B., 2007, MNRAS, 375, 958

Diego J. M., Broadhurst T., Zitrin A., Lam D., Lim J., Ford H. C., Zheng W., 2015, MNRAS, 451, 3920

Diego J. M., et al., 2018, MNRAS, 473, 4279

Dodelson S., 2017, Gravitational Lensing. Cambridge University Press, doi:10.1017/9781316424254

Doyon R., et al., 2012, in Clampin M. C., Fazio G. G., MacEwen H. A., Oschmann Jacobus M. J., eds, Society of Photo-Optical Instrumentation Engineers (SPIE) Conference Series Vol. 8442, Space Telescopes and Instrumentation 2012: Optical, Infrared, and Millimeter Wave. p. 84422R, doi:10.1117/12.926578

Drakos N. E., et al., 2021, arXiv e-prints, p. arXiv:2110.10703

Dubois Y., et al., 2021, A&A, 651, A109

Duncan K., et al., 2014, MNRAS, 444, 2960

Dunlop J. S., 2013, Observing the First Galaxies. Springer Verlag Berlin Heidelberg, p. 223, doi:10.1007/978-3-642-32362-1_5

Dunlop J. S., Peacock J. A., 1990, MNRAS, 247, 19

Dunlop J. S., Cirasuolo M., McLure R. J., 2007, MNRAS, 376, 1054

Dyson F. W., Eddington A. S., Davidson C., 1920, Philosophical Transactions of the Royal Society of London Series A, 220, 291

Einstein A., 1916, Annalen der Physik, 354, 769

Ellis R. S., et al., 2013, ApJ, 763, L7

Emami N., Siana B., Weisz D. R., Johnson B. D., Ma X., El-Badry K., 2019, ApJ, 881, 71

Emami N., et al., 2021, arXiv e-prints, p. arXiv:2108.08857

Endsley R., Stark D. P., Chevallard J., Charlot S., 2021, MNRAS, 500, 5229

Eyles L. P., Bunker A. J., Ellis R. S., Lacy M., Stanway E. R., Stark D. P., Chiu K., 2007, MNRAS, 374, 910

Faisst A. L., et al., 2020, ApJS, 247, 61

Fan X., et al., 2006, AJ, 132, 117

Fazio G. G., et al., 2004, ApJS, 154, 10

Ferland G. J., et al., 2013, Rev. Mex. Astron. Astrofis., 49, 137

Finkelstein S. L., et al., 2013, Nature, 502, 524

Finkelstein S. L., et al., 2015, ApJ, 810, 71

Finkelstein S. L., et al., 2021, arXiv e-prints, p. arXiv:2106.13813

Finlator K., Davé R., Oppenheimer B. D., 2007, MNRAS, 376, 1861

Finlator K., Oppenheimer B. D., Davé R., 2011, MNRAS, 410, 1703

Finlator K., Keating L., Oppenheimer B. D., Davé R., Zackrisson E., 2018, MNRAS, 480, 2628

Finlator K., Doughty C., Cai Z., Díaz G., 2020, MNRAS, 493, 3223

Foreman-Mackey D., Hogg D. W., Lang D., Goodman J., 2013, PASP, 125, 306

Friedmann A., 1922, Zeitschrift fur Physik, 10, 377

Friedmann A., 1924, Zeitschrift fur Physik, 21, 326

Fudamoto Y., et al., 2020, A&A, 643, A4

Fudamoto Y., et al., 2021, Nature, 597, 489–492

Fujimoto S., et al., 2020, ApJ, 900, 1

Furtak L. J., Atek H., Lehnert M. D., Chevallard J., Charlot S., 2021, MNRAS, 501, 1568

Garaldi E., Kannan R., Smith A., Springel V., Pakmor R., Vogelsberger M., Hernquist L., 2021, arXiv e-prints, p. arXiv:2110.01628

Gardner J. P., et al., 2006, Science with the James Webb space telescope. SPIE, p. 62650N, doi:10.1117/12.670492

Ghosh A., Williams L. L. R., Liesenborgs J., 2021, MNRAS,

Giavalisco M., et al., 2004, ApJ, 600, L93

Glover S., 2013, The First Stars. p. 103, doi:10.1007/978-3-642-32362-1_3

Gnedin N. Y., 2016, ApJ, 825, L17

González V., Labbé I., Bouwens R. J., Illingworth G., Franx M., Kriek M., 2011, ApJ, 735, L34

Goto H., et al., 2021, arXiv e-prints, p. arXiv:2110.14474

Grazian A., et al., 2015, A&A, 575, A96

Gregory P. C., Condon J. J., 1991, ApJS, 75, 1011

Grillo C., et al., 2015, ApJ, 800, 38

Grogin N. A., et al., 2011, ApJS, 197, 35

Gunn J. E., Peterson B. A., 1965, ApJ, 142, 1633

Gutkin J., Charlot S., Bruzual G., 2016, MNRAS, 462, 1757

Harikane Y., Laporte N., Ellis R. S., Matsuoka Y., 2020, ApJ, 902, 117

Hartle J. B., 2021, Gravity: An Introduction to Einstein's General Relativity. Cambridge University Press

Hashimoto T., et al., 2018, Nature, 557, 392

Hassan S., Davé R., Mitra S., Finlator K., Ciardi B., Santos M. G., 2017, Monthly Notices of the Royal Astronomical Society, 473, 227

Heger A., Woosley S. E., 2002, ApJ, 567, 532

Heger A., Woosley S. E., 2010, ApJ, 724, 341

Henry A., et al., 2021, arXiv e-prints, p. arXiv:2107.00672

Hu E. M., Cowie L. L., Capak P., McMahon R. G., Hayashino T., Komiyama Y., 2004, AJ, 127, 563

Hu W., et al., 2019, ApJ, 886, 90

Huang K.-H., Ferguson H. C., Ravindranath S., Su J., 2013, ApJ, 765, 68

Hubble E., 1929, Proceedings of the National Academy of Science, 15, 168

Hutchison T. A., et al., 2019, ApJ, 879, 70

Hutter A., Dayal P., Yepes G., Gottlöber S., Legrand L., Ucci G., 2020, arXiv e-prints, p. arXiv:2004.08401

Ilbert O., et al., 2006, A&A, 457, 841

Ilbert O., et al., 2013, A&A, 556, A55

Illingworth G. D., et al., 2013, ApJS, 209, 6

Inoue A. K., Shimizu I., Iwata I., Tanaka M., 2014, MNRAS, 442, 1805

Ishigaki M., Kawamata R., Ouchi M., Oguri M., Shimasaku K., Ono Y., 2018, ApJ, 854, 73

Ivanov V. D., Rieke M. J., Engelbracht C. W., Alonso-Herrero A., Rieke G. H., Luhman K. L., 2004, ApJS, 151, 387

Ivezić Ž., et al., 2019, ApJ, 873, 111

Jaacks J., Thompson R., Nagamine K., 2013, ApJ, 766, 94

Jackson R. A., et al., 2021, MNRAS, 502, 4262

Jarugula S., et al., 2021, arXiv e-prints, p. arXiv:2108.11319

Jauzac M., et al., 2012, MNRAS, 426, 3369

Jauzac M., et al., 2014, MNRAS, 443, 1549

Jauzac M., et al., 2015, MNRAS, 452, 1437

Jauzac M., et al., 2016, MNRAS, 463, 3876

Jeon J., et al., 2020, arXiv e-prints, p. arXiv:2011.05918

Jiang L., et al., 2021a, Nature Astronomy, 5, 256

Jiang L., et al., 2021b, Nature Astronomy, 5, 262

Johnson J. L., 2013, Formation of the First Galaxies: Theory and Simulations. Springer Berlin Heidelberg, Berlin, Heidelberg, pp 177–222, doi:10.1007/978-3-642-32362-1_4, `https://doi.org/10.1007/978-3-642-32362-1_4`

Johnson T. L., Sharon K., 2016, ApJ, 832, 82

Johnson T. L., Sharon K., Bayliss M. B., Gladders M. D., Coe D., Ebeling H., 2014, ApJ, 797, 48

Johnston R., 2011, A&ARv, 19, 41

Jones T., Sanders R., Roberts-Borsani G., Ellis R. S., Laporte N., Treu T., Harikane Y., 2020, ApJ, 903, 150

Jullo E., Kneib J. P., 2009, MNRAS, 395, 1319

Jullo E., Kneib J. P., Limousin M., Elíasdóttir Á., Marshall P. J., Verdugo T., 2007, New Journal of Physics, 9, 447

Jullo E., Pires S., Jauzac M., Kneib J. P., 2014, MNRAS, 437, 3969

Kannan R., Garaldi E., Smith A., Pakmor R., Springel V., Vogelsberger M., Hernquist L., 2021, arXiv e-prints, p. arXiv:2110.00584

Kashino D., et al., 2021, arXiv e-prints, p. arXiv:2109.06044

Kauffmann O. B., et al., 2020, A&A, 640, A67

Kaurov A. A., Hooper D., Gnedin N. Y., 2016, The Astrophysical Journal, 833, 162

Kawamata R., Ishigaki M., Shimasaku K., Oguri M., Ouchi M., 2015, ApJ, 804, 103

Kawamata R., Oguri M., Ishigaki M., Shimasaku K., Ouchi M., 2016, ApJ, 819, 114

Kawamata R., Ishigaki M., Shimasaku K., Oguri M., Ouchi M., Tanigawa S., 2018, ApJ, 855, 4

Kemp T. W., Dunlop J. S., McLure R. J., Schreiber C., Carnall A. C., Cullen F., 2019, MNRAS, 486, 3087

Khusanova Y., et al., 2021, A&A, 649, A152

Kikuchihara S., et al., 2020, ApJ, 893, 60

Kneib J.-P., Natarajan P., 2011, A&ARv, 19, 47

Kneib J. P., Ellis R. S., Smail I., Couch W. J., Sharples R. M., 1996, ApJ, 471, 643

Koekemoer A. M., et al., 2007, ApJS, 172, 196

Koekemoer A. M., et al., 2011, ApJS, 197, 36

Koopmans L., et al., 2015, in Advancing Astrophysics with the Square Kilometre Array (AASKA14). p. 1 (`arXiv:1505.07568`)

Kriek M., et al., 2015, ApJS, 218, 15

Krist J. E., Hook R. N., Stoehr F., 2011, 20 years of Hubble Space Telescope optical modeling using Tiny Tim. SPIE - International Society for Optical Engineering, pp 81270J–81270J–16, doi:10.1117/12.892762, `http://dx.doi.org/10.1117/12.892762`

Kroupa P., 2001, MNRAS, 322, 231

Lagattuta D. J., et al., 2017, MNRAS, 469, 3946

Lagattuta D. J., et al., 2019, MNRAS, 485, 3738

Laigle C., et al., 2016, ApJS, 224, 24

Laporte N., et al., 2017, ApJ, 837, L21

Laporte N., et al., 2019, MNRAS, 487, L81

Laporte N., Meyer R. A., Ellis R. S., Robertson B. E., Chisholm J., Roberts-Borsani G. W., 2021, MNRAS, 505, 3336

Latif M. A., Whalen D., Khochfar S., 2021, arXiv e-prints, p. arXiv:2109.10655

Lazar A., Bromm V., 2021, arXiv e-prints, p. arXiv:2110.11956

Le Fèvre O., et al., 2020, A&A, 643, A1

Leitherer C., Heckman T. M., 1995, ApJS, 96, 9

Leitherer C., et al., 1999, ApJS, 123, 3

Lemaître G., 1927, Annales de la Société Scientifique de Bruxelles, 47, 49

Lemaître G., 1933, Annales de la Société Scientifique de Bruxelles, 53, 51

Liesenborgs J., De Rijcke S., Dejonghe H., 2006, MNRAS, 367, 1209

Liesenborgs J., de Rijcke S., Dejonghe H., Bekaert P., 2007, MNRAS, 380, 1729

Limousin M., et al., 2016, A&A, 588, A99

Liu C., Mutch S. J., Angel P. W., Duffy A. R., Geil P. M., Poole G. B., Mesinger A., Wyithe J. S. B., 2016, MNRAS, 462, 235

Livermore R. C., Finkelstein S. L., Lotz J. M., 2017, ApJ, 835, 113

Livet F., Charnock T., Le Borgne D., de Lapparent V., 2021, A&A, 652, A62

Lotz J. M., et al., 2017, ApJ, 837, 97

Lynds R., Petrosian V., 1986, in Bulletin of the American Astronomical Society. p. 1014

Maddox S. J., Sutherland W. J., Efstathiou G., Loveday J., 1990, MNRAS, 243, 692

Mahler G., et al., 2018, MNRAS, 473, 663

Maizy A., Richard J., de Leo M. A., Pelló R., Kneib J. P., 2010, A&A, 509, A105

Malmquist G. K., 1920, Meddelanden fran Lunds Astronomiska Observatorium Serie II, 22, 3

Malmquist K. G., 1922, Meddelanden fran Lunds Astronomiska Observatorium Serie I, 100, 1

Maraston C., 2005, MNRAS, 362, 799

Maraston C., Strömbäck G., 2011, MNRAS, 418, 2785

Martinovic K., Perigois C., Regimbau T., Sakellariadou M., 2021, arXiv e-prints, p. arXiv:2109.09779

Maseda M. V., Franx M., Chevallard J., Curtis-Lake E., 2019, MNRAS, 486, 3290

McCully C., Keeton C. R., Wong K. C., Zabludoff A. I., 2014, MNRAS, 443, 3631

McLure R. J., et al., 2011, MNRAS, 418, 2074

McLure R. J., et al., 2013, MNRAS, 432, 2696

Meneghetti M., et al., 2017, MNRAS, 472, 3177

Merlin E., et al., 2016, A&A, 595, A97

Merten J., Cacciato M., Meneghetti M., Mignone C., Bartelmann M., 2009, A&A, 500, 681

Merten J., et al., 2011, MNRAS, 417, 333

Meurer G. R., Heckman T. M., Calzetti D., 1999, ApJ, 521, 64

Meylan G., North P., Jetzer P., eds, 2006, Gravitational Lensing: Strong, Weak and Micro (`arXiv:astro-ph/0407232`)

Mobasher B., et al., 2005, ApJ, 635, 832

Mohammed I., Liesenborgs J., Saha P., Williams L. L. R., 2014, MNRAS, 439, 2651

Moneti A., et al., 2021, arXiv e-prints, p. arXiv:2110.13928

Monna A., et al., 2014, MNRAS, 438, 1417

Monna A., et al., 2015, MNRAS, 447, 1224

Narayan R., Bartelmann M., 1996, ArXiv Astrophysics e-prints, Niemiec A., Jauzac M., Jullo E., Limousin M., Sharon K., Kneib J.-P., Natarajan P., Richard J., 2020, MNRAS, 493, 3331

Noll S., Burgarella D., Giovannoli E., Buat V., Marcillac D., Muñoz-Mateos J. C., 2009, A&A, 507, 1793

O'Shea B. W., Wise J. H., Xu H., Norman M. L., 2015, ApJ, 807, L12

Ocvirk P., et al., 2020, MNRAS, 496, 4087

Oesch P. A., et al., 2010, ApJ, 709, L16

Oesch P. A., et al., 2014, ApJ, 786, 108

Oesch P. A., et al., 2015, ApJ, 804, L30

Oesch P. A., et al., 2016, ApJ, 819, 129

Oesch P. A., Bouwens R. J., Illingworth G. D., Labbé I., Stefanon M., 2018, ApJ, 855, 105

Oke J. B., Gunn J. E., 1983, ApJ, 266, 713

Ono Y., Ouchi M., Shimasaku K., Dunlop J., Farrah D., McLure R., Okamura S., 2010, ApJ, 724, 1524

Osterbrock D. E., Ferland G. J., 2006, Astrophysics of gaseous nebulae and active galactic nuclei

Ouchi M., et al., 2008, ApJS, 176, 301

Ouchi M., et al., 2009, ApJ, 696, 1164

Pagul A., Sánchez F. J., Davidzon I., Mobasher B., 2021, arXiv e-prints, p. arXiv:2103.01952

Peebles P. J. E., 1993, Principles of Physical Cosmology. Princeton Series in Physics, Princeton University Press, 41 William Street, Princeton, New Jersey 08540, USA

Peeters E., Spoon H. W. W., Tielens A. G. G. M., 2004, ApJ, 613, 986

Pei Y. C., 1992, ApJ, 395, 130

Pentericci L., et al., 2018, A&A, 619, A147

Pickles A. J., 1998, PASP, 110, 863

Planck Collaboration et al., 2016, A&A, 596, A108

Planck Collaboration et al., 2020a, A&A, 641, A6

Planck Collaboration et al., 2020b, A&A, 641, A7

Postman M., et al., 2012, ApJS, 199, 25

Ravindranath S., et al., 2006, ApJ, 652, 963

Reddy N. A., et al., 2015, ApJ, 806, 259

Reddy N. A., et al., 2018a, ApJ, 853, 56

Reddy N. A., et al., 2018b, ApJ, 869, 92

Richard J., et al., 2014, MNRAS, 444, 268

Rieke M. J., Kelly D., Horner S., 2005, Overview of James Webb Space Telescope and NIRCam's Role. SPIE, pp 1–8, doi:10.1117/12.615554

Rieke G. H., et al., 2015, PASP, 127, 584

Robertson H. P., 1935, ApJ, 82, 284

Robertson H. P., 1936a, ApJ, 83, 187

Robertson H. P., 1936b, ApJ, 83, 257

Robertson B. E., et al., 2013, ApJ, 768, 71

Robertson B. E., Ellis R. S., Dunlop J. S., McLure R. J., Stark D. P., McLeod D., 2014, ApJ, 796, L27

Robertson B. E., Ellis R. S., Furlanetto S. R., Dunlop J. S., 2015, ApJ, 802, L19

Rowe B. T. P., et al., 2015, Astronomy and Computing, 10, 121

Rudakovskyi A., Mesinger A., Savchenko D., Gillet N., 2021, arXiv e-prints, p. arXiv:2104.04481

Ryden B., 2016, Introduction to Cosmology, 2 edn. Cambridge University Press, doi:10.1017/9781316651087

Sabti N., Muñoz J. B., Blas D., 2021a, arXiv e-prints, p. arXiv:2110.13161

Sabti N., Muñoz J. B., Blas D., 2021b, arXiv e-prints, p. arXiv:2110.13168

Salmon B., et al., 2018, ApJ, 864, L22

Salmon B., et al., 2020, ApJ, 889, 189

Salpeter E. E., 1955, ApJ, 121, 161

Sanders R. L., et al., 2020, arXiv e-prints, p. arXiv:2009.07292

Santos S., et al., 2021, MNRAS, 505, 1117

Scaramella R., et al., 2021, arXiv e-prints, p. arXiv:2108.01201

Schaerer D., de Barros S., 2009, A&A, 502, 423

Schaerer D., de Barros S., 2010, A&A, 515, A73

Schechter P., 1976, ApJ, 203, 297

Schenker M. A., Ellis R. S., Konidaris N. P., Stark D. P., 2014, ApJ, 795, 20

Schlegel D. J., Finkbeiner D. P., Davis M., 1998, ApJ, 500, 525

Schmidt M., 1968, ApJ, 151, 393

Schneider P., 2006, "Einführung in die extragalaktische Astronomie und Kosmologie". Springer-Verlag Berlin Heidelberg

Schneider P., Ehlers J., Falco E. E., 1992, Gravitational Lenses, 1 edn. Astronomy and Astrophysics Library, Springer-Verlag, doi:10.1007/978-3-662-03758-4

Scoville N., et al., 2007a, ApJS, 172, 1

Scoville N., et al., 2007b, ApJS, 172, 38

Scoville N., Faisst A., Capak P., Kakazu Y., Li G., Steinhardt C., 2015, ApJ, 800, 108

Sendra I., Diego J. M., Broadhurst T., Lazkoz R., 2014, MNRAS, 437, 2642

Sérsic J. L., 1963, Boletin de la Asociacion Argentina de Astronomia La Plata Argentina, 6, 41

Sharon K., Gladders M. D., Rigby J. R., Wuyts E., Koester B. P., Bayliss M. B., Barrientos L. F., 2012, ApJ, 746, 161

Shibuya T., Ouchi M., Harikane Y., 2015, ApJS, 219, 15

Shimasaku K., et al., 2006, PASJ, 58, 313

Shipley H. V., et al., 2018, ApJS, 235, 14

Shivaei I., et al., 2020, ApJ, 899, 117

Silva L., Granato G. L., Bressan A., Danese L., 1998, ApJ, 509, 103

Smit R., et al., 2014, ApJ, 784, 58

Smit R., et al., 2015, ApJ, 801, 122

Smit R., et al., 2018, Nature, 553, 178

Smith A., Kannan R., Garaldi E., Vogelsberger M., Pakmor R., Springel V., Hernquist L., 2021, arXiv e-prints, p. arXiv:2110.02966

Soldner J.-G., 1804, Astronomisches Jahrbuch für das Jahr 1804

Sommovigo L., Ferrara A., Pallottini A., Carniani S., Gallerani S., Decataldo D., 2020, MNRAS, 497, 956

Song M., et al., 2016a, ApJ, 825, 5

Song M., Finkelstein S. L., Livermore R. C., Capak P. L., Dickinson M., Fontana A., 2016b, ApJ, 826, 113

Soucail G., 1987, The Messenger, 48, 43

Sparre M., Hayward C. C., Feldmann R., Faucher-Giguère C.-A., Muratov A. L., Kereš D., Hopkins P. F., 2017, MNRAS, 466, 88

Spergel D., et al., 2015, arXiv e-prints, p. arXiv:1503.03757

Stark D. P., Ellis R. S., Bunker A., Bundy K., Targett T., Benson A., Lacy M., 2009, ApJ, 697, 1493

Stefanon M., Bouwens R. J., Labbé I., Muzzin A., Marchesini D., Oesch P., Gonzalez V., 2017, ApJ, 843, 36

Stefanon M., Bouwens R. J., Labbé I., Illingworth G. D., Oesch P. A., van Dokkum P., Gonzalez V., 2021a, arXiv e-prints, p. arXiv:2103.06279

Stefanon M., Bouwens R. J., Labbé I., Illingworth G. D., Gonzalez V., Oesch P. A., 2021b, arXiv e-prints, p. arXiv:2103.16571

Stefanon M., et al., 2021c, arXiv e-prints, p. arXiv:2110.06226

Steidel C. C., Giavalisco M., Pettini M., Dickinson M., Adelberger K. L., 1996, The Astrophysical Journal, 462, L17

Steinhardt C. L., et al., 2020, ApJS, 247, 64

Strait V., et al., 2018, ApJ, 868, 129

Strait V., et al., 2020, ApJ, 888, 124

Strait V., et al., 2021, ApJ, 910, 135

Strickland D. K., Heckman T. M., 2009, ApJ, 697, 2030

Sugahara Y., et al., 2021, arXiv e-prints, p. arXiv:2104.02201

Tamura Y., et al., 2019, ApJ, 874, 27

Taylor A. J., Cowie L. L., Barger A. J., Hu E. M., Songaila A., 2021, ApJ, 914, 79

Teplitz H. I., et al., 2013, AJ, 146, 159

Tinsley B. M., 1978, ApJ, 222, 14

Topping M. W., Shapley A. E., Stark D. P., Endsley R., Robertson B., Greene J. E., Furlanetto S. R., Tang M., 2021, arXiv e-prints, p. arXiv:2107.06295

Torres-Albà N., Bosch-Ramon V., Iwasawa K., 2020, A&A, 635, A57

Uzgil B. D., et al., 2021, ApJ, 912, 67

Vanzella E., et al., 2020, MNRAS, 494, L81

Vazdekis A., Sánchez-Blázquez P., Falcón-Barroso J., Cenarro A. J., Beasley M. A., Cardiel N., Gorgas J., Peletier R. F., 2010, MNRAS, 404, 1639

Verma A., Lehnert M. D., Förster Schreiber N. M., Bremer M. N., Douglas L., 2007, MNRAS, 377, 1024

Vernet J., et al., 2011, A&A, 536, A105

Walker A. G., 1937, Proceedings of the London Mathematical Society, 42, 90

Wang Y.-Y., Wang L., Xiang S.-P., Wang Y., Hao J.-M., Yuan Y.-F., 2010, Research in Astronomy and Astrophysics, 10, 199

Wang T., et al., 2019, Nature, 572, 211

Weaver J. R., et al., 2021, arXiv e-prints, p. arXiv:2110.13923

Weigel A. K., Schawinski K., Bruderer C., 2016, MNRAS, 459, 2150

Weisz D. R., et al., 2012, ApJ, 744, 44

Williams R. E., et al., 1996, AJ, 112, 1335

Wold I. G. B., et al., 2021, arXiv e-prints, p. arXiv:2105.12191

Woods T. E., Willott C. J., Regan J. A., Wise J. H., Downes T. P., Norman M. L., O'Shea B. W., 2021, arXiv e-prints, p. arXiv:2109.13279

Wright G. S., et al., 2015, PASP, 127, 595

Yan L., et al., 2020, ApJ, 905, 147

Yang L., Birrer S., Treu T., 2020, MNRAS, 496, 2648

Yue B., Ferrara A., Xu Y., 2016, MNRAS, 463, 1968

Zalesky L. M., 2021, in American Astronomical Society Meeting Abstracts. p. 215.05

Zheng W., et al., 2012, Nature, 489, 406

Zheng W., et al., 2014, ApJ, 795, 93

Zhu Y., et al., 2021, arXiv e-prints, p. arXiv:2109.06295

Zitrin A., Broadhurst T., Rephaeli Y., Sadeh S., 2009, The Astrophysical Journal, 707, L102

Zitrin A., et al., 2017, ApJ, 839, L11

da Cunha E., Charlot S., Elbaz D., 2008, MNRAS, 388, 1595

Appendix A

Appendices of chapter 3

I here provide the appendices of Furtak et al. (2021), which corresponds to chapter 3 of this work. They contain additional material relative to the degeneracy between $M_\star$ and stellar age in section A.1, the impact of missing IRAC photometry on $M_\star$ measurements in section A.2 and the computation of the HFF $z \sim 6-7$ GSMF in section A.3.

A.1 Stellar age constraints in SED-fitting

The estimate of stellar mass from SED-fitting is tightly correlated with stellar age (cf. section 2.4.2). As described in section 3.2, we place dynamical constraints on the range of allowed maximum stellar ages with a lower boundary of 20 Myr. To illustrate the impact of the allowed range of stellar age on the SED-fit, we ran a model which allows stellar ages as low as 10 Myr with the otherwise same parameter configuration as the reference model (including a flat initial distribution of the age priors). The resulting best-fit SEDs (i.e., those with the maximum in the *posterior* maximum likelihood probability distribution) tend towards extremely young, ~ 10 Myr, galaxies with masses lower by ~ 0.6 dex on average compared to the average values of the reference model (e.g., $\log(M_\star/\mathrm{M}_\odot)_{(M_\mathrm{UV}=-19.5)} \simeq 8.20 \pm 0.07$). The slope of the $M_\star - M_\mathrm{UV}$-relation remains the same in the two models (cf. Fig. A.1). The consequences for the GSMF are therefore similar to adopting an exponentially rising SFH (cf. section 3.5.3 and Fig. A.7) though more pronounced: A shallower low-mass end slope α and a lower turnover mass M_T.
These much lower stellar masses are an effect of nebular emission in the SED-fitting analysis: As can be seen in Fig. A.2, in the case where we allow stellar ages down to 10 Myr (red) the best-fitting SEDs have a much lower rest-frame optical continuum than the reference model (green) but nevertheless *higher* total flux in the IRAC1 band. Indeed, the best-fit SEDs of golden and silver sources (i.e., sources with trusted IRAC photometry) tend to have EWs of $\sim$ 7000 Å for both the [O III] 5007 Å line, which is typically redshifted to the IRAC1 band in our $z \sim 6-7$ sample, and the Hα line, typically redshifted to the IRAC2 band (cf. Fig. A.3). The Bayesian fit as performed by `BEAGLE` therefore seems to favor rest-frame optical photometry dominated by nebular emission rather than stellar continuum emission.

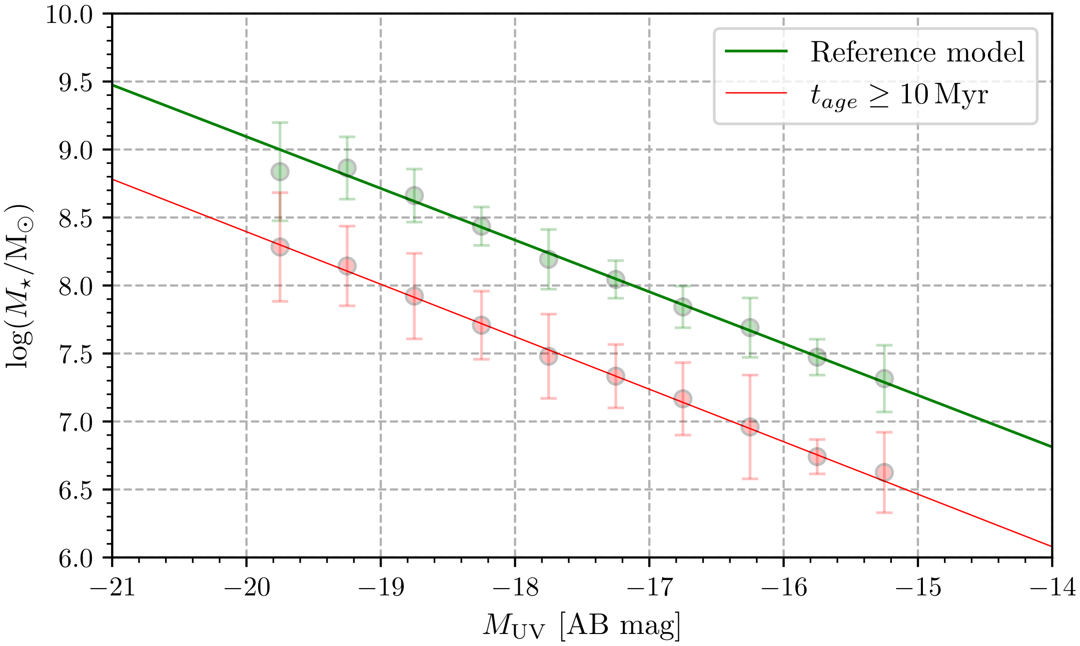

Figure A.1: Best-fit $M_\star - M_{\mathrm{UV}}$-relations for a model that allows stellar ages down to 10 Myr (red) and the reference model (green). The two relations have the same slope, $a \sim -0.38$, but allowing stellar ages down to 10 Myr yields considerably lower stellar masses (by ~ 0.6 dex).

Though these extremely high nebular EWs and subsequent young stellar ages represent maximum likelihood ('best-fit') solutions in the Bayesian fitting procedure, a closer look at the posterior distribution of the SED-fit parameters reveals the stellar age distribution to be bi-modal for most of the sources with IRAC photometry: A primary (maximum likelihood) peak close to $\sim$ 10 Myr and a secondary peak around 100 Myr. While the likelihood of the fit as estimated by `BEAGLE` favors the younger solution, observations favor the older solution since nebular EWs of $\sim$ 7000 Å have not yet been observed. Spectroscopic observations of low-redshift analogs of high-redshift galaxies merely found nebular emission line EWs < 2000 Å (Atek et al., 2011, 2014; Reddy et al., 2018b), which roughly corresponds to the order of magnitude of best-fit EWs in the reference model (cf. Fig. A.3). While it is indeed possible to find single very young galaxies of $\lesssim 10$ Myr at $z \sim 6-7$ (e.g. Ono et al., 2010; McLure et al., 2011), they are unlikely to represent our whole sample. These objects are furthermore modeled as single starbursts (McLure et al., 2011) which is not compatible with the continuous (constant and exponential) SFHs adopted in our SED-fitting technique. A small sample of bright and massive $z \sim 6-7$ galaxies has however recently been modeled with a continuous SFH and an ongoing starburst yielding very large optical EWs (up to 6240^{+1540}_{-3450} Å for [O III]+Hβ for one source; Endsley et al., 2021). The median UV continuum slope over our $z \sim 6-7$ sample $\beta_{\mathrm{UV}} \sim -2.1$ further supports stellar ages $\gtrsim 100$ Myr given the metallicities and SFHs that we probe rather than younger objects which would be expected to have bluer

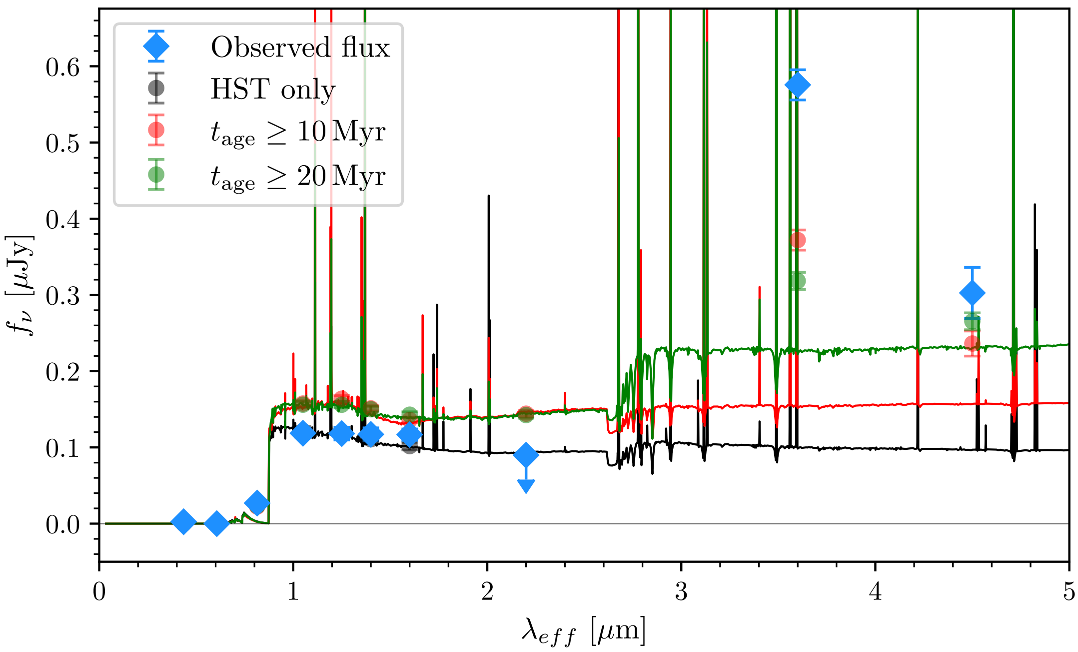

Figure A.2: Median-stacked best-fit SEDs of sources with reliable IRAC photometry at the median redshift of the golden and silver sources $z_{\rm med} = 6.28$. The blue squares represent the median observed fluxes in each band. The colored circles represent the maximum *a posteriori* fluxes of the stacked best-fit SEDs in each band. The green SED is for the reference model, the red SED allows for ages down to 10 Myr and the black SED is fit only to the seven HST bands and illustrates how the stellar mass in underestimated when only fitting rest-frame UV photometry. Note that since the majority sources are beyond the detection limit in the *Ks* band, we plot the upper limiting flux for the *Ks* band here.

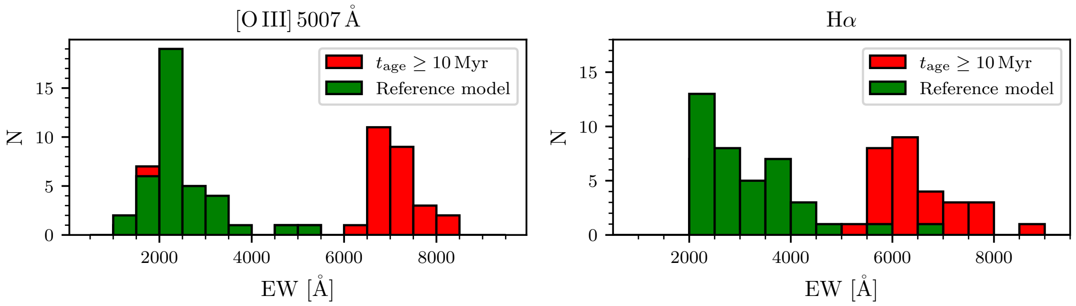

Figure A.3: Best-fit (maximum-a-posteriori) nebular EW distribution of [O III] 5007 Å (*upper panel*) and Hα (*lower panel*) from our SED-fit with `BEAGLE` for all golden and silver sources. EWs for the reference `BEAGLE` configuration are shown in green and the EWs for a model that allows stellar ages down to 10 Myr are shown in red.

UV slopes (Dunlop, 2013).

For these reasons, we favor the older ∼ 100 Myr solutions over the young maximum likelihood solutions. We therefore choose to place a lower boundary of 20 Myr on the maximum stellar age in our SED-fitting procedure in order to exclude these extremely young solutions from the overall likelihood estimates. Future observations of the rest-frame optical emission lines with JWST/NIRSpec will be required to measure the the EWs of the nebular emission lines and disentangle the nebular emission from the stellar continuum in order to robustly constrain stellar age and mass at $z \sim 6-7$ and probe possible very young starbursts.

A.2 Biases in correcting for missing IRAC photometry

As described in section 3.2.3, we correct the stellar masses for sources without reliable *Spitzer*/IRAC photometry either because they are contaminated with light from other galaxies or because they only have upper limits, using an empirical correction factor. We derived a constant correction factor $\langle\delta\rangle \simeq 0.62 \pm 0.05$ dex by comparing the stellar masses obtained from fitting SEDs to both HST+IRAC photometry and to HST photometry only. In order to quantitatively asses the applicability of the correction factor over the range of rest-frame UV luminosities probed in this study, we fit a linear relation to the mass offsets of the golden and silver sources as a function of $M_{\rm UV}$, excluding the three very luminous outliers mentioned in section 3.2.3. The fit is performed with 10^6 MCMC steps and the result can be seen in Fig. A.4. We find a best-fitting slope of $0.01^{+0.01}_{-0.04}$, which is consistent with a constant offset over the whole $M_{\rm UV}$-range probed in this analysis. Our constant correction factor is therefore applicable to our whole sample of galaxies without reliable IRAC photometry.

There is a possibility for this correction to be slightly biased towards higher stellar masses for any given rest-frame UV luminosity (obtained through HST photometry) because a rest-frame optically bright, probably more massive, galaxy is more likely to be detected in

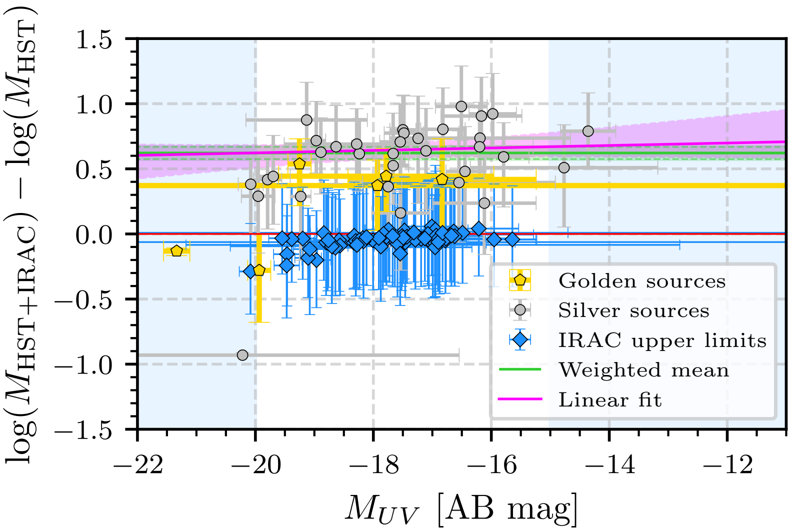

Figure A.4: Same plot as in Fig. 3.3 with in addition a linear fit to the golden and silver sources (excluding the three bright outliers described in section 3.2.3) shown as a magenta line and its 1σ-range as the magenta shaded area. The fit is clearly consistent with the constant correction factor $\langle\delta\rangle$ derived in section 3.2.3 (green line) over the effective M_{UV}-range probed in this analysis ($-20 \leq M_{\mathrm{UV}} \leq -15$, delimited by the blue shaded areas as in Fig. 3.4).

at least one of the IRAC bands. We show the median stacked best-fit SEDs of all IRAC detected galaxies and all IRAC non-detected galaxies with clean photometry (upper limits) in Fig. A.5 along with the median stacked best-fit SEDs derived including only HST photometry. The figure shows that the galaxies detected in at least one of the IRAC bands (red) are on average also brighter in their rest-frame UV magnitudes than galaxies not detected in IRAC (green). The best-fitting SEDs using only the HST photometry of the IRAC detected galaxies (black dashed curve) therefore also have higher median flux densities than the HST-only fits to the IRAC non-detected galaxies. This shows that while the HST photometry is not suited to constrain the stellar mass alone, it is sensitive enough to the stellar mass to take a possible difference in average stellar mass of the two samples into account and thus at least mitigate a possible bias towards higher mass galaxies in the constant correction factor $\langle\delta\rangle$. Fig. A.5 also shows that the stacked best-fit SEDs to HST+IRAC upper limits and the stacked best-fit SEDs to only HST photometry are identical. This demonstrates that the upper limits on the flux in both IRAC bands are not sufficient to constrain stellar mass any better than HST photometry alone (see also Fig. 3.3 and Fig. A.4).

We do not detect any flux in the stacked IRAC frames of the sources with only upper limits in the IRAC bands. This is not surprising however since we are observing exceptionally crowded fields where much brighter foreground sources lying near our sources and the ICL both contaminate the IRAC fluxes of high-redshift galaxies. We note that in particular, sources flagged as 'silver' are not completely isolated in the IRAC frames,

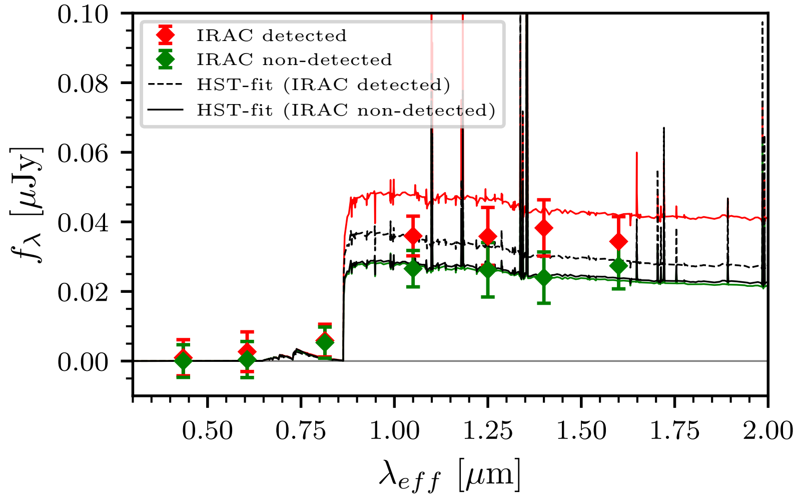

Figure A.5: Median-stacked best-fit SEDs of sources detected in at least one IRAC band (golden and silver sources; red line) and of sources that are not detected by the 3σ-limits in both IRAC1 and IRAC2 (green line) at the median redshift $z_{\rm med} = 6.08$. The colored pentagons represent the corresponding median flux in each band. The dashed and solid black lines show the median-stacked best-fit SEDs when only fitting HST-photometry for both galaxy samples respectively. The SEDs were trimmed down to only show the rest-frame UV emission probed by the HST-bands.

we merely estimate that the aperture in which we measure the IRAC photometry is not significantly contaminated by either sources of contaminating light (cf. section **??**). However, in the stack, this extra foreground light leads to unexpectedly high noise levels such that we do not gain a factor $\sqrt{N}$ in signal-to-noise through stacking. Furthermore, stacking sources at different locations over several strong lensing clusters neglects the fact that the magnification and its uncertainties depend on the source position. The stacked flux cannot be simply interpreted as saying much about the physical properties of a given population of galaxies. In the literature, a meticulous stacking analysis conducted in blank fields found low signal-to-noise galaxies to be indeed biased towards higher stellar masses (Song et al., 2016a). In a discussion on systematics, Behroozi et al. (2019) however argue that these results could also be due to SED-fitting degeneracies (e.g., degeneracy between stellar mass and stellar age). We therefore conclude that our average correction factor $\langle\delta\rangle$ is applicable over the range of UV luminosities probed in our sample of galaxies without IRAC photometry, even though we cannot *completely* rule out a bias towards slightly higher stellar masses with the available data.

A.3 Further GSMF material

In this section we provide additional material to the GSMFs computed in section 3.4. Tab. A.1 shows the stellar mass values of our GSMF points for each `BEAGLE` configuration

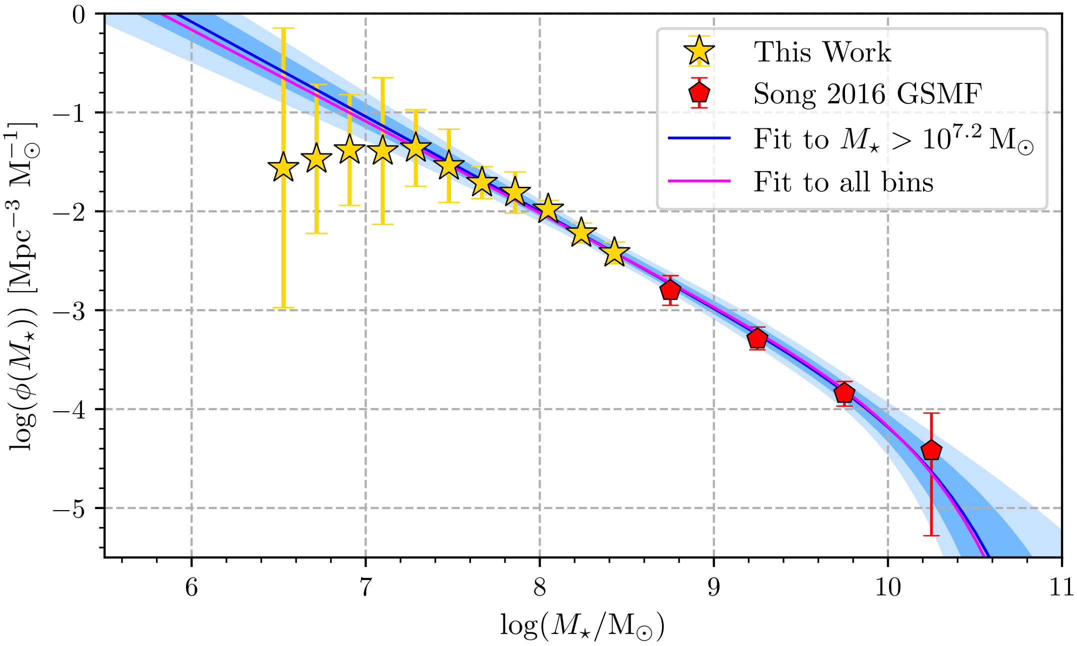

Figure A.6: The same graph as in the *left-hand* panel of Fig. 3.6 with in addition a 'classical' Schechter fit to all mass bins, including those $\log(M_\star/\mathrm{M}_\odot) < 7.2$, as the magenta curve. It shows that including the lowest-mass bins does not significantly affect the best-fit Schechter function in the reference model.

from Tab. 3.3, computed from the rest-frame UV luminosity bins in Atek et al. (2018). The four wide-area blank field high-mass GSMF points that we use in our GSMF-fits can be found in table 2 in Song et al. (2016a). The $\phi(M_\star)$ of our GSMFs are then shown in Tab. A.2 along with their total errors for each `BEAGLE` configuration. These errors combine gravitational lensing and rest-frame UV photometry uncertainties from Atek et al. (2018), cosmic variance uncertainty by Robertson et al. (2014) and uncertainties in the determination of stellar mass from our SED-fitting analysis including the uncertainty in the empirical correction factor derived in section 3.2.3. Note that the errors do not strongly differ between the different SED-fitting models which indicates them to be dominated by the lensing uncertainties.

We show in Fig. A.6 that including the lowest-mass bins ($\log(M_\star/\mathrm{M}_\odot) < 7.2$) in the the 'classical' Schechter function fit does not significantly affect the best-fitting parameters in the reference model. Fig. A.8 presents the posterior distributions for the four modified Schechter parameters of the GSMF fits for each SED-fitting model. As mentioned in section 3.4, the GSMF does not strongly depend on metallicity (upper left panel). The posterior distributions of the GSMF fit parameters for the SFH and dust attenuation tests (upper right and lower panels in Fig. A.8 respectively) further illustrate the strong impacts of SFH and dust attenuation on the GSMF, in particular its low-mass end slope α. They also emphasize the correlation between α and the low-mass end turnover

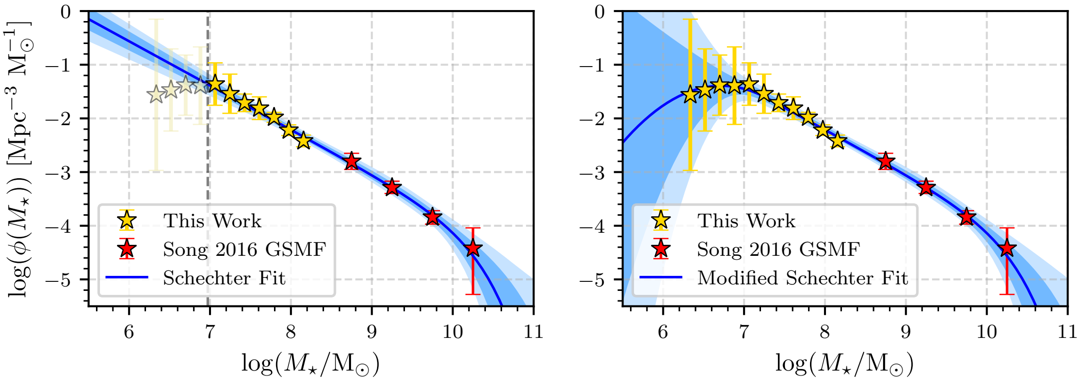

Figure A.7: The same graphs as in Fig. 3.6 but for the exponentially rising SFH model ($\psi(t) \propto \exp(t/\tau)$). This configuration allows for an upward turnover of the GSMF at the 1σ-level (blue shaded area in the right panel).

curvature β. The upper right and lower panels of Fig. A.8 in particular illustrate that the two models with the steepest low-mass end slopes α allow for a much wider range in β-space, resulting in the very large uncertainties in β discussed in section 3.4.
Apart from those two cases where β is very poorly constrained, only in the exponentially rising SFH case the MCMC fit of the GSMF allows for an upward turnover in the 1σ-range (blue shaded area in Fig. A.7) with a well constrained curvature. This is also the model that yields the shallowest low-mass end slope in our study with $\alpha \simeq -1.82^{+0.08}_{-0.07}$. Our modified Schechter parametrization of the GSMF, cf. equation (3.6), and the MCMC-fitting procedure therefore seem to disfavor $\beta < 0$ solutions for our measured GSMF points for steeper low-mass end slopes. This enables us to place a lower boundary on the range of low-mass end slopes that allow for an upward turnover at the 1σ level at $\alpha \gtrsim -1.82$ (cf. Tab. 3.5). Since the shallower α in the exponentially rising SFH case is a direct consequence of overall lower stellar masses, as discussed in section 3.5.3, this implies that $\beta \leq 0$ (i.e. the GSMF does not turn over or has an upward turnover) requires the majority of galaxies at $z \sim 6-7$ to be very very young, very low-mass galaxies with high exponentially increasing SFRs. Any conclusion of this sort would however require a much more robust derivation of the extremely low-mass end of the $z \sim 6-7$ GSMF.

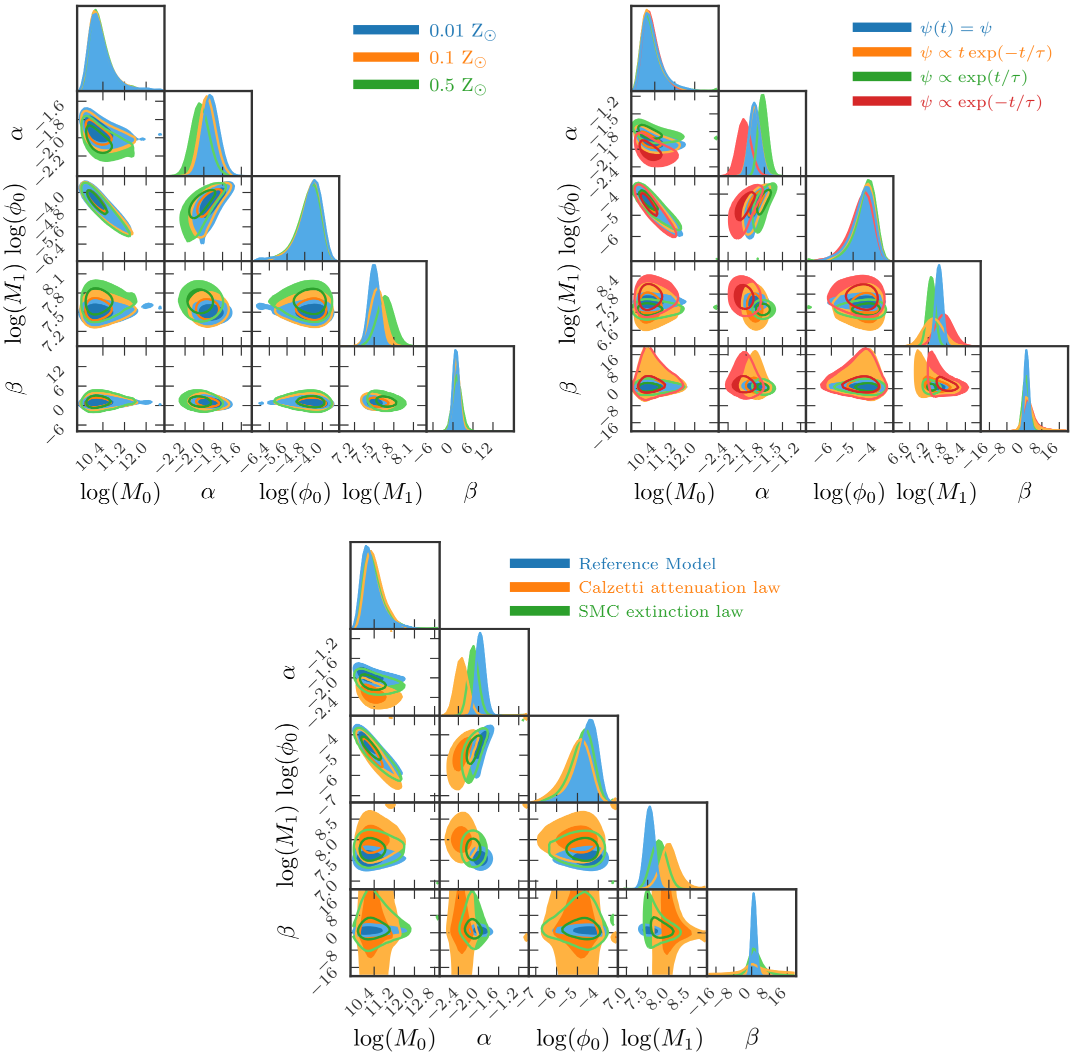

Figure A.8: *Upper left panel*: Posterior distributions of the four modified Schechter parameters for assuming different metallicities in the SED-fit. The resulting GSMF is not strongly impacted by metallicity. *Upper right panel*: Posterior distributions of the four modified Schechter parameters for assuming different SFHs in the SED-fit. The most notable impact of SFH is on the low-mass end slope α: A rising SFH results in a shallower and a declining SFH in a steeper low-mass end slope. The constant and the delayed SFH on the other hand almost yield the same GSMF. *Lower panel*: Posterior distributions of the four modified Schechter parameters for assuming different dust attenuation laws and values in the SED-fit: Calzetti law with $\hat{\tau}_V \in [0, 0.2]$ (blue), Calzetti law with $\hat{\tau}_V \in [0, 3]$ (orange) and SMC law with $\hat{\tau}_V \in [0, 3]$ (green). Dust attenuation mostly impacts the low-mass end of the GSMF, resulting in steeper low-mass end slopes α and in much larger uncertainties on the curvature β when allowing $\hat{\tau}_V \in [0, 3]$.

Table A.1: Stellar mass bins of our final $z \sim 6 - 7$ GSMFs computed from UV luminosity bins by Atek et al. (2018) using the $M_\star - M_{\rm UV}$-relations for all `BEAGLE` configurations in table 3.4.

Reference model	*Metallicity tests*		*SFH tests*			*Dust tests*	
$\log M_\star$ $\mathrm{M}_\odot$	$\log M_\star$ ($0.01\,\mathrm{Z}_\odot$) $\mathrm{M}_\odot$	$\log M_\star$ ($0.5\,\mathrm{Z}_\odot$) $\mathrm{M}_\odot$	$\log M_\star$ (delayed) $\mathrm{M}_\odot$	$\log M_\star$ (rising) $\mathrm{M}_\odot$	$\log M_\star$ (declining) $\mathrm{M}_\odot$	$\log M_\star$ ($\hat{\tau}_V \in [0,3]$) $\mathrm{M}_\odot$	$\log M_\star$ (SMC law) $\mathrm{M}_\odot$
8.43	8.36	8.55	8.46	8.16	8.68	8.67	8.49
8.24	8.17	8.36	8.26	7.97	8.50	8.58	8.36
8.05	7.98	8.17	8.07	7.79	8.32	8.48	8.22
7.86	7.79	7.99	7.87	7.61	8.15	8.39	8.09
7.67	7.60	7.80	7.68	7.43	7.97	8.30	7.96
7.48	7.42	7.61	7.48	7.25	7.80	8.20	7.83
7.29	7.23	7.42	7.29	7.06	7.62	8.11	7.69
7.10	7.04	7.23	7.10	6.88	7.44	8.01	7.56
6.91	6.85	7.05	6.90	6.70	7.27	7.92	7.43
6.72	6.66	6.86	6.71	6.52	7.09	7.82	7.29
6.53	6.47	6.67	6.51	6.34	6.91	7.73	7.16

Table A.2: Final $z \sim 6-7$ GSMF bins $\phi(M_\star)$ and their uncertainties for each `BEAGLE` configuration. The first column shows the mass bins of the reference model.

		Reference model	*Metallicity tests*		*SFH tests*			*Dust tests*	
$\log M_\star$ $\mathrm{M}_\odot$	$\log \phi(M_\star)$ $\mathrm{Mpc}^{-3}\mathrm{M}_\odot^{-1}$	$\Delta \log \phi$ $\mathrm{Mpc}^{-3}\mathrm{M}_\odot^{-1}$	$\Delta \log \phi$ ($0.01\,\mathrm{Z}_\odot$) $\mathrm{Mpc}^{-3}\mathrm{M}_\odot^{-1}$	$\Delta \log \phi$ ($0.5\,\mathrm{Z}_\odot$) $\mathrm{Mpc}^{-3}\mathrm{M}_\odot^{-1}$	$\Delta \log \phi$ (delayed) $\mathrm{Mpc}^{-3}\mathrm{M}_\odot^{-1}$	$\Delta \log \phi$ (rising) $\mathrm{Mpc}^{-3}\mathrm{M}_\odot^{-1}$	$\Delta \log \phi$ (declining) $\mathrm{Mpc}^{-3}\mathrm{M}_\odot^{-1}$	$\Delta \log \phi$ ($\hat{\tau}_V \in [0,3]$) $\mathrm{Mpc}^{-3}\mathrm{M}_\odot^{-1}$	$\Delta \log \phi$ (SMC law) $\mathrm{Mpc}^{-3}\mathrm{M}_\odot^{-1}$
8.43	−2.42	0.11	0.11	0.11	0.11	0.11	0.11	0.15	0.11
8.24	−2.22	0.10	0.10	0.10	0.11	0.10	0.10	0.11	0.11
8.05	−1.98	0.09	0.09	0.09	0.10	0.09	0.12	0.11	0.10
7.86	−1.81	0.21	0.21	0.21	0.20	0.21	0.20	0.21	0.21
7.67	−1.71	0.16	0.17	0.16	0.16	0.16	0.16	0.16	0.16
7.48	−1.54	0.37	0.37	0.38	0.37	0.36	0.37	0.37	0.37
7.29	−1.36	0.39	0.39	0.38	0.38	0.40	0.38	0.39	0.39
7.10	−1.39	0.74	0.74	0.75	0.74	0.72	0.73	0.72	0.72
6.91	−1.38	0.56	0.57	0.56	0.62	0.56	0.57	0.54	0.56
6.72	−1.47	0.75	0.74	0.76	0.74	0.77	0.85	0.74	0.75
6.53	−1.56	1.41	1.60	1.41	1.42	1.41	1.41	1.42	1.42

Appendix B

Technical details of the BUFFALO photometry strategy

In this appendix I relate some of the technical details of the BUFFALO data and HST photometry performed for our BUFFALO high-redshift catalogs in chapter 4. I briefly discuss the various fields and depths of the BUFFALO observations in section B.1 and provide a detailed account of our `SExtractor` setup strategy in section B.2.

B.1 The BUFFALO coverage pattern

As mentioned in section 4.2.1, the BUFFALO coverage is not of uniform depth. Instead, the new shorter (2/3 orbit) BUFFALO observations form a shallower region around the cluster cores previously observed in the HFF program (cf. section 2.3 and Tab. 3.1). The BUFFALO mosaics therefore show a pyramid-like pattern with the deep integrations of the cluster cores in the middle and the shallower BUFFALO area around. The same pattern applies to all six clusters and their parallel fields (cf. Fig. B.1). Throughout this work I have referred to these two areas as the *inner* and *outer* fields respectively as is illustrated for A370 in Fig. B.2. Note that the outer fields, the blue squares in Fig. B.2, are specifically designed to match the field-of-view of the NIRSpec instrument aboard the JWST (Steinhardt et al., 2020).

B.2 BUFFALO HST photometry

Our source detection and HST photometry measurements are done using `SExtractor v2.5.0` in dual mode with the detection stacks as detection images and the original mosaics as measurement images (cf. section 4.2.2). We use $\frac{0.06''}{\mathrm{pix}}$ mosaics for our analysis. The `SExtractor` runs are divided into two configurations in order to accommodate the difference in depth between the inner and the outer fields as shown in sections B.2.1 and B.2.2.

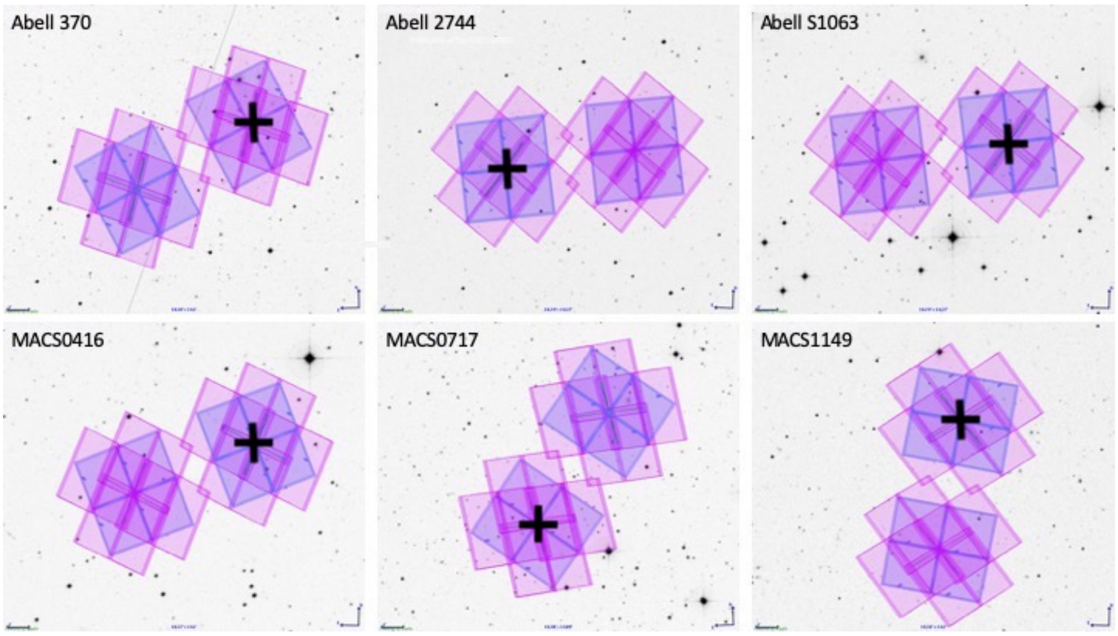

Figure B.1: BUFFALO coverage map for all six HFF clusters, produced with the HST Astronomer's Proposal Tool (APT). The observations with the WFC3 filters F105W, F125W and F160W (blue) each have 2/3 orbit depths and the ACS filters F606W and F814W (pink) have 2/3 and 4/3 orbit depths respectively. The black crosses each designate the cluster centers. Figure credit: Steinhardt et al. (2020).

Similarly to what was used in our work on the HFF, we extract isophotal (`FLUX_ISO`) and total fluxes (`FLUX_AUTO`). We run the same `SExtractor` configurations with the variance maps as the measurement images in order to accurately extract the flux errors in the same segmentations as the fluxes. This way, the pixel-wise variances are summed over the segmentation of each image such that the square root of this sum gives the uncertainty on the flux. In order to achieve this we modify the following parameters in the `SExtractor` configurations given in sections B.2.1 and B.2.2:

```
#------------------------------ Background -----------------------------------

BACK_TYPE        MANUAL
BACKPHOTO_TYPE   GLOBAL
BACK_VALUE       0.0
```

This configuration ensures that no background is subtracted from the variance maps in the process.

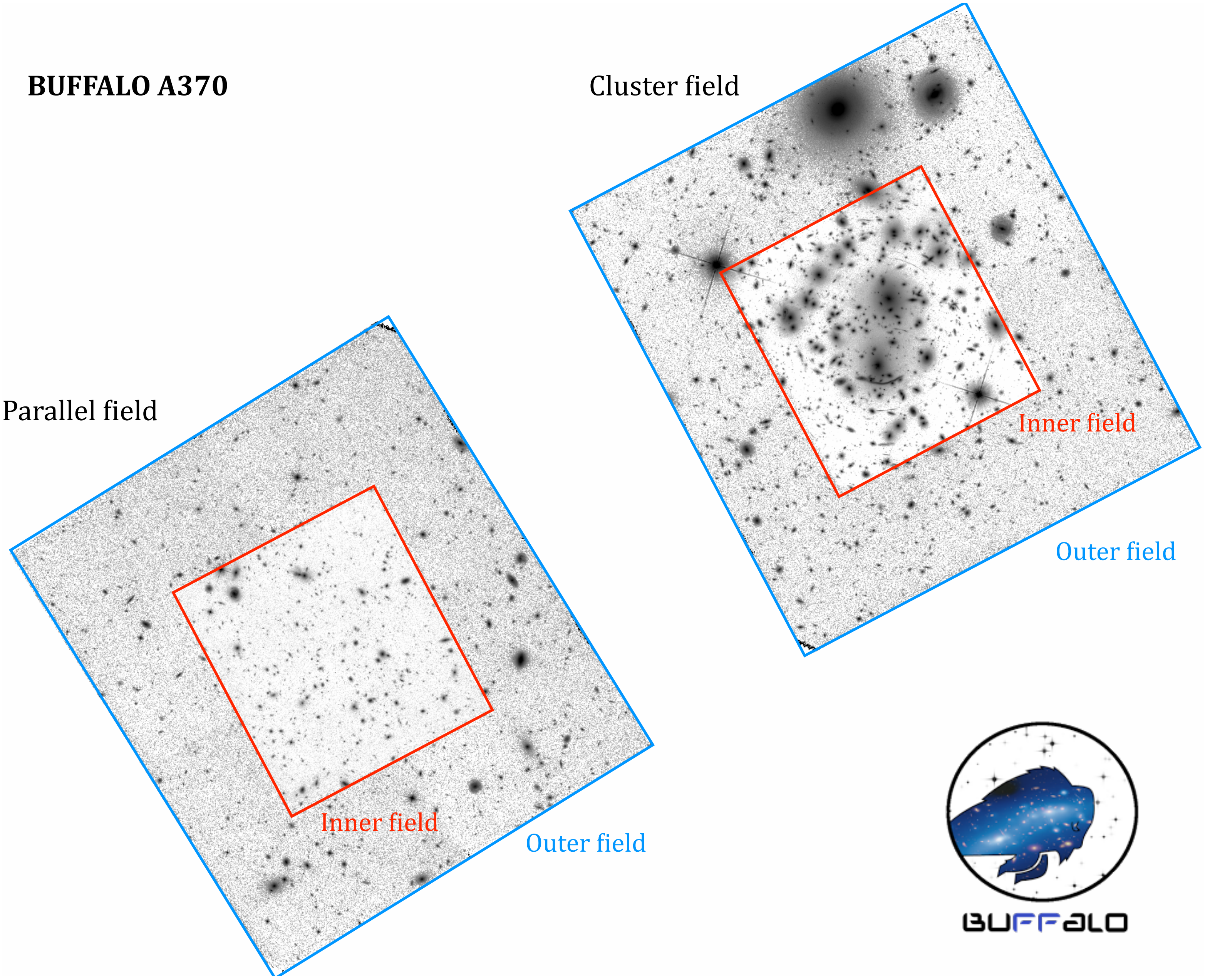

Figure B.2: Full BUFFALO WFC3/F125W mosaic of A370. The deeper *inner* regions (red) correspond to the initial HFF coverage and the shallower *outer* regions correspond to the newly added area with BUFFALO.

B.2.1 Inner field extraction — example `SExtractor` configuration file

In the following, I show a `SExtractor` configuration file used for cluster core detection (i.e. on the inner field) in the F105W band. This configuration is optimized for the detection of extremely small and faint sources in a crowded and deep field such as the cluster cores and was already used on the HFF in e.g. Atek et al. (2015a, 2018). All other `SExtractor` parameters not set in the following configuration file are left at their default values.

```
# BUFFALO high-redshift catalog configuration file for SExtractor 2.5.0

#-------------------------------- Catalog ------------------------------------

CATALOG_NAME    A370-core_F105W_deepIR_catalog.cat
CATALOG_TYPE    ASCII_HEAD

PARAMETERS_NAME SExtractor/buffalo.param

#------------------------------- Extraction ----------------------------------

DETECT_TYPE     CCD
DETECT_MINAREA  2
THRESH_TYPE     RELATIVE

DETECT_THRESH   3
ANALYSIS_THRESH 2.5

FILTER          Y
FILTER_NAME     SExtractor/gauss_2.0_3x3.conv
FILTER_THRESH

DEBLEND_NTHRESH 16
DEBLEND_MINCONT 1e-5

CLEAN           Y
CLEAN_PARAM     1.0

MASK_TYPE       CORRECT

#-------------------------------- WEIGHTing ----------------------------------

WEIGHT_TYPE     MAP_WEIGHT, MAP_RMS

WEIGHT_IMAGE    ../Data/A370_WFC3-stack_wht.fits,../Data/A370_F105W_rms.fits
```

```
WEIGHT_GAIN     N, Y
WEIGHT_THRESH

#------------------------------ Photometry ----------------------------------

PHOT_APERTURES          28.33
PHOT_AUTOPARAMS         2.5, 3.5
PHOT_PETROPARAMS        2.0, 3.5

PHOT_AUTOAPERS          0.0,0.0

PHOT_FLUXFRAC           0.5

SATUR_LEVEL             50000.0

MAG_ZEROPOINT           26.2687
MAG_GAMMA               4.0
GAIN                    1.0
PIXEL_SCALE             0.06

#------------------------- Star/Galaxy Separation ----------------------------

SEEING_FWHM     0.1
STARNNW_NAME    SExtractor/mynnw.nnw

#------------------------------ Background -----------------------------------

BACK_TYPE       AUTO
BACK_VALUE      0.0
BACK_SIZE       32
BACK_FILTERSIZE 3

BACKPHOTO_TYPE  LOCAL
BACKPHOTO_THICK 24
BACK_FILTTHRESH 0.0

#------------------------------ Check Image ----------------------------------

CHECKIMAGE_TYPE SEGMENTATION
CHECKIMAGE_NAME A370-core_F105W_deepIR_seg.fits
```

B.2.2 Outer field extraction

For the detection and photometry runs on the outer field, we only modify a few parameters of the above configuration in order to account for the higher noise levels in the shallower region and for less crowding. We therefore set the following parameters in order to achieve less aggressive deblending than was required in the crowded cluster cores and to avoid spurious detections in these noisier areas:

```
#------------------------------- Extraction ----------------------------------

DETECT_MINAREA  9

DEBLEND_NTHRESH 8
DEBLEND_MINCONT 1e-3
```

European Organisation for Astronomical Research in the Southern Hemisphere
Observing Programmes Office • Karl-Schwarzschild-Strasse 2 • D-85748 Garching bei München • email: opo@eso.org • Tel: +49 89 3200 6473

Cycle: P108
Type: Normal
Status: Valid
Printed: 24 Sep 2021

APPLICATION FOR OBSERVING TIME 108.22MV

IMPORTANT NOTICE

By submitting this proposal, the PI takes full responsibility for the content of the proposal, in particular with regard to the names of CoIs and the agreement to act according to the ESO policy and regulations, should observing time be granted.

A Primeval Galaxy under the Microscope I - Confirming the redshift of a highly magnified z~8 galaxy

ABSTRACT

Highly star-bursting galaxies at z~8 are at the frontier of observability. Their physical properties remain widely unknown because their rest-frame optical emission features are redshifted far beyond reach of current observing facilities. We therefore propose to obtain a rest-frame UV spectrum of a Lyman break galaxy at z_phot=7.78, identified in the strong lensing Hubble Frontier Fields cluster Abell 370. As this source at m = 25.24 AB has a particularly high gravitational magnification of μ>8, the study of its rest-frame UV Lyman-α and [CIII] emission lines will yield rare insight into the physics of a typical galaxy in the epoch of reionization. The accurate determination of its spectroscopic redshift will furthermore pave the way for follow-up observations with the Atacama Large Millimeter/submillimeter Array and identify a premium target for the upcoming James Webb Space Telescope.

SCIENTIFIC CATEGORY

A6 Reionization and cosmic dawn

RUNS

Run	Period	Instrument	Tel. Setup	Constraints	Mode	Type	Propr. Time	Time Constr.	Req. Time
108.22MV.001 • Main run	108	XSHOOTER	UT3	FLI: 100% • Turb.: 70% • pwv: 30.0mm • Sky: Clear	VM	Normal	12m	✗	10h32m

AWARDED AND FUTURE TIME REQUESTS

Time already awarded to this project

- none -

Future time requests to complete this project

- none -

Special Remarks

n/a

DESCRIPTION OF THE PROPOSED PROGRAMME

A- Scientific Rationale

The study of young star-bursting galaxies at the highest observable redshifts represents one of the major constraints on galaxy formation and evolution models and is one of the key challenges in modern astrophysics. With modern observing facilities the first generations of stars and galaxies in the epoch of cosmic reionization now lie within observational reach down to 400 million years after the Big Bang. These high-redshift galaxies at $z > 6$ represent the progenitors of present-day galaxies and are thus crucial in understanding galaxy evolution and the history of star-formation in the Universe. Recent deep imaging campaigns with the *Hubble Space Telescope* (HST) and supporting ancillary surveys with ground-based facilities have been enormously successful in detecting $z > 6$ galaxies and constraining their luminosity and stellar mass functions based on photometric redshifts (e.g. Song et al. 2016a, Atek et al. 2018, Kikuchihara et al. 2020). Detailed exploration of the end of the Dark Ages however requires accurate spectra of high-redshift galaxies in addition to the photometry. The observation of intrinsically faint high-redshift galaxies magnified through strong lensing (SL) clusters is therefore the method of choice to obtain spectroscopic information of $z > 6$ galaxies and to identify prime targets for the next generation of telescopes such as the *James Webb Space Telescope* (JWST) and the *European Extremely Large Telescope* (E-ELT). The *Hubble Frontier Fields* program (HFF, Lotz et al. 2017) has obtained deep HST observations of some of the most massive known strong lensing systems. Additional ancillary observing programs of the HFF clusters with *Spitzer Space Telescope* and other ground-based facilities make the six HFF clusters the best studied SL fields to date and thus the most valuable fields for high-redshift studies.

In this context, we report the identification of an intrinsically faint $z \sim 8$ galaxy candidate in Abell 370 (A370) from a complete sample, which benefits from a particularly high gravitational magnification (cf. Fig. 1). The source presents a break of $(F105W_{\mathrm{AB}} - F125W_{\mathrm{AB}}) = 0.85$ which is typical for $z \sim 8$ galaxies. It also presents a slight excess in the *Spitzer*/IRAC channel 2 ($4.5\,\mu$m), a typical indicator for a $z \sim 8$ galaxy whose optical [O III]$\lambda 5007$ Å and Hβ emission features are redshifted to IRAC channel 2 wavelengths (e.g. De Barros et al. 2019). This source is observed at an F160W band magnitude of $m_{F160W,AB} = 25.24$ and most recent SL models of A370 (e.g. Strait et al. 2019) yield gravitational magnification factors of order $\mu \gtrsim 8$ for $z_s = 8$ at the source's coordinates. This means this source is intrinsically faint with a de-lensed relative F160W band magnitude of $m_{F160W,\mathrm{AB}} = 27.50$ and an absolute rest-frame UV (1500 Å) magnitude of $M_{\mathrm{UV,AB}} = -19.5$. An SED fit with the `BayEsian Analysis of GaLaxy sEds` tool (`BEAGLE`, Chevallard & Charlot 2016) yields very tight constraints on the photometric redshift, with an estimate of $z \simeq 7.78 \pm 0.05$ and a stellar mass estimate of $\log\left(\frac{M_\star}{\mathrm{M}_\odot}\right) \simeq 8.60^{+0.12}_{-0.24}$ (cf. Figs. 2 & 3).

To date there are only five galaxies confirmed at $z \sim 8$ (Finkelstein et al. 2013, Oesch et al. 2015, Song et al. 2016b, Laporte et al. 2017, Tamura et al. 2019). All of them were either observed in blank fields or have relatively low gravitational magnification factors $\mu \lesssim 2$. They are therefore intrinsically bright and relatively massive ($M_\star \gtrsim 10^9\,\mathrm{M}_\odot$) and thus constitute an unrepresentative sample of galaxies at high redshift. **We therefore hereby propose to use X-SHOOTER to obtain rest-frame UV spectra of this highly magnified low-mass $\mathbf{z \sim 8}$ galaxy candidate in A370**. As this object is intrinsically too faint to be observed in a blank field, it constitutes a unique probe of low-mass galaxies at high redshift. Its study across observable wavelengths will therefore yield invaluable insight into the physics of typical galaxies in the epoch of reionization.

B- Immediate Objective

We propose to use X-SHOOTER to observe a low-mass $z \sim 8$ candidate galaxy to detect its Lyα emission line and possibly its [C III]$\lambda 1909$ Å and [C III]$\lambda 1907$ Å emission line doublet. Our main science objectives are as follows:

- To accurately determine the redshift of this $z \sim 8$ galaxy candidate and thus to confirm its high-redshift nature. If confirmed, this galaxy will add to the scarce numbers of known $z \sim 8$ galaxies (five to date and only one with measured [C III] emission lines, see Hutchison et al. 2019) and present a valuable target for future generations of telescopes, especially given its uniquely high magnification factor.

- To investigate properties such as metallicity, stellar age and ionization parameter of this $z \sim 8$ galaxy. As shown in Hutchison et al. 2019, the combination of [C III] equivalent widths with IRAC1-IRAC2 colors provides constraints on the physical parameters of galaxies at $z \sim 8$. These can be used to calibrate SED-fitting methods of statistically significant photometric high-redshift catalogs in order to treat some of the degeneracies inherent to estimating these parameters from broad-band photometry alone (see e.g. Furtak et al. 2021).

- To measure this galaxy's Lyα velocity offset ($\Delta v_{Ly\alpha}$) from its systemic redshift, inferred with the [C III] lines, which can provide valuable insight into the kinematics and Lyα escape fraction (e.g. Hutchison et al. 2019) of this relatively low-mass $z \sim 8$ galaxy. Constraints on the Lyα escape fraction have important implications on the ionizing power of low-mass high-redshift galaxies and their ability to reionize the Universe.

- To prepare deep high-resolution follow-up observations of this source with the *Atacama Large Millimeter/submillimeter Array* (ALMA). Rest-frame far-infrared (FIR) observations of high-redshift galaxies deep in the epoch of reionization have the potential to yield deep insight into early star-formation and the onset of chemical enrichment of the Universe at high redshifts as these wavelengths cover the [O III]$\lambda 88\,\mu$m, [C II]$\lambda 158\,\mu$m and dust continuum emission at $z \sim 8$ (e.g. Laporte et al. 2017; 2019, Tamura et al. 2019). The few observations of this kind have so far been carried out for relatively bright and massive galaxies at $z \sim 8$. Our low-mass $z \sim 8$ target would therefore enable new insight into the dust physics in a lower stellar mass range.

Figures

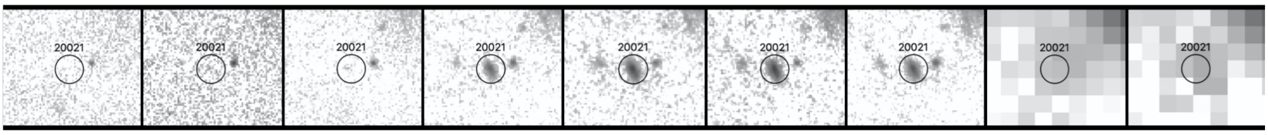

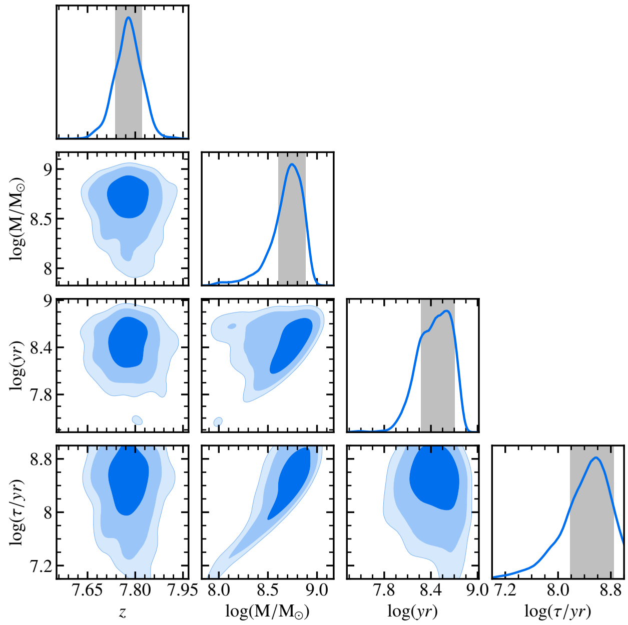

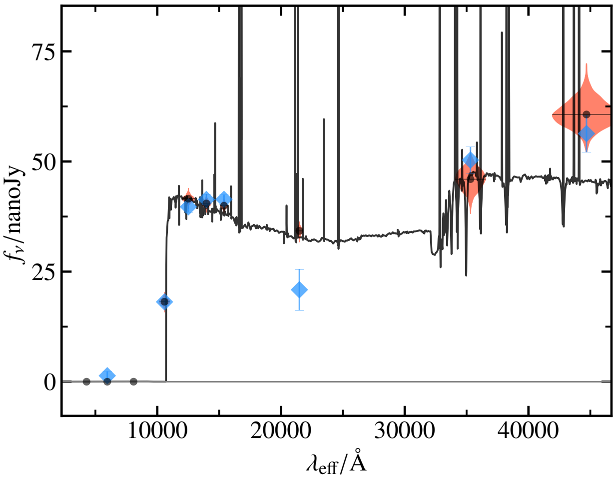

Fig.1 (*top panel*) Image cutouts of the $z \sim 8$ dropout candidate A370-20021. From left to right: F435W, F606W, F814W, F105W, F125W, F140W, F160W, IRAC1 and IRAC2. The source is clearly detected in the WFC3/IR bands but shows no detection at the 2σ-level in bands blueward of the break (i.e. the ACS bands). It also shows a slight excess in the IRAC channel 2 band, a typical feature of galaxies at $z \sim 8$. The black circle has a diameter of 1". **Fig.2** (*lower left panel*). Posterior distributions of the four fit-parameters (photometric redshift z, stellar mass M, maximum stellar age and star-formation e-folding time τ) in our SED-fit of A370-20021 with `BEAGLE`. **Fig.3** (*lower right panel*) Observed spectral energy distribution of the $z \sim 8$ dropout candidate A370-20021 (blue diamonds); maximum-a-posteriori spectrum predicted by `BEAGLE` (black curve); marginal posterior distribution of fluxes in each band predicted by `BEAGLE` (salmon "violins", with the black circle in each violin representing the posterior median of the predicted flux). Note the prominent [C III] emission features predicted by the best-fit SED at ~ 16760 Å.

References

1. Atek, H., et al. (2018), MNRAS, 479, 5184 – **2.** Chevallard, J. & S. Charlot (2016), MNRAS, 462, 1415 – **3.** De Barros, S., et al. (2019), MNRAS, 489, 2355 – **4.** Furtak, L. J., et al. (2021), MNRAS, 501, 1568 – **5.** Finkelstein, S. L., et al. (2013), Natur, 502, 524 – **6.** Hutchison, T. A., et al. (2019), ApJ, 879, 70 – **7.** Kikuchihara, S., et al. (2020), ApJ, 893, 60 – **8.** Laporte, N., et al. (2017), ApJL, 837, L21 – **9.** Laporte, N., et al. (2019), MNRAS, 487, L81 – **10.** Lotz, J. M., et al. (2017), ApJ, 837, 97 – **11.** Oesch, P. A., et al. (2015), ApJL, 804, L30 – **12.** Song, M., et al. (2016a), ApJ, 825, 5 – **13.** Song, M., et al. (2016b), ApJ, 826, 113 – **14.** Strait, V., et al. (2018), ApJ, 868, 129 – **15.** Tamura, Y., et al. (2019), ApJ, 874, 27

TARGETS

Name	RA	Dec	Coord	Runs	Comment
A370-20021	02:39:50.582	-01:34:26.979	J2000	1	
H=25.24; J=25.28; Y=26.13					

Target Notes

- none -

REMARKS & JUSTIFICATIONS

Lunar Phase and Constraints Justification

Please justify here the requested lunar phase and other observing constraints.

Our X-SHOOTER program aims at obtaining near-infrared spectroscopy of a high-redshift galaxy, which is not affected by moon illumination. We therefore do not request any lunar phase constraint as long as the moon is kept > 30° away from our target.

Time Justification

Please describe here a detailed computation of the necessary time to execute the observations, including time-critical aspects if any. Parameters used in the ETC should be mentioned so the computation can be reproduced.

A previously reported detection of a Lyman-α emission line at z = 8.38 by Laporte et al. 2017 yielded an integrated Lyα flux of (1.82 ± 0.46) × 10^−18 erg s^−1 cm^−2 at the 4σ-level with 7.5 hours of X-SHOOTER integration time on target (Laporte et al. 2017). Other observations of galaxies at z~8 reported Lyα fluxes up to 10 × 10^−18 erg s^−1 cm^−2 (e.g. Hutchison et al. 2019). A detection of the [CIII]1907 A emission line at z = 7.5 by Hutchison et al. 2019 yielded an integrated [CIII] flux of (2.63 ± 0.52) × 10^−18 erg s^−1 cm^−2 at the 5.6σ-level resulting in a [CIII]/Lyα ratio of 0.30 ± 0.04.

Using the latest version of the X-SHOOTER Exposure Time Calculator, we use a setup with a slit-width of 1.2″, slightly larger than our target, and assume a seeing of 1″ and an airmass of 1.4 to calculate the optimal exposure time required to achieve our science goals: Assuming a minimum line-flux estimated at 2 × 10^−18 erg s^−1 cm^−2 and a line FWHM of 0.5 nm, as reported by Hutchison et al. 2019 , we find a [CIII]1907 A emission line redshifted to 16761 A at our target's photometric redshift to be detectable with a S/N-ratio of 5 with 10 hours integration time on X-SHOOTER. Assuming a [CIII]/Lyα ratio of 0.30 and a slightly narrower line FWHM, this setup would yield a >7σ detection of Lyα redshifted to 10667 A.
Seeing as our source is slightly brighter (~1 magnitude) than the Laporte et al. 2017 source and at roughly the same F160W magnitude as the Hutchison et al. 2019 source, we expect its Lyα and [CIII] emission lines to be perfectly detectable with this setup.

Our target is visible for up to 7 hours per night with the requested maximum airmass of 2. To enable optimal observability of our target at its highest point in the sky we choose to divide the 10 hours total integration time on target into 4 integrations of 2.5 hours each.

We therefore request a total of 10 hours of X-SHOOTER integration time on our target, divided into four integrations of 2.5 hours each, spreadable over several nights. We expect telescope and instrument overheads of 4 x ~8 minutes, combining to a total of 10h 32min in cycle 108.

Telescope Justification

Please justify why the telescope requested is the best choice for this programme.

We expect to observe fluxes of the order of 2 × 10^−18 erg s^−1 cm^−2, where only an 8-m class telescope can observe to a sufficient depth in a reasonable amount of time. Our science goals furthermore require high spectral resolution coverage of the rest-frame UV emission of our target, redshifted to NIR wavelengths λ > 10600 A. X-SHOOTER on UT3 perfectly meets all of these requirements.

Observing Mode Justification

Please justify the choice of SM, VM or dVM.

Given the relative simplicity of our observing runs, this program can be carried out in service mode. We however favor visitor mode since our target is very small (~1''), of the order of the chosen slit-size, and very faint. Hence real time monitoring and slight adjustments to make sure the slit is well on target during the observation runs might be necessary.

Calibration Request

If you need any special calibration not included in the instrument calibration plan, please specify it here.

Standard Calibration

Duplication with ESO Science Archive

If observations of the same target(s) using the same instrument(s) already exist in the ESO archive, please justify why this programme requests further observations.

None of the requested data are in the ESO archive.

GTO & Survey Target Duplication Justification

If an instrument GTO or Public Survey team aims at the same target(s), please justify why this programme requests further observations.

There is no duplication with GTO/Public survey programs.

Background and Expertise

Short description of the background, expertise and roles of the various team members in the context of the science case discussed in the proposal. For small teams the applicants may wish to provide a sentence for the qualifications of each member, while for larger teams (e.g. in Large Programmes), only the leading roles need to be specified.

PI Lukas Furtak is an expert in high-redshift galaxy physics and observations with a particular focus on faint gravitationally lensed low-mass galaxies. He also has expertise in data reduction, catalog assembly and ground-based slit-spectroscopy.

Dr. Hakim Atek is an expert in high-redshift galaxies, starbursts and observations of lensed sources with extensive experience in data treatment and spectroscopy.

Dr. Matthew Lehnert is an expert in galaxy physics and has extensive expertise in galaxy observations, spectroscopy and ESO instrumentation.

REPORT ON PREVIOUS USAGE OF ESO FACILITIES

- none -

RECENT PI/CoIs PUBLICATIONS MOST RELEVANT TO THE SUBJECT OF THIS PROPOSAL

1. Furtak, L. J., et al. (2021) "How robustly can we constrain the low-mass end of the z □ 6-7 stellar mass function? The limits of lensing models and stellar population assumptions in the HFF," MNRAS, 501, 1568-1590 - 2021MNRAS.501.1568F

2. Steinhardt, C. L., Jauzac, M., Acebron, A., et al. (2020) "The BUFFALO HST Survey," ApJS, 247, 64 - 2020ApJS..247...64S

3. Atek, H., et al. (2018) "The extreme faint end of the UV luminosity function at z □ 6 through gravitational telescopes: a comprehensive assessment of strong lensing uncertainties," MNRAS, 479, 5184-5195 - 2018MNRAS.479.5184A

INVESTIGATORS

Lukas Furtak, Institut d'Astrophysique de Paris/CNRS and Sorbonne University, France (PI)
Hakim Atek, Institut d'Astrophysique de Paris/CNRS and Sorbonne University, France
Matthew Lehnert, Centre de Recherche Astrophysique de Lyon, France

OBSERVATIONS

In the table below, the repeat factor is applied to the complete observation on that target, including its overhead.

✔ The PI acknowledged that all the telescope times listed below include overheads.

Run 108.22MV.001 • Main run • P108 • XSHOOTER • VM Tel. Time: 10h32m

FLI: 100% • Turb.: 70% (Seeing < 1.0 arcsec) • pwv: 30.0mm • Sky: Clear • Airmass: 2.0

Target • A370-20021 • 02:39:50.582 • -01:34:26.979 Tel. Time: 10h32m

OS 1	SLT	SLT
Tel. Time: 9467 s	Telescope Overheads: 360 s	UVB Slit: 1.0x11
Repeat: 4 x		VIS Slit: 0.9x11
Total Tel. Time: 10h32m		NIR Slit: 1.2x11
		UVB readout mode: 100k/1pt/hg
		VIS readout mode: 100k/1pt/hg
		Integration Time: 9000 s
		Instrument Overheads: 107 s
		Signal/Noise: 5.0

Appendix C

Linking galaxy parameters to $M_\star$ and z

In the galaxy toy-model that we used for our completeness simulations, we linked several galaxy parameters, namely stellar age, dust extinction optical depth and gas-phase metallicity, to the uniformly distributed stellar mass and redshift (cf. section 5.2.1) of each galaxy. We here provide some more details of the relations used and show the PDFs from which the parameters are drawn.

C.1 Dynamical constraints on stellar age

The stellar age is drawn from a probability distribution based on the dynamical time scale which we compute as in Furtak et al. (2021) (cf. section 3.2.1) using equation 3.2. Since in our model, described in section 5.2.1, the UV-luminosity and thus the radius of each galaxy are computed *after* the SED is generated, we here need to make a crude estimate of the radius to compute t_{dyn}. To that end we use the $M_\star - M_{\mathrm{UV}}$-relation previously measured in section 3.3 (the delayed SFH case) to estimate the galaxy's UV luminosity which is then used to compute the *mean* half-light-radius of the corresponding log-normal size-luminosity relation by Kawamata et al. (2018) and Huang et al. (2013) (depending on the redshift). The width of the stellar age distribution is then computed by propagating the width of the size-luminosity relation σ_r to $\sigma_{t_{\mathrm{dyn}}}$. While this results in a relatively wide probability distribution, as can be seen in Fig. C.1, using t_{dyn} as the lower limit for stellar age results in a sharp cut-off on the lower age range in any specific redshift bin (Fig. C.1 shows the $z \sim 6-7$ case). This makes sure we do not get combinations in which very massive galaxies are very young which would result in unrealistically large nebular emission line EWs as in Furtak et al. (2021) (cf. section A.1) which is the main goal of using these dynamical constraints on the stellar age.

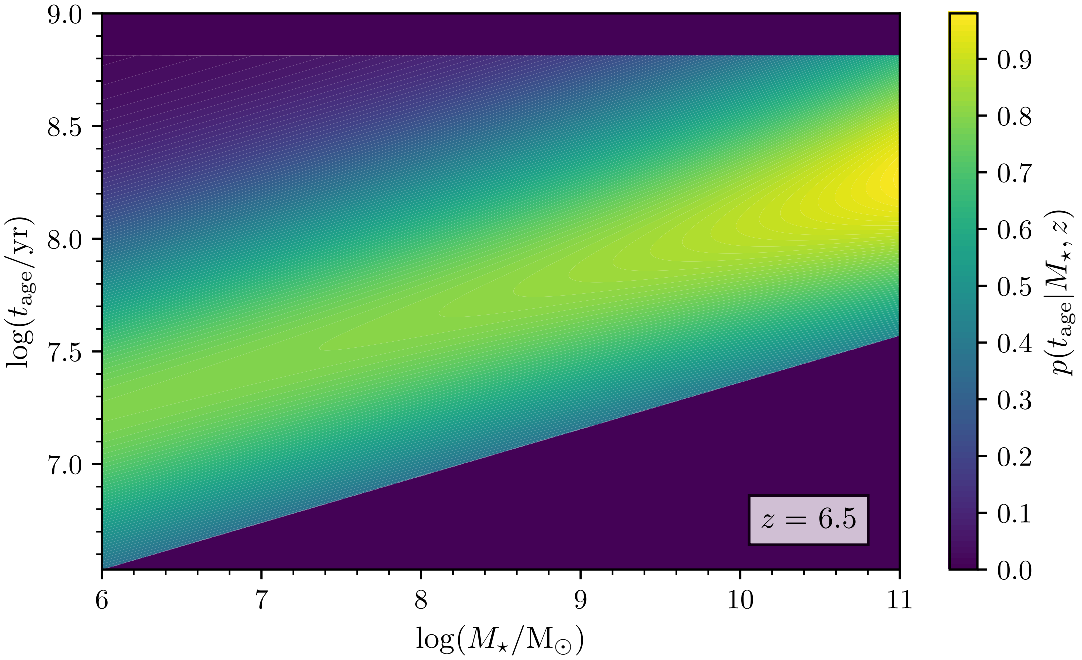

Figure C.1: Probability distribution of stellar age as a function of stellar mass in the $z \sim 6-7$ bin based on the dynamical time scale. Note the sharp lower limit on stellar age which excludes unrealistic young and massive galaxies.

C.2 Observational constraints on $\hat{\tau}_V$ and $Z_{\rm gas}$

The effective V-band dust extinction optical depth and the gas-phase metallicity are each drawn from observed relations measured in low-redshift analogs of star-forming galaxies at high redshifts in the scope of the *MOSFIRE Deep Evolution Field* survey (MOSDEF; Kriek et al., 2015).

For the first, $\hat{\tau}_V$, we use the stellar-mass reddening relations computed from the MOSFIRE spectroscopic sample of $z = 1.4-2.6$ star-forming galaxies by Shivaei et al. (2020). Note that we use the *stellar* extinction relation from Shivaei et al. (2020), not the nebular relation since `BEAGLE` only accepts stellar extinction. This relation was measured for relatively massive galaxies $10^{8.5}\,{\rm M}_\odot \leq M_\star \leq 10^{10.5}\,{\rm M}_\odot$. While we extrapolate it all the way down to $10^6\,{\rm M}_\odot$, it quickly converges to extremely low values at low stellar masses. We therefore truncate the resulting probability distribution of $\hat{\tau}_V$ at $\hat{\tau}_V = 0$ and $\hat{\tau}_V = 1$ to prevent negative and unrealistically high values. This resulting probability distribution is shown in Fig. C.2. The dust extinction remains relatively low over the whole stellar mass range which is consistent with what is expected for high-redshift galaxies (e.g. Bouwens et al., 2016; Bhatawdekar & Conselice, 2021).

For the gas-phase metallicity, we use a $z = 2.3-3.3$ MOSDEF star-forming galaxy mass-metallicity relation measured by Sanders et al. (2020). While this relation was also mea-

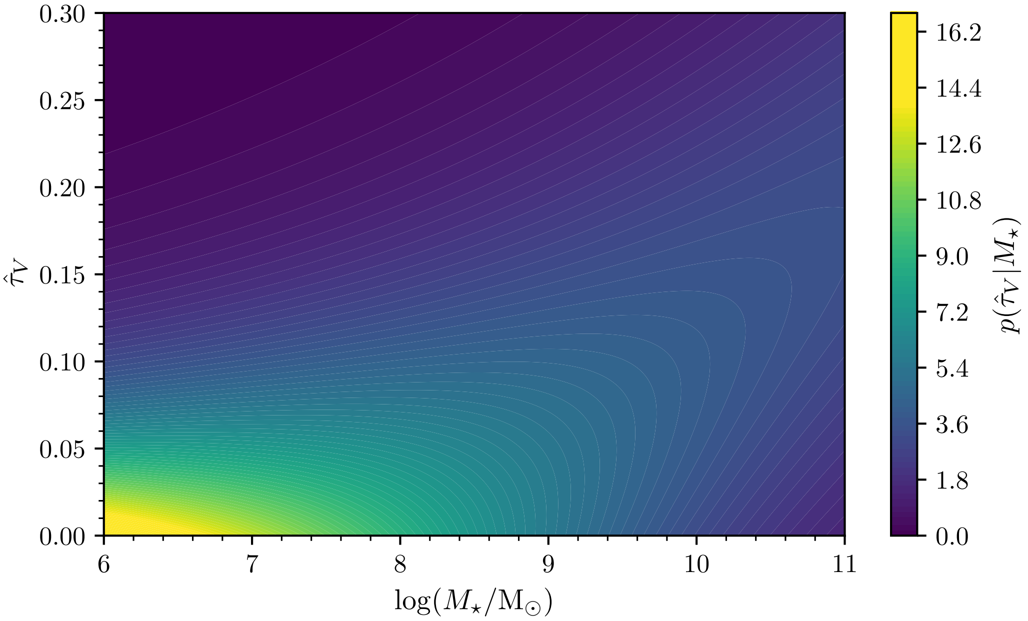

Figure C.2: Probability distribution of effective V-band dust extinction optical depth as a function of stellar mass based on low-redshift analogs of high-redshift galaxies observed by Shivaei et al. (2020).

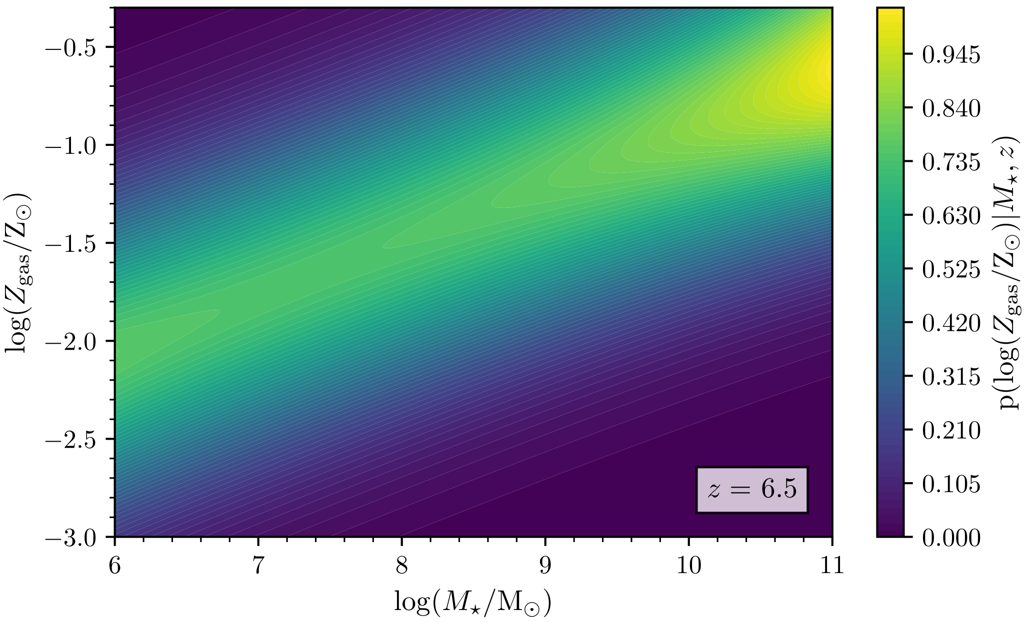

Figure C.3: Probability distribution of gas-phase metallicity as a function of stellar mass and redshift for $z = 6.5$ based on low-redshift analogs of high-redshift galaxies observed by Sanders et al. (2020).

sured in high-mass ($10^{8.5}\,\mathrm{M}_\odot \leq M_\star \leq 10^{10.5}\,\mathrm{M}_\odot$) galaxies, it is consistent with similar measurements at slightly lower redshifts (e.g. Henry et al., 2021) and extrapolates down to the low metallicities expected low-mass galaxies expected for high-redshift galaxies (cf. section 2.4.2). We extrapolate the redshift evolution of this mass-metallicity relation, also measured in Sanders et al. (2020), out to the redshift of each simulated galaxy in order to scale down the galaxy's mass-metallicity relation. As a result we obtain the redshift-dependent probability distribution shown in Fig. C.3 for each simulated galaxy.

C.3 $M_\star$ dependent size-luminosity relations

As explained in section 5.2.1, we use two size-luminosity relations in our completeness simulations: A simple Kawamata et al. (2018) relation (which becomes a Huang et al. (2013) relation for galaxies with $z < 5.5$) *and* a Kawamata et al. (2018) (or Huang et al., 2013) relation with a fixed $r_e = 0.003''$ for galaxies with $M_\mathrm{UV} \geq -16$ following Atek et al. (2018). The latter point was found to have significant impact on the completeness estimate of high-redshift galaxy samples (Atek et al., 2018).

Preliminary results of our completeness simulations however indicate there to be no significant difference between the selection functions derived from the two simulations as can be seen in Fig. C.4 in comparison to Fig. 5.7. Both size-luminosity relations result in total recovered galaxy fractions of order 50 % and yield identical results over the whole $(z, M_\star)$. This is due to the relative steepness of the Kawamata et al. (2018) size-luminosity relation which results in half-light radii of order $\lesssim 0.01''$ on the extreme faint end as opposed to the shallower Shibuya et al. (2015) relation used in Atek et al. (2018).

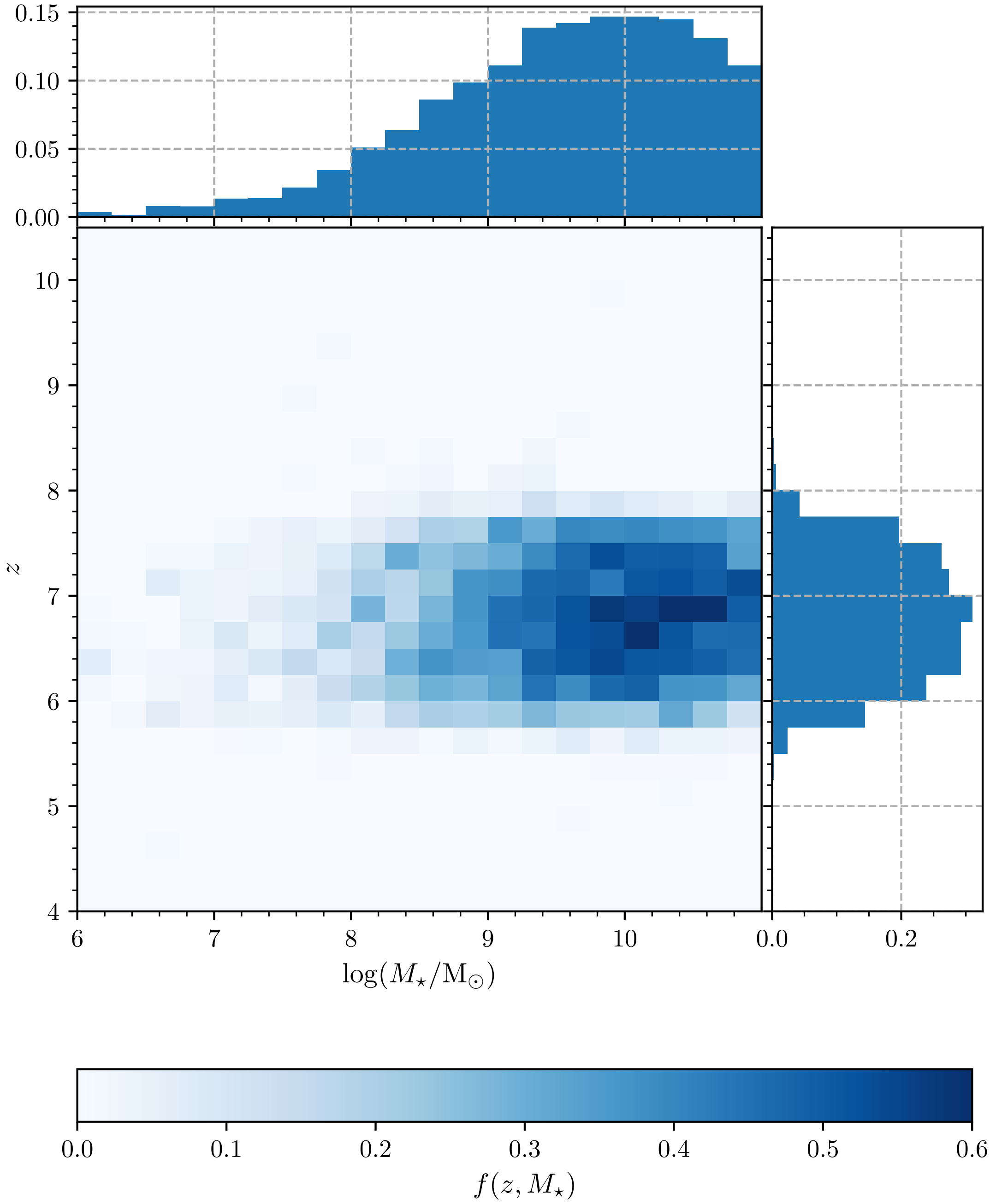

Figure C.4: Same plot, preliminary selection function $f(z, M_\star)$ as a function of redshift z and stellar mass $M_\star$ as computed from the CATS model simulation of A370, as in Fig. 5.7 but for a fixed $r_e = 0.003''$ for galaxies with $M_{\mathrm{UV}} \geq -16$ as in Atek et al. (2018) following the findings in Bouwens et al. (2017a).

Acknowledgements

> "The most important step a man can take. It's not the first one, is it? It's the next one. Always the next step, Dalinar."
>
> ---
>
> Brandon Sanderson,
> *The Stormlight Archive:*
> *Oathbringer*, 2017

Yes, I know what you are going to say: 'That epigraph is not a Sir Terry quote!'... Well yes but I do what I want and I have wanted to place a *Stormlight* quote somewhere forever now. Besides, I could argue that the ancient ideals of the Knights Radiant apply as much to a PhD thesis than to anything really. Anyway, while you're at it, you might also try to spot the not very cunningly concealed *Donjon de Naheulbeuk* reference floating around somewhere in this manuscript.

However, since a thesis does not exactly pop out of the ground like a mushroom without any exterior help, there are quite a few people I would need to express my gratitude to before closing this manuscript off for good. Without further ado, I would therefore first like to warmly thank my thesis committee for taking the time to actually read this whole thing and to attend and evaluate my defense. Next and most importantly, to the two people without whom, to use an overused phrase, I would not be where I am today: My supervisors, Matt and Hakim (in reverse alphabetical order this time) who not only beta-read this entire thesis (and multiple times) but also put up with me for three years, patiently went over technical details with me (including at 2am on observation night) and all but nursed me through the most difficult days of work during lockdown. Thank you for being my advisors and the excellent mentors that you are. Thanks also to Iary and Anton for coaching me through some of the most technical aspects of photometry and SED-fitting, to Valérie for always being nice and helpful, to Henry, who managed to make me swallow a coffee on occasion, and to all the BUFFALO and COSMOS people around the world for insightful discussions and equally insightful beers.

Life is not just work (yes, I know, funny coming from me of all people that, ain't it?). My special thanks therefore go to my friends at IAP and beyond, all those who lent me their support: To Lisa, my best friend and sister in arms, steadfast and dependable as ever and one of the best scientists that I know. To Pierre, my faithful morning tea companion in (nearly) every weather for three years, and to Alexandre who, equally faithful, was a friend from day 1 (just not before lunchtime). To my original office mates, the Knights of the (4th) Post-Newtonian Order, Quentin and François. To Iver, who arrived just in time to see the very end of my thesis but quickly became a close friend nonetheless. And also to Eduardo (SHAI-HULUD!), Shweta, Lucas, Aline the green dragon, Virginia ("J'ai faim! Il te reste des gateaux?"), Julien, Marko, Dani, Etienne (C'est CHOCOLATINE, bordel!), Clint/Clément, Lucie ("I am Kvothe [...] You may have heard of me."), Amaury, Louis ("Pause?"), Marie (Metal will never die!), Florian, John, the remaining Knights of the Moonsea Camilla and Geray, and the previous generation students who shall not be forgotten: Doogesh, Arno, Martin, Amael, Simon and Matteo. Thanks for making the last few years what they were.

Last but not least, as always, to my family who will undoubtedly once again point out they were not mentioned first but hey, you don't change a winning strategy and besides, you know already. Thanks for supporting me, as ever.

And finally, because it is so beautiful and one cannot simply quote Sir Terry Pratchett all over an astronomy thesis without mentioning the star turtle, let me conclude with:

> "*Through the fathomless deeps of space swims the star turtle Great A'Tuin, bearing on its back the four giant elephants who carry on their shoulders the mass of the Discworld. A tiny sun and moon spin around them, on a complicated orbit to induce seasons...*"

— Sir Terry Pratchett, *Wyrd Sisters*, 1997

List of Figures

List of Tables

“*Moi je n’ai pas besoin de torche, je suis nyctalope!*”

— John Lang, *À l’aventure compagnons*, 2013